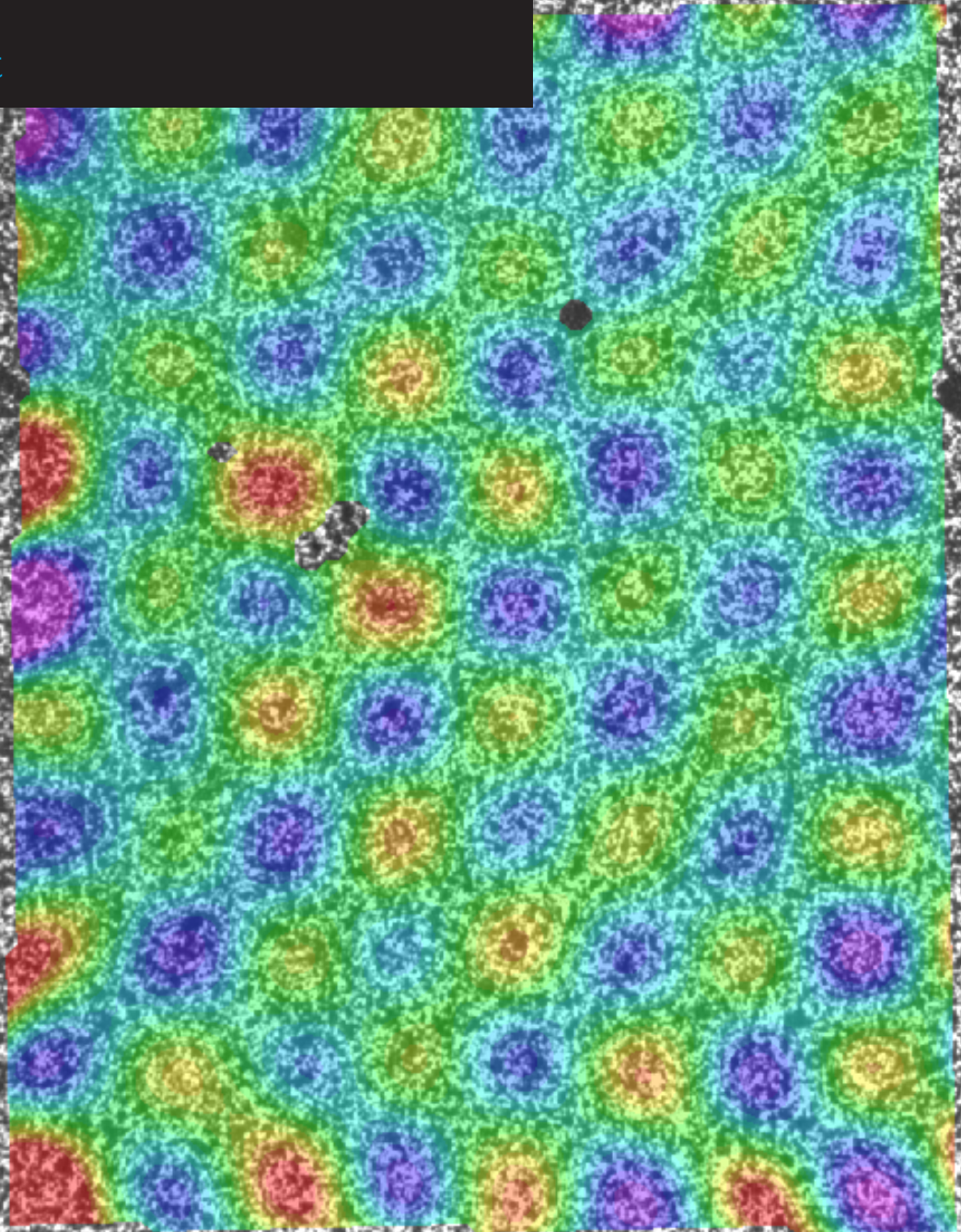


Compression-Compression and Tension-Compression Fatigue of Woven Carbon-Epoxy Composites

Experimental Testing and Instrumentation

S. Walraet

Technische Universiteit Delft



Compression-Compression and Tension-Compression Fatigue of Woven Carbon-Epoxy Composites

Experimental Testing and Instrumentation

by

S. Walraet

In partial fulfillment of the requirements for the degree of

Master of Science

in Aerospace Engineering

at the Delft University of Technology,

In collaboration with Ghent University,

to be defended publicly on Thursday June 22, 2017 at 9:30 AM.

Student number: 4178041
Project duration: September 1, 2016 – June 22, 2017
Supervisors: Dr. C. Kassapoglou, TU Delft
Ir. R. D. B. Sevenois, Ghent University
Prof. dr. ir. W. Van Paepegem, Ghent University
Thesis committee: Dr. R. De Breuker (Chairman), TU Delft
Dr. C. Kassapoglou, TU Delft
Ir. R. D. B. Sevenois, Ghent University
Prof. dr. ir. W. Van Paepegem, Ghent University

Preface

This M.Sc. thesis finalizes my research at the Mechanics of Materials and Structures research group at Ghent University in Belgium on experimental characterization of woven carbon-epoxy loaded in compression-compression and tension-compression fatigue. It also means the end of six years of studying aerospace engineering at Delft University of Technology, a challenging and enriching experience which would not have been possible without the help and company of many people.

First of all I would like to thank my direct supervisor, mentor and friend **Ruben Sevenois**. Under his supervision I had the freedom to design my own project and come up with new ideas, in a friendly environment. His insight, ideas and daily guidance motivated me throughout this last year to work better and faster, and to come up with innovative solutions.

For this project I have been lucky to have received guidance from not one but two renowned experts in the field, **Wim Van Paepegem** and **Christos Kassapoglou**. Despite their full agendas they have been a formidable help for this thesis project. Every discussion with one of them (or both) resulted in a major step forward for the quality of my research. Additional thanks goes to **Roeland De Breuker**, who serves as chairman of the thesis committee.

Many more people at the research group have been of help in one way or another, others have helped in proofreading of my thesis. I would therefore like to express my gratitude to **Klaas Allaer, Pascal Baele, Gabriele Chiesura, Ives De Baere, Aline De Bondt, Matthias Herthoge, Matthias Kersemans, Alfredo Lamberti, Nicolas Lammens, Aurélie Laureys, Simon Moreels, Mathijs Peeters, Joanna Schalnat, Cedric Schepens, Dries Schroyen, Siebe Spronk, Luc Van Den Broecke, Roger Van Hecke, Joachim Vanwalleghem** and **Ilse Vercruyse** for their help, insight, inspiration and/or the enjoyable coffee/lunch breaks.

I am very grateful to have such amazing friends and family for their loving support throughout these last 6 years. I would like to thank **Astrid**, for her love, patience and understanding throughout this last year. Finally, I would like to show my gratitude to my parents, **Greet** and **Joris**. For these past 24 years, they have provided me with a safe and loving environment and the freedom to study what I wanted and follow my dreams. These last six years have not all been straightforward, but you helped me get back up whenever I needed it, you are amazing parents.

*S. Walraet
Ghent, June 2017*

Summary

To reduce carbon emissions of their products, manufacturers in the transportation sector typically aim to reduce weight where possible. One of the keys to lightweight design is the use of lightweight materials. CFRP (carbon fiber-reinforced polymer) composites are considered the most promising in terms of potential weight reductions. While UD (unidirectional) composites can be used to achieve high strengths and stiffnesses, woven composites have the advantage of easier handling, and better resistance to out-of-plane loads. Fatigue failure of woven composite materials is a complex phenomenon occurring on different scales, which makes modeling of the behaviour difficult. Some modeling efforts based on the evolution of (shear) stiffness, permanent (shear) strain, Poisson's ratio and residual strength are promising but lack experimental input. When experiments are reported they are often based on S-N curves or CLDs (constant-life diagrams). DIC (Digital Image Correlation) was identified as a potentially powerful method to measure evolution of these properties. Experiments reported in literature typically only cover T-T (tension-tension) loading. However, many loading situations can be characterized as C-C (compression-compression) or T-C (tension-compression) fatigue.

In this work, results from C-C and T-C experiments on woven carbon-epoxy material are reported. To be able to effectively use DIC in combination with other measurement devices, it is important to consider the experimental set-up behind this. Two architectures were designed to be used based on availability of measurement equipment. Both use different software packages to control cameras and retrieve analog data. Time delays between analog signals and DIC are corrected for using a simulated annealing optimization algorithm with cubic interpolation of displacement data. Free edge delaminations are an artefact of coupon testing. A combined system with cameras at both front and side of a specimen proved to be of value in keeping track of this damage and linking it to its effect on stiffness evolution.

For coupon tests including compression, careful specimen design is required since buckling should be avoided at all cost. For these experiments, this was achieved by using specimens short enough for unstable modes not to occur. While this introduces stress concentrations near the clamping ends, other alternatives include questionable side loading or more complex stress states. Sizing is done based on analytical and finite element approaches. Load transfer can be done through shear loading of tab material or combined shear and end loading. Two specimen types were designed based on this with thin aluminum tabs for shear loading or thicker steel tabs for combined loading. Static and fatigue experiments with these specimens reveal that a combination of aluminum tabs with shear loading outperforms steel tabs, where failure occurs sooner and is initiated in the stress concentration region.

Experiments are performed for two lay-ups: $[(0/90)]_{24}$ and $[(\pm 45)]_{24}$. The first step was to perform static compression tests until failure for both lay-ups. Ultimate strength for loading aligned with fibers ($[(0/90)]_{24}$) is much higher compared to off-axis loading ($[(\pm 45)]_{24}$), where the stress-strain behaviour is strongly non-linear and strain at failure is significantly larger. The fact that loading of the latter is matrix-dominated gives rise to a strain rate dependence of the ultimate strength.

For each lay-up, fatigue experiments are limited to two R-ratios, $R = 10$ for C-C fatigue and $R = -1$ for T-C fatigue. The test program covers loading ranges from run-out loads (at which specimens last at least 500,000 cycles before stopping the test) to low cycle fatigue loading near the ultimate strength. While specimen heating was no issue for $[(0/90)]_{24}$, for $[(\pm 45)]_{24}$ laminates, shearing motion of fibers did induce significant heating of the specimens. This was coped with through adaptation of frequencies in combination with an air cooling system to limit heating. For high loading at $R = -1$, this still did not suffice and this case was omitted from the program, since it is an unlikely situation for real-life structures.

Despite a limited amount of experiments performed, S-N data indicates a relatively flat curve for C-C experiments compared to T-C experiments. Adding or removing $[(\pm 45)]_{24}$ tests where heating

occurred does not significantly influence the shape of the curve. Normalizing S-N curves to ultimate strengths shows that off-axis loading ($[\#(\pm 45)]_{24}$) is more sensitive to fatigue for both C-C and T-C.

Evolution of stiffness for $[\#(0/90)]_{24}$ laminates is only significantly measurable when substantial damage events are observed in the structure. Overall, the change in stiffness and permanent strain and size of hysteresis loops is minimal for both R-ratios. Microscopic investigations show only minor meta-delaminations in C-C run-out samples. For T-C run-outs, similar meta-delaminations are seen, together with cracks in transverse fiber bundles. Microscopic investigation at intervals throughout one of these tests shows that these do not initiate from the beginning of fatigue life.

For $[\#(\pm 45)]_{24}$ laminates loaded under C-C fatigue, an initial increase in (shear) stiffness followed by a steady decrease is observed for high cycle tests. For low cycle tests the decrease initiates from the start of fatigue life. This effect is visible in both longitudinal and transverse stiffness (which is defined using the strain perpendicular to the loading direction and the applied stress). Permanent (shear) strain and hysteresis are more significant for these laminates, in particular for high applied loads, which are situated in the more non-linear part of the static stress-strain curve. For $[\#(\pm 45)]_{24}$ laminates loaded under T-C fatigue, (shear) stiffness decreases close to linear throughout fatigue life, until structural integrity is fully lost and stiffness is close to zero. For both R-ratios, degrading stiffness combines with growing hysteresis loops. Microscopic investigation shows numerous cracks in fiber bundles for both R-ratios.

Contents

Preface	iii
Summary	v
Contents	ix
List of Figures	xi
List of Tables	xix
List of Symbols	xxiii
List of Abbreviations	xxv
1 Introduction	1
2 Literature Study	3
2.1 Failure of Woven Composites	3
2.1.1 Static behaviour	3
2.1.2 Fatigue behaviour	6
2.1.3 Conclusion	10
2.2 (Fatigue) Testing of Composites	11
2.2.1 Standards	11
2.2.2 Measurement	11
2.2.3 Conclusion	14
2.3 Composite Fatigue Modeling	15
2.3.1 Fatigue Life Models	15
2.3.2 Phenomenological Models for Residual Stiffness/Strength	16
2.3.3 Progressive Damage Models	17
2.3.4 Conclusion	18
2.4 M3Strength Project	18
3 Research Plan	19
3.1 Research Objective	19
3.2 Research Questions	19
4 Experimental Set-up	21
4.1 Experimental Infrastructure	21
4.1.1 Hydraulic test bench	21
4.1.2 Displacement/Strain Measurement	22
4.1.3 Temperature Measurement	22
4.1.4 Signal Processing	22
4.1.5 Microscopy	22
4.2 Assembly and Software	23
4.2.1 Measurement System Architecture	23
4.2.2 Camera set-up	28
4.2.3 Measurement System Evaluation	30
4.2.4 Post-processing software	32
5 Specimen Design	33
5.1 Material	33
5.2 Specimen Geometry	34
5.2.1 Buckling Prevention	35
5.2.2 Specimen Shape	36
5.2.3 Dimensioning	36

5.3	Load Transfer	40
5.3.1	Two Methods for Load Transfer	40
5.3.2	End Tabs.	40
5.3.3	Load Transfer Test	41
5.3.4	Stress Field Analysis.	43
5.4	Final design	44
6	Test Results	47
6.1	Program Overview and terminology	47
6.2	Quasi-Static Tests	48
6.2.1	$[(0/90)]_{24}$	48
6.2.2	$[(\pm 45)]_{24}$	49
6.3	Test Frequency and Temperature	50
6.3.1	$[(0/90)]_{24}$	51
6.3.2	$[(\pm 45)]_{24}$	52
6.4	Fatigue Life	53
6.4.1	Methodology.	54
6.4.2	Heating and Frequency Consideration	55
6.4.3	Results	56
6.5	Stress-Strain Combinations and Property Evolution	60
6.5.1	Definitions and Notes	60
6.5.2	Evolution for $[(0/90)]_{24}$ ($R = 10$)	62
6.5.3	Evolution for $[(0/90)]_{24}$ ($R = -1$)	64
6.5.4	Evolution for $[(\pm 45)]_{24}$ ($R = 10$)	70
6.5.5	Evolution for $[(\pm 45)]_{24}$ ($R = -1$)	75
6.6	Shear Properties	76
6.6.1	Error Assesment	77
6.6.2	Results	79
6.7	Microscopy	82
6.7.1	$[(0/90)]_{24}$	82
6.7.2	$[(\pm 45)]_{24}$	85
7	Evaluation of Results	87
7.1	Stress-Life	87
7.1.1	Effect of temperature	87
7.1.2	Curve Shape.	87
7.1.3	Off-axis loading	87
7.1.4	Effect of Frequency.	88
7.1.5	Scatter	89
7.2	Property Evolution and Stress-Strain Behavior	89
7.2.1	$[(0/90)]_{24}$	89
7.2.2	$[(\pm 45)]_{24}$	89
8	Conclusions and Recommendations	93
8.1	Conclusions	93
8.2	Recommendations for further work	94
A	Digital Image Correlation Analysis	97
A.1	Procedure	97
A.2	Evaluation	98
B	Abaqus Shell Element Selection	99
B.1	$[(0/90)]_8$	99
B.2	$[(\pm 45)]_8$	99
B.3	$[(0/90)]_{24}$	100
B.4	$[(\pm 45)]_{24}$	100
C	Specimen Preparation	101

D Overview of Tests performed	103
D.1 $[\#(0/90)]_{24}$ (Static)	103
D.2 $[\#(\pm 45)]_{24}$ (Static)	103
D.3 $[\#(0/90)]_{24}$ (R = 10)	104
D.4 $[\#(0/90)]_{24}$ (R = -1)	104
D.5 $[\#(\pm 45)]_{24}$ (R = 10)	105
D.6 $[\#(\pm 45)]_{24}$ (R = -1)	105
E Reproducibility of Test Results	107
E.1 $[\#(0/90)]_{24}$ (R = 10)	107
E.2 $[\#(0/90)]_{24}$ (R = -1)	108
E.3 $[\#(\pm 45)]_{24}$ (R = 10)	110
E.4 $[\#(\pm 45)]_{24}$ (R = -1)	111
Bibliography	115

List of Figures

1.1	Current state of the art for CFRP predictive modeling. [1]	2
2.1	Different failure modes when fibers are loaded in compression. (a) (Elastic) microbuckling, (b) kinking (plastic microbuckling), (c) fiber crushing, (d) matrix splitting, (e) Buckle delamination of a layer close to the surface and (f) shear band formation, as represented by Fleck [2]	4
2.2	Kink band essentials [3]	4
2.3	Kinking failure in a 2x2 twill specimen [4]	5
2.4	4 stages of fatigue life for a woven composite. [5]	6
2.5	Degradation of strength due to cyclic loading until the point where the structure can not cope with the applied loads anymore [6]	7
2.6	S-N curves for the same material (UD glass-epoxy) tested in different labs. [7]	8
2.7	S-N curves for the same material (UD carbon-epoxy) tested in different labs includes great variability and a flatter S-N curve. [7]	8
2.8	S-N data for different lay-ups and R-ratios including 10% and 90% probability of survival scatter bands by Quaresimin [8]	8
2.9	Plain weave carbon-epoxy under different orientations. S-N curve normalized to ultimate strength [9]	9
2.10	Plain weave carbon-epoxy under different orientations. Fatigue fracture surfaces show a clear distinction between off- and on-axis loading [9]	9
2.11	Stiffness degradation of a carbon-polyester fabric [10]	9
2.12	Stiffness degradation of a carbon-epoxy and carbon-phenolic fabric [11]	9
2.13	Stiffness degradation of 5 harness satin weave carbon-epoxy [6]	10
2.14	Hysteresis cycles under T-T loading [8]	10
2.15	Hysteresis cycles under T-C Loading [8]	10
2.16	Example of a typical speckle pattern and DIC setup for cyclic tension experiments [12]	12
2.17	Example of correlation of a subset of pixels before and after deformation. [13]	13
2.18	(a) subset of 10x10 pixels. (b) Bilinear interpolation. (c) bicubic interpolation [13]	13
2.19	Giancane shows a correlation between dissipated strain energy and Young's modulus [14]	14
2.20	Montesano's fatigue model predictions (a) compared with DIC measurements (b) [12]	14
2.21	Example of a representative unit cell (RUC (representative unit cell)) [15]	18
4.1	Two strain gages for longitudinal and transverse measurements	22
4.2	labview program front panel	24
4.3	labview program live outputs	25
4.4	Vic-snap triggered system	26
4.5	Labview triggered system	27
4.6	Measuring displacement using DIC and comparing this to an analog displacement signal for rigid body motion.	28
4.7	Camera set-up for 3D DIC	28
4.8	Camera concept with a mirror results in one of both images being out of focus and a lower resolution for the front DIC image.	29
4.9	Camera concept capturing two 2D images of a specimen rather than a single frontal 3D image.	30
4.10	Rigid body motion of 1 mm at 3 Hz shot at 20 fps shows a delay between signals.	30
4.11	Rigid body motion of 1 mm at 3 Hz shot at 30 fps shows a delay between signals.	30
4.12	Rigid body motion of 1 mm at 1 Hz shot at 25 fps shows a delay between signals.	31
4.13	Rigid body motion of 1 mm at 3 Hz shot at 20 fps with constant delay correction.	31
4.14	Rigid body motion of 1 mm at 3 Hz shot at 30 fps with constant delay correction.	31

4.15 Rigid body motion of 1 mm at 1 Hz shot at 25 fps with constant delay correction. . . .	31
5.1 cross-sectional microscopic view of the material (lay-up: $[(0/90)]_{24}$ used in this project. The weft (fill) direction is perpendicular to the picture (coming out of the page). Warp and stacking (z-) direction are indicated in the picture, as well as an approximation of the layer boundaries.	34
5.2 Material Data sheet from manufacturer	34
5.3 Testing the same material with anti-buckling guides results in lower strengths. [8] . . .	35
5.4 Hydraulic wedge clamps on the Instron test bench	36
5.5 A qualitative representation of the first buckling mode occurring in all cases under consideration.	38
5.6 Buckling loads for $[(0/90)]_8$ laminate	38
5.7 Buckling loads for $[(\pm 45)]_8$ laminate	38
5.8 Buckling loads for $[(0/90)]_{24}$ laminate	39
5.9 Buckling loads for $[(\pm 45)]_{24}$ laminate	39
5.10 Out-of-plane displacement of a $[(0/90)]_{24}$ laminate measured using DIC.	39
5.11 Measuring the displacement of the clamping head shows that clamping conditions are not ideal.	39
5.12 The effect of specimen width on the buckling load (mode 1) is negligible	40
5.13 Shear loading and end loading as visualized in [16].	40
5.14 Stress concentrations in the critical regions in function of the tab material stiffness [17]	41
5.15 Aluminum samples outperform steel in static performance	42
5.16 Aluminum sample 1. Broken in the middle under static loading.	42
5.17 Steel sample 1. Fracture initiates in the stress concentration region for static loading. .	42
5.18 Aluminum sample 4. Broken in the middle under cyclic compressive loading.	43
5.19 Steel sample 3. Fracture initiates in the stress concentration region for cyclic loading as well.	43
5.20 Three planes of symmetry used in the finite element model	43
5.21 Stress concentration decays to a homogeneous stress state at 380 MPa in the middle section for $[(0/90)]$ laminates. Stress on the graph refers to stress aligned with load in MPa.	44
5.22 Stress concentration decays to a homogeneous stress state at 95 MPa in the middle section for $[(\pm 45)]$ laminates. Stress on the graph refers to stress aligned with load in MPa.	44
5.23 Final specimen dimensions	45
6.1 Stress-strain behavior for static tests.	49
6.2 Typical temperature evolution in a $[(0/90)]_{24}$ specimen loaded under low cycle C-C fatigue.	51
6.3 Typical temperature evolution in a $[(0/90)]_{24}$ specimen loaded under high cycle C-C fatigue.	51
6.4 Typical temperature evolution in a $[(0/90)]_{24}$ specimen loaded under low cycle T-C fatigue.	51
6.5 Typical temperature evolution in a $[(0/90)]_{24}$ specimen loaded under high cycle T-C fatigue.	51
6.6 A 12V pc fan used to cool down $[(\pm 45)]_{24}$ specimens during cyclic loading.	52
6.7 Altering the frequency can successfully limit heating for C-C loading of $[(\pm 45)]_{24}$ laminates	53
6.8 Loading at 2 Hz does not induce significant temperature rises for T-C loading $\leq 40\% \sigma_{ult,c}$. At $50\% \sigma_{ult,c}$, the frequency must be lowered to keep heating at acceptable levels.	53
6.9 S-N curve for the case of $[(0/90)]_{24}$ with $R = 10$. All tests are performed at 3 Hz. Sendeckyj parameters: $[S = 0.0283, C = 0.4345, \alpha = 29.97, \beta = 519.09]$	56
6.10 S-N curve for the case of $[(0/90)]_{24}$ with $R = -1$. All tests are performed at 3 Hz. Sendeckyj parameters: $[S = 0.0809, C = 0.0288, \alpha = 23.6392, \beta = 512.44]$	57
6.11 S-N data points for the case of $[(\pm 45)]_{24}$ with $R = 10$. Frequencies of each test are indicated. Red points denote tests in which heating surpassed acceptable levels.	57

6.12 S-N curve for the case of $[\#(\pm 45)]_{24}$ with $R = 10$ including only data points where no heating occurred. Note that this curve is derived from tests at different frequencies.	
parameters: $[S = 0.037, C = 0.2976, \alpha = 104.24, \beta = 157.00]$	58
6.13 S-N curve for the case of $[\#(\pm 45)]_{24}$ with $R = 10$ including all data points. Note that this curve is derived from tests at different frequencies and tests which heated up.	
parameters: $[S = 0.038, C = 0.2477, \alpha = 81.58, \beta = 156.64]$	58
6.14 S-N data points for the case of $[\#(\pm 45)]_{24}$ with $R = -1$. Frequencies of each test are indicated. Red points denote tests in which heating surpassed acceptable levels.	59
6.15 S-N curve for the case of $[\#(\pm 45)]_{24}$ with $R = -1$ including only data points where no heating occurred. Note that this curve is derived from tests at different frequencies.	
Sendeckyj parameters: $[S = 0.0876, C = 1.00, \alpha = 63.30, \beta = 156.17]$	59
6.16 S-N curve for the case of $[\#(\pm 45)]_{24}$ with $R = -1$ including all data points. Note that this curve is derived from tests at different frequencies and tests which heated up.	
Sendeckyj parameters: $[S = 0.0940, C = 0.4952, \alpha = 49.61, \beta = 156.13]$	59
6.17 Laminate axis system used in this section	60
6.18 Definition of stiffness in the unloading section of a C-C loading pattern	61
6.19 Stiffness components in tension and compression for T-C loading.	61
6.20 ϵ_{perm} at cycle x' is defined as the difference in strain at the smallest compressive load applied in cycle x , compared to the strain at the start of the first fatigue cycle (with a compressive load of 10% σ_a already applied)	61
6.21 Stiffness of a $[\#(0/90)]_{24}$ laminate under 60% $\sigma_{ult,c}$ ($R = 10$) is pretty much unchanged throughout its fatigue life. $E_0 = 46.9$ GPa	62
6.22 No significant difference in stress-strain behavior throughout the fatigue life of a $[\#(0/90)]_{24}$ laminate under 60% $\sigma_{ult,c}$ ($R = 10$)	62
6.23 Stiffness of a $[\#(0/90)]_{24}$ laminate under 70% $\sigma_{ult,c}$ ($R = 10$) is pretty much unchanged throughout its fatigue life. $E_0 = 46.5$ GPa	62
6.24 Apart from a slight shift in permanent strain, there is little difference in a $[\#(0/90)]_{24}$ laminate under 70% $\sigma_{ult,c}$ ($R = 10$)	62
6.25 Stiffness of a $[\#(0/90)]_{24}$ laminate under 80% $\sigma_{ult,c}$ ($R = 10$) is almost constant. $E_0 = 45.2$ GPa	63
6.26 Very little difference in stress-strain behavior in a $[\#(0/90)]_{24}$ laminate under 80% $\sigma_{ult,c}$ ($R = 10$)	63
6.27 Stiffness of a $[\#(0/90)]_{24}$ laminate under 80% $\sigma_{ult,c}$ ($R = 10$) shows a drop in stiffness from 838 to 1,347 cycles. $E_0 = 47.5$ GPa	63
6.28 Stress-strain behavior in a $[\#(0/90)]_{24}$ laminate under 80% $\sigma_{ult,c}$ ($R = 10$). Note the drop in stiffness between 838 and 1,347 cycles.	63
6.29 Difference in image between 838 (a) and 1,347 (b) cycles can be linked to stiffness drop in figure 6.27.	64
6.30 Damage in frontal layers results in redistribution of stress.	64
6.31 Peak-to-peak stiffness of a $[\#(0/90)]_{24}$ laminate under 45% $\sigma_{ult,c}$ ($R = -1$) indicates little evolution in stiffness over time. $E_0 = 56.1$ GPa	65
6.32 Stress-strain behavior in a $[\#(0/90)]_{24}$ laminate under 45% $\sigma_{ult,c}$ ($R = -1$).	65
6.33 Stiffness in compression of a $[\#(0/90)]_{24}$ laminate under 45% $\sigma_{ult,c}$ ($R = -1$) shows some scatter. $E_{C,0} = 54.0$ GPa	65
6.34 Stiffness in tension of a $[\#(0/90)]_{24}$ laminate under 45% $\sigma_{ult,c}$ ($R = -1$) shows some scatter. $E_{T,0} = 58.4$ GPa	65
6.35 Delaminations growing over time in a $[\#(0/90)]_{24}$ laminate loaded at 45% $\sigma_{ult,c}$ ($R = -1$)	65
6.36 Stiffness of a $[\#(0/90)]_{24}$ laminate under 50% $\sigma_{ult,c}$ ($R = -1$) shows a steady but gentle stiffness descent, followed by a sudden drop near the end of life. $E_0 = 51.9$ GPa	66
6.37 Stress-strain behavior in a $[\#(0/90)]_{24}$ laminate under 50% $\sigma_{ult,c}$ ($R = -1$).	66
6.38 Stiffness in compression of a $[\#(0/90)]_{24}$ laminate under 50% $\sigma_{ult,c}$ ($R = -1$) indicates a slight decrease in both components, despite scatter. $E_{C,0} = 48.2$ GPa	66
6.39 Stiffness in tension of a $[\#(0/90)]_{24}$ laminate under 50% $\sigma_{ult,c}$ ($R = -1$) indicates a slight decrease in both components, despite scatter. $E_{T,0} = 57.4$ GPa	66

6.40	Significant damage created explains the stiffness drop in figures 6.36, 6.39 and 6.38	67
6.41	Stiffness of a $[\#(0/90)]_{24}$ laminate under 50% $\sigma_{ult,c}$ ($R = -1$) shows a steady but gentle stiffness descent, followed by a sudden drop near the end of life. $E_0 = 52.5$ GPa	67
6.42	Stress-strain behavior in a $[\#(0/90)]_{24}$ laminate under 50% $\sigma_{ult,c}$ ($R = -1$).	67
6.43	Damage evolution of the last three data points in figure 6.41	68
6.44	Stiffness of a $[\#(0/90)]_{24}$ laminate under 60% $\sigma_{ult,c}$ ($R = -1$) indicates a pretty much constant stiffness until final failure. $E_0 = 52.0$ GPa	68
6.45	Stress-strain behavior in a $[\#(0/90)]_{24}$ laminate under 60% $\sigma_{ult,c}$ ($R = -1$) changes very little when no significant damage events take place.	68
6.46	Stiffness of a $[\#(0/90)]_{24}$ laminate under 80% $\sigma_{ult,c}$ ($R = -1$) remains constant, except for a sudden drop a couple of cycles before final failure. $E_0 = 52.9$ GPa	69
6.47	Stress-strain behavior in a $[\#(0/90)]_{24}$ laminate under 80% $\sigma_{ult,c}$ ($R = -1$). Sudden stiffness drop is measurable here as well.	69
6.48	Damage evolution of the last two data points in figure 6.46	69
6.49	Stiffness evolution of a $[\#(\pm 45)]_{24}$ laminate under 60% $\sigma_{ult,c}$ ($R = 10$). As for all run-out samples under this loading, the stiffness seems to increase in the early stages of fatigue life before a steady decrease starts. $E_0 = 8.1$ GPa	70
6.50	Stress-strain behavior in a $[\#(\pm 45)]_{24}$ laminate under 60% $\sigma_{ult,c}$ ($R = 10$). Note the amount of permanent strain and clear differences in stiffness.	70
6.51	Permanent strain evolution of $[\#(\pm 45)]_{24}$ laminates under 60% $\sigma_{ult,c}$ ($R = 10$).	70
6.52	Stiffness evolution of a $[\#(\pm 45)]_{24}$ laminate under 70% $\sigma_{ult,c}$ ($R = 10$). As for all specimens under this loading, the stiffness seems to increase in the early stages of fatigue life before a steady decrease starts. $E_0 = 7.3$ GPa	71
6.53	Stress-strain behavior in a $[\#(\pm 45)]_{24}$ laminate under 70% $\sigma_{ult,c}$ ($R = 10$). Note the amount of permanent strain and clear differences in stiffness.	71
6.54	Permanent strain evolution of $[\#(\pm 45)]_{24}$ laminates under 70% $\sigma_{ult,c}$ ($R = 10$). Note that testID 39 is technically omitted due to heating.	71
6.55	Stiffness evolution of another $[\#(\pm 45)]_{24}$ laminate under 80% $\sigma_{ult,c}$ ($R = 10$). $E_0 = 6.0$ GPa	72
6.56	Stress-strain behavior in a $[\#(\pm 45)]_{24}$ laminate under 80% $\sigma_{ult,c}$ ($R = 10$).	72
6.57	Permanent strain evolution of $[\#(\pm 45)]_{24}$ laminates under 80% $\sigma_{ult,c}$ ($R = 10$). Note that tests which heated up are performed at higher frequencies. This means that the first 10-15 cycles for these tests still occur in the attack time of the machine (described earlier), which is why permanent deformation is lower for these laminates.	72
6.58	Stiffness monotonically decreases for a $[\#(\pm 45)]_{24}$ laminate under 90% $\sigma_{ult,c}$ ($R = 10$). $E_0 = 4.9$ GPa	73
6.59	Stress-strain behavior in a $[\#(\pm 45)]_{24}$ laminate under 90% $\sigma_{ult,c}$ ($R = 10$).	73
6.60	Permanent strain evolution of $[\#(\pm 45)]_{24}$ laminates under 90% $\sigma_{ult,c}$ ($R = 10$). Note that tests which heated up are performed at higher frequencies. This means that the first 10-15 cycles for these tests still occur in the attack time of the machine (described earlier), which is why permanent deformation is lower for these laminates.	73
6.61	$[\#(\pm 45)]_{24}$ laminates loaded at $R = 10$ at 90%, 80%, and 70% showing only minor delaminations right before failure. (a) testID 40, (b) testID 41, (c) testID 43	74
6.62	testID 44 $[\#(\pm 45)]_{24}$ under 70% $\sigma_{ult,c}$ shows macroscopic damage growing and initiating final failure.	74
6.63	Typical stiffness evolution for a $[\#(\pm 45)]_{24}$ laminate under 30% $\sigma_{ult,c}$ ($R = -1$). Stiffness remains constant initially and then decreases. The test did however survive 685,502 cycles after which it was stopped. Stiffness shows significant scatter. $E_0 = 10.8$ GPa	75
6.64	Stress-strain behavior in a $[\#(\pm 45)]_{24}$ laminate under 30% $\sigma_{ult,c}$ ($R = -1$). Stiffness decline seems to correlate with hysteresis.	75
6.65	Stiffness in compression of a $[\#(\pm 45)]_{24}$ laminate under 30% $\sigma_{ult,c}$ ($R = -1$) shows some scatter. $E_{C,0} = 10.57$ GPa	75
6.66	Stiffness in tension of a $[\#(\pm 45)]_{24}$ laminate under 30% $\sigma_{ult,c}$ ($R = -1$) shows some scatter. $E_{T,0} = 11.3$ GPa	75
6.67	Typical stiffness evolution for a $[\#(\pm 45)]_{24}$ laminate under 40% $\sigma_{ult,c}$ ($R = -1$). Stiffness degrades significantly before final failure. $E_0 = 9.6$ GPa	76

6.68 Stress-strain behavior in a $[\#(\pm 45)]_{24}$ laminate under 40% $\sigma_{ult,c}$ ($R = -1$). Stiffness decline seems to correlate with hysteresis.	76
6.69 Typical stiffness evolution for a $[\#(\pm 45)]_{24}$ laminate under 50% $\sigma_{ult,c}$ ($R = -1$). Stiffness degrades significantly before final failure. $E_0 = 8.3$ GPa	76
6.70 Stress-strain behavior in a $[\#(\pm 45)]_{24}$ laminate under 50% $\sigma_{ult,c}$ ($R = -1$). Stiffness decline seems to correlate with hysteresis.	76
6.71 Two coordinate systems for uniaxial loading of a woven $[\#(\pm 45)]$ laminate	77
6.72 Shear stress-strain behavior for static compressive tests of $[\#(\pm 45)]_{24}$	79
6.73 Stiffness evolution of a $[\#(\pm 45)]_{24}$ laminate under 60% $\sigma_{ult,c}$ ($R = 10$). Similarly to longitudinal stiffness, the shear stiffness seems to initially increase in the beginning of fatigue life until before a steady decline sets. $G_0 = 2.2$ GPa	80
6.74 Shear stress-strain behavior in a $[\#(\pm 45)]_{24}$ laminate under 60% $\sigma_{ult,c}$ ($R = 10$). Evolution of shear stiffness and permanent strain is well visible.	80
6.75 Shear Stiffness monotonically decreases for a $[\#(\pm 45)]_{24}$ laminate under 90% $\sigma_{ult,c}$ ($R = 10$). $G_0 = 1.3$ GPa	80
6.76 Shear stress-strain behavior in a $[\#(\pm 45)]_{24}$ laminate under 90% $\sigma_{ult,c}$ ($R = 10$) shows hysteresis and permanent shear strain deformations.	80
6.77 Permanent shear evolution for $[\#(\pm 45)]_{24}$ samples loaded under 60% $\sigma_{ult,c}$ ($R = 10$).	81
6.78 Permanent shear evolution for $[\#(\pm 45)]_{24}$ samples loaded under 70% $\sigma_{ult,c}$ ($R = 10$).	81
6.79 Permanent shear evolution for $[\#(\pm 45)]_{24}$ samples loaded under 80% $\sigma_{ult,c}$ ($R = 10$). Cycles normalized by fatigue life.	81
6.80 Permanent shear evolution for $[\#(\pm 45)]_{24}$ samples loaded under 90% $\sigma_{ult,c}$ ($R = 10$). Cycles normalized by fatigue life.	81
6.81 Stiffness evolution of a $[\#(\pm 45)]_{24}$ laminate under 40% $\sigma_{ult,c}$ ($R = -1$). Longitudinal stiffness remains somewhat constant for the first couple of cycles but then drops significantly until all stiffness is lost and final failure occurs. $G_0 = 2.6$ GPa	82
6.82 Shear stress-strain behavior in a $[\#(\pm 45)]_{24}$ laminate under 40% $\sigma_{ult,c}$ ($R = -1$). Stiffness loss is clearly visualized in the final cycles.	82
6.83 Shear stiffness component derived in unloading from a compressive cycle shows some scatter, but overall a similar trend compared to figure 6.81. $G_{C,0} = 2.7$ GPa	82
6.84 Shear stiffness component derived in unloading from a tensile cycle shows some scatter, but overall a similar trend compared to figure 6.81. $G_{T,0} = 2.7$ GPa	82
6.85 $[\#(0/90)]_{24}$ ($R = 10$) run-outs show no damage other than minor meta-delaminations. Loading direction indicated in red.	83
6.86 $[\#(0/90)]_{24}$ ($R = -1$) example of a crack in transverse fiber bundles. Loading direction indicated in red.	83
6.87 $[\#(0/90)]_{24}$ ($R = -1$) show numerous cracks in transverse fiber bundles. Loading direction indicated in red.	84
6.88 After 4,500 cycles, the sample showed a meta-delamination in the stress concentration region.	85
6.89 After 4,500 cycles, the sample showed the first cracks.	85
6.90 After 11,750 cycles, the meta-delamination has grown into a larger delamination. Note that the big spot is probably degraded matrix material which is expelled from the larger defect upon final cleaning of the polished surface.	85
6.91 For a $[\#(\pm 45)]_{24}$ laminate under C-C loading, cracks in bundles often combine through bundle debonding.	85
6.92 For a $[\#(\pm 45)]_{24}$ laminate under T-C loading, many cracks can be observed	85
7.1 S-N curves for C-C experiments. Off-axis loading of specimens is more sensitive to fatigue.	88
7.2 S-N curves for T-C experiments. Off-axis loading of specimens is more sensitive to fatigue here as well.	88
7.3 Normalizing stiffness evolution over fatigue life for C-C loading shows that evolution tends to be more severe in the initial stages of fatigue life and then drops somewhat less. Note that the 60% result is normalized to 725,000 cycles, after which the test was stopped and it was considered a run-out.	90

7.4	Stiffness degradation under T-C fatigue is almost linear throughout a specimens fatigue life until it reaches a value where the integrity of the structure is lost.	91
C.1	Subpanel after waterjet cutting	101
C.2	Subpanel fitted with a thick steel spacer	102
E.1	Stiffness evolution of #(0/90) laminates under 60% $\sigma_{ult,c}$ (R = 10) [$E_{0,13}$ = 46.6 GPa $E_{0,14}$ = 46.9 GPa]	107
E.2	Stiffness evolution of #(0/90) laminates under 70% $\sigma_{ult,c}$ (R = 10) [$E_{0,9}$ = 46.5 GPa $E_{0,10}$ = 46.6 GPa]	107
E.3	Stiffness evolution of #(0/90) laminates under 80% $\sigma_{ult,c}$ (R = 10) [$E_{0,8}$ = 48.2 GPa $E_{0,12}$ = 45.2 GPa $E_{0,15}$ = 47.5 GPa]	108
E.4	Stiffness evolution of #(0/90) laminates under 40% $\sigma_{ult,c}$ (R = -1) [$E_{0,18}$ = 50.3 GPa $E_{0,18}$ = 49.8 GPa]	108
E.5	Evolution of stiffness in compression of #(0/90) laminates under 40% $\sigma_{ult,c}$ (R = -1) [$E_{C0,18}$ = 47.7 GPa $E_{C0,26}$ = 48.2 GPa]	109
E.6	Evolution of stiffness in tension of #(0/90) laminates under 40% $\sigma_{ult,c}$ (R = -1) [$E_{T0,18}$ = 53.1 GPa $E_{T0,26}$ = 54.0 GPa]	109
E.7	Stiffness evolution of #(0/90) laminates under 50% $\sigma_{ult,c}$ (R = -1) [$E_{0,20}$ = 51.9 GPa $E_{0,23}$ = 52.2 GPa]	109
E.8	Evolution of stiffness in compression of #(0/90) laminates under 50% $\sigma_{ult,c}$ (R = -1) [$E_{C0,20}$ = 48.2 GPa $E_{C0,23}$ = 50.5 GPa]	109
E.9	Evolution of stiffness in tension of #(0/90) laminates under 50% $\sigma_{ult,c}$ (R = -1) [$E_{T0,20}$ = 57.4 GPa $E_{T0,23}$ = 57.8 GPa]	109
E.10	Stiffness evolution of #(0/90) laminates under 60% $\sigma_{ult,c}$ (R = -1) [$E_{0,16}$ = 50.0 GPa $E_{0,19}$ = 52.8 GPa]	110
E.11	Evolution of stiffness in compression of #(0/90) laminates under 60% $\sigma_{ult,c}$ (R = -1) [$E_{C0,16}$ = 46.9 GPa $E_{C0,19}$ = 51.0 GPa]	110
E.12	Evolution of stiffness in tension of #(0/90) laminates under 60% $\sigma_{ult,c}$ (R = -1) [$E_{T0,16}$ = 54.6 GPa $E_{T0,19}$ = 55.8 GPa]	110
E.13	Stiffness evolution of #(± 45) laminates under 60% $\sigma_{ult,c}$ (R = 10) [$E_{0,34}$ = 8.5 GPa $E_{0,37}$ = 8.7 GPa $E_{0,42}$ = 8.1 GPa]	110
E.14	Shear stiffness evolution of #(± 45) laminates under 60% $\sigma_{ult,c}$ (R = 10) [$G_{0,34}$ = 2.2 GPa $G_{0,37}$ = 2.3 GPa $G_{0,42}$ = 2.3 GPa]	110
E.15	Stiffness evolution of #(± 45) laminates under 70% $\sigma_{ult,c}$ (R = 10) [$E_{0,39}$ = 6.9 GPa $E_{0,43}$ = 7.2 GPa $E_{0,44}$ = 6.6 GPa]	111
E.16	Shear stiffness evolution of #(± 45) laminates under 70% $\sigma_{ult,c}$ (R = 10) [$G_{0,39}$ = 1.8 GPa $G_{0,43}$ = 1.9 GPa $G_{0,44}$ = 1.8 GPa]	111
E.17	Stiffness evolution of #(± 45) laminates under 80% $\sigma_{ult,c}$ (R = 10) [$E_{0,35}$ = 6.9 GPa $E_{0,36}$ = 6.1 GPa $E_{0,38}$ = 6.3 GPa $E_{0,41}$ = 6.1 GPa]	111
E.18	Shear stiffness evolution of #(± 45) laminates under 80% $\sigma_{ult,c}$ (R = 10) [$G_{0,35}$ = 1.8 GPa $G_{0,36}$ = 1.6 GPa $G_{0,38}$ = 1.7 GPa $G_{0,41}$ = 1.6 GPa]	111
E.19	Stiffness evolution of #(± 45) laminates under 30% $\sigma_{ult,c}$ (R = -1) [$E_{0,49}$ = 10.4 GPa $E_{0,50}$ = 10.7 GPa $E_{0,51}$ = 10.3 GPa]	112
E.20	Shear stiffness evolution of #(± 45) laminates under 30% $\sigma_{ult,c}$ (R = -1) [$G_{0,49}$ = 2.9 GPa $G_{0,50}$ = 2.9 GPa $G_{0,51}$ = 2.9 GPa]	112
E.21	Evolution of stiffness in compression of #(± 45) laminates under 30% $\sigma_{ult,c}$ (R = -1) [$E_{C0,49}$ = 10.7 GPa $E_{C0,50}$ = 10.9 GPa $E_{C0,51}$ = 11.6 GPa]	112
E.22	Evolution of shear stiffness in compression of #(± 45) laminates under 30% $\sigma_{ult,c}$ (R = -1) [$G_{C0,49}$ = 3.0 GPa $G_{C0,50}$ = 3.0 GPa $G_{C0,51}$ = 3.0 GPa]	112
E.23	Evolution of stiffness in tension of #(± 45) laminates under 30% $\sigma_{ult,c}$ (R = -1) [$E_{T0,49}$ = 10.6 GPa $E_{T0,50}$ = 11.1 GPa $E_{T0,51}$ = 10.7 GPa]	112
E.24	Evolution of shear stiffness in tension of #(± 45) laminates under 30% $\sigma_{ult,c}$ (R = -1) [$G_{T0,49}$ = 2.9 GPa $G_{T0,50}$ = 3.0 GPa $G_{T0,51}$ = 3.0 GPa]	112
E.25	Stiffness evolution of #(± 45) laminates under 40% $\sigma_{ult,c}$ (R = -1) [$E_{0,45}$ = 9.5 GPa $E_{0,46}$ = 9.8 GPa $E_{0,61}$ = 9.8 GPa]	113

E.26 Shear stiffness evolution of #(± 45) laminates under 40% $\sigma_{ult,c}$ (R = -1) [$G_{0,45} = 2.6$ GPa $G_{0,46} = 2.6$ GPa $G_{0,61} = 2.7$ GPa]	113
E.27 Evolution of stiffness in compression of #(± 45) laminates under 40% $\sigma_{ult,c}$ (R = -1) [$E_{C0,45} = 9.9$ GPa $E_{C0,46} = 10.0$ GPa $E_{C0,61} = 10.5$ GPa]	113
E.28 Evolution of shear stiffness in compression of #(± 45) laminates under 40% $\sigma_{ult,c}$ (R = -1) [$G_{C0,45} = 2.7$ GPa $G_{C0,46} = 2.7$ GPa $G_{C0,61} = 2.8$ GPa]	113
E.29 Evolution of stiffness in tension of #(± 45) laminates under 40% $\sigma_{ult,c}$ (R = -1) [$E_{T0,45} = 10.4$ GPa $E_{T0,46} = 10.2$ GPa $E_{T0,61} = 10.3$ GPa]	113
E.30 Evolution of shear stiffness in tension of #(± 45) laminates under 40% $\sigma_{ult,c}$ (R = -1) [$G_{T0,45} = 2.8$ GPa $G_{T0,46} = 2.8$ GPa $G_{T0,61} = 2.8$ GPa]	113
E.31 Stiffness evolution of #(± 45) laminates under 50% $\sigma_{ult,c}$ (R = -1) [$E_{0,52} = 8.8$ GPa $E_{0,53} = 8.2$ GPa $E_{0,55} = 7.5$ GPa]	114
E.32 Shear stiffness evolution of #(± 45) laminates under 50% $\sigma_{ult,c}$ (R = -1) [$G_{0,52} = 2.5$ GPa $G_{0,53} = 2.2$ GPa $G_{0,55} = 2.1$ GPa]	114
E.33 Evolution of stiffness in compression of #(± 45) laminates under 50% $\sigma_{ult,c}$ (R = -1) [$E_{C0,52} = 9.4$ GPa $E_{C0,53} = 9.0$ GPa $E_{C0,55} = 8.0$ GPa]	114
E.34 Evolution of shear stiffness in compression of #(± 45) laminates under 50% $\sigma_{ult,c}$ (R = -1) [$G_{C0,52} = 2.6$ GPa $G_{C0,53} = 2.5$ GPa $G_{C0,55} = 2.3$ GPa]	114
E.35 Evolution of stiffness in tension of #(± 45) laminates under 50% $\sigma_{ult,c}$ (R = -1) [$E_{T0,52} = 9.7$ GPa $E_{T0,53} = 9.3$ GPa $E_{T0,55} = 8.2$ GPa]	114
E.36 Evolution of shear stiffness in tension of #(± 45) laminates under 50% $\sigma_{ult,c}$ (R = -1) [$G_{T0,52} = 2.7$ GPa $G_{T0,53} = 2.5$ GPa $G_{T0,55} = 2.3$ GPa]	114

List of Tables

4.1	Shutter speed has an influence on the observed delays between analog and DIC data.	32
5.1	Fatigue life of steel and aluminum samples	43
6.1	Compressive failure strain and stress for 5 quasi-static compression tests on $[(0/90)]_{24}$ laminates.	48
6.2	Properties used for error assessment of shear properties	78
B.1	$[(0/90)]_8$ element selection	99
B.2	$[(\pm 45)]_8$ element selection	99
B.3	$[(0/90)]_{24}$ element selection	100
B.4	$[(\pm 45)]_{24}$ element selection	100
D.1	Test overview for $[(0/90)]_{24}$ (Static)	103
D.2	Test overview for $[(\pm 45)]_{24}$ (Static)	103
D.3	Test overview for $[(0/90)]_{24}$ (R = 10)	104
D.4	Test overview for $[(0/90)]_{24}$ (R = -1)	104
D.5	Test overview for $[(\pm 45)]_{24}$ (R = 10)	105
D.6	Test overview for $[(\pm 45)]_{24}$ (R = -1)	105

List of Symbols

α	Shape parameter of a two-parameter Weibull distribution, <i>unitless</i>
β	Scale parameter of a two-parameter Weibull distribution, <i>variable units</i>
ϵ	Normal strain , <i>unitless</i>
ϵ_L	Longitudinal strain, <i>unitless</i>
ϵ_T	Transverse strain, <i>unitless</i>
ϵ_{perm}	Permanent strain, <i>unitless</i>
$\epsilon_{ult,c}$	Ultimate compressive normal strain at failure, <i>unitless</i>
γ	Shear strain, <i>unitless</i>
γ_{ij}	Shear strain in directions (i,j), <i>unitless</i>
γ_{perm}	Permanent shear strain, <i>unitless</i>
σ_a	Minimum applied stress (fatigue context) [MPa]
σ_b	Buckling stress [MPa]
σ_e	Equivalent stress [MPa]
σ_i	Normal stress in direction i [MPa]
σ_{max}	Maximal applied stress [MPa]
σ_{min}	Minimal applied stress [MPa]
σ_r	Residual strength [MPa]
$\sigma_{ult,c}$	Ultimate compressive strength [MPa]
$\sigma_{ult,t}$	Ultimate tensile strength [MPa]
τ	Shear stress [MPa]
τ_{ij}	Shear stress in directions (i,j) [MPa]
$\tilde{\sigma}$	effective stress [MPa]
A	Time interval parameter for measurement software, <i>unitless</i>
C	Parameter in deterministic equation describing a Sendeckyj S-N curve, <i>unitless</i>
D	Damage Variable, <i>unitless</i>
D_{xy}	Element (x,y) of the D-matrix describing pure bending [Nmm]
E	Normal stiffness [GPa]
E_0	Initial Young's modulus [GPa]
E_C	Young's modulus in compression [GPa]

E_T	Young's modulus in tension [GPa]
F	Force [N]
f	Frequency [Hz]
G	Shear stiffness [GPa]
G_0	Initial shear stiffness [GPa]
G_C	Shear stiffness in compression [GPa]
G_T	Shear stiffness in tension [GPa]
H	Dissipated Mechanical Energy [J/mm^3]
N	Time interval parameter for measurement software, <i>unitless</i>
n, m	Sample population size, <i>unitless</i>
N, n	Number of Cycles, <i>unitless</i>
N_f	Number of Cycles until failure, <i>unitless</i>
N_x	Normal force per unit width in x-direction on a flat plate [N/mm]
N_y	Normal force per unit width in y-direction on a flat plate [N/mm]
N_{xy}	Shear force per unit width in xy-direction on a flat plate [N/mm]
q_a	Parameter used for determination of an A-basis value of a two-parameter Weibull distribution, <i>variable units</i>
q_b	Parameter used for determination of an B-basis value of a two-parameter Weibull distribution, <i>variable units</i>
R	Fatigue Ratio under constant amplitude loading, <i>unitless</i>
S	Absolute value of asymptotic slope at long life of a Sendeckyj S-N curve, <i>unitless</i>
S	Ultimate in-plane shear strength [MPa]
s	Standard deviation, <i>variable units</i>
T	Temperature [$^{\circ}C$]
t	Sample thickness [mm]
t	Statistic test score, <i>unitless</i>
t	Time [s]
u, v, w	Displacement in the direction of x,y,z axes, respectively [mm]
V	Voltage [V]
ν	Poisson's ratio, <i>unitless</i>
V_a	Parameter used for determination of an A-basis value of a two-parameter Weibull distribution, <i>unitless</i>
V_b	Parameter used for determination of an B-basis value of a two-parameter Weibull distribution, <i>unitless</i>

V_f	Fiber volume fraction, <i>unitless</i>
w	Sample width [<i>mm</i>]
x, y	Axes typically aligned with a flat plate, <i>unitless</i>
X^c	Ultimate compressive normal strength in x-direction [<i>MPa</i>]
X^t	Ultimate tensile normal strength in x-direction [<i>MPa</i>]
Y^c	Ultimate compressive normal strength in y-direction [<i>MPa</i>]
Y^t	Ultimate tensile normal strength in y-direction [<i>MPa</i>]
z	Axis typically perpendicular to a flat plate, <i>unitless</i>

List of Abbreviations

C-C	compression-compression
CFRP	carbon fiber-reinforced polymer
CLD	constant-life diagram
CV	coefficient of variation
DIC	Digital Image Correlation
FE	finite element
FRP	fiber-reinforced polymer
GFRP	glass fiber-reinforced polymer
GP	genetic programming
M3	Macro-level predictive modeling, design and optimization of advanced lightweight material systems
MLE	maximum-likelihood estimate
RUC	representative unit cell
T-C	tension-compression
T-T	tension-tension
UD	unidirectional

1

Introduction

In order to achieve the goal to limit global warming to 2.0°C over pre-industrial levels, the CO_2 stabilization target of 450 ppm should not be exceeded. To achieve this goal, manufacturers in transportation and machinery sector are focussing on creating lighter designs to reduce the carbon emissions of their products. Typical emission reductions reported are 6-10 g CO_2 /km for 100 kg weight reduction for cars. [18–20] One of the keys in lightweight design is the use of **lightweight materials**.

Looking at all lightweight materials, **CFRP (carbon fiber-reinforced polymer)** composites are the most promising in terms of potential weight reductions. **CFRPs** originated from high-end industries (such as aerospace), where cost is less of a design driver and performance is of the utmost importance. Nowadays, other industries such as automotive, sporting goods and wind energy are increasingly considering **CFRPs** in their design. Specific price and recyclability requirements of these industries make way for a new research direction for **CFRPs**, specifically for the automotive industry.

While **UD (unidirectional)** composites are often the go-to choice in the aerospace industry, for automotive applications, there seems to be a preference towards **woven composites**. The advantages include a better drapability, better resistance for out-of-plane loading and easier handling for larger scale production compared to **UD** composites. [21] However, the typical woven fibre architecture (waviness) does introduce stiffness and strength reductions, particularly for compressive loading. [8, 22]

The development of these woven composites is however largely limited by a knowledge **gap in predictive modeling** of their behaviour. A lack of knowledge often results in large safety factors, which limits the advantages this material could offer. This creates a strong demand for adequate predictions, based on physically sound principles, validated by experiments. In particular in the field of durability and impact, much work is still to be done for FRPs, see figure 1.1. This master thesis serves as part of a much bigger project called M3strength [23], see section 2.4, in which both impact and durability of **CFRPs** are addressed thoroughly.

While **fatigue** for metal structures can be considered to be a well-known and understood phenomenon, for **FRPs (fiber-reinforced polymers)**, the mechanics behind failure associated with fatigue loading (or failure in general) is much more complex. This makes predictions of fatigue effects or extrapolation of data-sets difficult. Many modeling attempts have been performed on different scales, from microscopical crack initiation and propagation behaviour to macroscopic models, each with its own shortcomings and weaknesses. The fact that material properties change (non-linearly) during loading make it all the more difficult. [6]

A common weakness in many models is the **lack of experimental data**. For fatigue, the largest part of the literature is focussed on S-N curves. Many other variables of interest for model development such as the evolution of (shear) stiffness and permanent (shear) strain over time are rarely measured, although these can yield valuable information which can be used to improve existing models. Literature also tends to focus mainly on **T-T (tension-tension)** cyclic loading, as these experiments are easier to perform since instability is not a consideration. However, many loading situations can typically be characterized as **T-C (tension-compression)** or **C-C (compression-compression)** loading. While **T-C** is

typically more detrimental for a structure and can be considered the limiting case, C-C testing allows one to distinguish the effects of compressive loading in cyclic patterns.

CAE for FRP: state-of-the-art

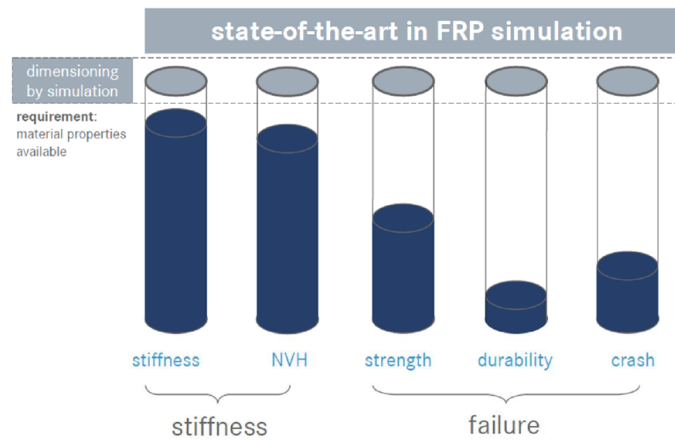


Figure 1.1: Current state of the art for CFRP predictive modeling. [1]

For the master thesis presented in this report, the goal is twofold. The first step was to develop a test setup for C-C and T-C testing of CFRPs, which can effectively capture strain information and other relevant variables with a reliable reference figure, so that effects such as hysteresis, stiffness and/or permanent strain evolution can be observed. This test setup is evaluated and used in a test program on woven carbon-epoxy material, in which fatigue performance under C-C and T-C loading is investigated, to be used for research on the behaviour of material properties under fatigue loading. Doing so allows for assessment of the possibilities of strain field measurements and the potential they offer for further developments of existing theories and models. This covers the second goal of this research.

This report is structured as follows: In chapter 2 "Literature Study", a literature study is presented which examines and evaluates relevant literature to set the stage for this research. This is followed by chapter 3 "Research Plan" where the research objective and questions which were set up in the beginning of this research are covered. In the next, chapter 4 "Experimental Set-up", the set-up of the measurement system is presented, discussing issues encountered during the development and the solutions. The design procedure and final design of the specimens, an important consideration when compression loading is included, is covered in chapter 5 "Specimen Design". Hereafter, in chapter 6 "Test Results", the results from the fatigue test program are discussed in-depth. Finally, in chapter 7 "Evaluation of Results", the conclusions from the test program are bundled and compared to literature. The report is finalized with chapter 8 "Conclusions and Recommendations".

2

Literature Study

The aim of this literature review is to identify, examine, review and evaluate relevant and up-to-date literature for the laboratory testing of plain woven carbon-epoxy composites loaded in C-C and T-C fatigue. The intent of this chapter is to present the literature used for setting the stage for this research.

Findings of this research are presented under four main sections, namely section 2.1, "*Failure of Woven Composites*", in which work is presented on static and fatigue failure of (woven) composite materials. Section 2.2, "*(Fatigue) Testing of Composites*", covers testing standards and data acquisition methods. Hereafter, in section 2.3, "*Composite Fatigue Modeling*", an overview of the state of the art regarding modeling is presented. Missing links in modeling set the stage for what is valuable to obtain from experiments. The final section 2.4, "*M3Strength Project*" shortly covers the project within which this thesis fits.

2.1. Failure of Woven Composites

Fabric composites, woven composites or textile composites are all terms used to describe an inter-laced (repetitive) structure of yarns, fibers or filaments, combined with a binding matrix. [24] While many composites are unidirectional, interest towards **woven composites** is increasing because of the opportunities and specific properties these materials have to offer. [24]

This section presents results from a literature study on the mechanical properties of woven composites. First, the static behaviour is discussed. Hereafter, focus shifts to fatigue behaviour. The section ends by drawing conclusions relevant for this master thesis.

2.1.1. Static behaviour

To better understand the static behaviour of woven composites, this subsection first presents a summary of microscopical failure mechanisms, with a focus on the mechanisms behind failure in compression. Hereafter, important qualitative macroscopical properties of woven composites are presented.

2.1.1.1. Microscopical Mechanisms Behind Static Failure of Woven Composites

The ultimate goal is to be able to better predict composite behaviour. To be able to do this, an important building brick is to understand different **failure mechanisms**. Mechanics of composite damage are currently of major interest for research and are thought to be critical for damage tolerance progress. [25]

While metal failure is most often dictated by a single propagating crack, the microscopic structure of composites results in a more general **damage accumulation**, involving far more complicated

processes. [7] Different failure modes exist and one may dominate in one load case but not in others.

Failure Mechanics in Tensile Loading When the fibers in a composite are loaded primarily in tension along their length, the dominant failure modes are fibers breaking, matrix cracks, delaminations and fiber-matrix interface failure. [26] Broken fibers are often related to final failure of a specimen since they serve the load carrying purpose of the composite. Matrix microcracks are typically one of the onsets of damage in composite failure. [27]

Failure Mechanics in Compressive Loading While the failure modes mentioned above are described under tensile loading, they can also occur under a compressive load. The most important failure mechanisms typical for compressive loading are mentioned below. [2, 3, 21, 28–35] The modes are qualitatively represented in figure 2.1 by Fleck. [2]

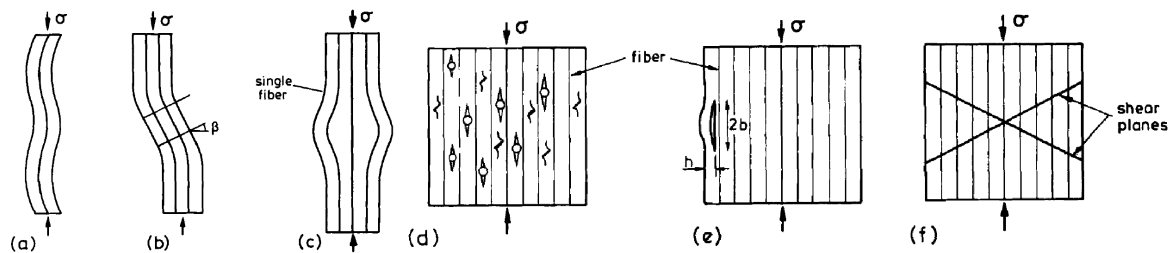


Figure 2.1: Different failure modes when fibers are loaded in compression. (a) (Elastic) microbuckling, (b) kinking (plastic microbuckling), (c) fiber crushing, (d) matrix splitting, (e) Buckle delamination of a layer close to the surface and (f) shear band formation, as represented by Fleck [2]

- **Microbuckling and Kinking:** Shear buckling instability in which the matrix deforms. Single fibers undergo buckling deformations called microbuckling. When these deformations are large enough, the surrounding matrix will undergo plastic deformation and kinking occurs. Kinking failure involves significant plastic deformation of the matrix, as well as highly loaded fibers on the outside of the kink bands, often resulting in fiber breakage. [31] Kinking is known to be of major importance in composite compressive failure for the widely used composites with stiff fibers and soft polymer matrix. [2]

Initial misalignment or waviness plays a significant role in the initiation of kink bands or microbuckling. Kinking of fiber tows aligned with the load is often the most important failure mechanism in woven composites under compression. [36] A qualitative representation of a kink band is shown below in figure 2.2.

Note that the terms ‘microbuckling’ and ‘kinking’ are sometimes referred to in literature as ‘elastic microbuckling’ and ‘plastic microbuckling’.

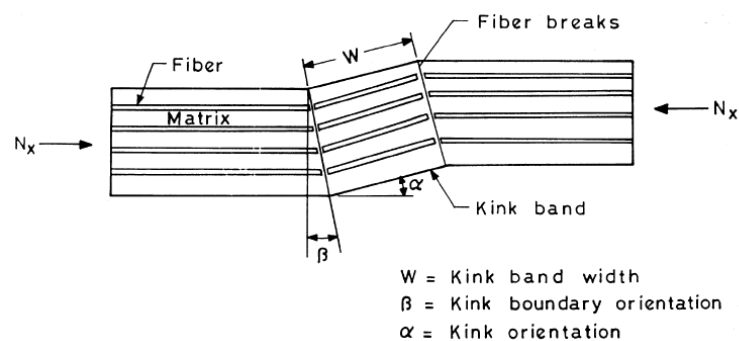


Figure 2.2: Kink band essentials [3]

- **Fiber Crushing:** Fibers failing in a compressive manner. In particular for weaker fibers such as Kevlar, this is of importance. For strong fibers such as carbon or glass, this failure mode is unlikely to occur in practice. [2]
- **Splitting:** Longitudinal matrix cracks aligned with the fibers (and load). [2, 37]
- **Buckle Delamination:** Buckling of a surface layer due to interlaminar bond failure. Often an important driver in compression after impact situations. [2, 32, 33]
- **Shear band formation:** Matrix failure occurring in a band, oriented about 45° with the fibers. Only relevant for very low fiber volume fractions and therefore omitted from this work. [2]

Failure Mechanics for Woven Composites Mechanisms described above apply in general also to woven composites. Woven laminates tend to show a **large resistance to delamination** and transverse rupture. [38, 39]. For brittle resins however, delaminations are often observed, while ductile resins seem to induce **kink band formations**. [4]

While the effect on tensile loading is negligible [40], **fiber waviness** is known to be detrimental to a composite under compressive loading. [36, 41] De Carvalho et al. investigated 2D woven carbon-epoxy composites under compression through the use of four point bending tests. They noticed damage initiation mainly at the **crimp regions**, for weft-dominated satin weaves more abruptly than for twill or warp-dominated satins. Failed tows showed **kink bands** in all investigated specimens and therefore kinking was identified as the governing mechanism of damage for load-aligned tows under this loading, followed by inter- and intra-ply delaminations, matrix cracking and transverse tow (weft) cracking, see figure 2.3. [4, 36]

2D woven laminates loaded under compression will be prone to out-of-plane displacements. Because of this, under compression, **adjacent layers will interact**. Studies have shown that how layers are stacked compared to each other might lead to a difference up to 32% of the compressive strength. [4, 36] For in-phase stacking of adjacent layers, the displacements tend to amplify each other, while for random stacking, some regions of out-of-phase tows will act to reduce the effect and can be expected to result in larger resistance to compressive loading. [4]

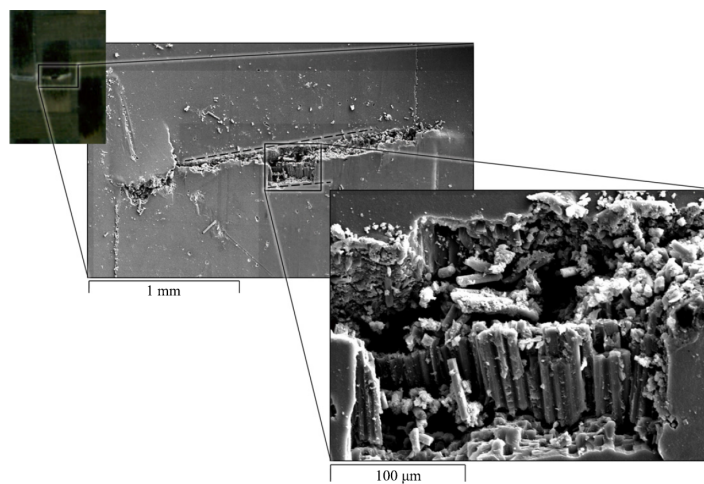


Figure 2.3: Kinking failure in a 2x2 twill specimen [4]

2.1.1.2. Macroscopical Properties of Static behaviour of Woven Composites

One of the most important advantages of woven composite materials is **reduced cost**, particularly due to improved drapability and handling capabilities. [21, 24, 42, 43] The second big advantage is that **complex shapes** can be created using weaves. Apart from that, fabrics typically also show higher impact resistance and damage tolerance compared to UD counterparts. [42, 43] Out-of-plane mechanical properties (strength, stiffness, toughness) are usually higher. [43, 44]

However, there are some downsides as well. **Axial strength and stiffness** will typically 10-25% lower than for UD counterparts. [42, 44] Since the in-plane properties are balanced, design space is somewhat limited compared to UD composites. [43] Although in compressive loading, the sensitivity to misalignment is much smaller than for UD composites [45, 46], Pandita et al. showed that their off- and on-axis behaviour is greatly different. [5] One of the largest current drawbacks of woven composites is that **predicting their mechanical behaviour is complex**.

2.1.2. Fatigue behaviour

In this subsection, fatigue behaviour of woven composites is discussed. It starts by applying failure mechanisms described above to cyclic behaviour, and hereafter macroscopical properties of fatigue behaviour such as stress-life observations and property evolutions are discussed.

2.1.2.1. Microscopical Mechanisms Behind Fatigue Failure of Woven Composites

For composites, fatigue is a **complex** phenomenon where **different failure modes interact**, in particular in textile composites. [44, 47] For similar loading conditions, fatigue failure may exhibit different failure modes compared to static failure. [33] Even very early in the fatigue life, damage effects can be seen in composites. [14, 47]

For woven composites loaded in cyclic tension along the warp fibers, damage initiation typically starts early in the fatigue life with **cracking of weft yarns**, figure 2.4 (a). [21, 44, 47] These are then followed by **meta-delaminations** (bundle debonds), **interply delaminations** and finally **broken load-aligned fibers**, figure 2.4 (c-d). Actual sequence and propagation of damage depends greatly on the lay-up and loading conditions. [44, 47] Damage stages are described by Pandita et al in [5] as shown in figure 2.4. In cyclic compression or tension-compression loading, the main mechanisms are the same as those for tensile loading. However, kinking and yarn buckling typically grows from microcracks and meta-delaminations, which result in extensively destabilised fiber bundles, allowing kinking to occur more easily. [21]

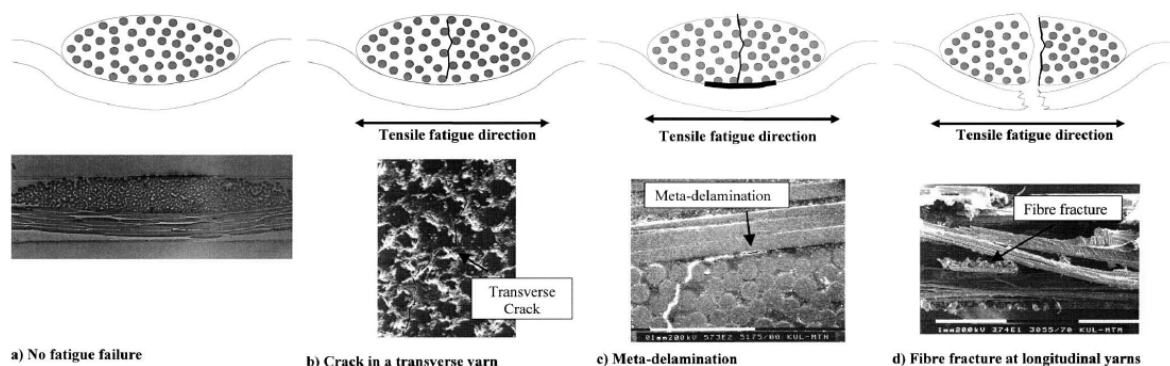


Figure 2.4: 4 stages of fatigue life for a woven composite. [5]

Quaresimin et al. investigated plain woven carbon-epoxy composites under different angles and different R-ratios. For weaves aligned under T-T loading, almost no delaminations were observed and failure was reported to be very sudden. The same laminate under T-C loading shows a large amount of damage mechanisms already in early stages of the fatigue life, including delaminations, which, together with the compressive loading, illustrate the detrimental effects of T-C loading. Final failure was however still dictated by fiber breakage. When the laminates are used under an angle (45°) however, the scenario changes entirely. In T-T as well as T-C loading, damage initiation is dictated by transverse matrix cracks followed by a large concentration of delaminations, being the mechanism dictating final failure. [8, 44]

Fruehmann et al. investigated fatigue damage evolution in woven E-glass epoxy under low loading and noticed weft fiber cracks even after loading at only 10% of the ultimate stress. [48]

2.1.2.2. Macroscopical Properties of Fatigue behaviour of Woven Composites

While fatigue research in metals has been a long ongoing process, for composites it is a relatively new field. Despite the completely different underlying mechanics, this has led to the use of **stress-life (S-N)** or **constant-life diagram (CLD (constant-life diagram))** representation of composite fatigue data. While this directly represents the experimental results of composite fatigue, it gives no indication of the underlying mechanisms, which may be different from one case to another. This is dangerous because it can lead to oversimplification (curve fitting of experimental data) and false generalizations. [7, 8, 44]

Composites typically suffer from a **decrease in strength and stiffness** throughout their fatigue life, which degrade until the point where the structure cannot resist the applied loads anymore, see figure 2.5. [6, 9–11, 14, 21, 24, 26, 32, 38, 42, 44, 49–57]

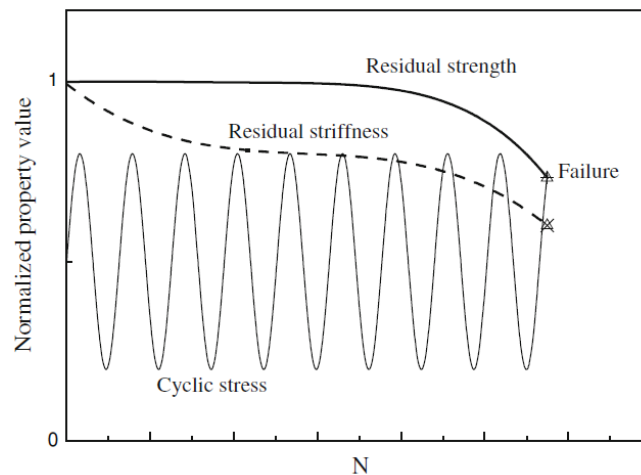


Figure 2.5: Degradation of strength due to cyclic loading until the point where the structure can not cope with the applied loads anymore [6]

In this subsection, macroscopical characteristics (stress-life behaviour and property evolution) of composites under fatigue are presented.

Stress-life Behaviour Originating from metal fatigue investigations, **S-N curves** are often applied in composites to give an idea about the fatigue behaviour under a certain cyclic loading. The main reason behind this is that an S-N curve can easily be generated using simple recording devices. Typically, composites show flat S-N curves. [32] A great part of laboratory tests are on T-T fatigue, since these experiments are easiest to perform, while T-C or C-C has often shown to be more detrimental [8, 27, 44] Due to the underlying nature of composite fatigue, composites are very sensitive to the mean stress effect and can be expected to have non-linear constant-life diagrams (CLDs). [6, 58]

When comparing two similar materials where one has a higher static strength than the other, this will not necessarily mean that its fatigue strength will also be higher, even though this assumption is often used in modeling. [32]

Montesano et al. investigated carbon-epoxy satin weave systems for their fatigue performance using thermography and SEM measurements to investigate the damage states of the material throughout the fatigue life. He confirmed the existence of a **fatigue limit** for high cycle loading, similar to metals. [55] This is in contradiction with other authors, who encounter damage effects at loads as small as 10% of the ultimate load and **claim there is no such limit**. [48]

Because of the complex nature of composite fatigue, the most important point regarding S-N curves is the **large experimental scatter** which is found in literature. Even when the loading pattern, materials used, lay-up, thickness, test method,... are the same, imperfections and manufacturing defects are unavoidable and result in a large amount of scatter compared to metal S-N curves. [30, 32, 59]

Additional sources of **variability** in results may include for example testing or specimen preparation done by different operators, on different machines, different environmental conditions... For a validation exercise, T-T fatigue tests ($R=0.1$) for a UD glass-fiber epoxy composite material were performed in a total of 9 labs. Sims and Harris [7] show the results include large scatter, as expected, see figure 2.6. Similar tests were performed on a carbon-fiber epoxy system, see figure 2.7. Two important trends can be noticed here: Firstly, the results show a **larger scatter** for the carbon-epoxy system, and secondly, the S-N behaviour seems to be more **flat**, giving an indication of a (higher) fatigue limit (if it exists) for carbon-epoxy. [7]

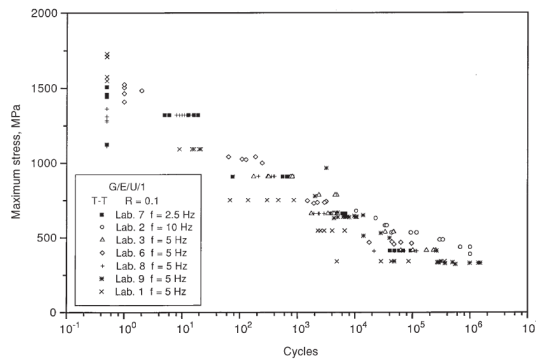


Figure 2.6: S-N curves for the same material (UD glass-epoxy) tested in different labs. [7]

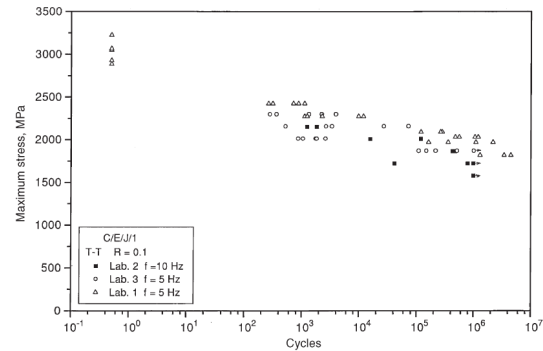


Figure 2.7: S-N curves for the same material (UD carbon-epoxy) tested in different labs includes great variability and a flatter S-N curve. [7]

Quaresimin investigated the behaviour of woven (twill 2x2) carbon-epoxy laminates under static and cyclic ($R = 0.05$ and $R = -1$) loading. [8] He used three different layups, namely $[\#(0/90)]_{10}$, $[\#(\pm 45)]_{10}$ and $[\#(0/90)_3/(\# \pm 45)_2]_s$. To generate S-N data he assumed that cycles to failure would be a log-normal distribution and curve-fitted the data obtained, see figure 2.8. He concludes from this that, regardless of lay-up, laminates turn out to be **sensitive to tension-compression** loading.

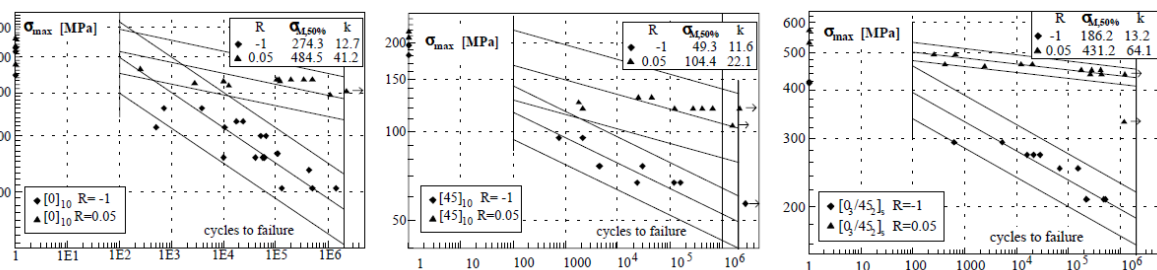


Figure 2.8: S-N data for different lay-ups and R-ratios including 10% and 90% probability of survival scatter bands by Quaresimin [8]

Composites are anisotropic. For loading aligned with fibers, typically, deformation before failure will be small. [30] However, this is not true when the fibers are not aligned with load application. Kawai et al. [9, 44] investigated the effect of **orientation** by loading plain weave carbon-epoxy composite structures under cyclic tensile loading in both on- and off-axis orientations. Even after normalizing the stress data to the ultimate stress of the material under the relevant orientation, the results show that **off-axis loading is detrimental to fatigue performance**, see figure 2.9. The reason behind this can be seen from investigating the corresponding fracture surfaces, see figure 2.10. It is clear from this photo that the nature behind this fracture is entirely different, with necking and fiber reorientation occurring for the off-axis specimens.

A final point on S-N curves is that some authors [6, 60] suggest that data from **static tests should not be included in S-N diagrams**, because they are typically obtained at different strain rates, which could influence the mechanical properties.

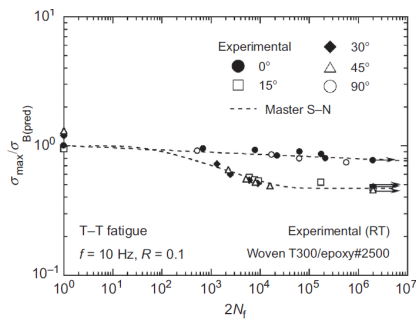


Figure 2.9: Plain weave carbon-epoxy under different orientations. S-N curve normalized to ultimate strength [9]

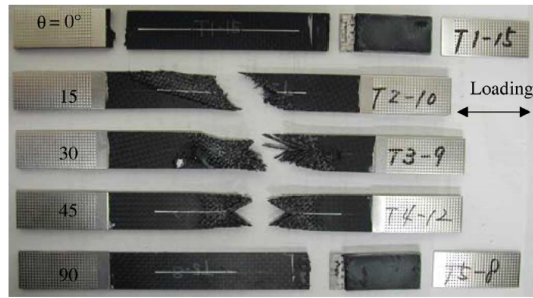


Figure 2.10: Plain weave carbon-epoxy under different orientations. Fatigue fracture surfaces show a clear distinction between off- and on-axis loading [9]

Property Degradation and Hysteresis Cycles Fatigue damage in composites is characterized by a reduction of properties such as **strength** and **stiffness** up until the point where the structure cannot cope with the applied loading anymore. [9–11, 14, 21, 24, 26, 32, 38, 42, 44, 49–57], see figure 2.5. Typically, damage effects can be observed early on in the fatigue life of a specimen, from the very beginning of load application. [11, 14, 21, 32, 47, 48]

Degradation of stiffness and (to a lesser extent) strength, is often used as basis for phenomenological fatigue modeling (see section 2.3). Overall, the effect of stiffness reduction for T-T loading can be qualitatively described by **three regions of the fatigue life**, as shown in figure 2.11. In the first portion (region I) of the fatigue life, a sudden reduction of stiffness is often observed, followed by a more constant and moderate degradation in region II. When the material is nearing final failure, the stiffness reduction is large again in region III. [6, 10, 53] Experimental results of this behaviour have been found by Khan et al. [10] for quasi-isotropic carbon-polyester fabric composites (see figure 2.11), by Yoshioka and Seferis [11] for carbon-epoxy and carbon-phenolic fabric composites (see figure 2.12) and by Montesano et al. [55] for a satin weave carbon-epoxy (see figure 2.13), all under T-T loading.

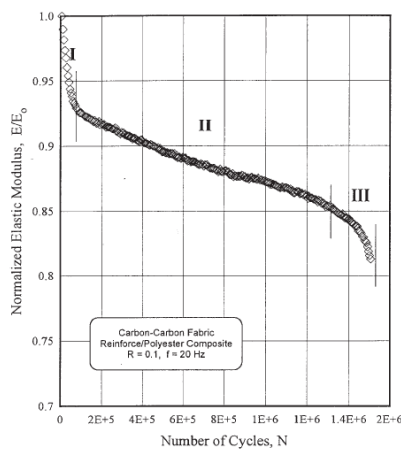


Figure 2.11: Stiffness degradation of a carbon-polyester fabric [10]

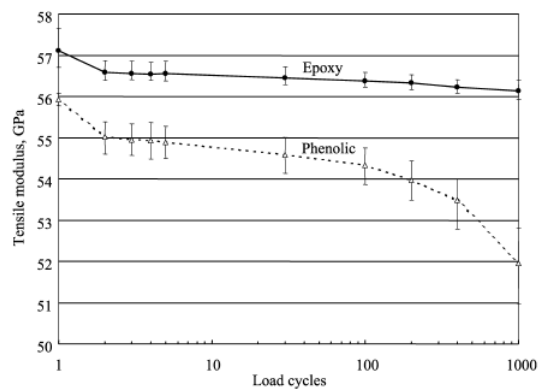


Figure 2.12: Stiffness degradation of a carbon-epoxy and carbon-phenolic fabric [11]

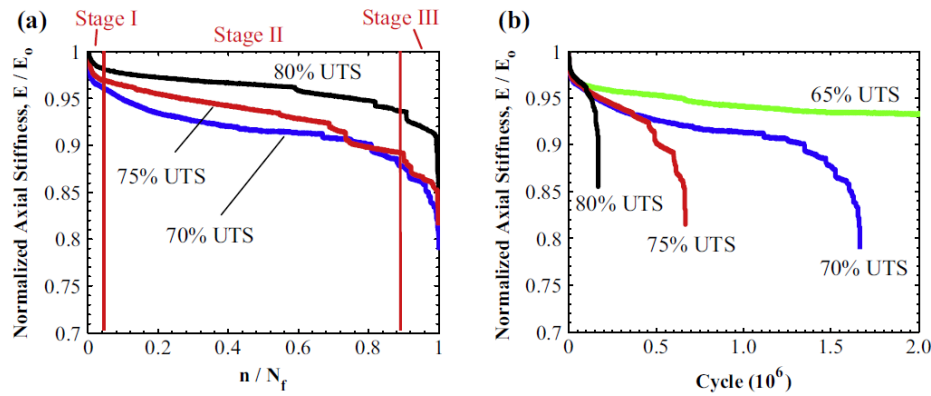


Figure 2.13: Stiffness degradation of 5 harness satin weave carbon-epoxy [6]

It has been mentioned before that most of the damage in woven composites loaded in tension in on-axis directions is mostly contained within the weft fibers (perpendicular to the loading). Since these fibers barely contribute to the stiffness performance of the overall laminate under this loading, this stiffness won't be affected by that much. On the contrary, for off-axis loading, a much larger dependence of stiffness on the fatigue damage can be expected. [5]

Hysteresis cycles and stiffness loss in stress-strain behaviour can be linked to energy dissipation and damage in the material. One example of this is Giancane et al. [14] who used DIC (Digital Image Correlation) to obtain good correlation between hysteresis area (dissipated energy) to the stiffness of a GFRP (glass fiber-reinforced polymer) laminate. Toubal et al. [61] also showed good correlation between heat dissipation and damage (defined as stiffness loss) in woven carbon-epoxy laminates. The effect of stiffness loss throughout the fatigue life can be seen in figures 2.14 and 2.15 by Quaresimin et. al [8, 44]. Here the detrimental effect of T-C loading compared to T-T loading can clearly be seen by the larger hysteresis cycle and larger reduction of slope of the stress-strain curves throughout the fatigue life. They also linked this to a much larger temperature increase (25 °C) for the T-C loading compared to T-T, where temperature stayed more or less constant. Note that this in itself makes a comparison between the two somewhat biased since thermal stresses will have been present for T-C loading in this case.

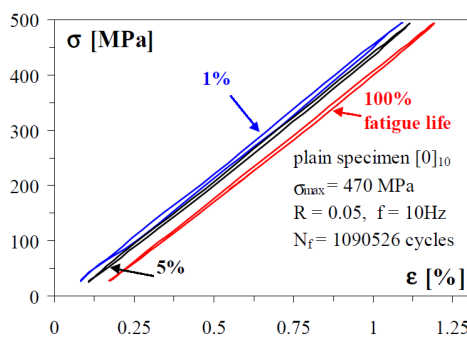


Figure 2.14: Hysteresis cycles under T-T loading [8]

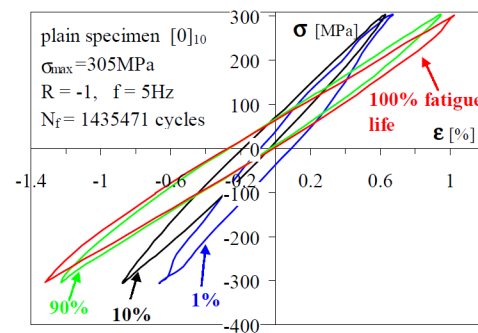


Figure 2.15: Hysteresis cycles under T-C Loading [8]

2.1.3. Conclusion

Failure of woven composites and in particular fatigue failure has already been investigated and characterized. Studies on governing failure mechanisms, stress-life behaviour and evolution of properties focusses mainly on T-T loading. Data for C-C or T-C loading is rarely found in literature for these materials. Where it is presented, the focus is on longitudinal stiffness or stress-strain behaviour. Data regarding shear property evolution or transverse stiffness is missing in literature.

2.2. (Fatigue) Testing of Composites

Experimental characterization of fatigue performance has been an important part of durability research for a long period of time. This section mentions some testing standards which have been produced and can be relevant for this research. Hereafter, the focus is on measurement techniques, followed by a conclusion of this section.

2.2.1. Standards

Over the years, a large interest has gone into developing test standards for composite materials. The main reason for this is that results are often highly dependent on the test method, which causes large scatter in properties reported by many authors [7, 8, 62]. Relevant standards are produced by ISO (International Standardization Organisation), ASTM (American Society for Testing and Materials), SACMA (Suppliers of Advanced Composite Materials Association) and CEN (Comité Européen de Normalisation). [7, 28]

The most relevant testing standards for **fatigue testing of coupon composites** are *ASTM D3410* or *ISO 14126* (shear loading only) [7, 63] and *ASTM D6641 "combined loading compression"* (including end loading) [17] *ASTM3039*, *ISO 13003:2003m "Fiber-reinforced plastics: Determination of fatigue properties under cyclic loading conditions"*, *ASTM D3479 "Standard test method for tension-tension fatigue of polymer matrix composite materials"* and *JIS K 7083-93 "Testing method for constant-load amplitude tension-tension fatigue of carbon fiber-reinforced plastic"* for tensional loading can be relevant for tension experiments. [7, 44, 64]

In order to derive **in-plane shear properties from uniaxial tests**, ASTM standard D3518 [65] can be used. This standard is developed for UD composites loaded under tension but the concept could be applied to woven composite materials as well, see section 6.

It should be noted that for all of these test methods, a uniaxial test is used on relatively small specimens. This results in **free edges** which are prone to delaminations [32]. These free edge delaminations are however less likely to occur in real life structures, where free edges are less frequently observed and where they are, they are typically in the proximity of a fastener. On the other hand, they are difficult to avoid for coupon testing. It should be noted that material tests merely serve as a first step in the bigger process of a design phase, where tests of the actual (sub)structures are always performed as well before being put into service.

However, when considering measuring of evolution of properties such as stiffness, no standard test methods exist.

2.2.2. Measurement

A literature investigation on measurement techniques results in many widely used and well known techniques such as strain gages and extensometers for strain measurements, thermocouples and thermography for temperature measurements and microscopy to investigate microscopic behaviour of a specimen after failure. These techniques are well-known and are therefore not extensively covered in this study. **Digital image correlation (DIC)** is a less widely used technique which is gaining new grounds. For this research in specific, it has potential since it can be used to capture displacement fields and thereby measure strains in all directions.

DIC is a technique for measuring strain and displacement based on optics, with no contact required. DIC works by comparing images of a specimen with a reference. On this specimen some sort of high contrast pattern is applied (if required) which allows for tracking of blocks of pixels. [66] From these displacements, a strain field can be obtained. DIC is a powerful and promising technology, and its potential for application to experimental mechanics was already put forward in the 1980s [67].

Throughout this thesis, DIC has proven to be a method which can offer a range of advantages over conventional methods used for fatigue characterization today:

- **Strain gages have to tendency to debond** after a number of cycles. Measuring fatigue behaviour using strain gages can therefore be considered unreliable since one cannot tell with

certainty that debonding has started and what the effect of that on strain data is.

- Extensometers are therefore often applied in fatigue experiments. However, these **only measure displacement in one direction**. The advantage of **DIC** is that displacements can be measured in any direction by comparing displacements of two points. This is helpful for example to characterize shear stress/strain behaviour of $\#(\pm 45)$ laminates.
- When strain fields are non-uniform, strain gages and extensometers fail to effectively show and map this. For this experiment of woven laminates, **DIC** can characterize material behaviour and for example show differences between warp/weft in terms of strains, local Poisson's ratio,... These values could never be measured using strain gages or extensometers.
- **DIC** is often denoted as being expensive and time consuming. However, while the start-up cost can be relatively large compared to for example strain gages, once this system is set up, applying a speckle pattern and calibrating the system can be done relatively fast. The effort involved in bonding strain gages for a large batch of tests is considerable and over time can become very costly as well.

2.2.2.1. Set-up

A typical **DIC** setup is shown in figure 2.16 [12]. In this setup we see a camera pointed at a specimen with a hole loaded in cyclic tension. A light source is present since constant lighting of the specimen is important due to the nature of the technique. On the left in figure 2.16, we can see a typical random **speckle pattern**, examples of which are found all over literature. This can easily be applied using a kind of spray-paint and results in a high contrast image. The high contrast makes it possible for the camera to follow deformation and displacement of the entire field upon load application. From this a strain field and other valuable information can be deduced. Note that **DIC** is in principle even not only limited to optical images, also surface roughness maps can be used for example. [66]

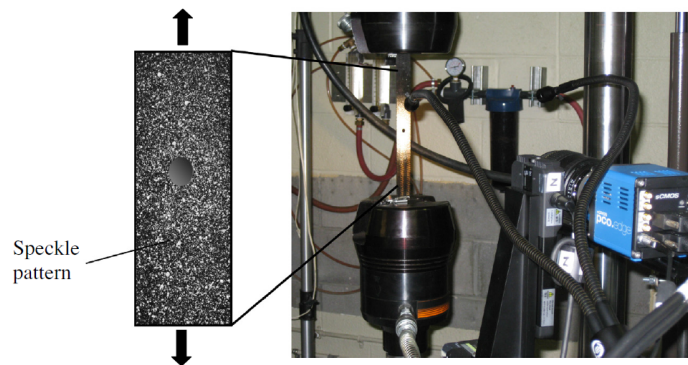


Figure 2.16: Example of a typical speckle pattern and **DIC** setup for cyclic tension experiments [12]

2.2.2.2. Principle

The principle of **DIC** is to detect displacement from digital images taken at different times. Since it is practically impossible to follow the movement of 1 pixel from one image to the next, generally a point is characterized by a subset of pixel points to be matched. An example of subset correlation is shown in figure 2.17. Note that this average based scheme could introduce issues near edges or in the neighbourhood of cracks for example. Despite this, **DIC** is regularly used successfully to determine crack properties [68, 69] or even detect cracks [66, 70].

Each subset area is expected to have a unique gray level distribution in its set. One big assumption is that this level does not change during deformation. [13] While this is generally true, care must be taken when comparing high cycle fatigue test images for example, when day and night might have an influence and sunlight in the lab could introduce issues. Additional issues could come from shadows due to clamps, particularly for this research, where small compression samples might be used.

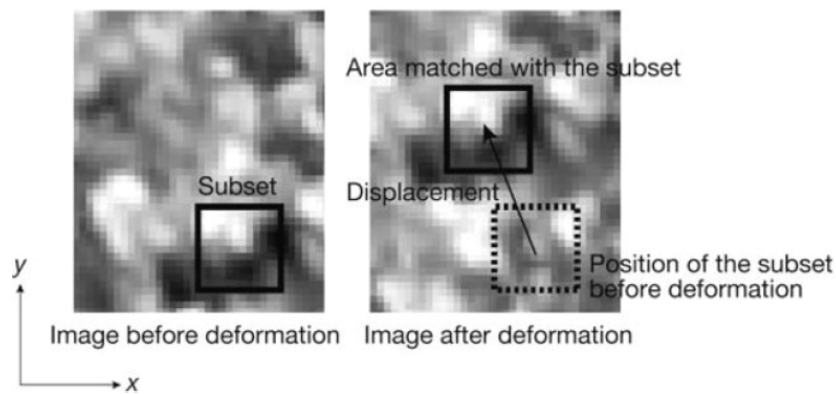


Figure 2.17: Example of correlation of a subset of pixels before and after deformation. [13]

In order to correlate two images by their gray levels, they are mapped. This can be done through all types of **interpolations**. [13, 69] A simple example of this is shown in figure 2.18, where first a set of 10x10 pixels is shown, after which the bilinear (b) and bicubic (c) interpolation results are shown. Other interpolation techniques exist as well. It is obvious that the interpolation type will affect the result in terms of accuracy (particularly for large displacements), but also in terms of time consumption. [13] Issues with convergence might be solved through mechanical assisted DIC, as proposed by Roux et al. [71]. However, this would be more difficult to implement.

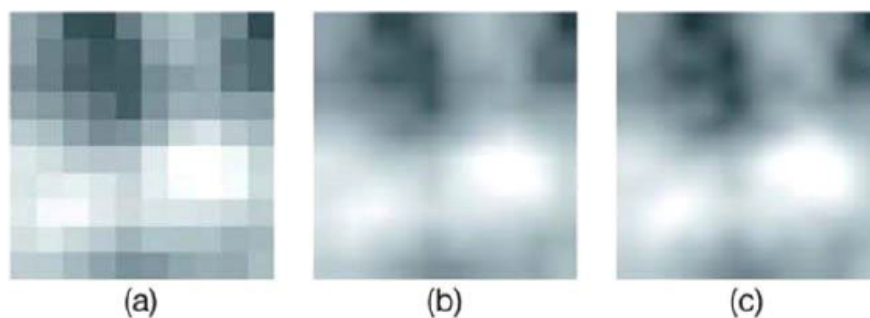


Figure 2.18: (a) subset of 10x10 pixels. (b) Bilinear interpolation. (c) bicubic interpolation [13]

2.2.2.3. 3D Imaging

For some purposes, researchers can also be interested in the out of plane displacement of a specimen. To do this, the eyesight principle is imitated, where 2 cameras are used to obtain a 3D image, capable of detecting out of plane motion. [72]

2.2.2.4. Results

DIC can be used for many purposes. Giancane et al. [14] used DIC to obtain the stiffness degradation and dissipated mechanical energy [J/mm^3] from strain maps during tensile fatigue tests. Averaging these out over the thickness shows good correlation between the two, see figure 2.19. Montesano et al. [12] predicted fatigue damage in composites and compare this to DIC measurements, as shown in figure 2.20. Laurin et al. [70] also used DIC in their work to better understand failure mechanisms in aeronautical composite structures. DIC was used to validate boundary conditions of the tests, cross-check with other measurements, understand the underlying physics behind the behaviour and validate finite element method predictions. Faes et al. [73] used DIC to obtain full field strain measurements as to characterize tensile behaviour of ductile steel fabric/epoxy composites.

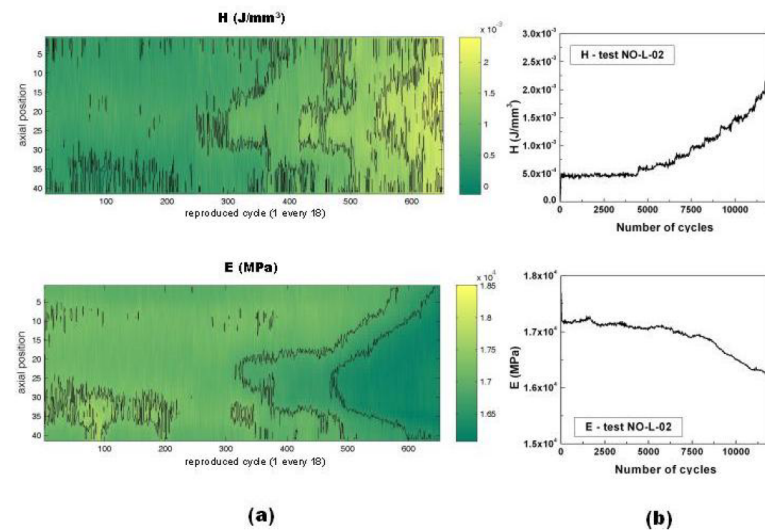


Figure 2.19: Giancane shows a correlation between dissipated strain energy and Young's modulus [14]

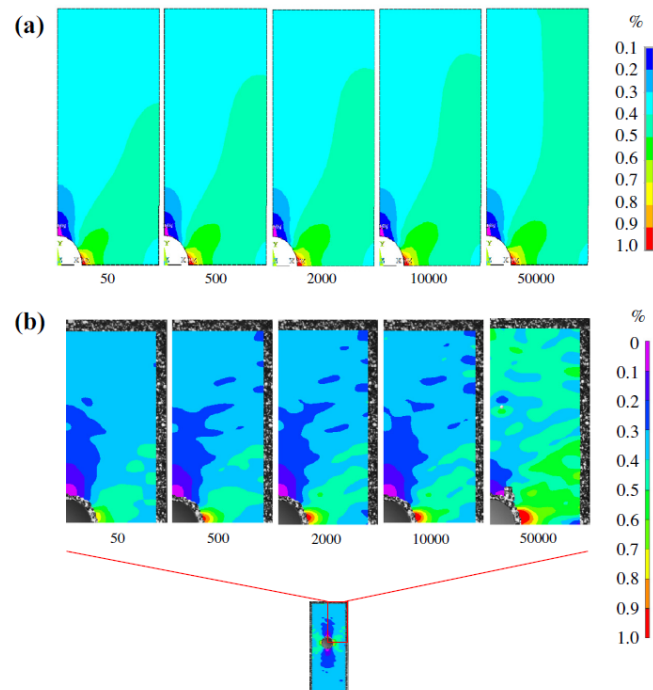


Figure 2.20: Montesano's fatigue model predictions (a) compared with DIC measurements (b) [12]

2.2.3. Conclusion

While some standard test methods exist for coupon testing of composites in compression and tension, no standards exist for measurements of the evolution of properties such as stiffness, permanent strain and hysteresis throughout a specimen's fatigue life. Strain gages tend to debond after a few fatigue cycles and extensometers only measure strains in one direction. DIC can prove to be of value here. Through the measurement of displacement fields, shear properties from uniaxial tests and strains in different directions can be obtained.

2.3. Composite Fatigue Modeling

The lack of good prediction methodologies often leads to composite structures being overdesigned, since large safety factors are required. Improved modeling of composite structures under fatigue can reduce these safety factors and lead to more efficient designs. This section covers the state of the art regarding modeling of composite fatigue.

Sendeckyj describes the ideal composite fatigue theory as

“one based on a damage metric that accurately models the experimentally observed damage accumulation process, takes into account all pertinent material, test and environmental variables, correlates the data for a large class of materials, permits the accurate prediction of laminate fatigue behaviour from lamina fatigue data, is readily extendable to two-stage and spectrum fatigue loading, and takes into account data scatter.” [58, 74]

This theory is obviously impractical for many reasons. [74] Van Paepegem mentions two main reasons why composite damage modeling and in particular composite fatigue modeling is difficult. The first reason is that **specimens are never perfectly produced** and variability in these is only controllable up to a certain level, which makes drawing conclusions from experiments a cumbersome task. The second is that damage mechanisms are present at **many scales** ranging from fiber-diameter scale through component and structural levels. Covering all of these would require a tremendous computational effort, which would still run into issues due to the material variability. [44] Therefore, some type of curve fitting is often included. [32]

Many modeling attempts have been performed however. The peculiarity here is that most of them are performed uniaxially for a certain material, with a certain stacking sequence, boundary conditions, frequency, stress amplitude,... Which raises questions about their applicability to real world structures, where extremely large number of degrees of freedom are possible, with varying or higher frequencies and amplitudes, loaded biaxially, varying damage mechanisms, ... [44, 75]

Degrieck and Van Paepegem propose a classification of fatigue models for fiber reinforced plastics in [76], based on the classification by Sendekyj in [74]. They categorize existing fatigue life models as follows [21, 44, 58, 76]:

1. **Fatigue life models:** Don't account for actual damage mechanisms but rely on S-N curves or CLD diagrams. Requires a large amount of experiments for every material, load case,... This makes them difficult to extend for more general cases. However, the models are straightforward and don't require detailed information.
2. **Phenomenological models for residual stiffness or strength:** Propose an evolution law of stiffness or strength throughout a specimen's fatigue life based on continuum mechanics theory.
3. **Progressive damage models:** Predict fatigue in relation to specific damage variables (crack initiation and propagation, delaminations,...)

For this short overview on fatigue modeling, the same classification will be applied. Since the focus of this master thesis lies on experiments, this overview is not exhaustive and serves a more illustrative purpose.

2.3.1. Fatigue Life Models

Fatigue life models are most often dictated by curve fitting with certain parameters. [21] Experimental input is based merely on fatigue data obtained at different load levels (and R-ratios), and in some cases even only static data.

For **S-N** formulations, many different primitive functions have been used. A short overview is presented in [6], using logarithmic, semi-logarithmic, Whitney's Weibull based or Sendekyj's wear-out model as basis for S-N curve fitting. Additionally, the use of genetic programming (**GP (genetic programming)**) often also is used for curve fitting of S-N data. [6, 7, 58] They have been compared by Vassilopoulos for different materials, orientations and loading conditions and the results were only minor differences for limited data sets.

It has already been mentioned that composites show a large dependence on the mean stress applied. [6, 58] While the well-known **Goodman diagram**, linearly based on a single S-N curve, is most commonly used due to the origin of fatigue modeling from metals, it is less suitable for FRPs due to the different failure mechanisms at hand. Several other **constant life diagrams** have been proposed by different researchers and they are combined in [6]. The piecewise linear CLD is the first obvious alternative, obtained from linearly interpolating between different R-ratios in the plane. Harris' CLD is based on semi-empirical data from different CFRPs and GFRPs. Kawai's CLD is asymmetric but based on a single S-N curve, obtained at the critical R-ratio (Around -0.55, depending on temperature) defined by Kawai [9, 44, 77]. Boerstra proposed a more complex model which does not consider the R-ratio in the analysis. Kassapoglou proposes a model based on the assumption that the failure probability during a cycle is constant [78, 79] and later adapted this with variable failure probability to account for damage effects. [32, 40, 80] This model allows for estimation of a distribution based merely on static strength data (and the involved scatter) and can be extended to for example spectrum loading. [32, 78, 79] For all abovementioned models, **simplicity is a trade-off with accuracy**.

Many other modeling attempts have been performed, not all of which will be included in this paper. One more example is an approach promising reduced experimental data and was proposed by Vania and Carvelli [81]. They used a function similar to the sigmoid function to reduce the amount of data required to fit the T-T S-N curve of plain weave glass-epoxy material.

2.3.2. Phenomenological Models for Residual Stiffness/Strength

Models based on macroscopically measurable parameters such as residual stiffness or strength have been presented by several authors. Despite the fact that both are known to degrade throughout the fatigue life, in terms of modeling based on either one of both, there are some significant differences:

- The first is available **experimental data**. While stiffness measurements can be performed throughout a fatigue test, to perform a residual strength test means prematurely ending the test. A single fatigue test can generate a set of stiffness data points, but only a single data point for residual strength, which is still at the cost of not knowing where exactly in the fatigue life the specimen is at that point. [44, 58]
- **Strength decreases only minimally** compared to stiffness throughout a composite's fatigue life, until the very end of fatigue life. [6]
- Strength in function of fatigue life typically involves **larger scatter**. [6]
- Residual strength is often a **parameter of interest** for a structure throughout its fatigue life.
- Strength-based models involve an **inherent failure criterion**: Failure occurs when the residual strength has degraded to the applied maximum (or minimum) stress. [44, 76] For residual stiffness, the case is somewhat different. Different proposals for a failure criterion include one based on a critical stiffness level or certain percentage of stiffness loss, one based on the strain and the static ultimate strain, or based on the fatigue secant modulus degradation to the critical static secant modulus. [6, 44, 76]

While both approaches have their advantages, the focus here is on **residual stiffness** based models, which are more commonly found in literature and can be evaluated using a more limited experimental effort.

The concept of **continuum damage mechanics** theory and the **damage variable D** were first introduced by Kachanov in 1958. The variable indicates a state of damage within a system, where $D = 0$ indicates undamaged material and $D = 1$ indicates a state in which integrity of the material structure is fully lost. From the concept of strain equivalence (a damaged volume of material under nominal stress σ shows the same strain response as a comparable undamaged volume under effective stress $\tilde{\sigma}$ [58]), the variable becomes a measure of stiffness loss [57, 58, 61]:

$$D = 1 - \frac{E}{E_0} \quad (2.1)$$

It was already mentioned that stiffness in composites typically degrades in 3 distinct stage in composites loaded in fatigue, figure 2.11. The models are typically described as **phenomenological** since they describe damage evolution dD/dN in terms of macroscopically observable properties rather than actual damage mechanisms. [76]

One of the first methods based on residual stiffness was presented by Khan et al. in 2001 [10]. They attempted to curve fit test results to match dD/dN through a power law to the stress amplitude.

Yoshioka and Seferis [11] applied a crimp and shear-lag model to develop a stiffness degradation model for woven carbon-epoxy loaded in T-T fatigue. Their model predicted correctly that property change occurred in the first stages of fatigue life.

From 2001 to 2005, Van Paepegem and Degrieck published several papers [51–53, 82–84] presenting experimental results for fully reversed bending of plain woven specimens, including a residual stiffness model incorporating damage, stress redistribution in damaged zones and keeping track of permanent strain evolution. For this model, the damage is presented as a tensor describing damage in all principal directions, each with their own degradation laws, including whether the loading is tension or compression. They then incorporated this model as a material rule in finite element software to allow for stress redistribution calculations.

Tate and Kelkar [50] performed T-T fatigue tests on braided carbon-epoxy composites at different braid angles and used the fitted S-N curve for this data as input to describe the stiffness degradation mathematically using a log-log relation.

Hochard et al. also applied the continuum damage approach to model fatigue [85–87] and static [38, 39, 88] failure in woven composite structures. In order to model the woven ply behaviour, they assumed a single woven ply to be consisting of 2 UD plies with correct thicknesses to account for warp/weft fibers. Then they applied an earlier model by Payan and Hochard [89] for UD materials to this. The conclusion was that predictions correlated well with experiments but were conservative near stress concentrations.

Apart from stiffness reductions aligned with the load, other elastic properties could also be used to characterize fatigue damage. Examples include Poisson's ratio, in-plane shear modulus, transverse stiffness and permanent shear strain evolution. Most models currently do not account for this. This mainly has to do with extensive experimental input that is required for this. Developments of techniques such as DIC allows for potential of improvement here. [44, 54, 58]

2.3.3. Progressive Damage Models

While fatigue life models and phenomenological models based on residual stiffness and strength require minimal computational effort, they rely to some extent on (semi-)empirical determination of fatigue behaviour prediction, and typically only very little extension is possible towards other materials or loading situations. The major drawback of these modeling techniques is that they do not cover actual damage mechanisms and how they interact. Progressive damage models are promising in that they require very little experimental input and, once established, can be easily extended to materials with other constituents, other lay-ups,... While at this moment they are limited by computational possibilities, they can be promising for future applications. [44] Note that these models are typically at the micro-(fiber filament scale) or meso-(fiber yarn scale) and that upscaling towards the macroscale and therefore experimental validation is not straightforward. [21]

Stresses at the level of fiber and matrix can differ significantly from the ply level stresses [90] Many models for different materials, UD and woven, have been developed so far. Many of them are based on a unit-cell approach. In which microscopic behaviour is modeled by assuming the ply or material consists of a periodic architecture in which repeating unit cells are present. Predicting the behaviour of one of these cells with periodic boundary conditions can serve as a solution for the (idealized) complete material behaviour. [15, 21, 91]

Potluri et al. [92] and Ruijter et al. [93] applied this unit cell approach with a finite element method to describe static behaviour of woven composite materials. Naik et al. [94, 95] applied a unit cell approach to determine material properties of plain weave fabric composites under compressive loading and transverse static loading, and obtained a decent match with experimentally obtain results. Huang

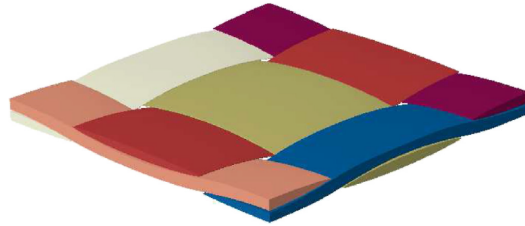


Figure 2.21: Example of a representative unit cell (RUC) [15]

[43] used the unit cell approach for a bridging model to determine fatigue properties of biaxially loaded woven composites to obtain reasonable agreement with predictions. Xu et al. [96] predicted fatigue properties using a progressive damage method for textile composites on the meso-scale by assuming the yarns to be homogeneous and transverse isotropic.

Not only simple 2D composites can be investigated. Mishra et al. [97] investigated the static in-plane properties of triaxial woven fabric through a unit-cell based FE (finite element) method. Zhang et al. [98, 99] applied a unit cell approach to braided 3D composites to simulate the free edge effect. To do this, they applied 3 different unit cells, to cope with actual edges of the material to predict behaviour there.

An example of a representative unit cell (RUC (representative unit cell)) can be seen in figure 2.21.

2.3.4. Conclusion

Composite fatigue modeling can be powerful to improve the efficiency of a design. However, reliable composite fatigue modeling is difficult since damage occurs on different scales and real life structures or specimens will always suffer from imperfections which are only controllable up to a certain level.

Many modeling attempts have been carried out. However, some potentially promising approaches lack experimental input for validation. Because of this, not much work has yet been performed. Measurements of parameters such as transverse stiffness, permanent shear strain and shear stiffness evolution can support further development of these approaches.

2.4. M3Strength Project

This project fits within the **M3Strength** project, organized by Strategic Initiative Materials (or 'SIM') flandres together with multiple industry and university partners. This project stands for "*Macro-level predictive modeling, design and optimization of advanced lightweight material systems*". The consortium consist of multiple teams from three academic research institutions (KU Leuven, Ghent University and Free University of Brussels), one knowledge research center (Flanders Make) and 11 industrial partners.

In order to obtain CO₂ norms, the automotive industry is looking at innovation in the materials industry as well. CFRPs have the most promising weight reductions but are currently challenged by cost. Only when significant weight savings are possible they become a viable competitor for current materials used for chassis, suspension,... The most important objective is to investigate the knowledge gap for efficient modeling for new lightweight materials. This is required to allow for smaller safety factors and hence more weight savings. While stiffness is currently well predicted, the most important knowledge gaps are in the field of failure (strength, durability, impact).

One main point of this project is to aid in development of predictive modeling for static, fatigue and impact loading situations. The main objective of this master thesis is not so much modeling as it is performing experiments which generate reliable fatigue data. These can be used later on to develop new, or improve existing models. [23]

3

Research Plan

3.1. Research Objective

The objective of this research is to generate reliable fatigue test data for woven CFRPs loaded in compression-compression and tension-compression fatigue and compare these with results from literature. The aim is to keep track of evolution of parameters like stiffness, Poisson's ratio, permanent (shear) strain and residual strength throughout the fatigue life. Based on this objective, the following research questions were formulated:

3.2. Research Questions

1. What experimental set-up is capable of reliably observing the evolution of properties such as *Poisson's ratio, stiffness, permanent shear deformation, residual strength and micro crack initiation* throughout the fatigue life of a woven CFRP under cyclic T-C and C-C loading?
2. How does the loading pattern and lay-up relate to evolution of *stiffness, Poisson's ratio, permanent shear strain, residual strength and micro crack initiation* throughout the fatigue life of woven CFRPs under cyclic compressive loading?
3. Can this property evolution behaviour be predicted using existing models or is an adaptation or elaboration required?

Question 1 can further be split up into sub-questions. The following sub-questions have been defined:

- i. What specimen shapes and lay-ups result in a reliable test set-up to observe T-C and C-C fatigue life and evolution of these properties?
- ii. What measures can be taken to prevent buckling and how do these measures influence the behaviour of the specimen?
- iii. How can reliable data on properties such as stiffness, Poisson's ratio and permanent shear deformation throughout the fatigue life of a specimen be obtained?
- iv. How can micro crack initiation in CFRPs under cyclic T-C or C-C loading be detected?

Question 2 can also be divided further into sub-questions:

- i. What influence does the lay-up have on T-C and C-C fatigue behaviour of woven CFRP laminates?
- ii. Are there any key differences for high and low cycle fatigue in woven CFRP laminates? If so, which?
- iii. How does this behaviour relate to T-T fatigue in woven CFRPs?

Question 3 can also be further divided as follows:

- i. Which models from literature are exist for the prediction of T-C or C-C fatigue behaviour in woven FRPs?
- ii. What behaviour is predicted by these models?
- iii. How accurate are these models?
- iv. Should current models be adapted/elaborated based on the experimental results obtained in this thesis?
- v. Can the conclusions from this research be expanded for other lay-ups, other materials,..?

4

Experimental Set-up

The first part of this master thesis consists of the design of a test set-up to perform fatigue experiments and capture relevant parameters in the process with a reliable reference figure. The system should be capable of the following:

- **Perform fatigue experiments** reliably so that they can be representative for a material's fatigue behavior under relatable loads.
- **Capture relevant data** reliably at intervals sufficient to characterize the fatigue behavior.
- The system should be relatively **simple in use**.
- Ideally, the system should hold **potential to be used for future related experiments** through minor adaptations.

In this chapter, the available infrastructure used for this research is presented first, followed by the final assembly of the data acquisition architecture and the software written to accommodate it, including evaluation of delays in the set-up

4.1. Experimental Infrastructure

Both quasi-static and fatigue tests have been performed for this master thesis. The available used infrastructure and measurement equipment is shortly discussed here.

4.1.1. Hydraulic test bench

All experiments have been carried out on an Instron 8801 (100kN) **servohydraulic fatigue testing system**, suitable for both high and low cycle fatigue. This system is capable of handling loads up to 100kN both in compression and in tension.

The 100kN dynacell fatigue **load cell** is mounted to the top actuator. Before the start of the test program, the accuracy (and repeatability error) of the load cell has been verified in accordance to Annex C of ISO 7500-1 by the Instron Calibration Laboratory. [100] From 3 test runs in tension and 3 in compression covering the full loading spectrum of the load cell (2-100 kN), the returned relative uncertainty is based on a standard uncertainty with coverage factor of $k=2$, resulting in a confidence of approximately 95 %. The largest relative uncertainties occur at 5 kN for both and are 0.33% and 0.32% for tension and compression, respectively.

For compression testing, the machine is fitted with an **alignment kit** to ensure proper alignment of the clamps in all directions. It is fitted with hydraulic wedge grips rated for fatigue for which the pressure can be controlled if required. The test bench is controlled by a control PC fitted with fast-track software by Instron, with which you can control the system using force, strain (extensometer) or displacement control. Hydraulics can be controlled as well and the machine has a specimen protection setting, to

avoid damage to specimens before the start of a test. The machine can output force, displacement and extensometer strain as analog signals.

4.1.2. Displacement/Strain Measurement

The most important source of data acquisition for this thesis has been DIC. Two sets of cameras have been utilised. Both camera types allow for external (hardware) triggering. Most measurements were performed using a set of Point Grey Grasshopper USB 3.0 cameras (GS3-U3-51S5M-C). These monochrome cameras have a resolution of 2448 x 2048 (5 MP) and can reach up to 75 FPS. The other cameras are AVT Stingray F-201 firewire cameras. They have a maximum resolution of 1600 x 1200 pixels and can reach up to 15 fps. The software for camera triggering and image retrieval is written to recognize both of the cameras, so that cameras could be changed fast if required. DIC images are processed using vic software by Correlated Solutions, see also appendix A.

Static strain measurements have also been confirmed using strain gages. These are manufactured by Vishay (micro-measurements) and are of the type CEA-06-125UN-350. They only allow for 5% of strain, which is more than enough in most cases. These models were selected since they are sufficiently small, which is required since two strain gages and one thermocouple were used on a single side of the small compression specimens, see below. It must be noted that strain gages typically only provide reliable information in the first cycles of fatigue life, after which the bonding between the specimen and strain gage fails.

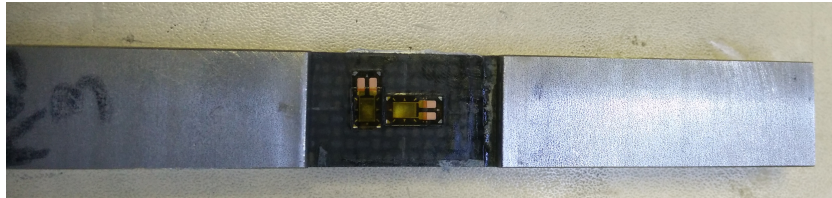


Figure 4.1: Two strain gages for longitudinal and transverse measurements

4.1.3. Temperature Measurement

Specimen heating during cyclic tests should be avoided. Heating can become so severe that material properties are altered and test results become difficult to interpret, see section 6.3. [7] Particularly when off-axis fibers are included, heating can become severe. [5, 7, 9] In order to keep track of this, samples were fitted with a thermocouple during measurements.

4.1.4. Signal Processing

In the set-up developed throughout this master thesis, signal processing to obtain inputs and send outputs from different sources or to different receivers has been an important concern. Data acquisition and output signalling was performed using National Instruments X- and C-series hardware. The X-series card (NI USB-6343) is used for general multifunction data acquisition and pulse sending, such as reading analog signals from the test bench and extensometers and camera triggering for DIC. C-series cards are used for strain gage measurements (NI 9237), camera triggering through a DSUB connection (NI 9401), thermocouple input module (NI 9211) and analog signal reading with BNC connectors (NI 9215). They are combined in a USB2 chassis with hardware timing for analog and digital I/O, and the possibility for counter tasks (cDAQ-9174). Task management, hardware configuration and system testing are performed using National Instruments MAX (Measurement & Automation Explorer). Signal processing on the computer is done through labview, National Instruments' graphical programming software.

4.1.5. Microscopy

The three most important branches of microscopy are optical, electron and scanning probe microscopy, however, only optical microscopes have been used for damage assessment for this thesis. Two types

have been used, a Carl Zeiss Jenavert metallurgical microscope with possible magnifications up to 100x and a Keyence VHX-2000 digital microscope, with possible magnifications up to 2500x, possibilities for image stitching and depth-up 3D imaging.

4.2. Assembly and Software

For this test series we want to be able to not only gather data, but also be sufficiently confident in terms of synchronisation of data. With data coming from different sources (DIC, thermocouple, load cell, ...), it is important to consider the measurement architecture and the software behind it.

4.2.1. Measurement System Architecture

The main requirements for this fatigue measurement system is that it should be able to capture effects such as stiffness degradation sufficiently while limiting the effort required in post-processing (The processing and analysing of DIC images is a tedious task). At the same time it should be capable of handling temperature, strain gage, force,... measurements, with a confidence on its reference frame in time. The system should also stand alone, being able to run a fatigue test on the push of a button.

Two possible system lay-outs have been designed and tested, to be used based on in-house availability of measurement equipment, data acquisition hardware and software dongles. While the backbone of both systems is the same labview program, they are differentiated in the way cameras are controlled and analog data is retrieved. The first system triggers cameras through an X-series card using camera manufacturers' camera drivers, the second works solely through National Instruments' drivers and triggers using a C-series card. Both architectures are shortly presented further below after a short elaboration on the labview backbone used for both systems.

4.2.1.1. Labview Backbone

While two different systems have been developed, to a large extent, they both follow similar principles. The backbone used for this system is based somewhat on a system developed by an intern in 2016, but it has been drastically altered to fit the purposes of these types of tests.

The software has 2 modes, namely '**quasi-static testing**' mode, which measures analog signals continuously and triggers cameras (if present) as such as well. The second and most important mode, '**fatigue testing**', works through the use of increasing time intervals during which the system records nothing. After every interval the system will measure and record signals and trigger cameras. The extent of these time intervals can be altered in the system inputs. The reasoning behind this is that using DIC results in significant data sizes and a large post-processing effort. Continuous measuring at high rates is thereby unfeasible. From literature, it could be expected that the most significant changes in stiffness occur in the beginning of fatigue life and flatten out hereafter towards the end. This justifies the increasing time intervals between measurements.

The front panel of the program is shown in figure 4.2.

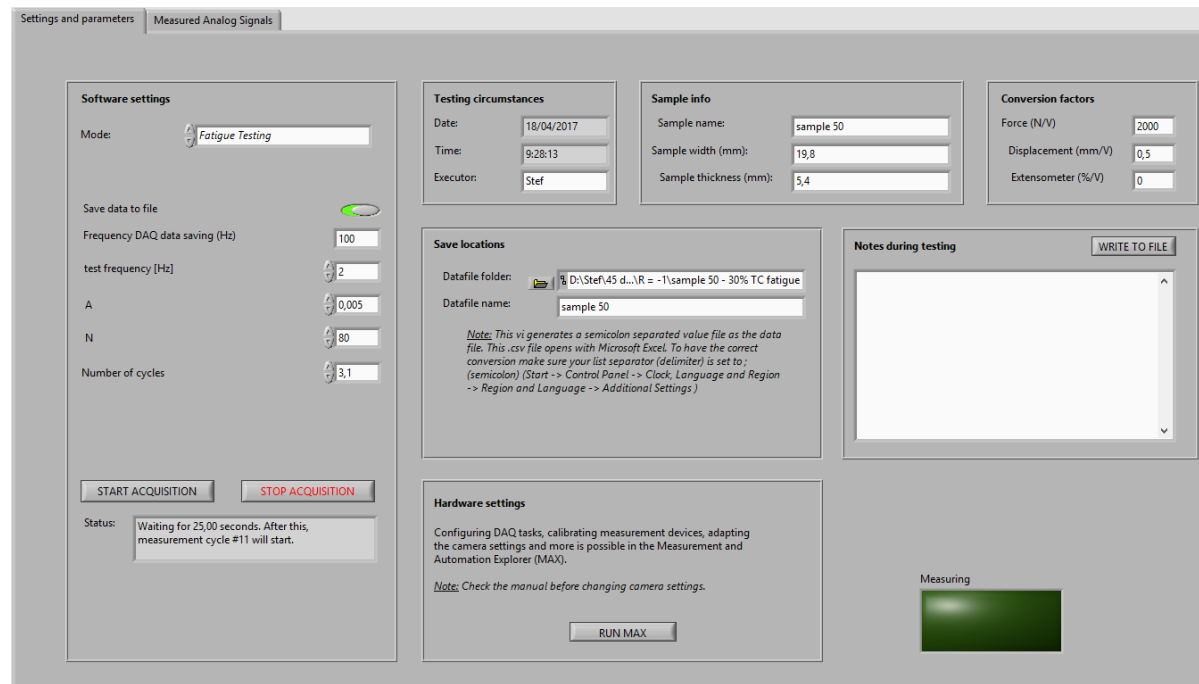


Figure 4.2: labview program front panel

The front panel has different features, all of which are saved to its output file as well.

- **Mode:** The current mode of the program. Options are 'Initialization', 'Quasi-static Testing' and 'Fatigue Testing'
- **Frequency DAQ data saving:** Indicates frequency at which analog signals (force, displacement, strain gage, extensometer, thermocouple) are retrieved and stored.
- **Test frequency, A, N, Number of Cycles:** These inputs are used to determine the times during which measurements take place (in fatigue mode). In the example of this figure, the system will take pictures at a fixed high frame rate and retrieve data for 3.1 cycles on a test at 2 Hz (so 1.55 second). The time intervals are calculated as a function of A and N. In the first stages of the project, this function was exponential. Afterwards some trial and error lead to an improved 4th order polynomial, resulting in a good balance between sufficient knowledge throughout a fatigue life and manageable data size.
- **Status:** A status description showing progress of the measurements
- **Testing Circumstances:** Saves data and time (automatically) and executor of the tests in the output file.
- **Save Location:** Folder and name for data saving (and picture saving in case of the labview-triggered system).
- **Sample info:** Name and cross-sectional measurements of each sample to be tested.
- **Conversion factors:** Analog signals are transmitted as voltages. To obtain optimal resolution, conversion factors can be changed to use the available voltage spectrum effectively.

As mentioned, this system will store data at a fixed rate, uninterrupted in quasi-static mode, or with intervals in fatigue mode. The analog data with timestamps is stored as a .tdms file which can then be used for post-processing. During measurements, a second panel of the program is available. This panel shows a live output of analog data, see an example in figure 4.3.

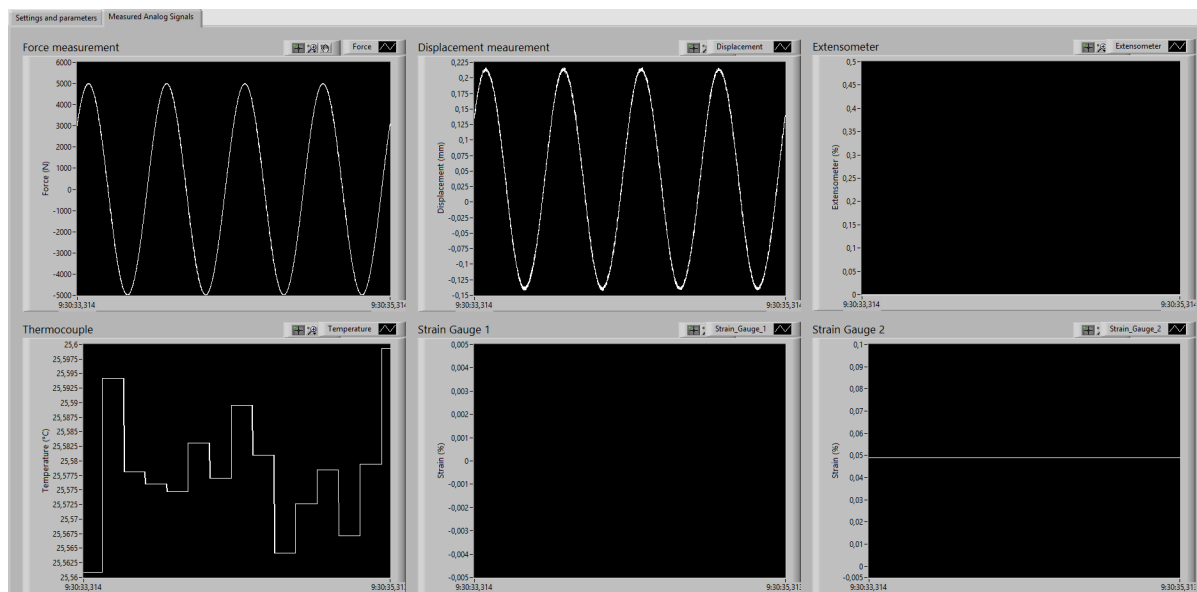


Figure 4.3: labview program live outputs

4.2.1.2. Vic-Snap Triggered System

The first and most important system is one which is triggered using *Vic-Snap*, by *correlated solutions*. The architecture is shown below in figure 4.4. For fatigue measurements, this system is designed to measure a certain amount of cycles, with increasing time intervals in between, based on the backbone mentioned above.

Triggering cameras using Vic-Snap with the camera manufacturers' drivers allows for the highest possible frame rate-resolution combination. This high frame rate is crucial for fatigue experiments. In this system a fast burst (50-75 fps) of DIC images is used, alternated by increasing time intervals, to characterize displacement fields of the specimen throughout cyclic loading with a sufficient amount of points. When testing at 2-4 Hz, frame rates of 50-75 fps are necessary to capture the full scope of the loading pattern with sufficient accuracy.

Analog signals (force and displacement) are retrieved twice. The first retrieval of the analog data occurs through the X-series card. This is stored through the vic-snap software, and occurs simultaneously with camera triggering (more on this in 4.2.3). This allows for comparison of DIC images with force and displacement signals. The second retrieval occurs through the C-series card, and is stored by the abovementioned labview backbone program. This data is used to process strain gage and thermocouple data, for a live view of data and for redundancy.

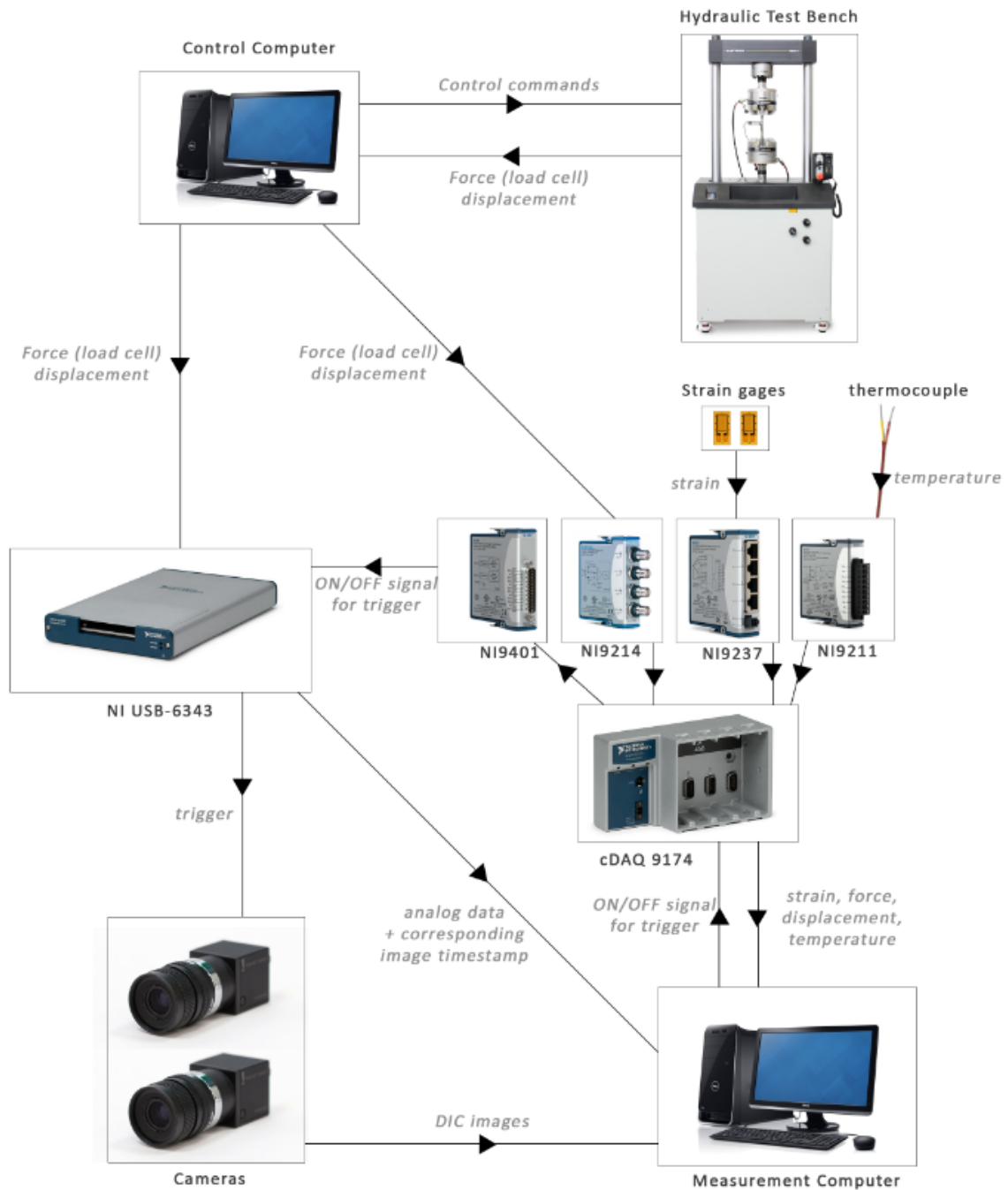


Figure 4.4: Vic-snap triggered system

4.2.1.3. Labview Triggered System

The second system was used when not all equipment in the above system was available and can be considered to be a simpler system with certain drawbacks, but good enough for certain tests such as quasi-static tests, for which it was mainly used. Data acquisition, image processing and camera triggering is all done through C-series cards with NI Labview, using National Instruments camera drivers. The main drawback is a lower frame rate-resolution combination, which, for quasi-static tests, is irrelevant for DIC performance.

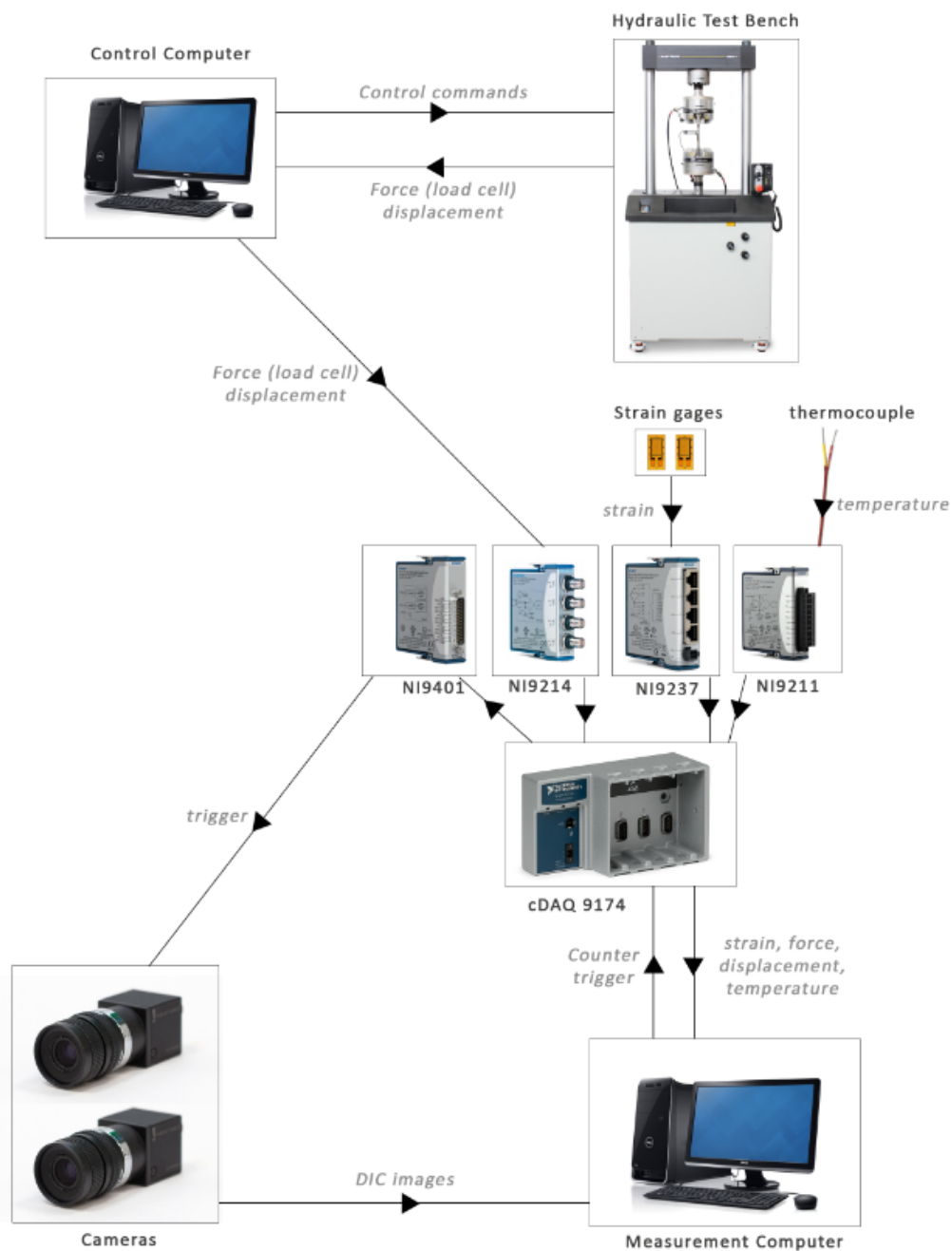


Figure 4.5: Labview triggered system

In an attempt to use this system for **fatigue measurements** in a similar sense as explained before, the low frame rates of the cameras are the main issue. To counter this, basically two options are at hand. The first is to try and trigger the cameras exactly at critical moments throughout a cycle (maximum/minimum stress). However, this proved to be very challenging and even if it could work, it would be a sacrifice compared to the other system.

Another attempt to cope with low frame rates was somewhat more successful, however the method proved to be somewhat fragile. In this system, the basic idea is to trigger cameras such that triggering is out of phase with the test frequency. After a certain amount of cycles, this would then cover the entire loading spectrum. This is based on the assumption that within this set of cycles, nothing changes and

every cycle is exactly the same. While this assumption can be considered valid once a certain amount of cycles have passed, it raises questions about building a correct image in the first cycles. The technique was however implemented and tested for a rigid body displacement (sine of 1 mm amplitude) at 1 Hz, the results can be seen in figure 4.6. This test was successful, however, due to large availability of the testing equipment (cameras), it turned out not to be necessary in the end and therefore further testing of this system was not done.

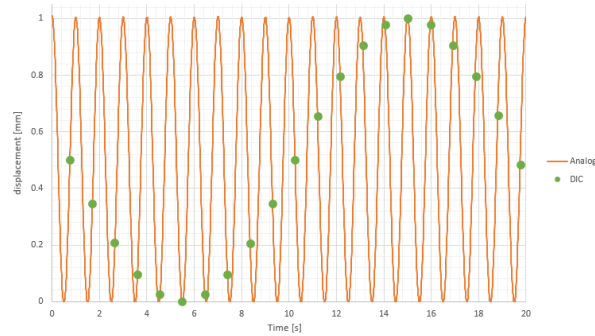


Figure 4.6: Measuring displacement using DIC and comparing this to an analog displacement signal for rigid body motion.

4.2.2. Camera set-up

As mentioned before in this report, the use of DIC has been an important asset for this thesis. It allows for entire displacement field quantifications for quasi-static and fatigue tests, which results in a much larger pool of information compared to conventional strain measuring methods (extensometer, strain gage,..). In order to use DIC to its full advantage, it is important to consider how exactly cameras can be used. Due to equipment limitations and other projects running, set-ups are limited to two cameras. The working principle and variables used for DIC are described in appendix A.

4.2.2.1. 3D DIC

To obtain a 3D displacement field using DIC, the eyesight principle is imitated, where 2 cameras are used to obtain a 3D image, capable of detecting out of plane motion. [72] This is done by placing the cameras at an angle compared to each other. Due to practical issues (view obstruction by clamps), this must be done in the horizontal field in line with the sample's gage length. To measure in-plane properties such as stiffness degradations in both directions, they are placed such as to capture an image of one of the two outer laminate layers.



Figure 4.7: Camera set-up for 3D DIC

4.2.2.2. Mirror Image

During the first tests under cyclic compression, it became clear that **free edge delaminations** were an important damage phenomenon occurring in most of the tests. It should be emphasised that this is an artefact of coupon testing which is less common in actual structures. In places where free edges are found in actual structures, they are often in the proximity of fasteners which suppresses the damaging effect. On the other hand, for material testing, it is difficult to avoid this effect without introducing more complex structures (for example tubes) which drive cost and effort up very high and have other potential issues as well. Therefore, the results from these tests should be analysed as such. In order to investigate this effect, the idea originated to somehow capture the side of the specimen as well. Doing so could enable damage tracking throughout fatigue life, synchronised with load and displacement measurements. In an initial attempt of accomplishing this, a mirror was used to expand a 3D DIC system to follow the side of the specimen as well.

The system has two major drawbacks. The first is that the actual focus distances differ too much to have both images acceptably focussed, see figure 4.8. Resolving this with cameras far away is not only unpractical, but also raises questions with regards to calibration in terms of lens correction and camera placements. The second drawback is that a mirror can only be placed within a certain distance of the specimen. This requires a large field of view, effectively resulting in a lower resolution of the front edge image for DIC, see figure 4.8.

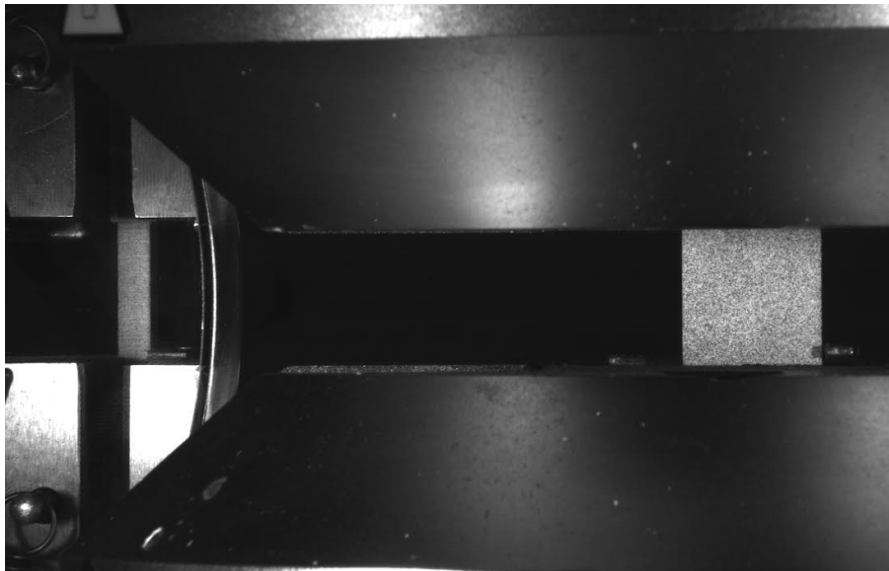


Figure 4.8: Camera concept with a mirror results in one of both images being out of focus and a lower resolution for the front DIC image.

4.2.2.3. 2D DIC on Front and Side of a Specimen

In a second attempt at capturing damage phenomena from the side of specimens, a system with two cameras each capturing one side of the specimen was tested. The side of the specimens can also be covered with a speckle pattern to allow for image correlation on the side of a specimen. This pattern is applied together with the front DIC pattern and is similar in terms of resolution. Through camera triggering in the same manner as for 3D DIC (in terms of software or hardware set-up nothing changes but the camera placement), images are still captured simultaneously and information of both can be combined. The lay-out is shown below in figure 4.9.

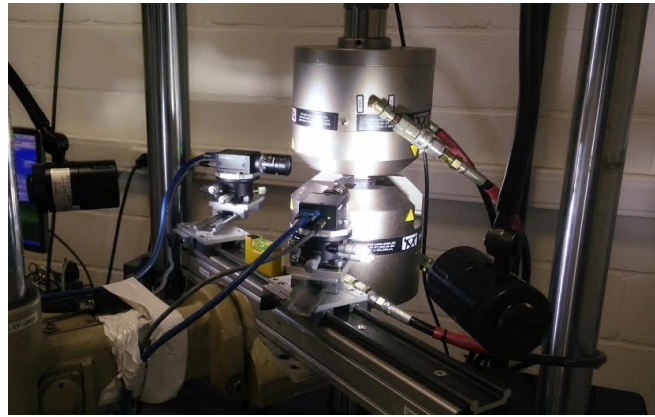


Figure 4.9: Camera concept capturing two 2D images of a specimen rather than a single frontal 3D image.

Not using 3D **DIC** means omitting any out-of-plane displacement data. However, this can be justified since previous tests confirmed minimal out-of-plane displacements for all load cases. If out-of-plane displacements would have been present despite this, they can be expected to be picked up by the camera aimed at the side of the specimen.

This system proved to be of value in linking damage events on one side of the specimen to stiffness reductions observed from **DIC** on the front camera. Delaminations can be picked up through the surrounding strain field even before being visible to the naked eye before processing. Results are discussed more in depth in chapter 6

4.2.3. Measurement System Evaluation

The first measurement system architecture ("vic-snap based system"), presented earlier on in this chapter, is the one used for fatigue experiments throughout this thesis. Before applying this system to actual fatigue tests, control tests were performed. Quasi-static tests on dummy material show good correlations and **DIC** data and strain gage data correspond well.

In order to test the performance of the system in cyclic loading, the test bench was used to create a **rigid body motion** (sine wave) of a sample. Analog displacement sensor data was compared to displacement data from **DIC** measurements. This was done for different motion frequencies and camera frame rates. As can be seen in figures 4.10, 4.11 and 4.12, there is a clear delay between the analog signal and **DIC** images, presumably obtained at the exact same moment.

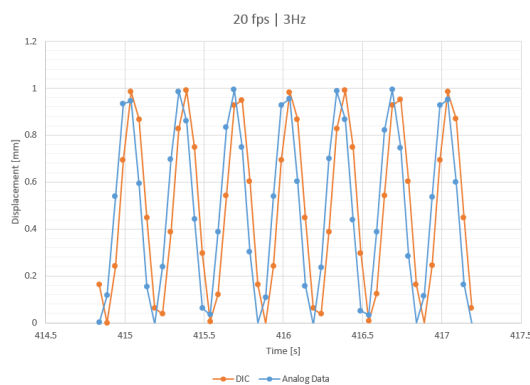


Figure 4.10: Rigid body motion of 1 mm at 3 Hz shot at 20 fps shows a delay between signals.

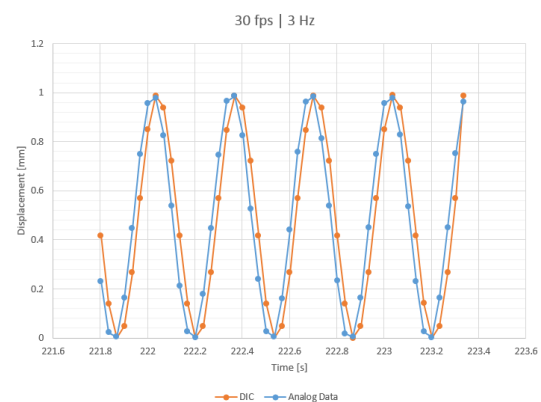


Figure 4.11: Rigid body motion of 1 mm at 3 Hz shot at 30 fps shows a delay between signals.

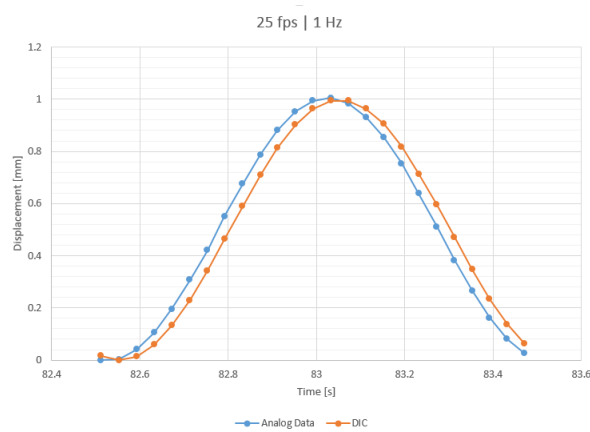


Figure 4.12: Rigid body motion of 1 mm at 1 Hz shot at 25 fps shows a delay between signals.

This delay is however constant. A constant shift in time seems to be enough to correct for the observed delays. The graphs with a time correction added to the DIC dataset shows much better correlation between both signals.

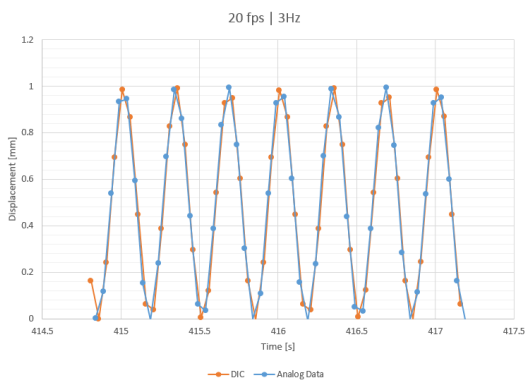


Figure 4.13: Rigid body motion of 1 mm at 3 Hz shot at 20 fps with constant delay correction.

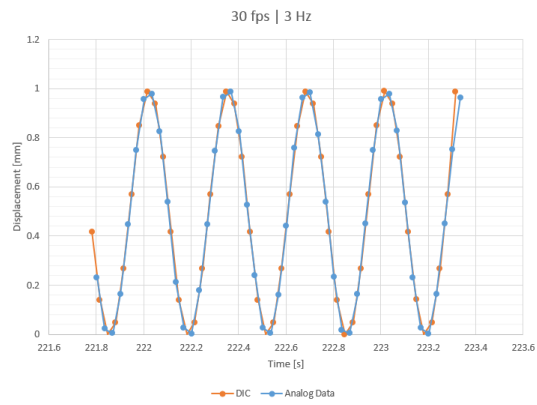


Figure 4.14: Rigid body motion of 1 mm at 3 Hz shot at 30 fps with constant delay correction.

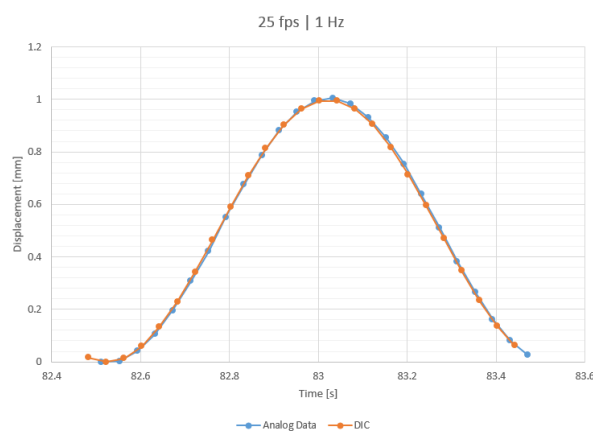


Figure 4.15: Rigid body motion of 1 mm at 1 Hz shot at 25 fps with constant delay correction.

By determining this delay, it is possible to correlate analog and DIC data using a shift in time together with interpolation, which is required to match force data with DIC data at exactly the same time point.

Since the observed delays are in the order of milliseconds, it was expected that the shutter speed of the camera (which is in the order of 5-20 ms) would have a certain influence on this. To confirm this belief, additional rigid body motion tests were performed with variable shutter speeds. The delays observed for every shutter speed tested are shown in table 4.1. The result can be approximated as:

$$t_{delay} = 12 + \frac{t_{shutter}}{2} [ms] \quad (4.1)$$

Table 4.1: Shutter speed has an influence on the observed delays between analog and DIC data.

Shutter Speed [ms]	Delay [ms]
5	15
10	17
20	22
30	27

However, it cannot be confirmed that shutter speed is the only influence on this delay. Therefore, it was decided to determine the delay for every measurement point throughout the fatigue life, confirm that this varies little throughout a sample's fatigue life and correct for it as such, the process is explained more in depth in the next subsection.

4.2.4. Post-processing software

With respect to the problems with delays mentioned earlier, and to ensure efficient post-processing of data of the entire test program, matlab software was created to post-process, save and visualize data from fatigue tests.

After reading and analysing both data files (analog and DIC data), the program corrects for delays as follows:

- Displacement of a point on a sample close to the moving clamp of the test bench is compared to analog displacement signal of the clamp, for every set of measurement points between time intervals.
- through a simulated annealing optimization algorithm, the program determines the set of parameters (delay, offset and scale factor) applied to the analog signal which minimize the difference between both curves through least squares.
- Least squares comparison of the signals is performed using cubic interpolation of the analog displacement signal. Extrapolated points are not considered here.
- From the set (delay, offset, scale factor) which minimizes the difference, the delay is stored in a vector.
- If the variation of delay values is high (the largest delay value is 50% larger than the smallest delay value), an error is reported, since this could indicate that the optimization algorithm optimized to a local minimum rather than the global minimum. If not, the delay is applied to the force signal using cubic interpolation once more (again removing the extrapolated value(s)). The result is a force (stress) signal that can be compared to DIC results such as strains.

Hereafter, strain and stress vectors can be changed into local coordinates if required, and are then used for the creation of hysteresis (stress-strain) plots, permanent strain plots and stiffness calculations. After this, the relevant processed data is saved on the hard drive to be recovered later on without requiring the (lengthy) optimization again.

5

Specimen Design

Careful design and preparation of specimens to be used for fatigue testing is essential to obtain reliable and reproducible results. In this section, the available material is presented, followed by the specimen geometry design. Hereafter load transfer is discussed, after which the final design is presented.

5.1. Material

The material under investigation for this master thesis is plain woven carbon-epoxy. Carbon-epoxy is one of the most widely investigated composite materials, thanks to its promising properties. For this thesis, plates were available in 8 or 24 layers, with all layers oriented in the same direction. Average layer thickness is 0.25 for laminates with 8 layers, and 0.225 for laminates 24 layers (**CV (coefficient of variation)** of 0.75%). This average layer thickness is determined from measurements of plate thickness divided by the total number of layers. Determination of individual layer thicknesses is difficult since layer boundaries are difficult to define and, in particular for woven composites, will not be a flat surface.

The plates are produced by Mitsubishi Rayon Co., Ltd., one of the industrial partners involved in the **M3** project. They are made using Pyrofil fibers denoted by TR30S 3L, with epoxy resin #360, at a resin content of 40 wt%. The laminates are cured in the autoclave for 60 minutes at 130 °C with a gauge pressure of 0.6 MPa. A microscopical visualization of a perpendicular cut of a 24-layer plate (along the fibers) is presented in figure 5.1. The material properties as reported by the manufacturer are shown below in figure 5.2. The test methods used to determine the properties are included as well. Material elasticity parameters for this material have been determined in all directions using a unit cell approach, and validated experimentally in [15]. These were used as input for the analytical and finite element sizing approaches in this chapter.

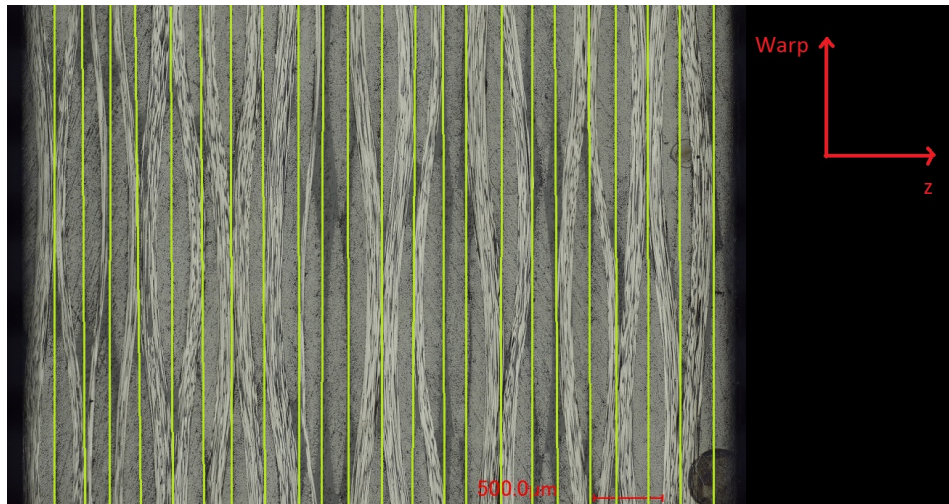


Figure 5.1: cross-sectional microscopic view of the material (lay-up: $[\#(0/90)]_{24}$ used in this project. The weft (fill) direction is perpendicular to the picture (coming out of the page). Warp and stacking (z-) direction are indicated in the picture, as well as an approximation of the layer boundaries.

Mechanical Properties		Unit	Value	Method
Tensile Properties				
[0°/90°]	Strength	MPa	693	ASTM D 3039 Vf 50 vol%
Warp direction	Modulus	GPa	60	
	Strain	%	1.1	
[90°/0°]	Strength	MPa	598	ASTM D 3039 Vf 49vol%
Fill direction	Modulus	GPa	59	
	Strain	%	1.0	
Compressive Properties				
[0°/90°]	Strength	MPa	538	ASTM D 3410 Vf 49 vol%
Warp direction	Modulus	GPa	54	
	Strain	%	1.1	
[90°/0°]	Strength	MPa	496	ASTM D 3410 Vf 49 vol%
Fill direction	Modulus	GPa	52	
	Strain	%	1.1	
Flexural Properties				
[0°/90°]	Strength	MPa	828	ASTM D 790 L/d=40 Without cushion Vf 49 vol%
Warp direction	Modulus	GPa	54	
	Strain	%	1.7	
	Strength	MPa	857	ASTM D 790 L/d=40 With cushion Vf 49 vol%
	Modulus	GPa	55	
	Strain	%	1.7	
[90°/0°]	Strength	MPa	801	ASTM D 790 L/d=40 Without cushion Vf 53 vol%
Fill direction	Modulus	GPa	55	
	Strain	%	1.6	
	Strength	MPa	750	ASTM D 790 L/d=40 With cushion Vf 52 vol%
	Modulus	GPa	53	
	Strain	%	1.5	
Shear Properties				
	In-Plane Shear Strength	MPa	92	ASTM D 3518 Modulus range : 2000-6000μ Vf 51 vol%
	Shear Modulus	GPa	3.4	
	Interlaminar Shear Strength	MPa	60	ASTM D 2344 L/D=4 Vf 50 vol%

Note) Test environment 23±2°C, 50±5%RH
mechanical properties are calculated at actual of fiber volume.

Figure 5.2: Material Data sheet from manufacturer

5.2. Specimen Geometry

To avoid undesirable failure modes, specimens must be designed properly. In particular for compression testing, **buckling** is to be avoided at all cost, since out-of-plane deformation introduces non-uniform stress fields and detrimental peel forces at fibre bundle edges. [21] The shape and dimensions of a

specimen are critical to ensure that the part of the specimen under consideration will fail first, under a known load which is of interest.

5.2.1. Buckling Prevention

To effectively prevent buckling, two options can be used.

The first option is to design specimens such that **unstable modes do not occur** (i.e. final failure is expected well before buckling). One example which is based on this is the ASTM 3410 standard [63]. For simple geometries, this can be determined analytically, for more complex shapes some finite element modeling and testing may be required. Typically, this results in short gauge lengths, with certain implications:

- A short specimens clamped at both ends, results in a restriction of a certain amount of Poisson contraction (or expansion) due to the clamping effects at the ends. [62].
- Strain gage, thermocouple and/or extensometer measurements become unpractical since they have to be performed on a small space.

The second option is to create specimens which could buckle before final failure, but prevent the buckling through the use of **anti-buckling guides**. [7] The concept is straightforward: A large stiff guide is placed in which the specimen only just fits. This will induce sideways forces which don't allow the specimen to buckle in any direction. Often a window will be introduced as well which can then be used for DIC or strain gage attachment for example. While Curtis et al. state that anti-buckling guides do not induce uncharacteristic failures due to stress concentrations typical for the guides, several studies report lower static compressive strengths when anti-buckling guides are used. A series of comparative measurements on woven carbon-epoxy material by Quaresimin et al. [8] showed lower compressive strengths when anti-buckling guides were used, leading to the choice for short, unsupported gauge lengths, see figure 5.3.

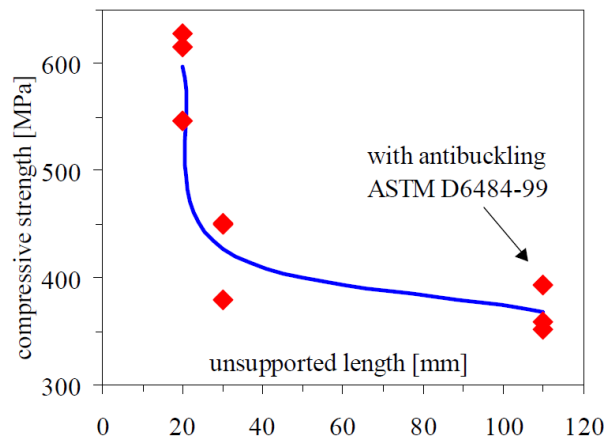


Figure 5.3: Testing the same material with anti-buckling guides results in lower strengths. [8]

Other, more exotic techniques exist in which for example a (sandwich) structure is created and tested in bending. This is however only possible with very thin composite layers and will introduce difficulties to derive material properties from since highly non-uniform stress fields are often observed. [7, 28] It is therefore omitted from this study.

The use of anti-buckling guides show lower static strengths. On top of this, the effect of the contact with the side in fatigue loading can be considered questionable. This resulted in the decision to **design specimens so that unstable failure modes do not occur**.

5.2.2. Specimen Shape

A lot of research has been performed on specimen geometry and its influence on test results. [101–103] Particularly avoiding stress concentrations at unwanted locations and correctly predicting stress concentrations where failure is expected is critical. For uniaxial tensile tests, both static and cyclic, in general two types of specimens dominate literature. Either the specimen is rectangular, or some type of dogbone shape is used. [47, 101, 102, 104] However, for short specimens to be tested under compression, where space is limited, the choice was made to use straight specimens, as is done in ASTM 3410 standard for compression testing. [63]

5.2.3. Dimensioning

Sizing of the specimens has been done by looking into the clamping method and comparing buckling loads with final compression failure using an analytical and finite element approach. It is important to account for failure endured during fatigue testing, imperfections in the specimens and idealized boundary conditions used in the analyses. The method described in test standard D3410 for static compression testing of composites compensates for this by assuming pinned end conditions. Under the approach described in 5.2.3.2, this results in a buckling load 2-4 times lower than for clamped end conditions. In this document, a safety factor of 3 was included in the sizing, see equation 5.1.

$$\sigma_{buckling} = 3\sigma_{c,ult} \quad (5.1)$$

Where $\sigma_{buckling}$ is the load at which the first buckling mode occurs and $\sigma_{c,ult}$ is the load at which pure compressive failure can be expected. Afterwards the specimens were produced and this performance was reviewed in real life, which is discussed later in this chapter.

5.2.3.1. End Clamping

Specimens are fixed into the test bench using hydraulically controlled wedge clamps, see figure 5.4. The clamping length can be up to 55mm. All tests were performed with a clamping pressure of 100 bar.



Figure 5.4: Hydraulic wedge clamps on the Instron test bench

5.2.3.2. Analytical Sizing Approach

The analytical derivation of the buckling load can be derived from the methods by Kassapoglou, based on the approach by Whitney [105]. This derivation determines the buckling load for a laminated plate for which the Kirchoff assumption remains true and plane stress can be assumed. It is also assumed

that on laminate and ply scales, the combination of fibres and matrix can be treated as a homogeneous material, including a perfect bond between fibres and matrix and between separate plies. Note that the plate is also assumed to be balanced and symmetric and bending twisting coupling can be reduced. This results in the first Von Karman equation, shown below with distributed loads ignored [105]:

$$D_{11} \frac{\partial^4 w}{\partial x^4} + 2(D_{12} + 2D_{66}) \frac{\partial^4 w}{\partial x^2 \partial y^2} + D_{22} \frac{\partial^4 w}{\partial y^4} = N_x \frac{\partial^2 w}{\partial x^2} + N_y \frac{\partial^2 w}{\partial y^2} + 2N_{xy} \frac{\partial^2 w}{\partial x \partial y} \quad (5.2)$$

Assuming that N_y and N_{xy} are 0, a solution for N_x can be determined which represents the buckling load, depending on the boundary conditions applied. For this case, it can be assumed that the edges are free ($\frac{\partial^2 w}{\partial y^2} = 0$ at the sides of the specimen). For the boundary conditions at the other edge, the case is somewhat tricky. One could question whether or not the constraints where the clamping occurs can be considered as clamped ($w = 0$ and $\frac{\partial w}{\partial x} = 0$ at the ends), simply supported ($w = 0$ and $\frac{\partial^2 w}{\partial x^2} = 0$ at the ends) or something else. Since deviations due to (amongst others) clamped boundary conditions were already accounted for in equation 5.1, it was decided to perform the analysis using **clamped boundary conditions**.

Above, it was mentioned that the **Kirchoff assumption** (during bending, plane subsections remain plane and perpendicular to the neutral axis) was applied to determine governing equations. However, it is important to realise that, while this assumption can be considered valid when two dimensions are considerably larger than the third, this will generally not always be the case for these purposes. With typically short gauge lengths and potentially thick specimens, this assumption is no longer valid. [28] Kassapoglou [105] describes a correction for the buckling load, based on the Timoshenko theory:

$$N_{xcrit} = \frac{N_{Ecrit}}{1 + \frac{kN_{Ecrit}}{tG_{xz}}} \quad (5.3)$$

In which k for a composite plate is equal to 5/6.

5.2.3.3. Finite Element Sizing Approach

Sizing has also been performed using a finite element buckling load calculation in abaqus using a 3D shell structure. From this approach, the first sets of unstable eigenmodes are determined from an eigenmode solver. Similarly to the analytical analysis, clamped boundary conditions are assumed on both sides of the specimen. Practically this is done by allowing no movement in all nodes of one of the clamped edges (encastred boundary condition), and only movement along the loading direction for the other. This approach results in the buckling stresses for each mode. Using this, the effects of width and free length on the buckling load were assessed for each lay-up.

The first step in this analysis is **element selection**. To do so, a buckling analysis was performed for the same mesh seeds, on the same computer with no other programs running. From this, the buckling load of the first one, two or three eigenmodes is compared with a situation of a very fine mesh under S8R elements to check for convergence. Apart from this, the computation time is also considered. The element selection is carried out for specimens with a width of 20 mm, a clamped length of 50 mm and a free length of 15 mm for the 8 layers case, and a width of 25 mm, clamped length of 50 mm and free length of 50 mm in the 24 layers case. The elements under consideration are:

- **S3:** A 3-node triangular general-purpose shell, finite membrane strains.
- **S4:** A 4-node doubly curved general purpose shell with finite membrane strains
- **S4R:** A 4-node doubly curved thin or thick shell, reduced integration, hourglass control, finite membrane strains.
- **S8R:** An 8-node doubly curved thick shell, reduced integration.
- **S4R5:** A 4-node doubly curved thin shell, reduced integration, hourglass control, using five degrees of freedom per node.

Note that S4R5 assumes small membrane strains and is in principle only applied for very thin shell structures, which is why it is not applicable for thick shells, however it is included here as a reference. The results are shown in Appendix B. From these results, It shows that using **S8R** elements with the

number of elements used (2640 for 8 layers, 1520 for 24 layers) is close enough to the converged result within reasonable computation time.

For this analysis, the only buckling mode of interest is the first buckling mode, the only one occurring in practice. Which, for every reasonable combination of free length and width, is the mode pictured below.

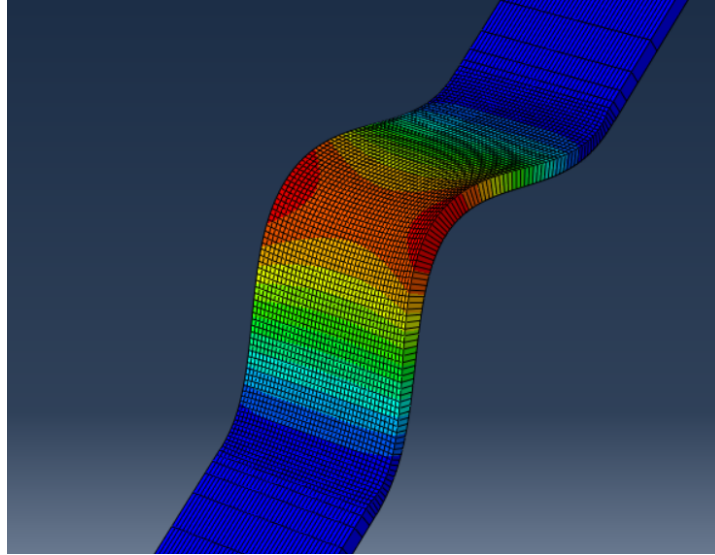


Figure 5.5: A qualitative representation of the first buckling mode occurring in all cases under consideration.

5.2.3.4. Results and Final Dimensions

Using the two approaches as mentioned above with the sizing criterion (equation 5.1), final specimen dimensioning was performed for laminates of both 8 and 24 layers.

Free Length The most important influence is the effect of the free length. To investigate this, buckling calculations are performed using a fixed width of 20 mm for each specimen, and the corresponding buckling loads are calculated for varying free lengths. The results are shown below in figures 5.6 and 5.7 for 8 layers and in figures 5.8 and 5.9 for 24 layers.

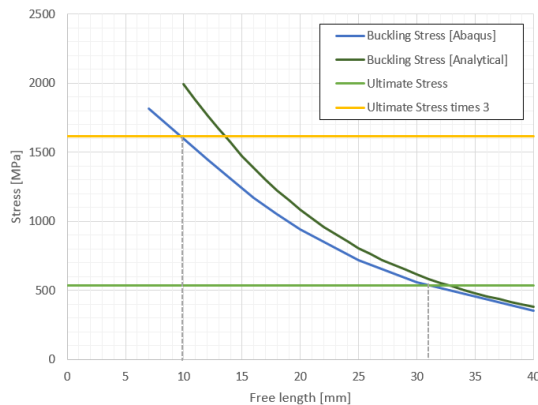


Figure 5.6: Buckling loads for $[(0/90)_8]$ laminate

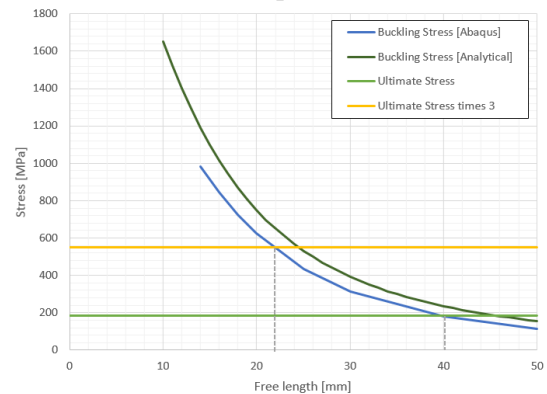


Figure 5.7: Buckling loads for $[(\pm 45)_8]$ laminate

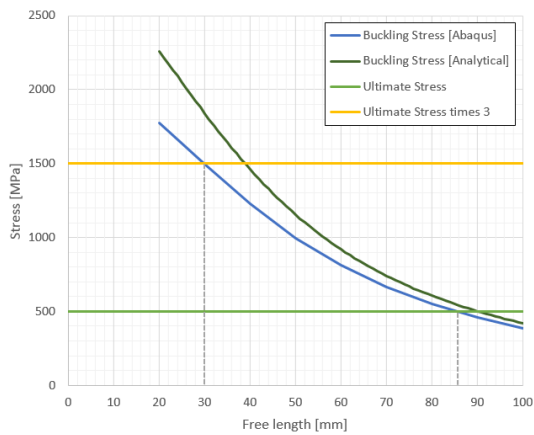


Figure 5.8: Buckling loads for $[(0/90)_{24}]$ laminate

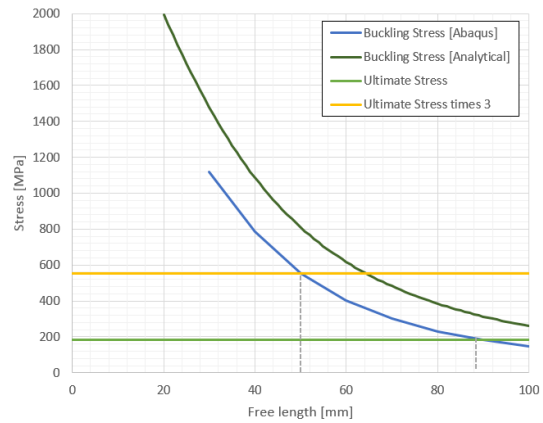


Figure 5.9: Buckling loads for $[(\pm 45)_{24}]$ laminate

In the case of 8 layers, the free length of the specimens would have to be approximately **11 mm** to fit the criterion for both $[(0/90)]$ and $[(\pm 45)]$ laminates. For 24 layers, this length becomes approximately **30 mm**. Because of this, the choice was made to use laminates of 24 layers for this research, since a free length of 11 mm raised questions towards the vanishing of clamping effects on for example Poisson’s ratio and also for practical considerations with regards to **DIC**.

Free length revision During initial tests of $[(0/90)]_{24}$ specimens with a free length of 30 mm , it was noticed from **DIC** measurements that clamping boundary conditions were somewhat idealized compared to the real life situation. **DIC** measurements show out-of-plane displacements of the specimen up until 0.2 mm of the specimens. Measurements using mechanical displacement measuring show that the **clamping head itself** moves somewhat out-of-plane. Although the out-of-plane displacement is considered still within reasonable limits, the decision was made to shorten the specimens from 30 mm to **25 mm** and carefully track out-of-plane movement during measurements. No significant out-of-plane displacement could be observed hereafter.

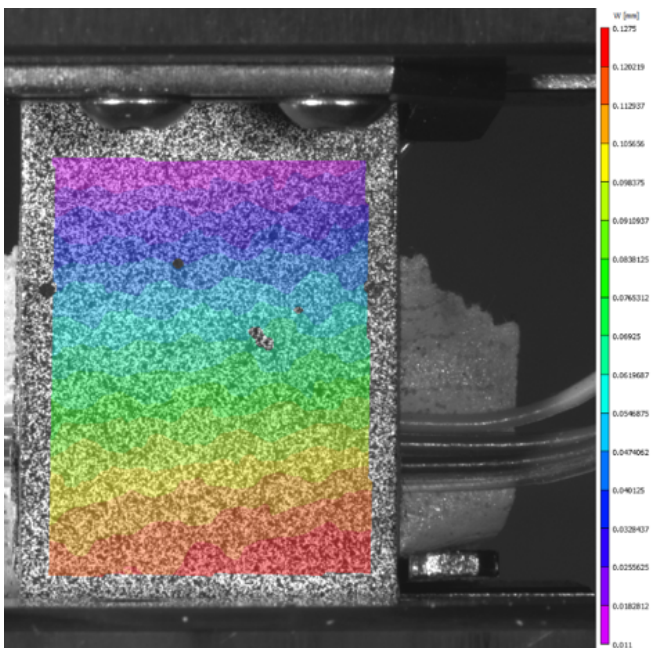


Figure 5.10: Out-of-plane displacement of a $[(0/90)_{24}]$ laminate measured using **DIC**.

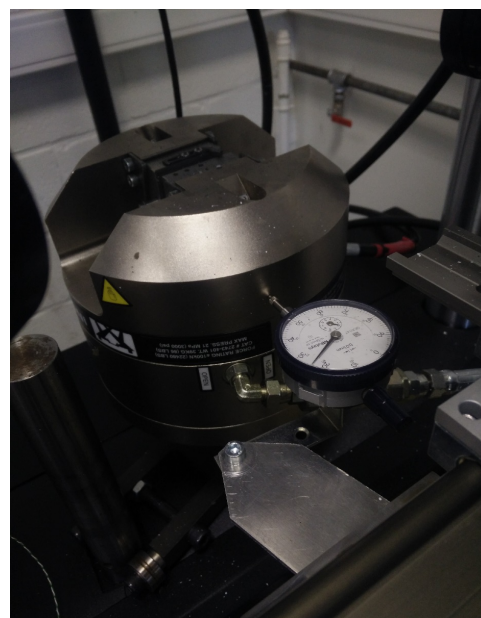


Figure 5.11: Measuring the displacement of the clamping head shows that clamping conditions are not ideal.

Width For the effect of specimen width, the finite element calculations for the $[\#(0/90)]_{24}$ laminate were performed using a free length of 30 mm and variable width. The effect is negligible (see figure 5.12) unless the first buckling mode changes, which only happens at unreasonably high widths (>100 mm). Therefore, a specimen width of **20 mm** was selected for this research to reduce excessive material use but still have significant rigidity and stability in the width direction during tests.

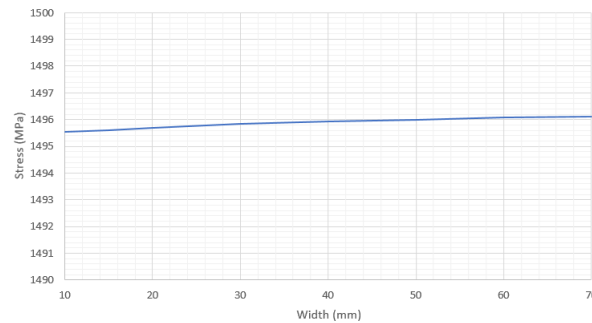


Figure 5.12: The effect of specimen width on the buckling load (mode 1) is negligible

5.3. Load Transfer

To transfer the load from the clamps to the laminate, two methods are possible. At least partially, the load is transferred through tabbing material. In this section, methods of load transfer are shortly presented followed by possibilities regarding end tabs. Two options were considered for the end tab design, which were evaluated in a test series later on, covered in the last subsection.

5.3.1. Two Methods for Load Transfer

When considering load application in compression testing of composites, two obvious choices are at hand: Compression can be applied through end loading or shear loading (clamps), see figure 5.13. A combination of both is also possible [106].

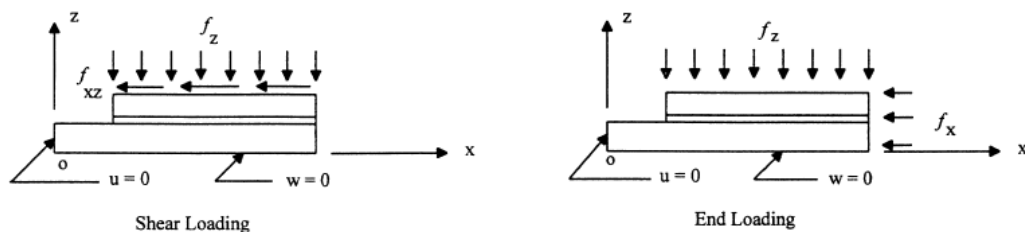


Figure 5.13: Shear loading and end loading as visualized in [16].

Xie et al. [16] performed analyses on the loading methods in compression testing of composite materials. They concluded that the shear loading method always yields higher stress concentrations at tab tips while the end loading method yields higher shear stress concentrations at the loading end of the specimen. They propose a combined method which reduce both stress concentrations. On top of this, for end loading of specimens, perfectly straight and square ends are required in the specimens to avoid brooming. [62] This is not the case when specimens are loaded in shear only. Schultheisz and Waas [28] also mention that it is the consensus that shear loading of specimens results in the best compression strength measurements, ASTM D3410 also suggests the use of shear loading. [63].

5.3.2. End Tabs

Considering end tabs, two important parameters should be considered: tab geometry and tabbing material.

Many different **tabbing materials** are reported by authors such as steel, glass-epoxy and aluminum [77]. Tapered tabs are often applied in tensile specimens to reduce stress concentrations. However, in compression, specimens will typically be very small and we need the largest possible surface area to analyse them. So while tapered tabs might relieve stress concentrations, they do induce a boundary condition closer to hinged rather than clamped and therefore will result in a smaller free length to perform measurements upon. Adams et al. follow this and also advise against the use of tapered tabs [17]. The use of tapered tabs was therefore omitted from the start.

Adams et al. [17] investigated the use of end tabs for both compressive and tensile specimens. For compression they used a combined loading method through the end and through shear. For compression tabbing materials, they concluded that the material requires sufficient strength to transmit the required load. However stiffness should not be too different from the material to be tested to avoid stress concentrations in the stress termination zone (too stiff) or in the ends (not stiff enough). The result of both stress concentrations are shown in figure 5.14.

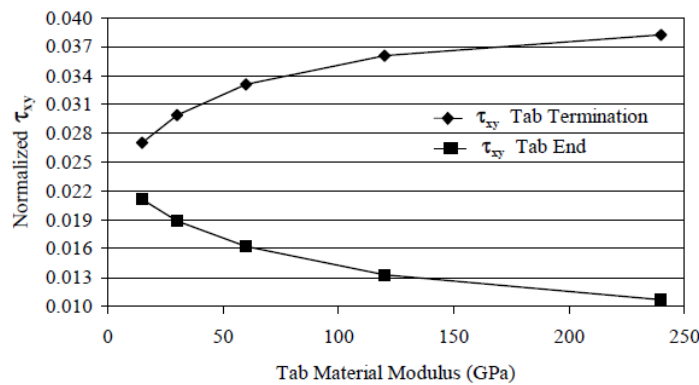


Figure 5.14: Stress concentrations in the critical regions in function of the tab material stiffness [17]

Regarding tab thickness, there is no large influence on tab termination stress concentrations. However, for end loading, a thicker tab reduces the stress on the end causing brooming, so here it could be stated that thicker tabs are a good choice. [17]

5.3.3. Load Transfer Test

Based on the literature study from the previous two subsections, it can be concluded that there is no consensus amongst researchers about one go-to method for compression testing of composites.

Even with tapered tabs excluded, still a large set of combinations of materials, adhesives, tab thicknesses and loading methods is possible. An in-depth investigation for the perfect specimen is far outside of the scope of this thesis. Therefore, 2 candidate designs have been selected and evaluated.

The first is a well-tested method using thin (1-1.5 mm) aluminum tab material, fit for shear load introduction only. The second design uses thicker (4 mm) steel tabs, this stiffer design allows for (partial) load introduction through end loading. While 3D abaqus simulations show higher stress concentrations for the steel tabs even when the larger portion of the load (75%) is applied through end loading, steel tabs can be expected to have a better fatigue life and provide a stiffer support.

Specimens of both designs have been created with $[\#(0/90)]_{24}$ material according to the procedure described in appendix C, and evaluated based on their performance.

5.3.3.1. Quasi-static performance

Quasi-static compression performance was evaluated by testing two samples of each design at a displacement rate of 0.5 mm/min. The results are shown in a stress-strain curve in figure 5.15. Aluminum samples show higher strength (501-514 MPa) compared to steel (389-410 MPa), with similar stiffness.

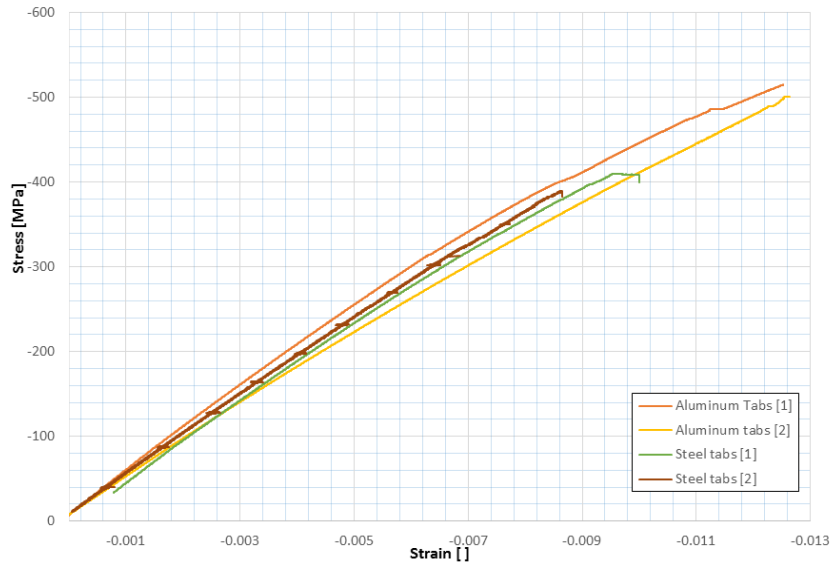


Figure 5.15: Aluminum samples outperform steel in static performance

Observing the fracture surfaces indicates fracture occurring in the middle of the aluminum samples (figure 5.16), while initiation at the steel samples seems to occur in the stress concentration regions (figure 5.17), which can explain the lower strength.



Figure 5.16: Aluminum sample 1. Broken in the middle under static loading.



Figure 5.17: Steel sample 1. Fracture initiates in the stress concentration region for static loading.

5.3.3.2. Fatigue performance

Fatigue performance was evaluated through cyclic tests at $R = 10$ at a test frequency of 3 Hz. For the steel samples, a minimum stress of -350 MPa was applied. For the first aluminum sample this was used as well, however, this test was interrupted after 800,000 cycles with almost no sign of damage, therefore the second test was performed at a minimum stress of -450 MPa, above what steel tab samples could reach statically. The results are shown below in table 5.1. Fracture surfaces are similar to static fracture, with failure initiating in the stress concentration regions for steel tab samples.

Table 5.1: Fatigue life of steel and aluminum samples

Sample	σ_{min} [MPa]	Cycles to failure
Steel 3	-350	4,500
Steel 4	-350	46,000
Aluminum 3	-350	Run-out at 780,000 cycles
Aluminum 4	-450	3,500



Figure 5.18: Aluminum sample 4. Broken in the middle under cyclic compressive loading.

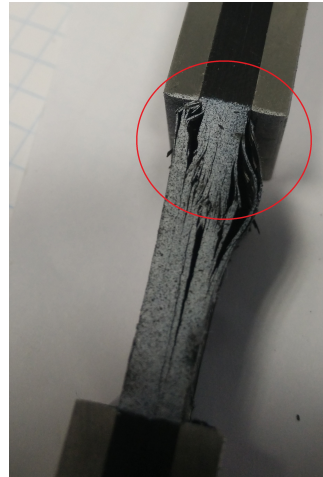


Figure 5.19: Steel sample 3. Fracture initiates in the stress concentration region for cyclic loading as well.

5.3.3.3. Conclusion

From both quasi-static and fatigue tests, it can be concluded that specimens with **aluminum tabs** outperform the design with steel tabs, where failure occurs sooner and initiates in the stress concentration zone.

5.3.4. Stress Field Analysis

One of the disadvantages of using short specimens is that region of interest of a specimen (over the free length) is always close to the clamping region and therefore under the influence of unavoidable stress concentrations. It is therefore important to investigate the homogeneity of the stress field, since significant variations may cause premature failure. A 3D linear finite element model was created using abaqus to assess this homogeneity. The model is built up as follows:

- The model has three planes of **symmetry**, indicated in blue, orange and green in figure 5.20. While the blue and orange symmetry planes could be disputed for #(± 45) laminates when stiffnesses in warp and weft directions are different, in this case, they are assumed to be equal for efficient modeling.

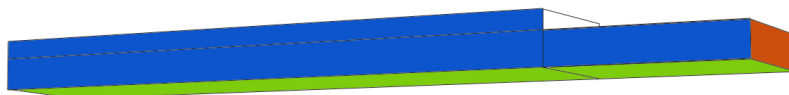


Figure 5.20: Three planes of symmetry used in the finite element model

- The model is built up of three **materials**: Woven carbon-epoxy (5.4 mm thick), aluminum for the tabs (1.5 mm thick) and an epoxy layer to model the thin (0.05 mm) glue layer in between.
- All materials are modeled using **C3D8R** elements: An 8-node brick with reduced integration and hourglass control

- In the first step, the **clamping** pressure of 10 MPa is applied onto the clamping surface. Since the clamp will also restrict movement of the outer surface of the tab material, this movement is restricted.
- In the following step, the **compressive load** is applied through shear displacement on the outer surface of the aluminum tabs. The load is chosen so that it is well below the ultimate compressive load of the material.

The model was used to analyse the stress fields for both lay-ups loaded under compression. For the $[\#(0/90)]_{24}$ lay-up, the effect of the stress concentration decays towards the middle where the stress field is uniform, see figure 5.21. In the proximity of the stress concentration, the outer layers are under a higher stress and the middle layers under a lower stress, as expected. For the $[\#(\pm 45)]_{24}$ laminate, the case is similar, see figure 5.22. The stress state is homogeneous in the middle but near the stress concentration the outer layers are loaded more severely. Note that this laminate will also typically show significant expansion upon compression. This is however limited by the clamped tabs, which also has an effect on the stress state in this area.

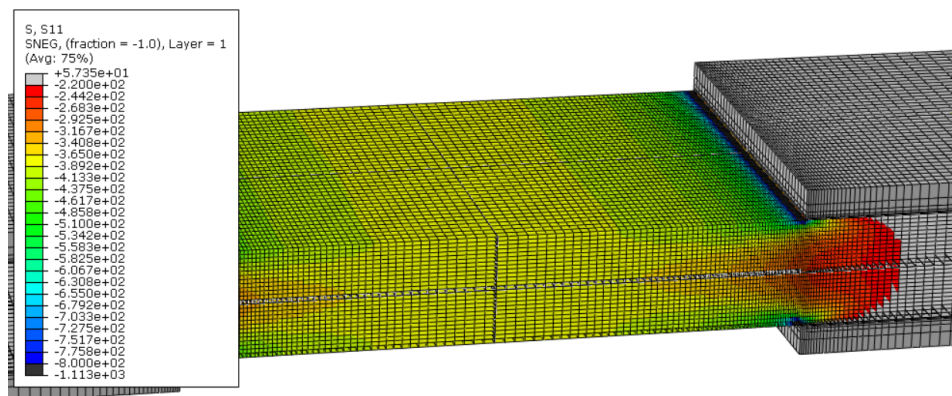


Figure 5.21: Stress concentration decays to a homogeneous stress state at 380 MPa in the middle section for $\#(0/90)$ laminates. Stress on the graph refers to stress aligned with load in MPa.

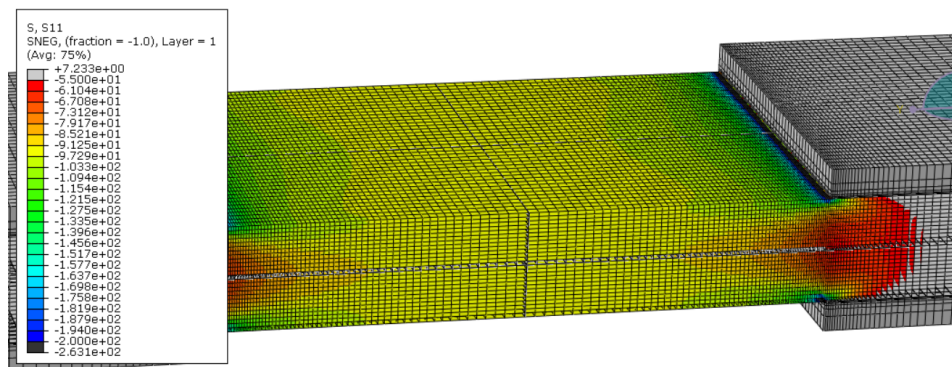


Figure 5.22: Stress concentration decays to a homogeneous stress state at 95 MPa in the middle section for $\#(\pm 45)$ laminates. Stress on the graph refers to stress aligned with load in MPa.

5.4. Final design

From this test series, **aluminum tabbed samples** have proven to be a good design, with fracture occurring in the middle of the samples rather than the stress concentration regions. This results in higher strengths and fatigue lives due to a better stress distribution. Therefore the final sample design has **aluminum tabs** of 1-1.5 mm thick and 55 mm long for all specimens, with load introduced through **shear loading**, a width of 20 mm and a free length of 25 mm. The composite material used has 24

layers oriented in a single direction with a total thickness of 5.3-5.5 mm for all specimens. The final design is shown below in figure 5.23.

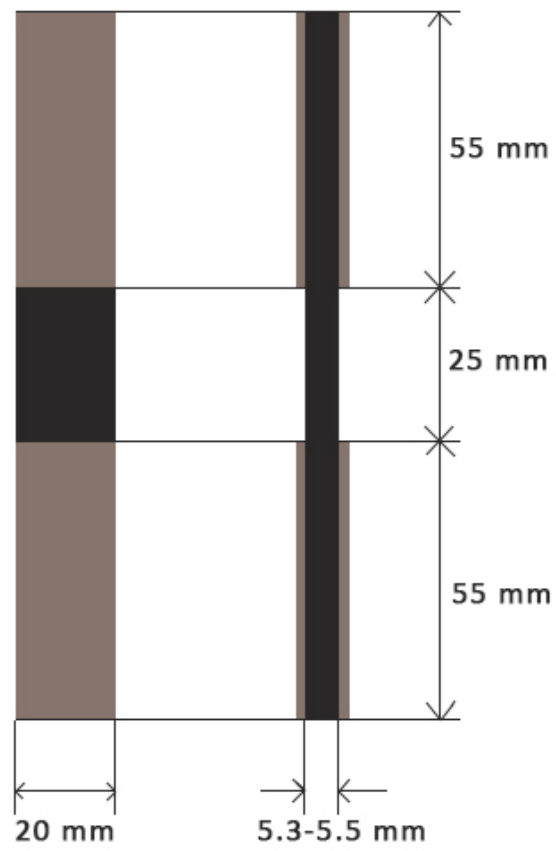


Figure 5.23: Final specimen dimensions

6

Test Results

The second large part of this thesis was to develop and perform a test program with a twofold objective. In the first place it serves as a larger evaluation of the test set-up designed. Recommendations originating from this can then later on be used to improve the set-up for other or similar experiments. In the second place, results of this test program can aid for characterization of fatigue behaviour of plain woven carbon-epoxy material, loaded under C-C and T-C fatigue.

This chapter starts off with a small overview of the program and terminology used throughout this chapter. Hereafter, in section 6.2, results of static tests until failure are presented. Fatigue tests proved to be a challenge in terms of specimen heating. This is addressed in section 6.3. Hereafter, in section 6.4, results of fatigue life are presented for the test program. The next section, 6.5, deals with stress-strain measurements and evolution of stiffness throughout fatigue life. For #(± 45) laminates, uniaxial loading is mainly based on internal shear. These shearing effects are addressed in section 6.6. Finally, this chapter is concluded with microscopy images in section 6.7.

6.1. Program Overview and terminology

A fatigue test program was performed on the woven carbon-epoxy material. The idea behind it is to capture relevant characteristics regarding C-C and T-C fatigue, sufficiently but within the bounds of what can be done within the timeframe of a master thesis project. In this section, an overview of the tests which have been performed is shortly presented.

The **material** used is a 24 layer composite (all layers oriented in the same direction). The material is described in chapter 5. Two orientations of the material are under investigation: #($0/90$), in which '#' is used to denote that it is a fabric and ' $0/90$ ' denotes that warp and weft directions are under an angle of 0 and 90 degrees with the load, respectively. The second orientation under investigation is #(± 45), in which warp and weft directions are under an angle of +45 and -45 degrees with the load direction.

When fatigue is typically mentioned, it depicts a phenomenon in which a sample is damaged through cyclic loading at levels below which static failure can be expected. In this sense it is of interest to know exactly what load levels result in (quasi-)static failure of a sample. A total of 15 **static tests until failure** have been performed, mainly to assess the ultimate compressive strengths of both lay-ups.

With regards to **R-ratio**, the experiments have been limited to 2 values. For C-C loading, the critical case to consider is a full loading/unloading cycle of the structure, i.e. a large value of R. However, to avoid overshooting to tensile loading, load is not returned completely to 0 but rather to a value of 10% of the maximum compressive load. This corresponds to **R = 10**. This R-value is often encountered in composite fatigue literature for S-N diagrams and CLDs [6, 7, 58, 77, 107], as well as its tensile equivalent of $R = 0.1$ [9, 10, 12, 14, 27, 61, 81]. While other R-ratios for C-C loading are encountered in literature and can be useful for further characterization of fatigue behavior, the program is limited

to $R = 10$. To characterize T-C loading, the typical method is to use fully reversed loading ($R = -1$), which is frequently encountered in literature as well. [8, 27, 33, 108]

The aim of this test program has been to cover all loading ranges of constant amplitude cyclic loading at R-ratios of 10 and -1. A test is denoted throughout the project as 'a test at X %', with X a number between 30 and 90. This percentage depicts a test where $\sigma_{min} = X(\%) \sigma_{ult,c}$, where $\sigma_{ult,c}$ is the mean ultimate compressive strength (quasi-static, at a displacement rate of 0.5 mm) of a specimen with the same lay-up (see section 6.2).

For all combinations of lay-up and R-ratio, the aim has been to characterize fatigue behavior from its fatigue limit ($N_f = \infty$) until low cycle fatigue. To define a specimen's fatigue limit, the approach has been to set a fatigue life threshold (500,000 - 1,000,000 cycles). When a specimen under cyclic loading surpasses this threshold, it is considered a **run-out** and the test is ended prematurely.

For every lay-up/R-ratio combination, a number of tests are then performed at different load levels above the fatigue limit. A special case is low cycle fatigue of specimens loaded under $R = -1$. This combination turned out to be detrimental for both lay-ups. This loading is not very common in typical designs. Therefore, focus is somewhat at high cycle fatigue for both lay-ups. The following sections elaborate on this. A full overview of all tests performed throughout this program is added as an appendix (appendix D).

6.2. Quasi-Static Tests

To perform fatigue experiments under a constant amplitude cyclic load, it is important to be able to relate the applied load to what a specimen can ultimately cope with. To do this, quasi-static tests can be used to compare the applied load in % to a specimen's ultimate strength. For this test series, a set of quasi-static tests in compression have been performed on specimens for both $[\#(0/90)]_{24}$ and $[\#(\pm 45)]_{24}$ lay-up. The results are reported in this section.

6.2.1. $[\#(0/90)]_{24}$

Uniaxial loading of a $[\#(0/90)]_{24}$ lay-up can be expected to be **fiber-dominated**. Therefore, strain-rate dependence can be expected to be negligible for both strength and stiffness, with final failure occurring at low strains. To assess ultimate compressive strength of the $[\#(0/90)]_{24}$ laminates, 5 specimens were tested at a displacement rate of 0.5 mm/min. Initial cross-sectional areas were measured with a caliper before every test and these were used for stress calculations using analog force data. Strains are assessed using DIC.

Figure 6.1 shows the stress-strain behavior for static compressive tests. Failure strains and stresses for $[\#(0/90)]_{24}$ are summarized in table 6.1. As expected, stress-strain behavior is close to linear until failure, and failure strains are rather small. The mean ultimate compressive strength ($\sigma_{ult,c}$) from this test series is 513 MPa. Despite the limited batch size (only 5 samples), we can determine the CV of the ultimate compressive strength ($\sigma_{ult,c}$) of this sample set, which is equal to 1.8%. In a similar manner we can derive the mean (1.19%) and CV (4.8%) of the strain at failure ($\epsilon_{ult,c}$). The black line in figure 6.1 indicates a single test (testID2) which is representative for all five because of the small CV in both stress and strain. The CV values should be treated with caution, keeping in mind the small amount of samples, the fact that the samples stem from the same material batch and that they are tested in the same laboratory. However, it does indicate typical variation of this test series.

Table 6.1: Compressive failure strain and stress for 5 quasi-static compression tests on $[\#(0/90)]_{24}$ laminates.

TestID	$\epsilon_{ult,c}$ [%]	$\sigma_{ult,c}$ [MPa]
1	1.24	530
2	1.21	511
3	1.09	511
A1	1.25	514
A2	1.20	501

6.2.2. $[\#(\pm 45)]_{24}$

For a $[\#(\pm 45)]_{24}$ lay-up, where **failure is matrix-dominated** under uniaxial compression, the case is somewhat different. As can be expected, much larger strain until failure can be observed. This caused some troubles with the first samples with speckle patterns debonding from the surface upon large deformations. This caused loss of some strain data in the initial tests. However, since the main concern for these tests was ultimate strength assessment of the samples, strength data could still be used. After solving the paint issue through a better surface treatment, some tests were repeated to observe strain behavior as well.

To assess **ultimate compressive strength** of these laminates, in total 7 specimens were tested at a displacement rate of 0.5 mm/min. Initial cross-sectional areas were measured with a caliper before every test and these were used for stress calculations from analog force data. Strains are assessed using DIC. For matrix dominated lay-ups, a clear effect of strain rate can be expected. Of interest here is the ultimate strength, to be used in S-N curves. As a control measure, 3 additional compression tests until failure were performed at the highest displacement rate which can be encountered during fatigue experiments at 3 Hz, which is approximately 450 mm/min. The results of all tests are summarized in appendix D in table D.2. Stress-strain behavior for both situations (high and low strain rates) are presented in figure 6.1. Due to loss of some of the DIC data as mentioned above, these curves each come from a single test and should be treated with care. Despite loss of DIC data for these tests, analog force and displacement data is still available for each test and these are similar to the two tests shown below.

The mean ultimate compressive strength ($\sigma_{ult,c}$) based on the 7 low strain rate tests is 156 MPa, with a CV in these values of 1.4%. For the 3 high strain rates this is 177 MPa, with a CV of 1.5%. Here as well, caution is required with these very low CV values. They are obtained in the same lab set-up by the same operator, come from the same material batch,... However, the numbers give an indication of strength variations. The difference between both means is discussed further below.

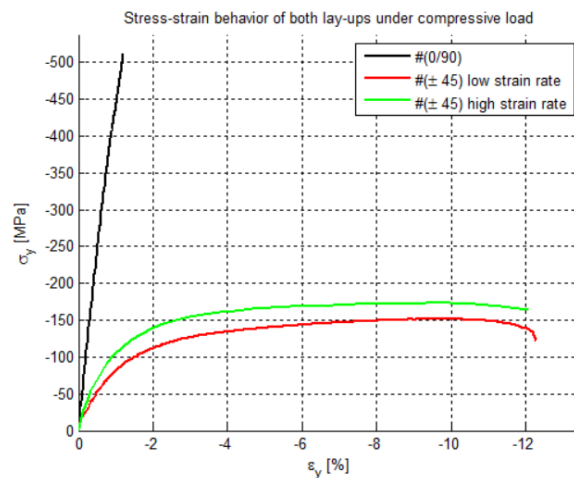


Figure 6.1: Stress-strain behavior for static tests.

Statistical Significance To assess the significance of the effect of strain rate on the ultimate compressive strength of a sample, a statistical **t-test** is used. This test can be used to test the null hypothesis that the means of two different populations (in this case 'strength at low strain rate' and 'strength at high strain rate') are equal. [109]

One of the assumptions here is that both populations should follow a *normal distribution*. [109] Regarding the relatively small population sizes, this assumption could be questioned. However, as a first order approximation, it can be accepted. To further assess this assumption, a Kolmogorov-Smirnov test can be used, which is available as a function in matlab's statistics and machine learning toolbox. For both populations, the null Hypothesis ('the data in this vector comes from a normal distribution') was accepted with a p-value of 0.79 and 0.75 for the slow strain rate and high strain rate strengths,

respectively. A second assumption is based on the fact that *variances of both populations must be equal*. [109] Again, as a first order approximation this can be assumed true. To further assess this, an F-test can be used, also built in in matlab's statistics and machine learning toolbox. The null hypothesis that both populations have indeed equal variances is accepted with a p-value of 0.58.

For the t-test in this case, we would like to assess whether or not changing the displacement rate from 0.5 mm/min to 450 mm/min significantly changes the ultimate strength of this specimens. Therefore the **null hypothesis** (H_0) and **alternative hypothesis** (H_a) become:

- H_0 - Changing the displacement rate from 0.5 mm/min to 450 mm/min does not affect the ultimate compressive strength of a $[\#(\pm 45)]_{24}$ sample.
- H_a - Changing the displacement rate from 0.5 mm/min to 450 mm/min has an effect on the ultimate compressive strength of a $[\#(\pm 45)]_{24}$ sample.

An unpaired two-tailed t-test is performed through the following test statistic t [109]:

$$t = \frac{\bar{x} - \bar{y}}{\sqrt{\frac{s}{n} + \frac{s}{m}}} \quad (6.1)$$

In which x and y are vectors describing ultimate compressive stresses at low and high strain rates, respectively, \bar{x} and \bar{y} are the means of these vectors, n and m are the sizes of these vectors and s is the pooled standard deviation [109]:

$$s = \sqrt{\frac{(n-1)s_x^2 + (m-1)s_y^2}{n+m-2}} \quad (6.2)$$

Where s_x and s_y are the standard deviations of vectors x and y . From this a value for t of 13.55 is obtained. With 8 ($=m+n-2$) degrees of freedom, this results in a p-value below 0.0001, which means **the null hypothesis can be rejected with sufficient confidence**, and the alternative hypothesis can be accepted. The difference of both means is 21.29 MPa. The 99% confidence interval of this difference is [16.02, 26.55] MPa.

6.3. Test Frequency and Temperature

Practically, it is desirable to perform fatigue experiments at the highest possible frequency to lower the test time (which can run up to days at typical frequencies). However, it is important to consider **heating of the material due to cyclic loading**. Heating can become so severe that material properties are altered by it and test results become useless. [7] Heating is typically much more severe in specimens with off-axis fibers due to fiber friction. [5, 7, 9] Additionally, there is also the intrinsic dependence on loading frequency (regardless of the temperature), although it is difficult to analyse these two independently. [9] Kawai et al. [9] investigated carbon-epoxy weave fabric laminates in on- and off axis direction and reported on the frequency effect. They showed the effect of frequency on off-axis loading, namely that the heating can be suppressed by lowering the test frequency to 2 Hz rather than 10 Hz. For the on-axis data however, similar effects are observed at 10 Hz, namely that the heating effect is sufficiently suppressed.

To avoid heating effects throughout this test program, temperature was **monitored** throughout every test and the program was adapted accordingly. It should be noted that a perfect constant temperature throughout tests which may run up to a couple of days is not achievable in practice, considering for example variable lab temperatures between day and night. Therefore, for this test series, temperature variation was considered acceptable when it stays within a few degrees (max 8-10 °C). When the temperature variation was higher, the data may still be useful but should be treated with care.

While it can be argued that 8-10 °C is somewhat on the lower side since it is well below the glass transition temperature of any typical epoxy resin, and some authors report fatigue results with much larger temperature differences throughout a fatigue test in S-N curves and stiffness evolutions [8, 9], the limits are set for multiple reasons. The first is that it is difficult to prove that there is no other

intrinsic temperature effect on a complex damage phenomenon even below an epoxy's T_g . On top of this, it is important to realise that temperature measurements have been done using a thermocouple attached to the specimens. While this thermocouple measures temperature at that location (outer lamina, in the middle), this gives no indication about local variations in temperature throughout the specimen, where temperatures might reach higher levels.

6.3.1. $[\#(0/90)]_{24}$

Based on literature references mentioned before [5, 7, 9], the decision was made not to test above 3 Hz for this research. For $[\#(0/90)]_{24}$ laminates loaded under C-C and T-C fatigue, no significant heating was observed in any of the tests performed. Typical specimen temperature variations throughout tests are shown in figures 6.2 and 6.3 for, respectively, low and high cycle C-C fatigue, and in figures 6.4 and 6.5 for, respectively, low and high cycle T-C fatigue. From these figures can be concluded that specimen heating never exceeded unacceptable values and therefore, the use of 3 Hz as a test frequency for all $[\#(0/90)]_{24}$ samples is justified. These differences are typically very small and cannot be correlated with any significant damage event or stiffness evolution.

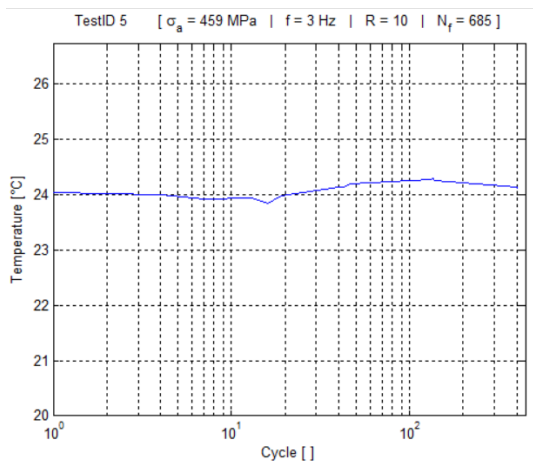


Figure 6.2: Typical temperature evolution in a $[\#(0/90)]_{24}$ specimen loaded under low cycle C-C fatigue.

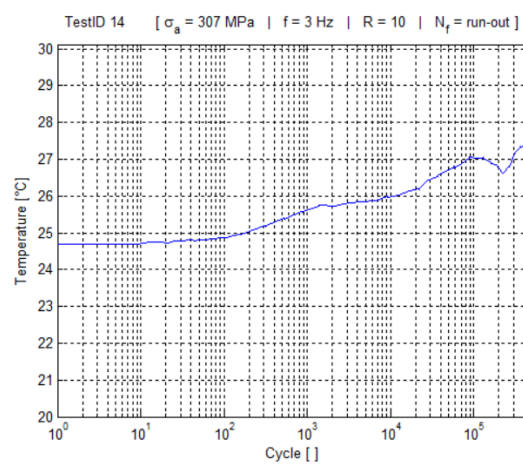


Figure 6.3: Typical temperature evolution in a $[\#(0/90)]_{24}$ specimen loaded under high cycle C-C fatigue.

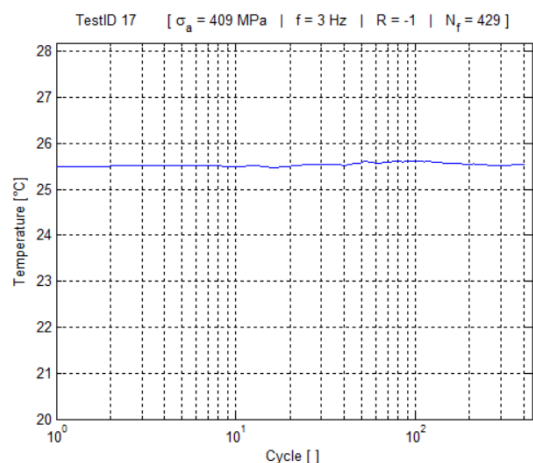


Figure 6.4: Typical temperature evolution in a $[\#(0/90)]_{24}$ specimen loaded under low cycle T-C fatigue.

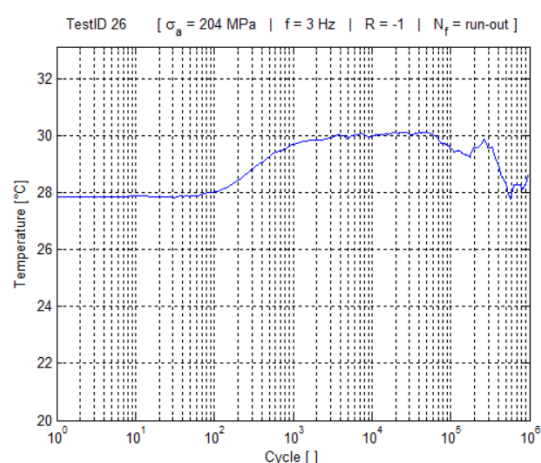


Figure 6.5: Typical temperature evolution in a $[\#(0/90)]_{24}$ specimen loaded under high cycle T-C fatigue.

6.3.2. $[\#(\pm 45)]_{24}$

For $[\#(\pm 45)]_{24}$ laminates, the case is somewhat different. Throughout the beginning of the $[\#(\pm 45)]_{24}$ portion of the test program, specimen heating has been a challenge. Two factors were observed to influence specimen heating for this case: **test frequency** and **maximum applied compressive stress**. Simply put, a high test frequency and/or high applied stress level can result in specimen heating beyond acceptable levels. In particular for T-C loading, the effect is significant.

To limit heating as much as possible, a 12V desktop **pc fan** was installed on the hydraulic test bench, with a cardboard 'tunnel' to ensure proper guidance of airflow towards the specimen during a test as much as possible, see figure 6.6. To ensure proper temperature measurement, the thermocouple used in each experiment has been covered using insulating tape, to avoid direct exposure to cooling airflow which could potentially influence the measurement.

Particularly when heating happens slowly (over the course of minutes/hours), air cooling is expected to have an effect. When heating occurs much more rapidly, this technique is expected to barely have any influence. Even if successful cooling could be achieved for fast heating specimens, this would then raise questions on temperature variations throughout the thickness, considering the relatively thick specimens (5.3-5.5 mm) and insulating properties of epoxy separating fiber bundles (although this should be less of an issue in woven composites).

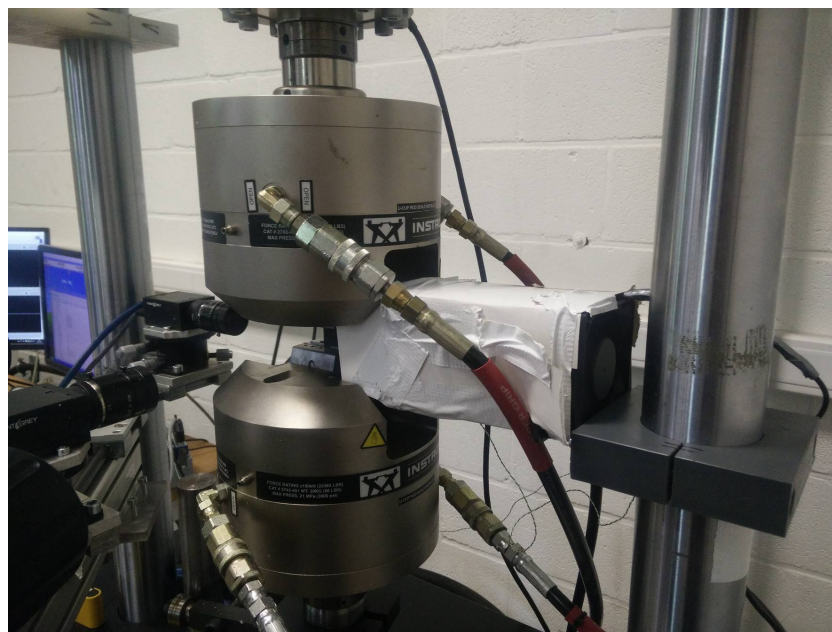


Figure 6.6: A 12V pc fan used to cool down $[\#(\pm 45)]_{24}$ specimens during cyclic loading.

In the initial stages of the test program of these laminates, specimen heating proved to be a challenge. For $R = 10$, specimens loaded at high stresses (low cycle fatigue) required frequencies as low as 0.25 Hz to keep heating limited. On the other hand, for loading at $R = 10$ at high cycle fatigue (run-out samples), frequencies of 3 Hz cause no heating issues, see figure 6.7. While low frequencies are perfectly feasible for low cycle tests which end rapidly, for run-out samples this results in a timeframe of 1-2 weeks per test, which is, at least for the sake of this master thesis, unreasonably long. This leaves two options: either accept heating to occur, which has already been discussed above to be unacceptable, or perform the program **using lower frequencies for higher applied loads and vice versa**. This is the option that has been chosen for the C-C part of the $[\#(\pm 45)]_{24}$ laminates.

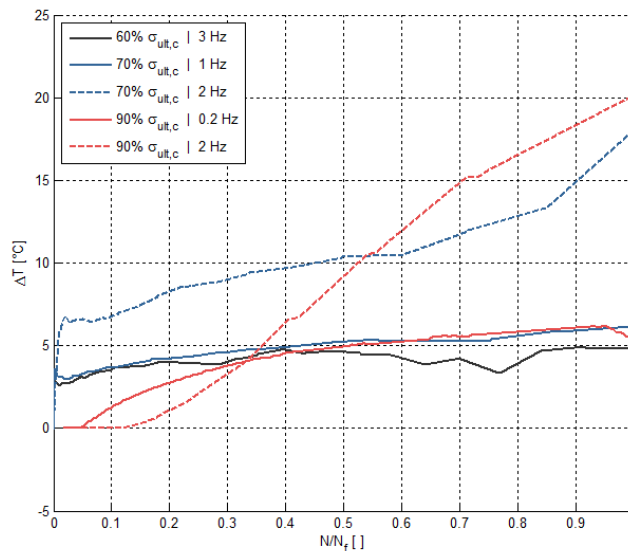


Figure 6.7: Altering the frequency can successfully limit heating for C-C loading of $[\#(\pm 45)]_{24}$ laminates

For loading at $R = -1$, going as low as 0.1 Hz with fan cooling still did not suffice in limiting heating at high loads ($\geq 60\% \sigma_{ult,c}$). For most designs however, $[\#(\pm 45)]_{24}$ laminates will rarely be used at such severe reversing loads, thereby limiting the relevance of these experiments. Therefore the decision was made to omit low cycle fatigue tests for $R = -1$ from the test program for these laminates, and to focus on the more relevant high cycle fatigue behavior. Tests at $30\% \sigma_{ult,c}$ all resulted in run-outs. At $30 - 40\% \sigma_{ult,c}$, heating could be limited by testing at 2 Hz. However, slightly higher at $50\% \sigma_{ult,c}$, the frequency had to be lowered to 0.2 Hz to limit heating (figure 6.8). Applied stresses higher than this are omitted from the program for reasons mentioned above.

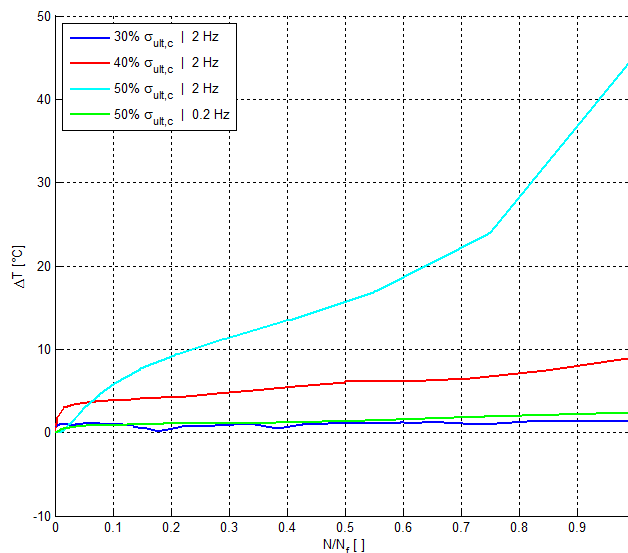


Figure 6.8: Loading at 2 Hz does not induce significant temperature rises for T-C loading $\leq 40\% \sigma_{ult,c}$. At $50\% \sigma_{ult,c}$, the frequency must be lowered to keep heating at acceptable levels.

6.4. Fatigue Life

This subsection covers the fatigue life results for this test series. It starts off with an explanation of the Sendeckyj method to describe a deterministic S-N equation and scatter quantification. After this, fatigue life results of the test program are presented.

6.4.1. Methodology

6.4.1.1. S-N curve

The global analysis of fatigue data and scatter (S-N) curves is performed using the **Sendeckyj wearout model**. [110, 111] This widely accepted method is preferred since it includes static data, runouts and residual strength data to describe a deterministic equation of the S-N curve and a probabilistic description of scatter involved. The method is based on transforming different data sources (static tests, regular fatigue data, run-outs, residual strength tests) into a value, the **equivalent static strength** σ_e . Based on these equivalent static strengths, a two-parameter Weibull distribution is determined. Based on this distribution, the model parameters are updated and the process is repeated until it converges to the largest **MLE (maximum-likelihood estimate)** of the shape parameter α . [110] For S-N characterization, the model is based on three assumptions as stated in [110, 111]:

- S-N behavior can be described by a deterministic equation which can be based on theoretical consideration or experiments of the fatigue damage process.
- The "*Strength-life equal rank assumption*". Static strengths are uniquely related to fatigue lives and run-out residual strengths. Stronger specimens can be expected to have higher residual strength at run-out or longer fatigue life at a given load. This assumption may be invalid in some cases (For example when different load cases compete).
- Variation of (equivalent) static strength data can be characterized as a two-parameter Weibull distribution

Concerning the first assumption, it is important to note that different load levels can result in different failure modes and the damage mode can even change throughout the fatigue life. Thereby, this method is merely based on curve-fitting of experimental data, without theoretical consideration of the actual mechanisms behind this.

The wearout model used in this approach is based on the following deterministic equation:

$$\sigma_e = \sigma_a [(\sigma_r/\sigma_a)^{1/S} + (n-1)C]^S \quad (6.3)$$

Where S and C define the asymptotic slope on the log-log plot and extent of initial "flat" region of the S-N curve. σ_e , σ_a , σ_r and n depict the equivalent static strength, maximum applied cyclic stress, residual strength and number of cycles, respectively. To show how this parameter S is an indication of the asymptotic slope on the log-log plot in this model, consider the model for fatigue failure at high fatigue life n. For fatigue failure, $\sigma_r = \sigma_a$ and we get:

$$\sigma_e = \sigma_a [1 + (n-1)C]^S \quad (6.4)$$

Since we are assuming n to be large we can say that

$$1 + (n-1)C \approx Cn \quad (6.5)$$

which leads to

$$\sigma_a = \sigma_e [Cn]^{-S} \quad (6.6)$$

Which indeed indicates the asymptotic slope for a high value of n.

From initial guesses for fatigue model parameters C and S (described in [110]), the data from different tests (static, fatigue, run-out and residual strength) can be converted into a set of equivalent strength data. To this data set, a two-parameter Weibull distribution is fitted, including right-censoring for run-out data. This is done using matlab function 'wblfit'. Using an optimization algorithm (gradient ascent) the model parameters are optimized until the highest value of the shape parameter α is found. The model parameters and Weibull parameters associated with this value are used to describe the S-N curve.

An S-N curve in this work is presented based on the number of cycles and the largest applied compressive stress σ_a . It is in particular important for reporting of tests with R = -1 to realise that this stress does not depict the difference between σ_{max} and σ_{min} .

6.4.1.2. A- and B-Basis curves

A- and B-basis values are described as the values describing the 1st and 10th percentile, respectively, with a confidence of 95%. To describe A- and B-basis S-N curves, we can determine the A- and B-basis values for the optimized Weibull distribution of the equivalent strength. From these values, equation 6.3 can be used to determine the S-N basis curves. Typically, for this master thesis a low number of samples has been used due to time constraints, this causes A- and B-basis curves to be somewhat wide.

The approach to determine A- and B-basis values of a two-parameter Weibull distribution is described in [112]. The **A-basis** value of a two-parameter Weibull distribution with shape parameter α and scale parameter β is

$$A = q_a \cdot \exp\left\{\frac{-V_a}{\alpha\sqrt{n}}\right\} \quad (6.7)$$

In which n is the amount of data points and V_a can be approximated as

$$V_a = 6.649 + \exp\left\{2.55 - 0.526\ln(n) + \frac{4.76}{n}\right\} \quad (6.8)$$

and q_a is determined as

$$q_a = \beta(0.01005)^{1/\alpha} \quad (6.9)$$

Similarly for the **B-basis** value:

$$B = q_b \cdot \exp\left\{\frac{-V_b}{\alpha\sqrt{n}}\right\} \quad (6.10)$$

In which n is the amount of data points and V_b can be approximated as

$$V_b = 3.803 + \exp\left\{1.79 - 0.516\ln(n) + \frac{5.1}{n-1}\right\} \quad (6.11)$$

and q_b is determined as

$$q_b = \beta(0.10536)^{1/\alpha} \quad (6.12)$$

6.4.2. Heating and Frequency Consideration

Concerning S-N curves of $[\#(\pm 45)]_{24}$, caution is required. Unlike the first part of the test program, on $[\#(0/90)]_{24}$ laminates, specimen heating was an important consideration here, see section 6.3. This has three implications when attempting to create S-N diagrams:

- Specimen heating could potentially affect a specimen's fatigue life. Throughout this part of the test program **several specimens experienced heating beyond acceptable levels**. As mentioned before, it threshold be guaranteed that specimen heating does not affect the fatigue life of a specimen under constant amplitude loading.
- In order to cope with specimen heating, the **frequency was lowered for higher applied stresses**, for both R-ratios. Note that some authors do indicate an intrinsic dependency of fatigue life on test frequency. [9, 58] Note as well the static tests reported in section 6.2, which show a dependency of the ultimate compressive strength on the loading rate.
- For $[\#(\pm 45)]_{24}$ laminates loaded under $R = -1$, heating could not be avoided even at frequencies below 0.1 Hz for high loading cases. Therefore, **no valid tests at high loadings have been performed for $R = -1$** . In deriving an S-N curve using only high cycle fatigue results together with static data, its validity in the low cycle fatigue region is questionable.

6.4.3. Results

6.4.3.1. $[\#(0/90)]_{24}$ ($R = 10$)

An S-N curve for the case of $[\#(0/90)]_{24}$ **with $R = 10$** is shown in figure 6.9. Data points are presented in appendix D in table D.3. Note that:

- All tests are performed at 3 Hz and excessive heating was never measured.
- Tests at 307 MPa (60% $\sigma_{ult,c}$) all resulted in run-outs.
- 5 quasi-static tests and 13 fatigue tests at approximately 60-90% have been performed.
- One of the run-outs was tested for residual strength.
- S-N curve can be said to be relatively flat.
- Due to scatter in the results and a relatively low number of tests, the A- and B-basis curves in this case are still relatively wide.

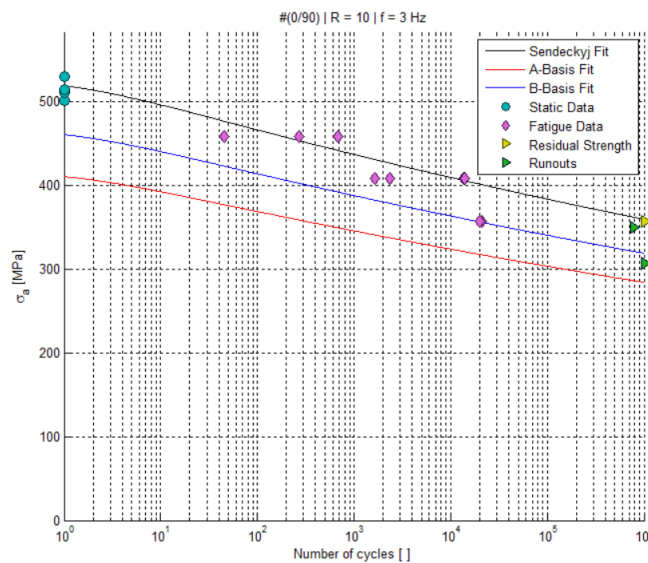


Figure 6.9: S-N curve for the case of $[\#(0/90)]_{24}$ with $R = 10$. All tests are performed at 3 Hz.

Sendekyj parameters: $[S = 0.0283, C = 0.4345, \alpha = 29.97, \beta = 519.09]$

6.4.3.2. $[\#(0/90)]_{24}$ ($R = -1$)

An S-N curve for the case of $[\#(0/90)]_{24}$ **with $R = -1$** is shown in figure 6.10. Data points are presented in appendix D in table D.4. Note that:

- All tests are performed at 3 Hz and excessive heating was never measured.
- When the largest applied compressive stress σ_a was equal to 204 or 230 MPa (40 – 45% $\sigma_{ult,c}$), tests resulted in run-outs.
- 5 quasi-static tests and 12 fatigue tests at approximately 40-90% have been performed, with a focus on high cycle fatigue
- One test at 60 % $\sigma_{ult,c}$ was used for interval microscopy, and taken out of the machine after multiple time intervals, see section 6.7. However, multiple cycles of clamping/unclamping combined with loading cause the adhesive to break down during one of the microscopy cycles. Since the sample itself did not fail here after enduring these cycles, it is taken into account in the S-N curve as a run-out (right-censored).
- The curve is steeper compared to $R = 10$. Note however that stress σ_a in this case refers to the largest applied compressive stress, and that the stress amplitude is larger here.
- Due to scatter in the results and a relatively low number of tests, the A- and B-basis curves are relatively wide.

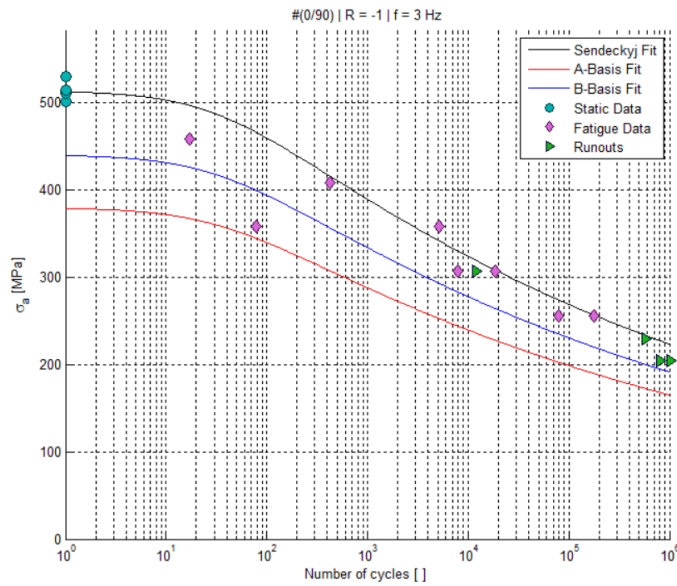


Figure 6.10: S-N curve for the case of $[\#(0/90)]_{24}$ with $R = -1$. All tests are performed at 3 Hz.

Sendeckyj parameters: $[S = 0.0809, C = 0.0288, \alpha = 23.6392, \beta = 512.44]$

6.4.3.3. $[\#(\pm 45)]_{24}$ ($R = 10$)

Data points for $[\#(\pm 45)]_{24}$ at $R = 10$ are presented in appendix D in table D.5. They are represented in figure 6.11. In this figure, for every test the frequency is indicated. Points denoted in red indicate points where heating surpassed acceptable levels. Note the following:

- Test frequencies vary from 0.25 - 3 Hz
- A combination of elevated load and frequency often results in heating
- Tests at 94 MPa (60% $\sigma_{ult,c}$) all resulted in run-outs.
- In total, 14 fatigue tests at 60-90% have been performed, 5 of which heated up above the threshold.

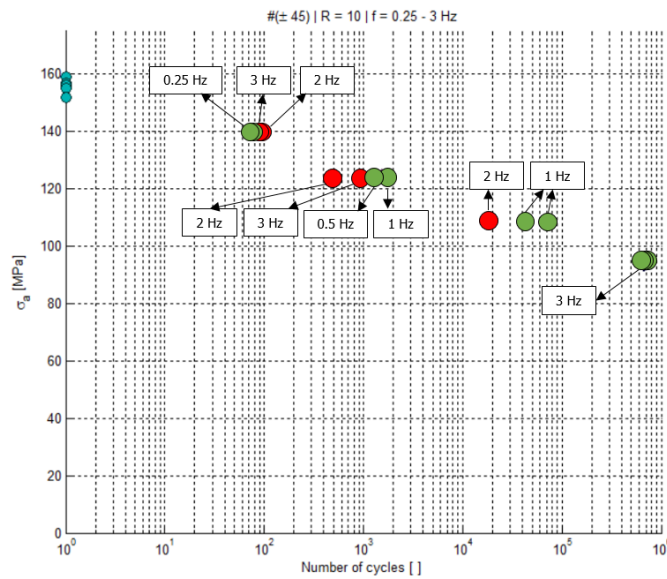


Figure 6.11: S-N data points for the case of $[\#(\pm 45)]_{24}$ with $R = 10$. Frequencies of each test are indicated. Red points denote tests in which heating surpassed acceptable levels.

Deriving a reliable stress-life curve from a dataset like this is difficult. Even if tests with heating are eliminated, the variation in frequency could still have an influence. A curve can be generated from these data points, see figure 6.12. With much lower frequencies being used, loading rates are also remarkably lower, which is why for this graph, the quasi-static tests at slow loading rates are used rather than the ones at higher rates. While this curve could be used to give a first impression of material behavior or as a first order approximation, the fact that only 9 fatigue data points are used and frequency varies between them requires **great caution** in using curves like this.

Figure 6.11 shows that, despite heating effects, fatigue life does not seem to be drastically affected. Caution is required in deriving conclusions from this. **If** it is assumed that the observed heating does not significantly affect the fatigue properties of the specimen, we can derive an S-N curve for all data-points as well. This curve is presented in figure 6.13. Comparing this to figure 6.12 indicates that the curve is barely affected.

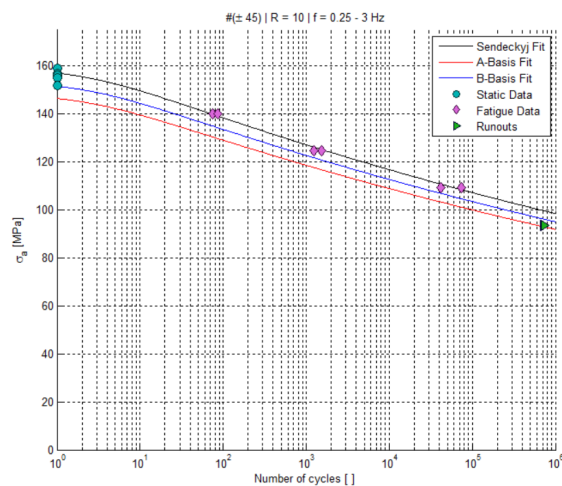


Figure 6.12: S-N curve for the case of $[\#(\pm 45)]_{24}$ with $R = 10$ including only data points where no heating occurred. **Note that this curve is derived from tests at different frequencies.**

Sendeckyj parameters: $[S = 0.037, C = 0.2976, \alpha = 104.24, \beta = 157.00]$

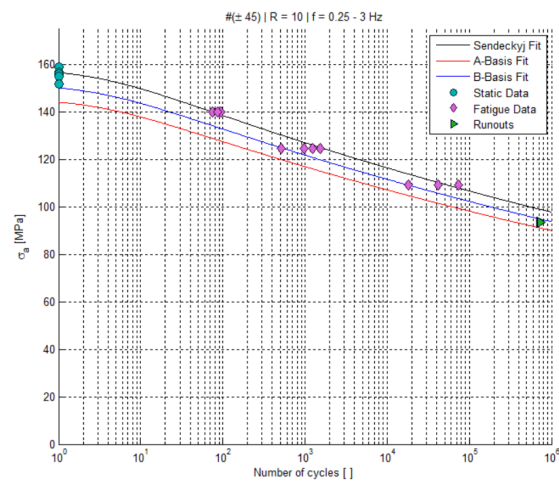


Figure 6.13: S-N curve for the case of $[\#(\pm 45)]_{24}$ with $R = 10$ including all data points. **Note that this curve is derived from tests at different frequencies and tests which heated up.**

Sendeckyj parameters: $[S = 0.038, C = 0.2477, \alpha = 81.58, \beta = 156.64]$

6.4.3.4. $[\#(\pm 45)]_{24}$ ($R = -1$)

Data points for $[\#(\pm 45)]_{24}$ at $R = -1$ are presented in appendix D in table D.6. They are represented in figure 6.14. In this figure, for every test the frequency is indicated. Points denoted in red indicate points where heating surpassed acceptable levels. Note the following:

- Test frequencies vary from 0.2 - 2 Hz
- Some frequency variation was required to perform tests at 50 % ($\sigma_a = 78$ MPa). At higher frequencies no tests could be performed without heating.
- Tests at 47 MPa (30% $\sigma_{ult,c}$) all resulted in run-outs.
- In total, 10 fatigue tests at 30-80% have been performed, 2 of which heated up above the threshold

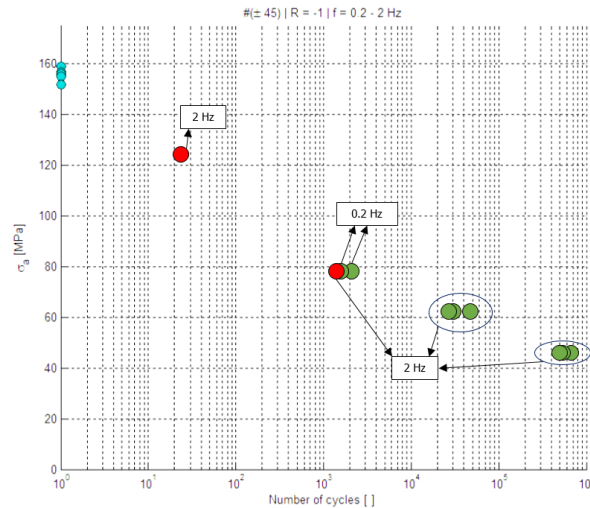


Figure 6.14: S-N data points for the case of $[\#(\pm 45)]_{24}$ with $R = -1$. Frequencies of each test are indicated. Red points denote tests in which heating surpassed acceptable levels.

In a similar manner as for $R = 10$, we can also derive an S-N curve using data points with no heating here. However, here it is even more important to be careful. The curve is based merely on data points of the high cycle region (no data points above $\sigma_a = 78$ MPa) and it is based on just 8 fatigue data points, of which 2 are at a different frequency than the others. The result can be seen in figure 6.15. This curve should by no means be used in low cycle fatigue regions. Although the algorithm limits it to 1, the C-value of the Sendekyj fitting approach actually optimizes around 9, which would indicate an overly steep descent of the curve rather than a flat region, which is seen in all other S-N curves and more characteristic for fatigue. Since there is no valid fatigue data in this region, no conclusions can be drawn from this.

Under the same assumption that heating has little or no effect, we can again derive an S-N curve for all data points in this case, see figure 6.16. Once again, caution is required in the use of graphs like this for design purposes. The curve is again not changed much by adding these two points.

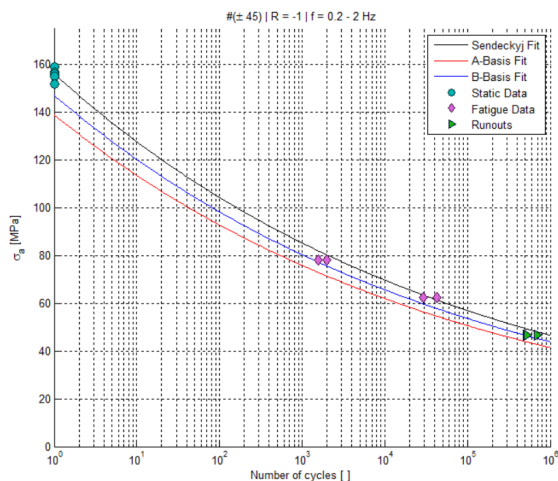


Figure 6.15: S-N curve for the case of $[\#(\pm 45)]_{24}$ with $R = -1$ including only data points where no heating occurred. **Note that this curve is derived from tests at different frequencies.**

Sendekyj parameters: $[S = 0.0876, C = 1.00, \alpha = 63.30, \beta = 156.17]$

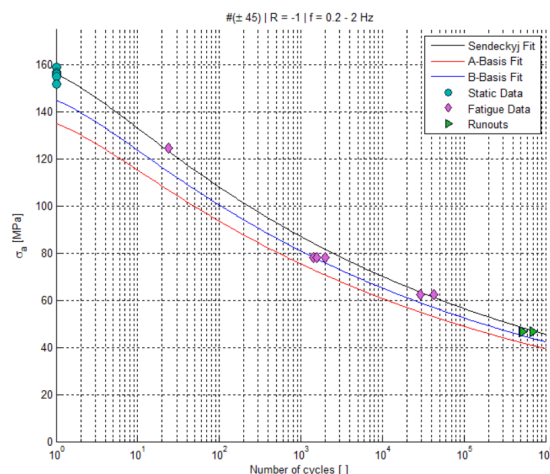


Figure 6.16: S-N curve for the case of $[\#(\pm 45)]_{24}$ with $R = -1$ including all data points. **Note that this curve is derived from tests at different frequencies and tests which heated up.**

Sendekyj parameters: $[S = 0.0940, C = 0.4952, \alpha = 49.61, \beta = 156.13]$

6.5. Stress-Strain Combinations and Property Evolution

As was mentioned in the literature study (chapter 2), composite fatigue is often linked to an evolution of properties, most importantly stiffness. In this section, stiffness and permanent strain evolution results from DIC are analysed, together with cyclic stress-strain (hysteresis) behavior. Using the approach including DIC on the side of specimens, stiffness drops can be connected with damage events observed.

6.5.1. Definitions and Notes

Axis system In this section, all properties (strain, stress, stiffness) are denoted in the **laminata axis system**, see figure 6.17:

- the **y-axis** is defined as the axis aligned with the loading direction, upward positive.
- the **z-axis** is defined as the normal to the laminate plane, coming out of the DIC pattern.
- the **x-axis** is chosen as to complete the right hand axis system.

Note that for DIC images taken from the side of a specimen, **y** is still aligned with the load but **x** is taken to complete the plane describing the *side* of the specimen in this case. In all other cases, the axis system described above will be used.

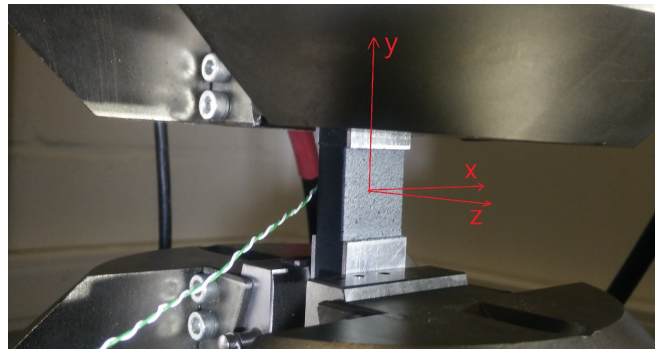


Figure 6.17: Laminata axis system used in this section

Stiffness definitions Defining **stiffness** is important for this section. It is important to note how stiffness is defined. To define stiffness, the approach applied here is to take two time points in a cycle and compare stress and strain to obtain stiffness. Caution for selecting these points is important. For cyclic loading, there will be a distinction on the definition of stiffness with respect to R-ratio. In particular when potential permanent strain is considered, the logical approach is to define stiffness in an *unloading* part of a cycle, the hypothesis being that no new damage is developed in this part of the cycle. For **R = 10**, the approach is therefore to use stress and strain at a peak point (at largest compressive load), and choose the following valley point (around 10% of this peak stress) and define stiffness through these two points, see figure 6.18.

For **R = -1** however, both loading and unloading occurs from a peak to the next valley. Because of this, two additional definitions of stiffness are used. '**Stiffness in compression**' (E_c) and '**Stiffness in tension**' (E_T) denote the stiffness defined by using the unloading parts of a cycle, from a peak/valley to the point of zero stress, see figure 6.19. This approach allows for a decoupled view on what happens in tension and compression components of the cycle. The downside however is that this approach tends to result in a large amount of scatter. The cause of this scatter is thought to lie mainly in the fact that, for $R = -1$, the point of zero stress is also the point where the sine wave moves the fastest. DIC images are obtained at constant frame rates so typically, in this region of the stress-strain behavior, interpolation is required between points spread relatively wide apart compared to the peak zones. On top of this, the machine is operated in 'amplitude control mode'. In this case this means that the machine will control hydraulics such that the desired load peaks are reached without over- or undershooting, even if this is at the cost of deviating from the sine wave of the load. Both of these reasons can result in scatter in

the derived stiffness definitions. Therefore, the abovementioned definition of stiffness (E , from peak to valley) for C-C loading is used as well for some T-C tests.

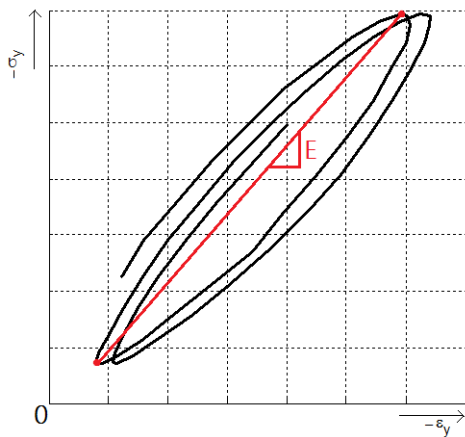


Figure 6.18: Definition of stiffness in the unloading section of a C-C loading pattern

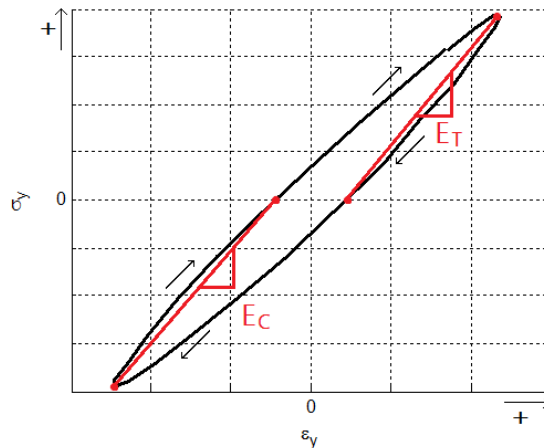


Figure 6.19: Stiffness components in tension and compression for T-C loading.

Normalization For safety of the machine and the specimen, the hydraulic test bench has an ‘**attack time**’ setting. This means that the first cycles of a fatigue test will be of an increasing amplitude from 0 to the actual load amplitude. This attack time does mean that for the first cycles, the specimen will experience smaller stress amplitudes compared to the rest of the fatigue life. Since stress-strain behavior is not perfectly linear (especially for $[\#(\pm 45)]_{24}$ specimens), the abovementioned stiffness definitions could potentially lead to misleading results in these cycles. The results in the first couple of cycles are therefore typically higher. When results are plotted with regards to their initial stiffness E_0 , **this initial stiffness is the stiffness of the first data point right after the attack time.**

Permanent Strain In particular for C-C tests of $[\#(\pm 45)]_{24}$ laminates, **permanent strain** ϵ_{perm} is a parameter of interest. It is defined in this work as the difference in strain at the smallest compressive load applied in cycle x , compared to the strain at the start of the first fatigue cycle (with a compressive load of 10% σ_a already applied). See figure 6.20.

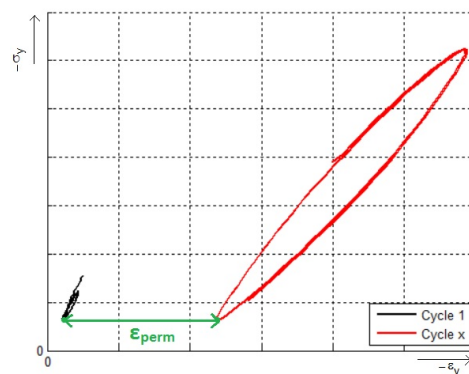


Figure 6.20: ‘ ϵ_{perm} at cycle x ’ is defined as the difference in strain at the smallest compressive load applied in cycle x , compared to the strain at the start of the first fatigue cycle (with a compressive load of 10% σ_a already applied)

Fatigue limit In this work, when the **fatigue limit** is mentioned, this means the load level at which all tests survived at least 500,000 - 1,000,000 cycles.

Reproducibility of Results In order to efficiently show stress-strain and stiffness evolutions, the graphs presented in this chapter are those for a single or two samples per load level for every case. However, in most cases, more than one test has been performed. To provide an indication for the scatter involved in this, comparative stiffness graphs are presented in appendix E.

6.5.2. Evolution for $[\#(0/90)]_{24}$ ($R = 10$)

For **C-C** loading of $[\#(0/90)]_{24}$ laminates, in general, little hysteresis can be observed, both for high and low cycle patterns. In terms of stiffness, the patterns seems to be that little changes can be observed until final failure occurs.

For **high cycle fatigue**, stiffness is pretty much unchanged throughout fatigue life. To illustrate this, the stiffness evolution and stress-strain cycles at different points in fatigue life of a run-out sample (60%) are shown in figures 6.21 and 6.22. A similar pattern is observed for the other sample. For the run-out sample at 70%, the stiffness drops somewhat more significantly, and some permanent strain evolution can be observed, see figures 6.23 and 6.24. Despite these small effects, overall, no significant changes can be observed for run-outs

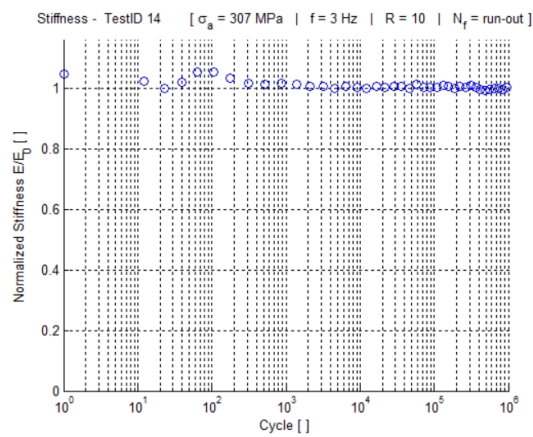


Figure 6.21: Stiffness of a $[\#(0/90)]_{24}$ laminate under 60% $\sigma_{ult,c}$ ($R = 10$) is pretty much unchanged throughout its fatigue life. $E_0 = 46.9$ GPa

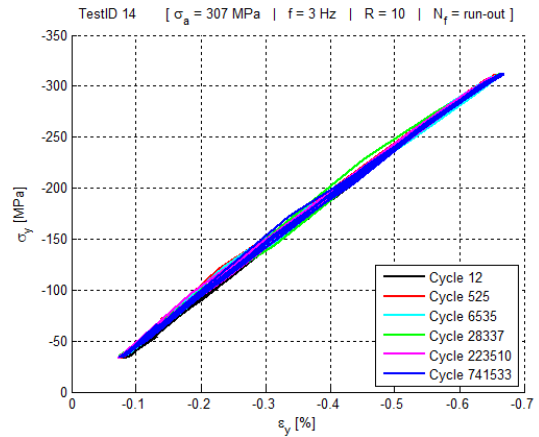


Figure 6.22: No significant difference in stress-strain behavior throughout the fatigue life of a $[\#(0/90)]_{24}$ laminate under 60% $\sigma_{ult,c}$ ($R = 10$)

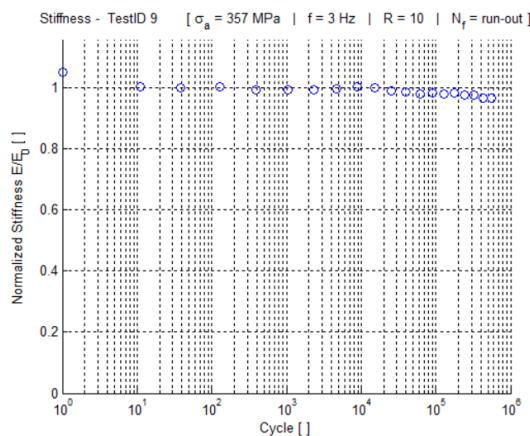


Figure 6.23: Stiffness of a $[\#(0/90)]_{24}$ laminate under 70% $\sigma_{ult,c}$ ($R = 10$) is pretty much unchanged throughout its fatigue life. $E_0 = 46.5$ GPa

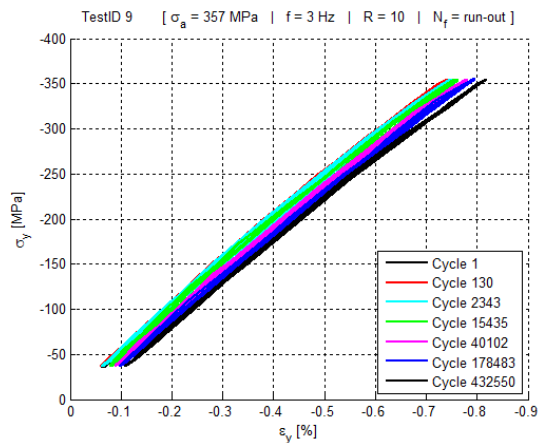


Figure 6.24: Apart from a slight shift in permanent strain, there is little difference in a $[\#(0/90)]_{24}$ laminate under 70% $\sigma_{ult,c}$ ($R = 10$)

For **low cycle fatigue**, one test indicates very little property evolution throughout fatigue life (see figures 6.25 and 6.26).

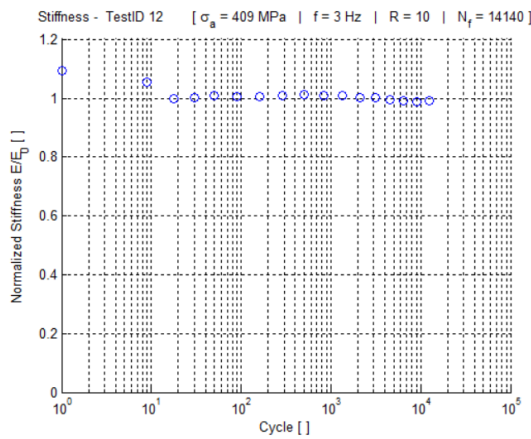


Figure 6.25: Stiffness of a [#(0/90)₂₄] laminate under 80% $\sigma_{ult,c}$ ($R = 10$) is almost constant. $E_0 = 45.2$ GPa

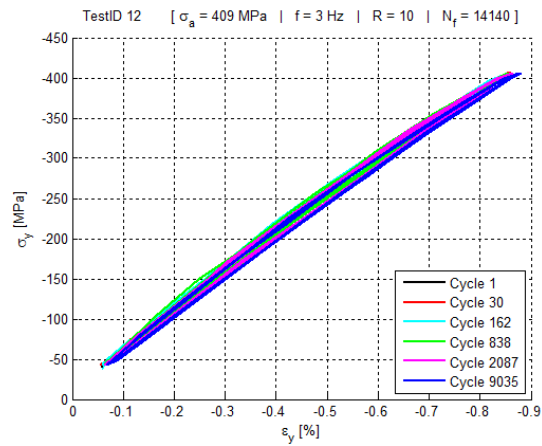


Figure 6.26: Very little difference in stress-strain behavior in a [#(0/90)₂₄] laminate under 80% $\sigma_{ult,c}$ ($R = 10$)

In the others, the effect is somewhat more pronounced. In one test (testID 15), a pronounced stiffness drop can be observed (figures 6.27 and 6.28). When observing DIC images from the side of the specimen, in these cycles it can be seen that a significant additional damage site is formed (figure 6.29). Throughout this project it became clear that a DIC analysis on the side of a specimen is helpful in detecting damage. Delaminations are visible in DIC images on the side of a specimen as zones where horizontal strain ϵ_{xx} is large and/or damage is so large that correlation fails in this region. This damage event seems to have initiated final failure. Upon investigation of DIC images on the front of this sample, it can be seen that, because of the damage at this location, zones above this delamination experience almost zero strain upon compression, as this part of this layer is incapable of handling buckling loads (figure 6.30). Logically, this part of the load is redistributed over the rest of the structure, thereby enhancing final failure.

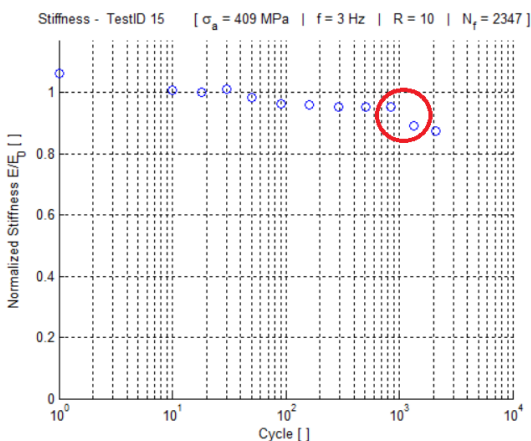


Figure 6.27: Stiffness of a [#(0/90)₂₄] laminate under 80% $\sigma_{ult,c}$ ($R = 10$) shows a drop in stiffness from 838 to 1,347 cycles. $E_0 = 47.5$ GPa

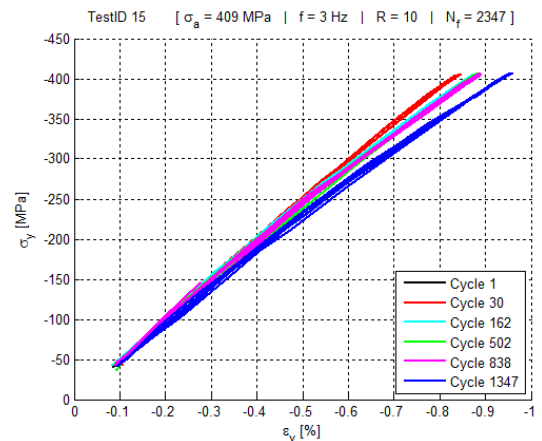


Figure 6.28: Stress-strain behavior in a [#(0/90)₂₄] laminate under 80% $\sigma_{ult,c}$ ($R = 10$). Note the drop in stiffness between 838 and 1,347 cycles.

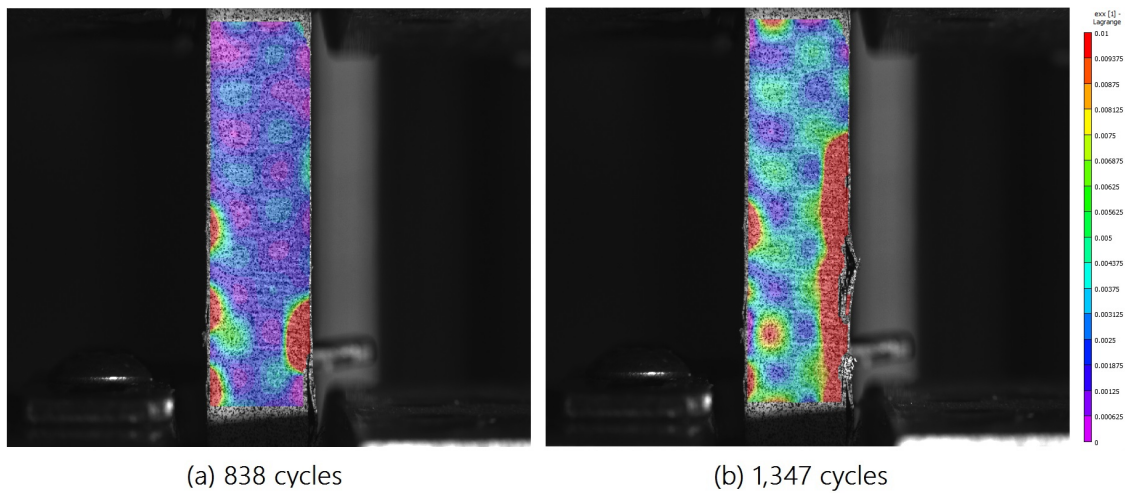


Figure 6.29: Difference in image between 838 (a) and 1,347 (b) cycles can be linked to stiffness drop in figure 6.27.

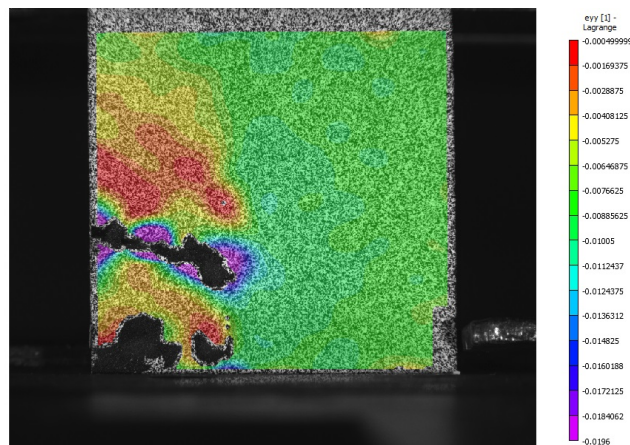


Figure 6.30: Damage in frontal layers results in redistribution of stress.

This example indicates the potential this combined DIC method holds compared to conventional methods such as extensometers, strain gages or even regular DIC. By obtaining a strain field on the side of the specimen, where free edge delaminations seem to initiate damage events, one can link these damage events to other effects occurring in the structure, hence telling a more complete story of what is happening.

6.5.3. Evolution for $[\#(0/90)]_{24}$ ($R = -1$)

T-C loading of $[\#(0/90)]_{24}$ laminates typically show little evolution in stiffness through time, little hysteresis and little permanent deformations for all loads applied.

For **high cycle fatigue** (run-outs), this can be observed in figures 6.31 and 6.32 for a test at 45% $\sigma_{ult,c}$. The figures indicate a steady but gentle stiffness reduction over time. Figures 6.34 and 6.33 indicate the abovementioned scatter in determining stiffness components for compression and tension separately. Despite scatter, figure 6.34 indicates a slightly more significant drop in stiffness in compression. Looking at DIC images reveals an explanation for this. As can be seen in figure 6.35, fatigue damage is governed by growing and joining of delaminations.

For the other run-out tests (at slightly lower loads), the stiffness decrease is much smaller, and no damage could be observed in the DIC images. This could indicate that this load is very close to the fatigue limit for this lay-up and R-ratio combination.

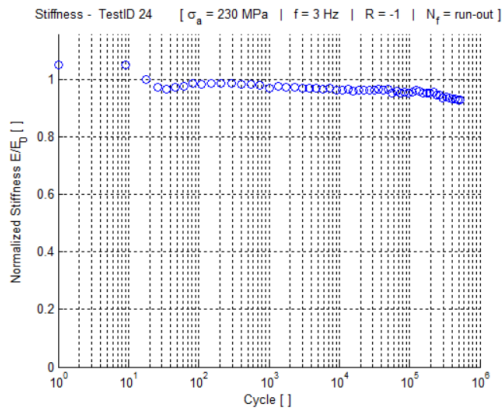


Figure 6.31: Peak-to-peak stiffness of a $[\#(0/90)]_{24}$ laminate under 45% $\sigma_{ult,c}$ ($R = -1$) indicates little evolution in stiffness over time. $E_0 = 56.1$ GPa

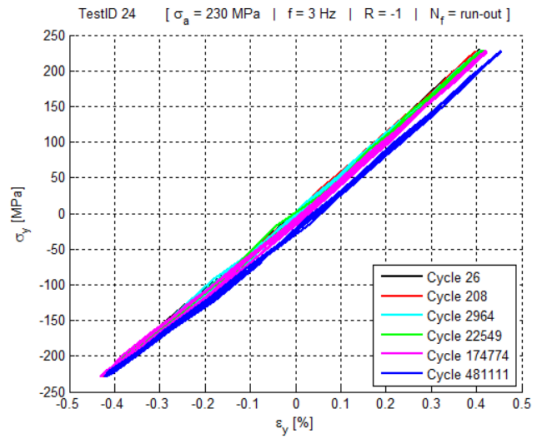


Figure 6.32: Stress-strain behavior in a $[\#(0/90)]_{24}$ laminate under 45% $\sigma_{ult,c}$ ($R = -1$).

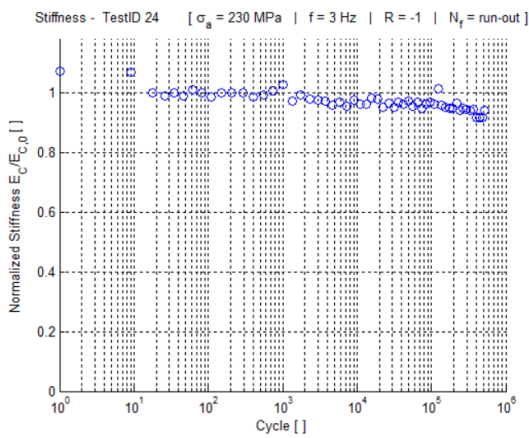


Figure 6.33: Stiffness in compression of a $[\#(0/90)]_{24}$ laminate under 45% $\sigma_{ult,c}$ ($R = -1$) shows some scatter. $E_{C,0} = 54.0$ GPa

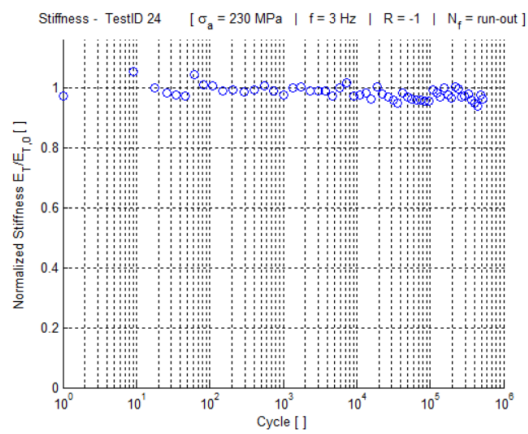


Figure 6.34: Stiffness in tension of a $[\#(0/90)]_{24}$ laminate under 45% $\sigma_{ult,c}$ ($R = -1$) shows some scatter. $E_{T,0} = 58.4$ GPa

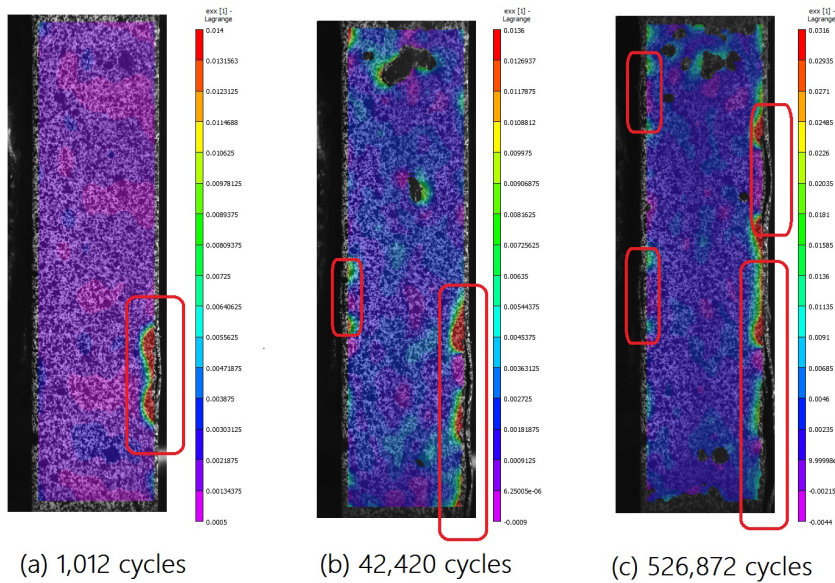


Figure 6.35: Delaminations growing over time in a $[\#(0/90)]_{24}$ laminate loaded at 45% $\sigma_{ult,c}$ ($R = -1$)

Moving onto **higher loads**, at 50% $\sigma_{ult,c}$, two tests have been performed. Both show little to no decrease in stiffness over time, except for a sudden drop near the end of life. The results for one test (testID 20) are shown in figures 6.36 and 6.37. Despite a little more scatter, stiffness components E_C and E_T show similar trends, figures 6.38 and 6.39. Investigating the side results reveals again that this drop can be linked to a significant damage event, with broken fibers and multiple layers delaminating, see figure 6.40.

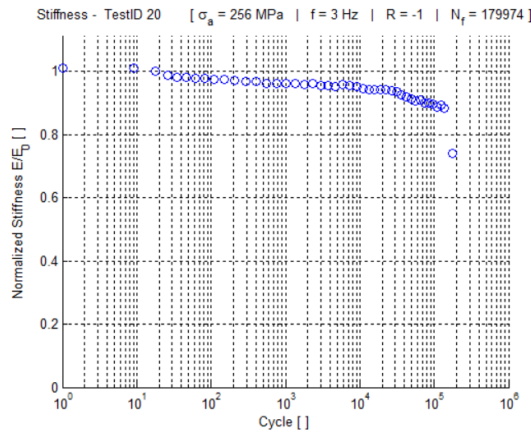


Figure 6.36: Stiffness of a $[\#(0/90)]_{24}$ laminate under 50% $\sigma_{ult,c}$ ($R = -1$) shows a steady but gentle stiffness descent, followed by a sudden drop near the end of life. $E_0 = 51.9$ GPa

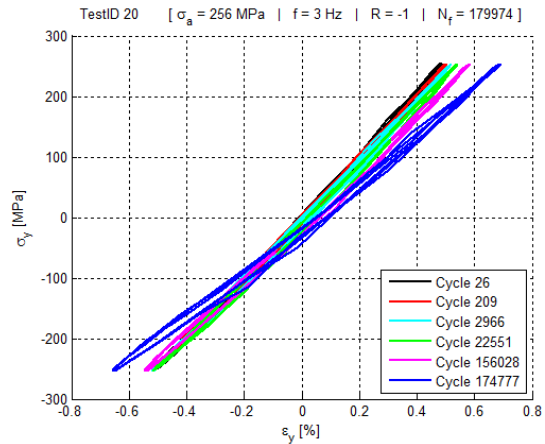


Figure 6.37: Stress-strain behavior in a $[\#(0/90)]_{24}$ laminate under 50% $\sigma_{ult,c}$ ($R = -1$).

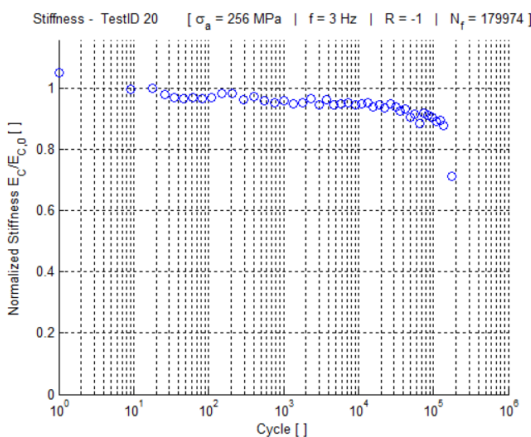


Figure 6.38: Stiffness in compression of a $[\#(0/90)]_{24}$ laminate under 50% $\sigma_{ult,c}$ ($R = -1$) indicates a slight decrease in both components, despite scatter. $E_{C,0} = 48.2$ GPa

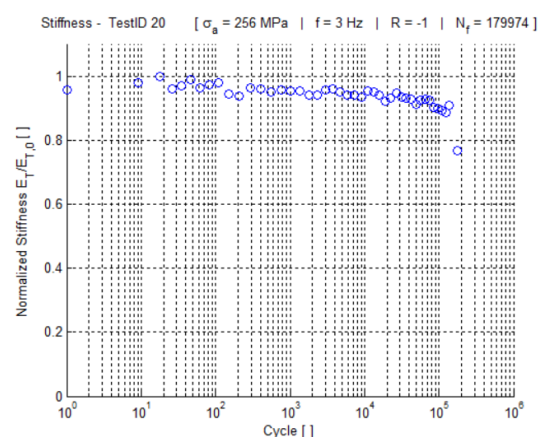


Figure 6.39: Stiffness in tension of a $[\#(0/90)]_{24}$ laminate under 50% $\sigma_{ult,c}$ ($R = -1$) indicates a slight decrease in both components, despite scatter. $E_{T,0} = 57.4$ GPa

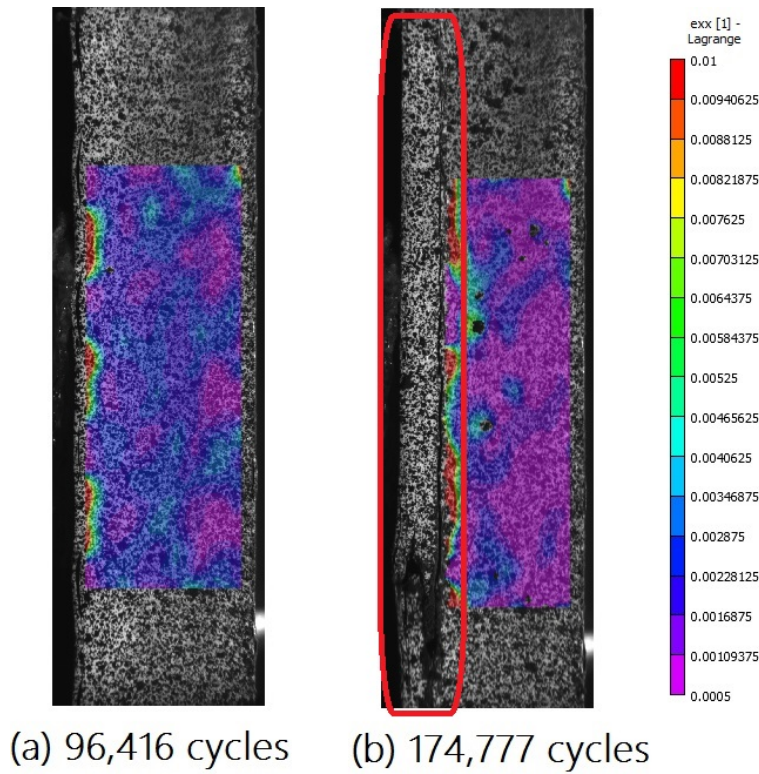


Figure 6.40: Significant damage created explains the stiffness drop in figures 6.36, 6.39 and 6.38

Similarly, the other sample at 50% $\sigma_{ult,c}$ shows sudden drop near the end of its fatigue life, see figures 6.41 and 6.42. Again this comes back as a significant damage event visible in the side view images. For this sample, a test was performed to see how imaging on the side of a specimen works when its side is sanded down to show contrast longitudinal fiber bundles by sanding down half of the specimen and covering the other half in a speckle pattern. This sanded region provides good imaging of significant damage events. However, using DIC to capture damages of smaller sizes was considered more advantageous, so this technique was discontinued hereafter.

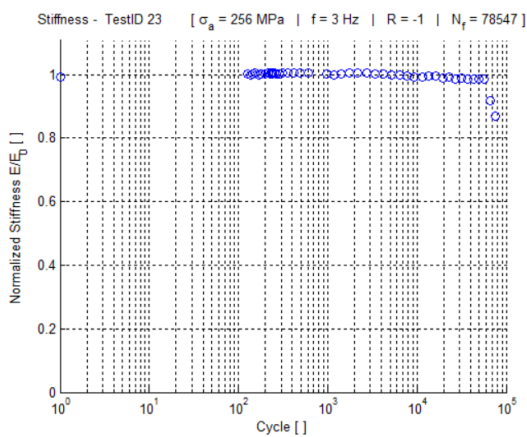


Figure 6.41: Stiffness of a $[\#(0/90)]_{24}$ laminate under 50% $\sigma_{ult,c}$ ($R = -1$) shows a steady but gentle stiffness descent, followed by a sudden drop near the end of life. $E_0 = 52.5$ GPa

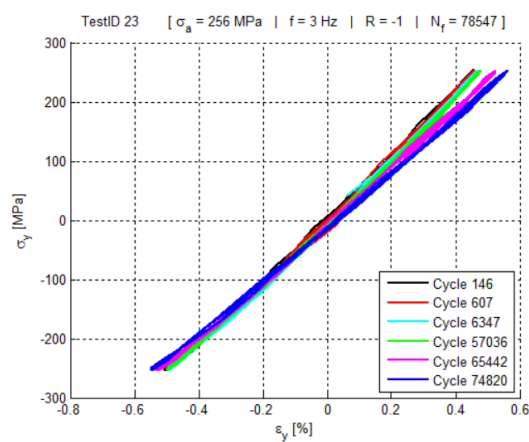


Figure 6.42: Stress-strain behavior in a $[\#(0/90)]_{24}$ laminate under 50% $\sigma_{ult,c}$ ($R = -1$).

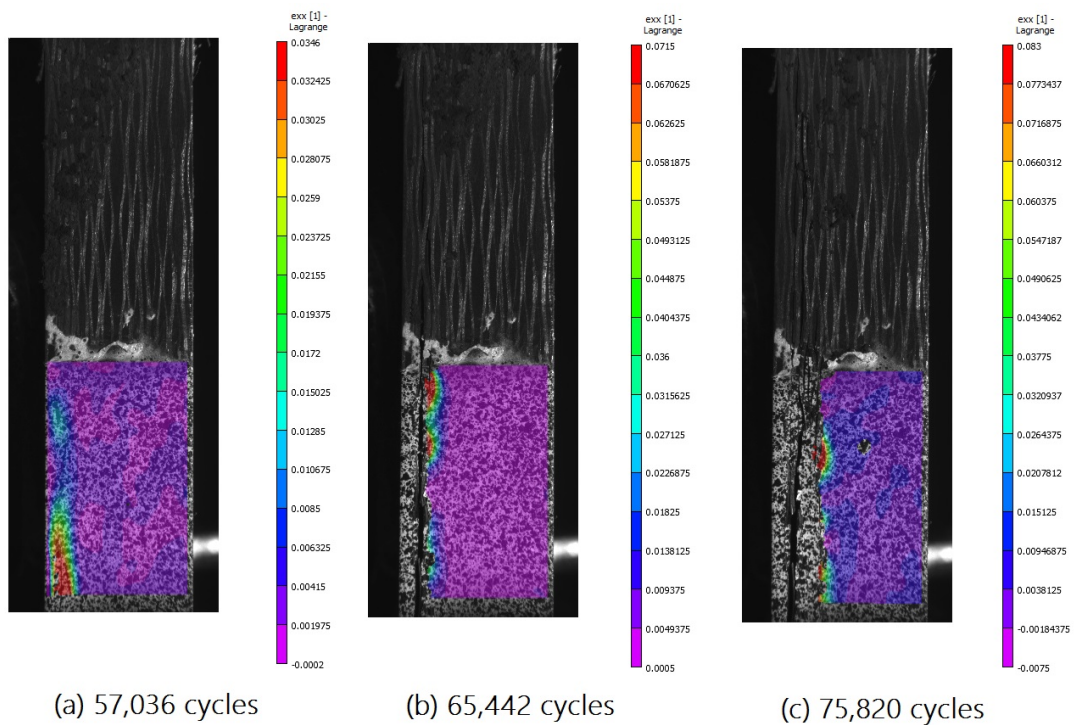


Figure 6.43: Damage evolution of the last three data points in figure 6.41

Moving onto **low cycle fatigue**, the pattern observed is always a steady stiffness which changes little over time. Near the end of life, one of two things occur. In some cases nothing was measured and the system experiences a sort of 'sudden death' phenomenon. See for example the results of one test at 60% $\sigma_{ult,c}$ (testID 19, figures 6.44 and 6.45). Other cases exhibit the effect mentioned above, where, after little to no significant evolution in stiffness, a sudden drop occurs. In all tests, when this drop is of significant size, it could be related with a significant damage event visible in images on the side camera, see for example the examples mentioned above, as well as a test with testID 17 at 80% $\sigma_{ult,c}$, see figures 6.46, 6.47 and 6.48. These damage events typically involve a couple of layers delaminating, including broken fibers in these layers, effectively rendering them useless in carrying both compressive and tensile loads. This leads to a redistribution of stress, effectively increasing the load on the remaining layers, accelerating damage creation towards final failure.

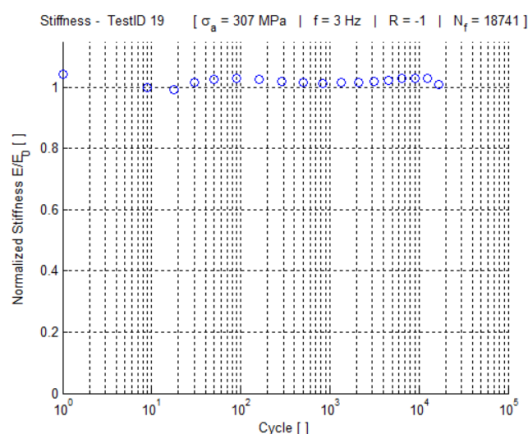


Figure 6.44: Stiffness of a $[\#(0/90)]_{24}$ laminate under 60% $\sigma_{ult,c}$ ($R = -1$) indicates a pretty much constant stiffness until final failure. $E_0 = 52.0$ GPa

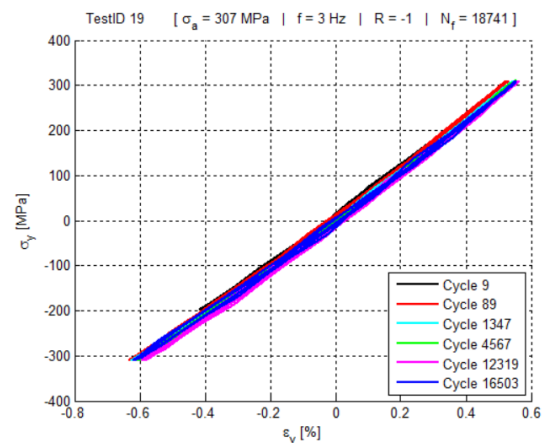


Figure 6.45: Stress-strain behavior in a $[\#(0/90)]_{24}$ laminate under 60% $\sigma_{ult,c}$ ($R = -1$) changes very little when no significant damage events take place.

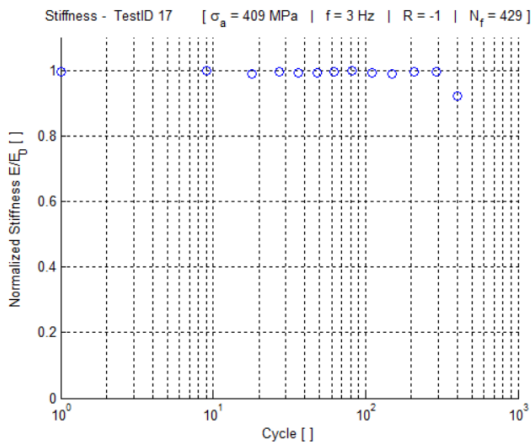


Figure 6.46: Stiffness of a [#(0/90)₂₄] laminate under 80% $\sigma_{ult,c}$ ($R = -1$) remains constant, except for a sudden drop a couple of cycles before final failure. $E_0 = 52.9$ GPa

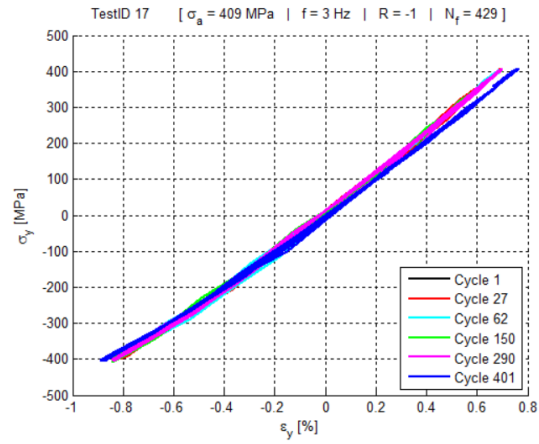


Figure 6.47: Stress-strain behavior in a [#(0/90)₂₄] laminate under 80% $\sigma_{ult,c}$ ($R = -1$). Sudden stiffness drop is measurable here as well.

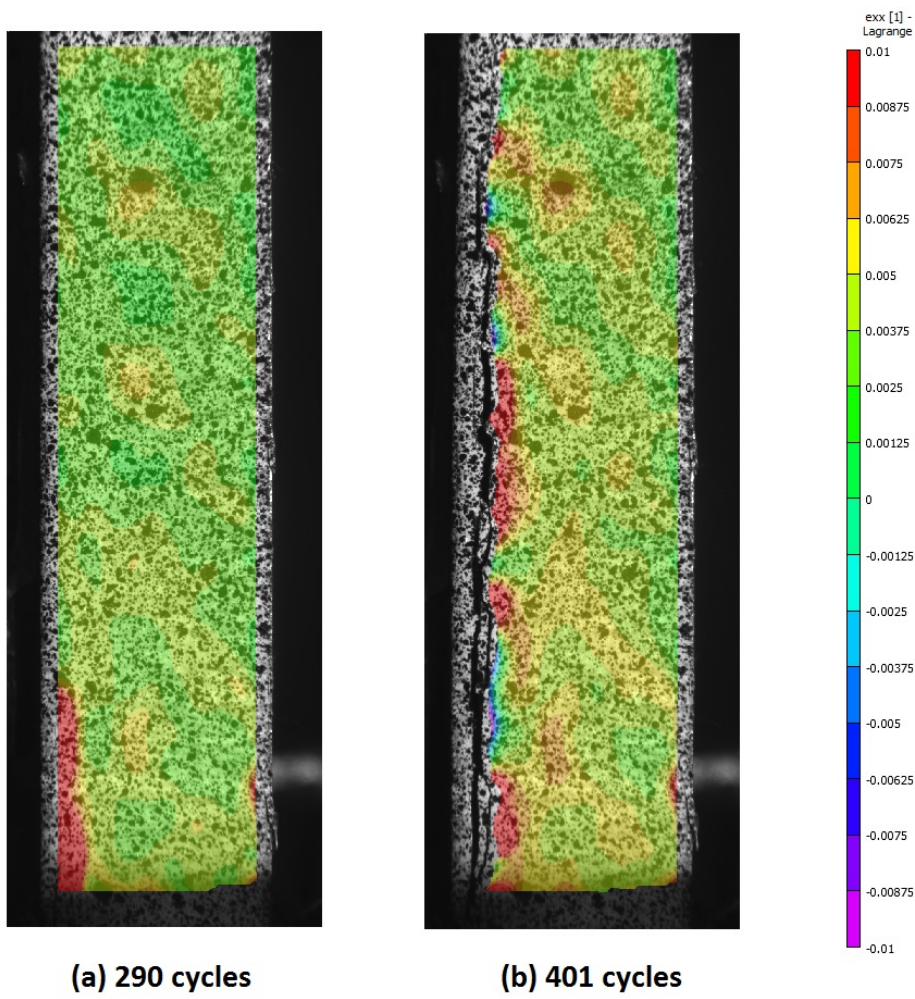


Figure 6.48: Damage evolution of the last two data points in figure 6.46

6.5.4. Evolution for $[\#(\pm 45)]_{24}$ ($R = 10$)

As can be expected, laminates with only $[\#(\pm 45)]_{24}$ layers behave entirely different compared to $[\#(0/90)]_{24}$ laminates. Comparing both laminates, it can be stated that for $[\#(\pm 45)]_{24}$ laminates, hysteresis is much more apparent, as well as stiffness evolution and permanent strain deformations. This subsection summarizes results for $[\#(\pm 45)]_{24}$ laminates tested at $R = 10$.

For **high cycle fatigue**, all tests at $60\% \sigma_{ult,c}$ resulted in run-outs. For all three of these tests, results are similar. One of them (testID 42) is shown as an example below in figures 6.49 and 6.50. Several things are noteworthy about these results. First, due to the highly non-linear behavior of $\#(\pm 45)$ layers, the first two stiffness data points clearly indicate a much higher stiffness compared to the others. A second remark is the larger hysteresis cycles here compared to images for $[\#(0/90)]_{24}$ laminates. Another effect is that stiffness rises in very first cycles of fatigue life (note logarithmic x-axis), reaches a certain peak to then initiate its decline. This effect was observed for all run-out samples, with the plateau around 4,000-8,000 cycles at $1.1-1.2 E_0$. This is clearly visible in stress-strain plot as well. Finally, these tests show a large amount of permanent strain. The result for all three is shown in figure 6.51.

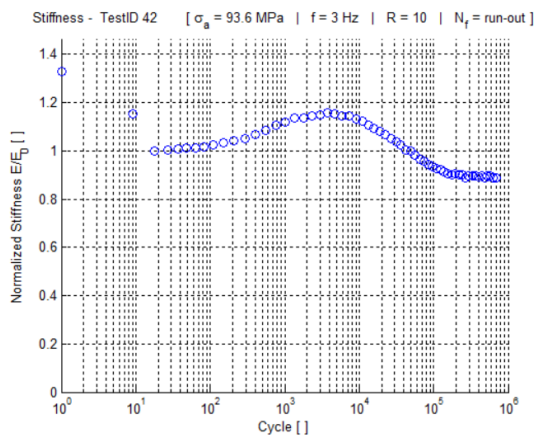


Figure 6.49: Stiffness evolution of a $[\#(\pm 45)]_{24}$ laminate under $60\% \sigma_{ult,c}$ ($R = 10$). As for all run-out samples under this loading, the stiffness seems to increase in the early stages of fatigue life before a steady decrease starts. $E_0 = 8.1$ GPa

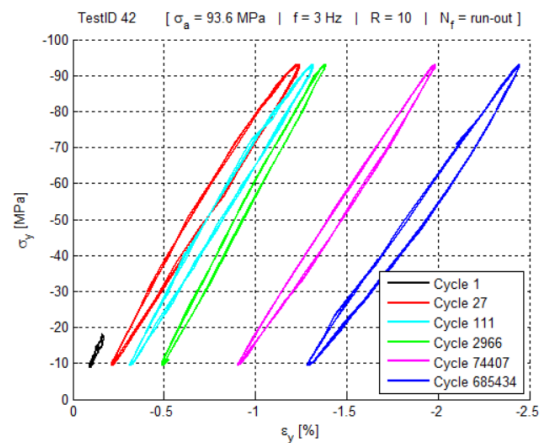


Figure 6.50: Stress-strain behavior in a $[\#(\pm 45)]_{24}$ laminate under $60\% \sigma_{ult,c}$ ($R = 10$). Note the amount of permanent strain and clear differences in stiffness.

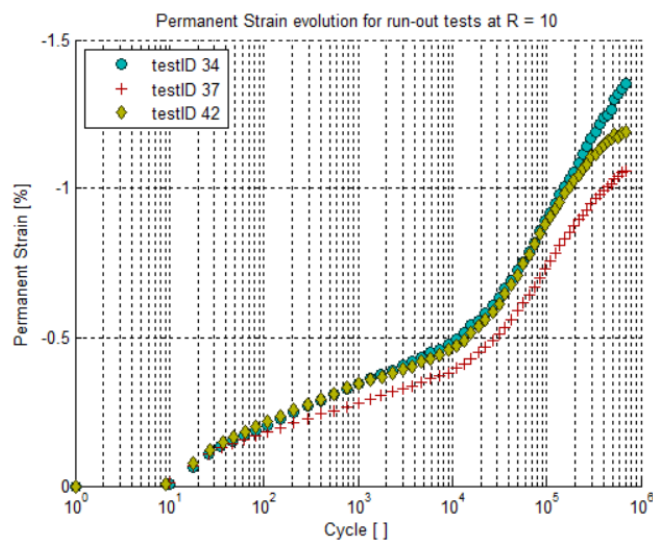


Figure 6.51: Permanent strain evolution of $[\#(\pm 45)]_{24}$ laminates under $60\% \sigma_{ult,c}$ ($R = 10$).

A similar image can be seen in for all tests at 70% $\sigma_{ult,c}$ (although one of these (testID 39) heated up 18 °C and is technically discarded). For these tests as well, we can see an initial increase of stiffness which reaches a peak early in fatigue life after which a steady stiffness decrease is observed. Unlike the run-out tests, where stiffness seemed to level out at a high number of cycles around 80-90% of its initial value, for these tests stiffness continued to drop until final failure. What is apparent for these tests as well as the run-outs, is the **correlation of stiffness with hysteresis**. When stiffness initially increases, the stress-strain plot shows less hysteresis as for the first cycles. When stiffness reduces again however, hysteresis tends to be more pronounced as well. This was noticed for all tests at 60 – 70% $\sigma_{ult,c}$. For these tests, **permanent strain** at the end of life is higher than for the run-outs at the end of the test, see figure 6.54.

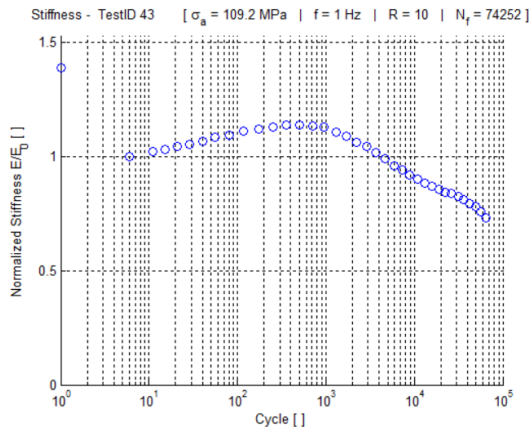


Figure 6.52: Stiffness evolution of a $[(\pm 45)]_{24}$ laminate under 70% $\sigma_{ult,c}$ ($R = 10$). As for all specimens under this loading, the stiffness seems to increase in the early stages of fatigue life before a steady decrease starts. $E_0 = 7.3$ GPa

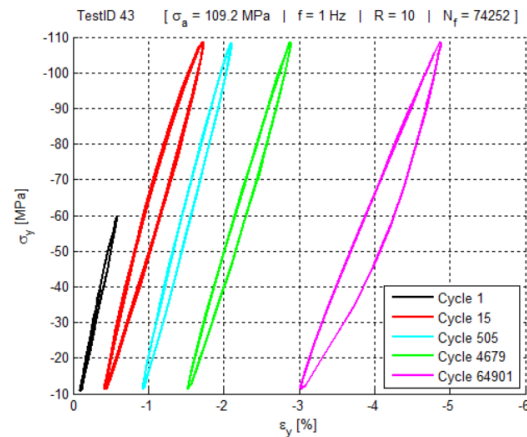


Figure 6.53: Stress-strain behavior in a $[(\pm 45)]_{24}$ laminate under 70% $\sigma_{ult,c}$ ($R = 10$). Note the amount of permanent strain and clear differences in stiffness.

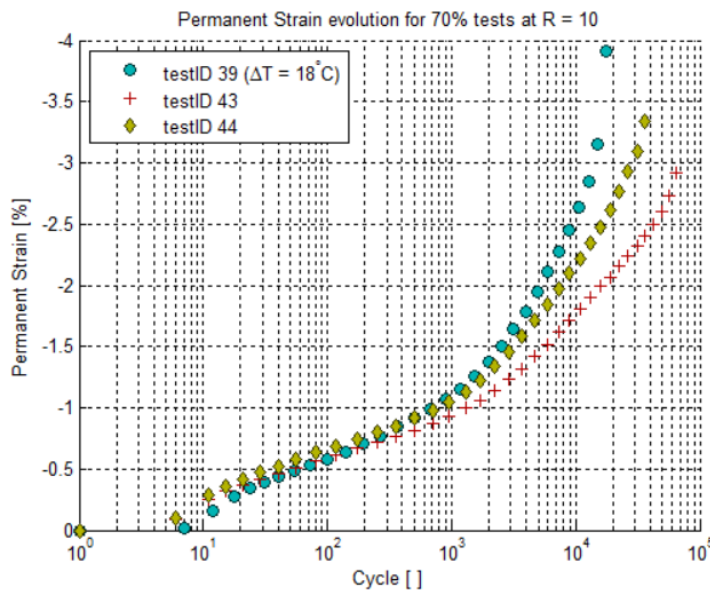


Figure 6.54: Permanent strain evolution of $[(\pm 45)]_{24}$ laminates under 70% $\sigma_{ult,c}$ ($R = 10$). Note that testID 39 is technically omitted due to heating.

At 80% $\sigma_{ult,c}$, two tests are omitted from the analysis due to heating. What can be seen in the other two samples is that stiffness is constant in the first couple of cycles before monotonically declining until final failure, see figure 6.55. Hysteresis effects and plastic deformation are very pronounced in the

beginning of fatigue life, see figure 6.56. This can be explained from the more non-linear stress-strain behaviour at higher stresses. After some initial large hysteresis and plastic deformation, hysteresis effects are less pronounced. With decreasing stiffness however, the hysteresis effect is again more pronounced. The events noticed in the analysis of the 2 omitted tests with heating over the threshold, are similar to the ones mentioned here, see appendix E Permanent strain deformation before failure are typically higher for higher loads, see figure 6.57. Heated specimens are depicted in the legend with their ΔT .

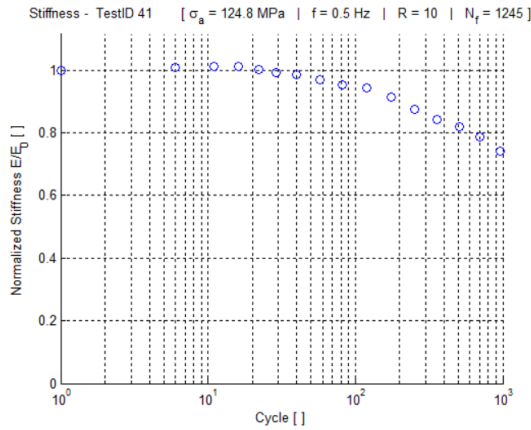


Figure 6.55: Stiffness evolution of another $[(\pm 45)_{24}]$ laminate under 80% $\sigma_{ult,c}$ ($R = 10$). $E_0 = 6.0$ GPa

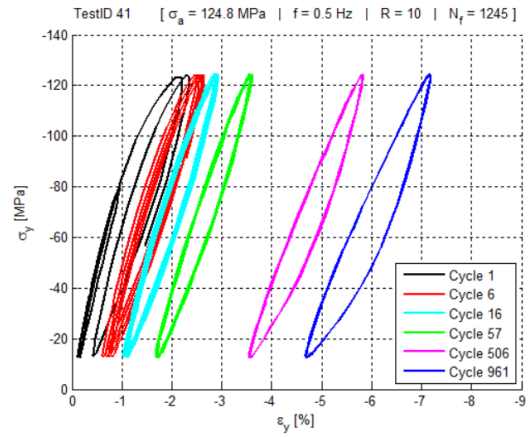


Figure 6.56: Stress-strain behavior in a $[(\pm 45)_{24}]$ laminate under 80% $\sigma_{ult,c}$ ($R = 10$).

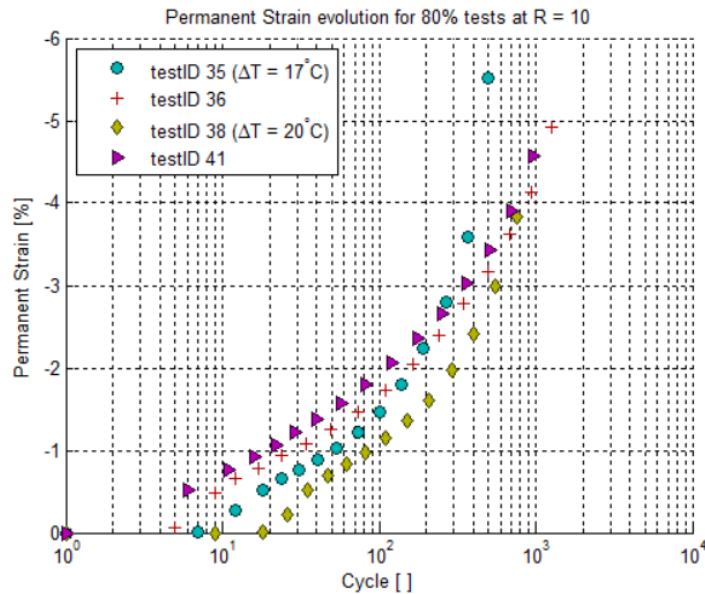


Figure 6.57: Permanent strain evolution of $[(\pm 45)_{24}]$ laminates under 80% $\sigma_{ult,c}$ ($R = 10$). Note that tests which heated up are performed at higher frequencies. This means that the first 10-15 cycles for these tests still occur in the attack time of the machine (described earlier), which is why permanent deformation is lower for these laminates.

At the edge of **low cycle fatigue** (90% $\sigma_{ult,c}$) fatigue lives are typically very short (<100) with monotonically decreasing stiffness. 4 tests at this load level have been performed, one of these heated up more than 20°C , another had issues with the speckle pattern application, rendering DIC analysis useless. In the other two, the measurements show a monotonically decreasing stiffness, with apparent permanent strain evolutions from cycle to cycle, including significant hysteresis. Permanent strain deformations are again combined in figure 6.60. A similar effect can be seen for these tests.

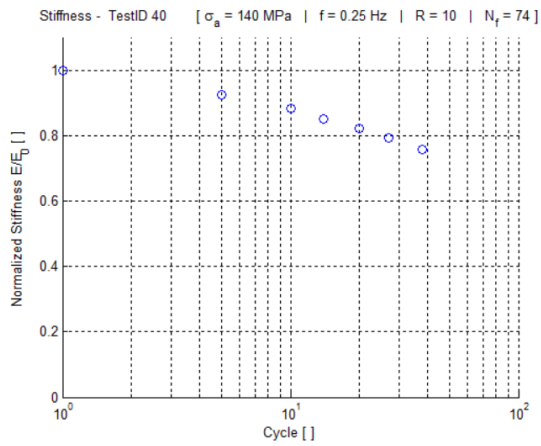


Figure 6.58: Stiffness monotonically decreases for a $[(\pm 45)_{24}]$ laminate under 90% $\sigma_{ult,c}$ ($R = 10$). $E_0 = 4.9$ GPa

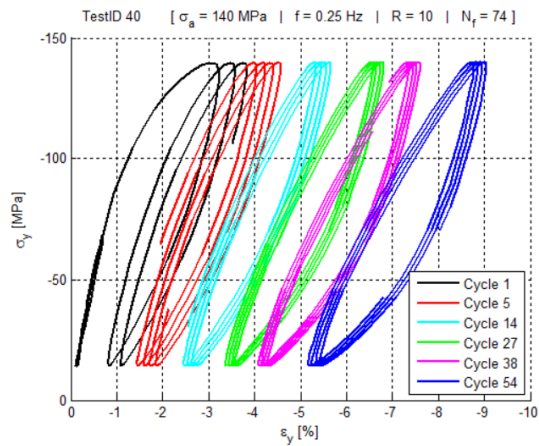


Figure 6.59: Stress-strain behavior in a $[(\pm 45)_{24}]$ laminate under 90% $\sigma_{ult,c}$ ($R = 10$).

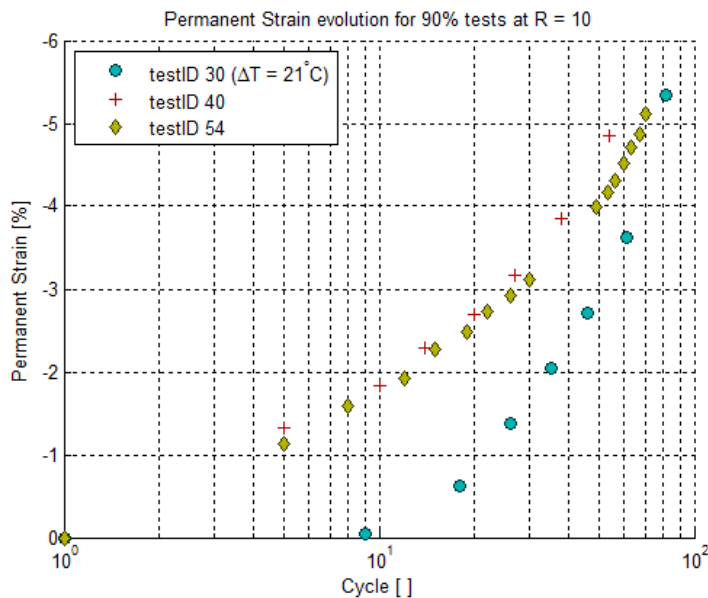


Figure 6.60: Permanent strain evolution of $[(\pm 45)_{24}]$ laminates under 90% $\sigma_{ult,c}$ ($R = 10$). Note that tests which heated up are performed at higher frequencies. This means that the first 10-15 cycles for these tests still occur in the attack time of the machine (described earlier), which is why permanent deformation is lower for these laminates.

Compared to the $[(0/90)_{24}]$ specimens, **final failure occurs without significant macroscopic damage** being visible in side DIC images, besides small delaminations, typically not larger than a unit cell of the composite weave and occurring only in the outer layers of the material. Many specimens show no macroscopically observable damage in the side DIC images before failure. When damage can be seen, it typically involves minor delaminations, see figure 6.61. One exception to this was one test at 70% $\sigma_{ult,c}$ (testID 44). This test is the only sample in which large zones with significant tensile horizontal strain can be observed upon compression. These zones grow and seem to have a significant debond between two layers potentially upon final failure, potentially initiated by damage effects which can be seen formed in figure 6.62 (a), (b) and (c).

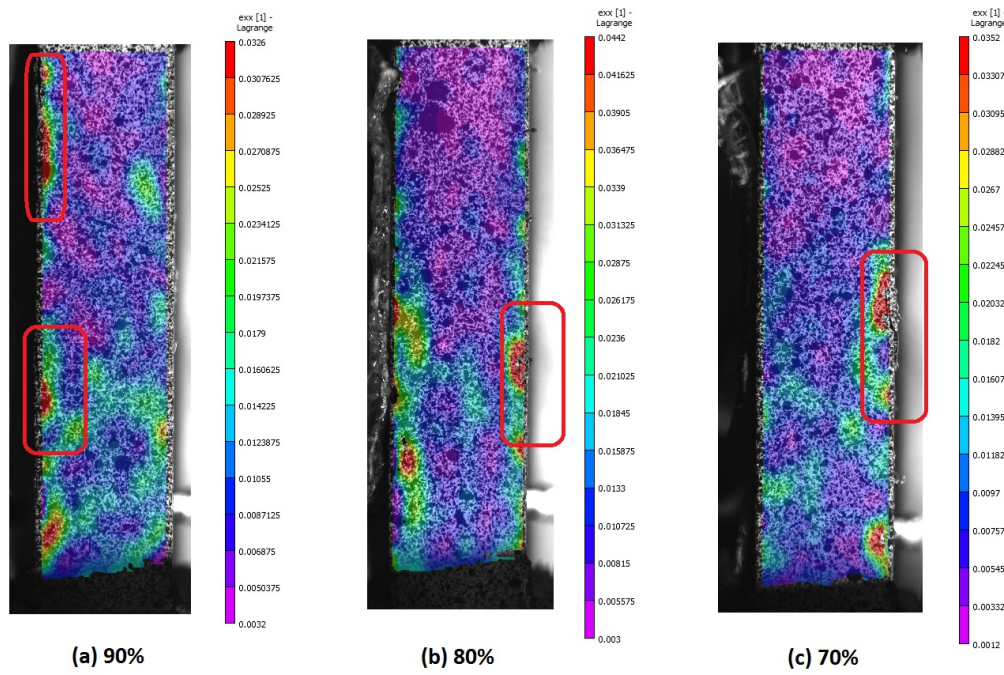


Figure 6.61: $[\#(\pm 45)]_{24}$ laminates loaded at $R = 10$ at 90%, 80%, and 70% showing only minor delaminations right before failure. (a) testID 40, (b) testID 41, (c) testID 43

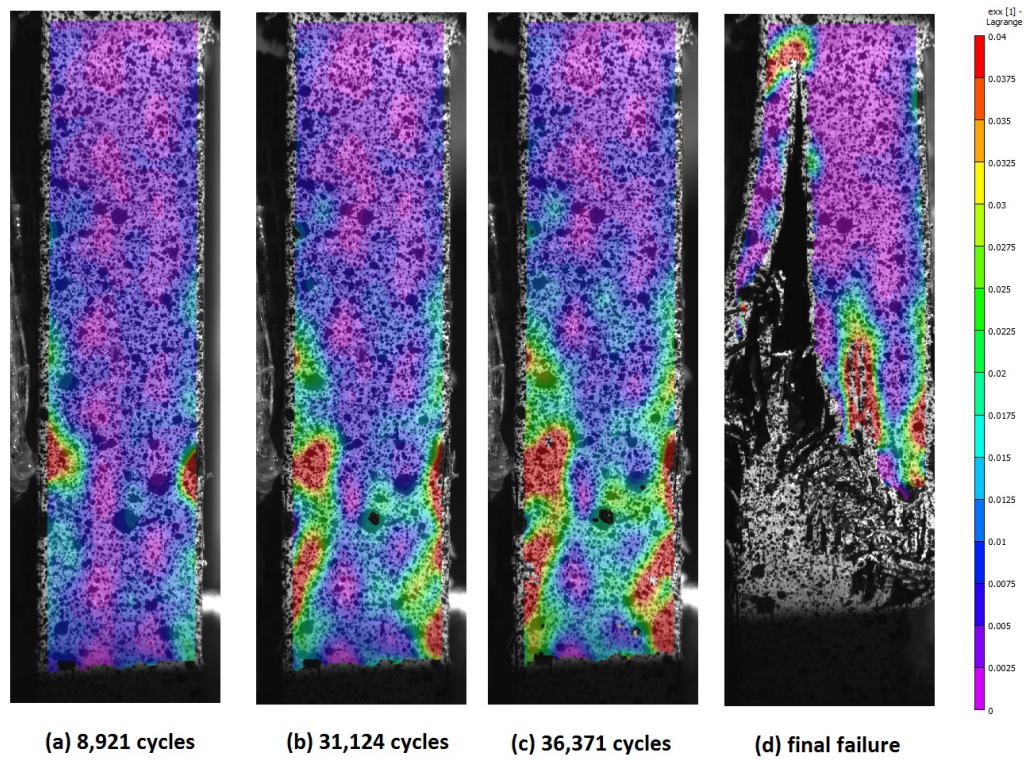


Figure 6.62: testID 44 $[\#(\pm 45)]_{24}$ under $70\% \sigma_{ult,c}$ shows macroscopic damage growing and initiating final failure.

6.5.5. Evolution for $[\#(\pm 45)]_{24}$ ($R = -1$)

The final load case is the one for $[\#(\pm 45)]_{24}$ laminates under **fully reversed loading**. It has already been substantiated that for this loading sequence, only the lower load cases have been tested (50, 40 and 30%), since the higher ones proved to be very difficult to test due to heating issues and are unlikely to be found in actual structures. This loading/lay-up combination seems to be characterized by a considerably decreasing stiffness with large hysteresis cycles towards the end of life of a specimen.

Three samples were tested at 30% $\sigma_{ult,c}$. They all survived at least 500,000 cycles before the test was ended without significant macroscopic damage. Despite the fact that samples ran out, a **clear decline in stiffness** is still visible, see an example in figures 6.63 and 6.64. Other tests have similar results. These figures show a steady decline in stiffness, which again seems to correlate with more significant hysteresis as well. This raises questions about the behavior of this load case for longer lives, and the **conclusion that this load level is the fatigue limit should not be drawn from this data**. Splitting up stiffness components shows similar trends, albeit with larger scatter (figures 6.65 and 6.66).

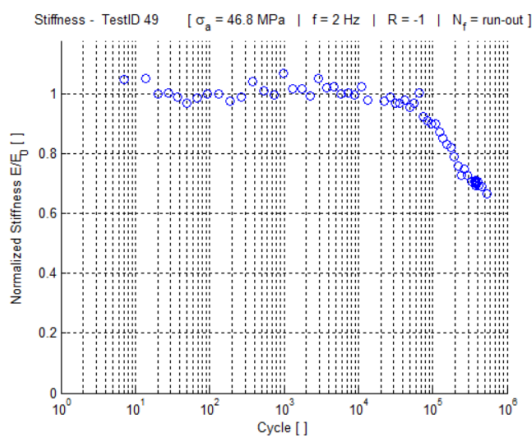


Figure 6.63: Typical stiffness evolution for a $[\#(\pm 45)]_{24}$ laminate under 30% $\sigma_{ult,c}$ ($R = -1$). Stiffness remains constant initially and then decreases. The test did however survive 685,502 cycles after which it was stopped. Stiffness shows significant scatter. $E_0 = 10.8$ GPa

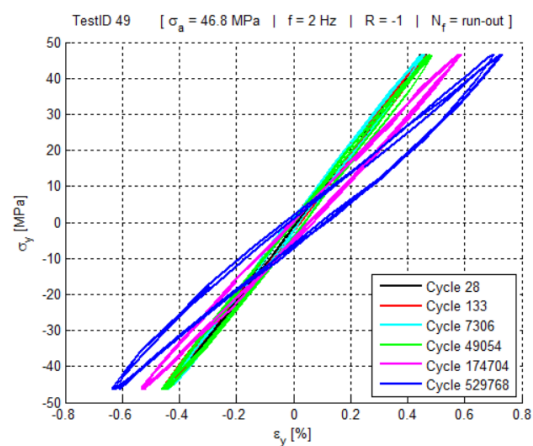


Figure 6.64: Stress-strain behavior in a $[\#(\pm 45)]_{24}$ laminate under 30% $\sigma_{ult,c}$ ($R = -1$). Stiffness decline seems to correlate with hysteresis.

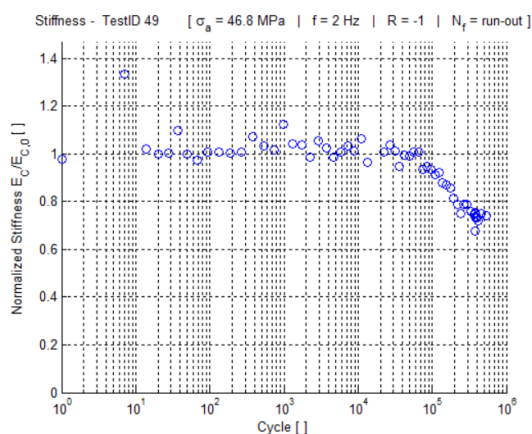


Figure 6.65: Stiffness in compression of a $[\#(\pm 45)]_{24}$ laminate under 30% $\sigma_{ult,c}$ ($R = -1$) shows some scatter. $E_{C,0} = 10.57$ GPa

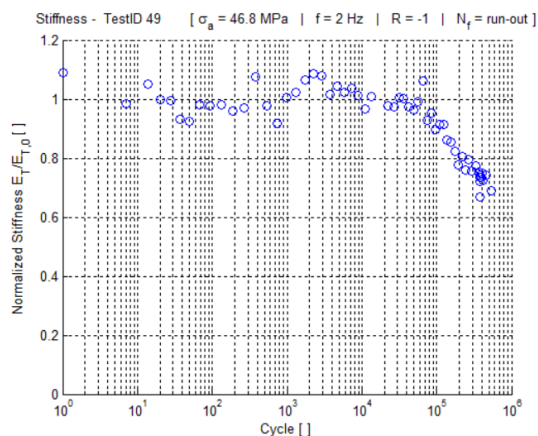


Figure 6.66: Stiffness in tension of a $[\#(\pm 45)]_{24}$ laminate under 30% $\sigma_{ult,c}$ ($R = -1$) shows some scatter. $E_{T,0} = 11.3$ GPa

Samples tested at 40 – 50% $\sigma_{ult,c}$ indicate a **significant stiffness loss before failure**. See figures 6.67 and 6.68 for 40% and 6.69 and 6.70 for 50%. This stiffness loss is again correlated to larger hysteresis cycles. What is noteworthy however, is the capability of a structure to cope with the loads. In all tests performed, a stiffness loss of 50% happened approximately near half of its fatigue life, after which it could still survive a significant amount of cycles before final failure.

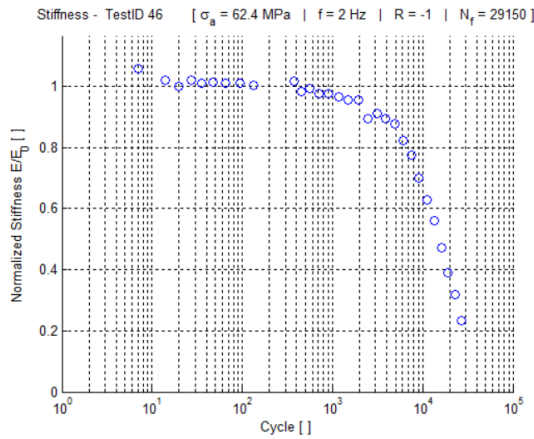


Figure 6.67: Typical stiffness evolution for a $[(\pm 45)]_{24}$ laminate under 40% $\sigma_{ult,c}$ ($R = -1$). Stiffness degrades significantly before final failure. $E_0 = 9.6$ GPa

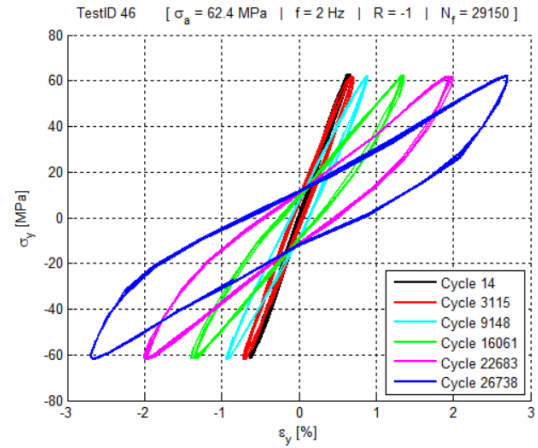


Figure 6.68: Stress-strain behavior in a $[(\pm 45)]_{24}$ laminate under 40% $\sigma_{ult,c}$ ($R = -1$). Stiffness decline seems to correlate with hysteresis.

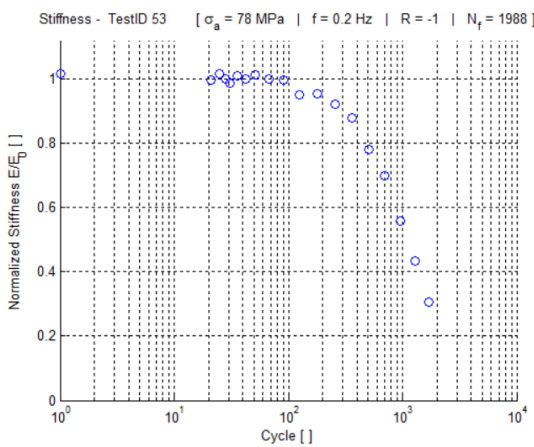


Figure 6.69: Typical stiffness evolution for a $[(\pm 45)]_{24}$ laminate under 50% $\sigma_{ult,c}$ ($R = -1$). Stiffness degrades significantly before final failure. $E_0 = 8.3$ GPa

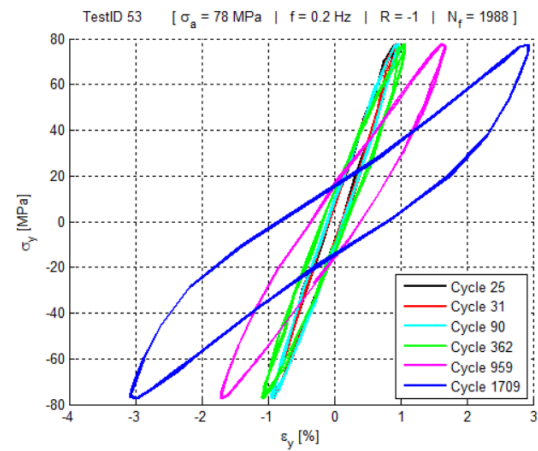


Figure 6.70: Stress-strain behavior in a $[(\pm 45)]_{24}$ laminate under 50% $\sigma_{ult,c}$ ($R = -1$). Stiffness decline seems to correlate with hysteresis.

6.6. Shear Properties

Up until this point in this thesis, material fatigue behavior is described through its properties as a laminate, with strains, stresses and stiffnesses in a coordinate system aligned with the loading direction (coordinate system (x,y) in figure 6.71) with 24 layers. However, for the $[(\pm 45)]_{24}$ lay-up, the predominant mechanism in pure compression and/or tension is **shear deformation**. For material model development, the shear properties of these materials can be of interest.

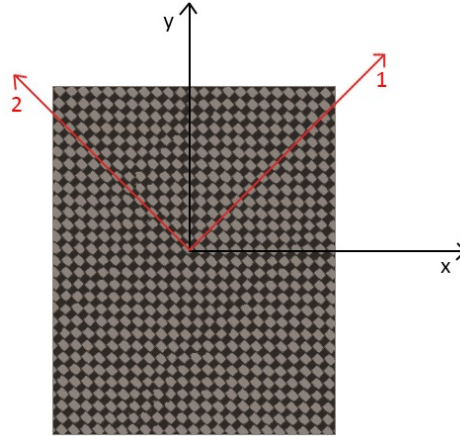


Figure 6.71: Two coordinate systems for uniaxial loading of a woven $[\#(\pm 45)]$ laminate

To obtain shear properties of a $[\#(\pm 45)]_{24}$ lay-up under uniaxial loading, stresses and strains should be rotated by 45 degrees. This does however have an important implication. When rotating this stress state to the material's frame of reference ((1,2) in figure 6.71), apart from shear stress τ_{12} one also has to take into account **two equal normal stresses** σ_1 and σ_2 . Stresses can be transformed as follows [105]:

$$\begin{bmatrix} \sigma_1 \\ \sigma_2 \\ \tau_{12} \end{bmatrix} = \begin{bmatrix} \cos^2(45^\circ) & \sin^2(45^\circ) & 2\sin(45^\circ)\cos(45^\circ) \\ \sin^2(45^\circ) & \cos^2(45^\circ) & -2\sin(45^\circ)\cos(45^\circ) \\ -\sin(45^\circ)\cos(45^\circ) & \sin(45^\circ)\cos(45^\circ) & (\cos^2(45^\circ) - \sin^2(45^\circ)) \end{bmatrix} \begin{bmatrix} \sigma_x \\ \sigma_y \\ \tau_{xy} \end{bmatrix} \quad (6.13)$$

And, by using $\sigma_x = \tau_{xy} = 0$:

$$\begin{bmatrix} \sigma_1 \\ \sigma_2 \\ \tau_{12} \end{bmatrix} = \frac{\sigma_y}{2} \begin{bmatrix} 1 \\ 1 \\ 1 \end{bmatrix} \quad (6.14)$$

It should be obvious that, in this coordinate system, the material is under a **combined state of stress**. This is similar to astm standard D3518 [65]. This standard method is used to derive in-plane shear properties from laminates by testing UD $\pm 45^\circ$ laminates under tension. In the standard, the concern for normal stresses is also assessed. In the standard it is stated that the method should provide reliable material response well into the non-linear region. For ultimate strength however, it is stated that material failure is typically initiated through transverse normal stress failure in the outer layers. However, since this research deals with fabric materials which do not possess low strengths in transverse normal direction, this effect should not be expected here.

However, in deriving shear properties from uniaxial experiments like this, caution is necessary. The first subsection further addresses considerations regarding this combined state of stress. The second subsection discusses results from this research in terms of shear strains and stresses, in which these consideration should be kept in mind.

6.6.1. Error Assessment

To further assess the error introduced from ignoring normal stresses, a typical $[\#(\pm 45)]_{24}$ laminate is analysed using classical laminated plate theory to transform stresses, apply a failure criterion and obtain an estimation of the error, assuming a balanced, symmetric lay-up.

The inputs used come partially from the manufacturer data-sheets (figure 5.2) or from tests if available:

Table 6.2: Properties used for error assessment of shear properties

$E_{1,t}$ [GPa]	60	X^t [MPa]	693
$E_{1,c}$ [GPa]	54	X^c [MPa]	513
$E_{2,t}$ [GPa]	59	Y^t [MPa]	598
$E_{2,c}$ [GPa]	52	Y^c [MPa]	496
G_{12} [GPa]	3.4	S [MPa]	92
ν_{12} []	0.04	t_{ply} [mm]	0.22

After rotation to obtain stress-strain equations of a rotated ply, the A-matrix can be calculated. From this, the mid-plane strains in response to a compressive or tensile load N_y can be calculated. These can then be used to obtain stresses in a ply, which can be transformed into stresses in ply axes. Once this is done, a failure criterion can be applied to the obtained stress values in a ply. This approach is described in [105]. Two failure criteria can be applied. The first is the 'Maximum stress failure theory', the other is the 'Tsai-Hill' criterion.

6.6.1.1. Maximum Stress Failure

For maximum stress failure, a ply is assumed to fail when one of its stress components is equal to the relevant strength. [105] For a compressive load of 184 MPa (2S), for every ply this results in:

$$\begin{cases} |\tau_{12}| = 1.000S \\ |\sigma_1| = 0.183X^c \\ |\sigma_2| = 0.182Y^c \end{cases} \quad (6.15)$$

For a tensile load of 184 MPa, this becomes:

$$\begin{cases} |\tau_{12}| = 1.000S \\ |\sigma_1| = 0.133X^t \\ |\sigma_2| = 0.153Y^t \end{cases} \quad (6.16)$$

Which indicates that shear failure is indeed the governing failure mechanism here. This can be traced back to high strength values of both normal components for woven composites. Note that this argument does not hold for UD composites, where Y^t and Y^c will be significantly lower.

6.6.1.2. Tsai-Hill Criterion

One problem in the previous criterion is that it fails to assess **interaction of failure mechanisms** in different components. Therefore, the Tsai-Hill criterion can be used to assess the error involved in ignoring normal stress components. The criterion is defined as follows [105]:

$$C_{TH} = \frac{\sigma_x^2}{X^2} - \frac{\sigma_x\sigma_y}{X^2} + \frac{\sigma_y^2}{Y^2} + \frac{\tau_{xy}^2}{S^2} \quad (6.17)$$

In which X and Y are equal to X^t or X^c and Y^t or Y^c , depending on whether σ_x and σ_y are tensile or compressive. We are interested in the influence of normal components on C_{TH} . This is done by calculating the percentage of difference between C_{TH} for the actual case, and the case where we assume that σ_x and σ_y are 0. Since all stress components are linearly related to the applied stress, the actual value of applied stress (apart from its sign) does not influence this percentage. For compression, this difference is 2.3%, for tension, the difference is 3.3%. So while these differences can be considered small, the reader should be aware of this in interpreting the results presented in the following subsection.

6.6.2. Results

Keeping in mind the error discussed above, fatigue properties in terms of shear stress, strain and stiffness can be derived for $[\#(\pm 45)]_{24}$ laminates. What can be concluded from this is that overall behavior is very similar to what is found in section 6.5. A simple example using a strain transformation from laminate to ply axes can illustrate this:

$$\begin{bmatrix} \epsilon_1 \\ \epsilon_2 \\ \gamma_{12} \end{bmatrix} = \begin{bmatrix} \cos^2(45^\circ) & \sin^2(45^\circ) & \sin(45^\circ)\cos(45^\circ) \\ \sin^2(45^\circ) & \cos^2(45^\circ) & -\sin(45^\circ)\cos(45^\circ) \\ -2\sin(45^\circ)\cos(45^\circ) & 2\sin(45^\circ)\cos(45^\circ) & (\cos^2(45^\circ) - \sin^2(45^\circ)) \end{bmatrix} \begin{bmatrix} \epsilon_x \\ \epsilon_y \\ \gamma_{xy} \end{bmatrix} \quad (6.18)$$

Now, assuming that shear deformation in laminate axes γ_{xy} is small due to symmetry gives:

$$\begin{bmatrix} \epsilon_1 \\ \epsilon_2 \\ \gamma_{12} \end{bmatrix} = \epsilon_x \begin{bmatrix} 0.5 \\ 0.5 \\ -1 \end{bmatrix} + \epsilon_y \begin{bmatrix} 0.5 \\ 0.5 \\ 1 \end{bmatrix} \quad (6.19)$$

Now, scissoring effects will introduce strains in both longitudinal and transverse directions of opposing signs. If the absolute values of these strains are in the same order of magnitude (which was found to be the case), this results in a shear strain approximately the (negative) double of ϵ_y . If we remember that from equation 6.14 shear stress τ_{12} is half of the normal stress, this explains close relation between results in (x,y) axes in terms of normal components and results in (1,2) axes in shear components.

Under the assumptions mentioned in this section, **static shear stress-strain curves** can be generated from the compression tests until failure, see figure 6.72. The shape is similar to the curves based on longitudinal stresses and strains.

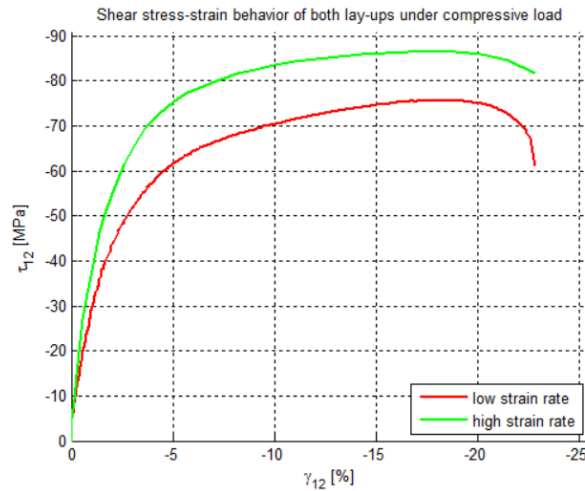


Figure 6.72: Shear stress-strain behavior for static compressive tests of $[\#(\pm 45)]_{24}$

Overall, the evolution of shear stiffness throughout a fatigue life is qualitatively similar to the longitudinal stiffness evolution. A similar conclusion can be drawn with regards to permanent shear strain compared to permanent longitudinal strain. Therefore, only a few test results are repeated below. A full overview is again present in appendix E.

6.6.2.1. Evolution for $[\#(\pm 45)]_{24}$ ($R = 10$)

When analysing the data for $R = 10$, similarities with the analysis based on laminate coordinates is striking. To show this, in this subsection, one example covered in section 6.5 for **high cycle fatigue** and an example covered for low cycle fatigue are shortly presented here again but in terms of shear coordinates. For high cycle fatigue, shear stiffness shows a similar evolution which can be

traced back in the hysteresis plots as well, see figures 6.73 and 6.74. The increase in stiffness early on in fatigue life is similar and higher/lower stiffness can again be linked somewhat with more/less hysteresis. Shear strain values are typically close to double of what is observed for longitudinal strain values.

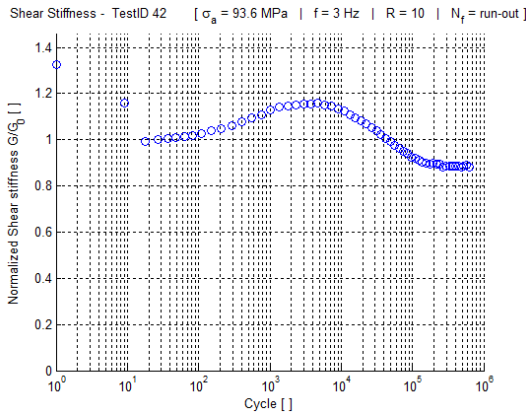


Figure 6.73: Stiffness evolution of a $[\#(\pm 45)]_{24}$ laminate under 60% $\sigma_{ult,c}$ ($R = 10$). Similarly to longitudinal stiffness, the shear stiffness seems to initially increase in the beginning of fatigue life until before a steady decline sets. $G_0 = 2.2$ GPa

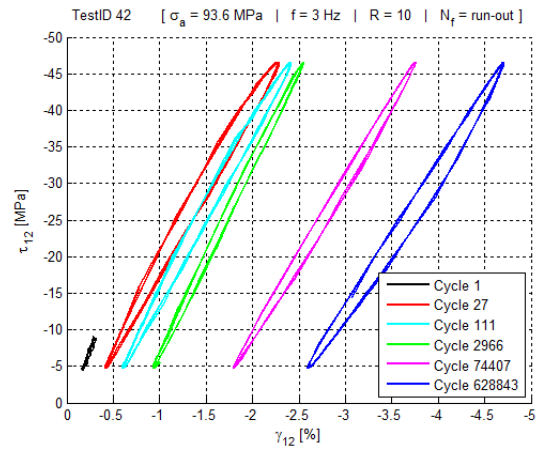


Figure 6.74: Shear stress-strain behavior in a $[\#(\pm 45)]_{24}$ laminate under 60% $\sigma_{ult,c}$ ($R = 10$). Evolution of shear stiffness and permanent strain is well visible.

An example for **low cycle fatigue** is presented here as well with similar conclusions, see figures 6.75 and 6.76. Similarly to longitudinal properties, shear properties show a steady decline in stiffness until final failure. In the first cycles of fatigue life, hysteresis and plastic deformation are clearly visible in the shear stress/strain plot. These effects continue throughout fatigue life but less pronounced.

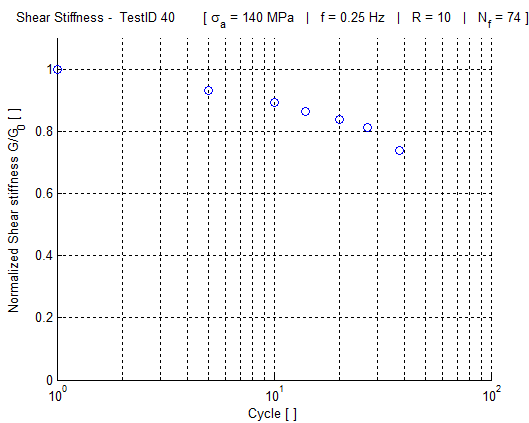


Figure 6.75: Shear Stiffness monotonically decreases for a $[\#(\pm 45)]_{24}$ laminate under 90% $\sigma_{ult,c}$ ($R = 10$). $G_0 = 1.3$ GPa

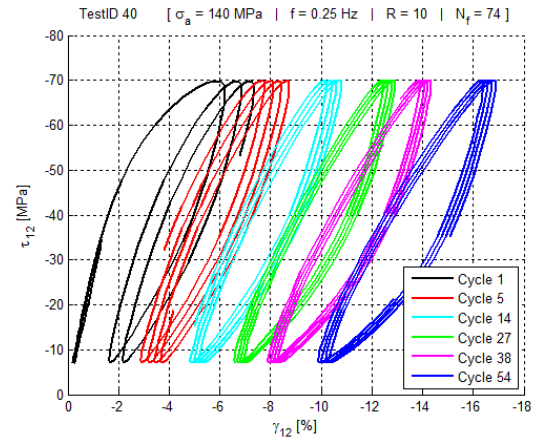


Figure 6.76: Shear stress-strain behavior in a $[\#(\pm 45)]_{24}$ laminate under 90% $\sigma_{ult,c}$ ($R = 10$) shows hysteresis and permanent shear strain deformations.

Permanent shear strain is defined in a similar manner as permanent longitudinal strain. The results for permanent shear strains are presented in figures 6.77, 6.78, 6.79 and 6.80. Heated samples are included in these graphs but they are indicated with their ΔT in the legend. What can be seen from the figures below is that permanent shear strain before failure is larger for higher applied loads, with values up to 10-11 % shear strain for low cycle fatigue. Again, the link between shear and longitudinal strain is obvious from these figures.

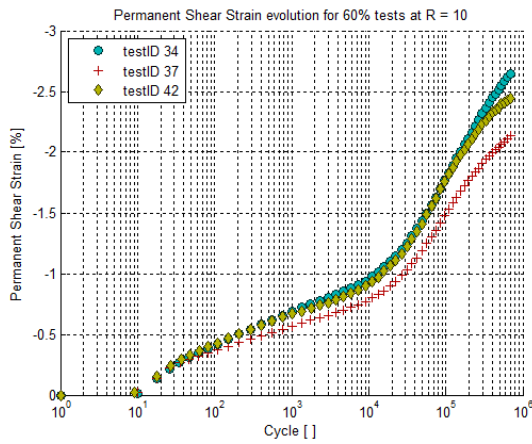


Figure 6.77: Permanent shear evolution for $[\#(\pm 45)]_{24}$ samples loaded under 60% $\sigma_{ult,c}$ ($R = 10$).

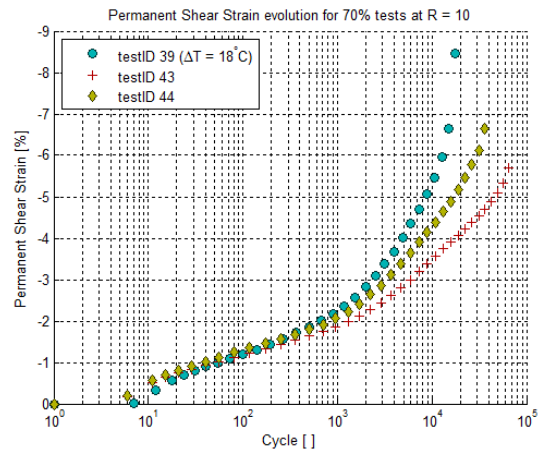


Figure 6.78: Permanent shear evolution for $[\#(\pm 45)]_{24}$ samples loaded under 70% $\sigma_{ult,c}$ ($R = 10$).

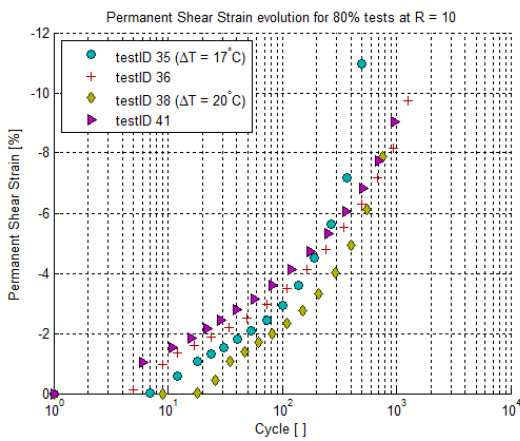


Figure 6.79: Permanent shear evolution for $[\#(\pm 45)]_{24}$ samples loaded under 80% $\sigma_{ult,c}$ ($R = 10$). Cycles normalized by fatigue life.

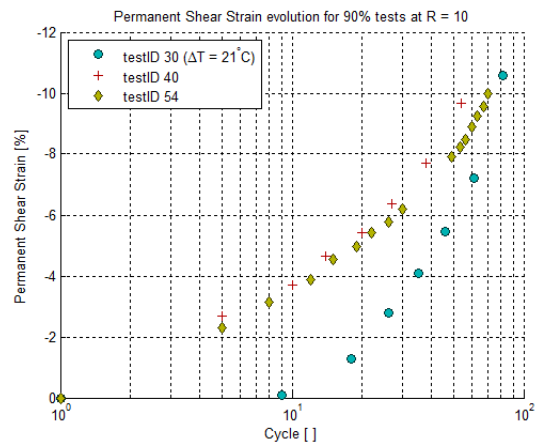


Figure 6.80: Permanent shear evolution for $[\#(\pm 45)]_{24}$ samples loaded under 90% $\sigma_{ult,c}$ ($R = 10$). Cycles normalized by fatigue life.

6.6.2.2. Evolution for $[\#(\pm 45)]_{24}$ ($R = -1$)

For $R = -1$, qualitative stress-strain behavior and stiffness evolution is very similar for shear properties. As an illustration, a single test is presented here, one at 40% $\sigma_{ult,c}$. For T-C loading of these laminates, we can define decomposed shear stiffnesses G_c and G_T (compression and tension) in a similar way as described for longitudinal stiffness in 6.19. Shear stiffness shows a constant value initially in fatigue life after which a significant decline occurs until final failure when all structural integrity is lost, see figure 6.81. Hysteresis is clearly visible in shear components as well. Decomposed shear stiffnesses show some scatter similarly to longitudinal decomposed stiffnesses. However, here as well, similar trends compared to stiffness as derived from peak to valley can be seen: an initial steady stiffness degrading rapidly until final failure.

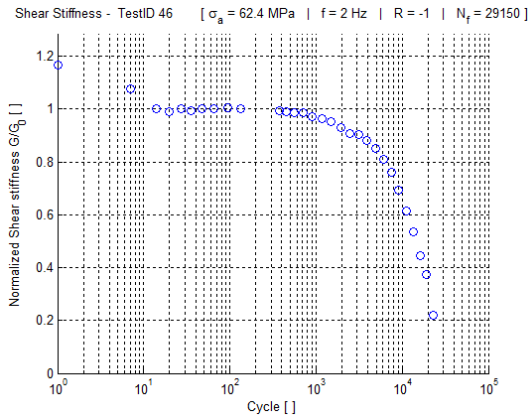


Figure 6.81: Stiffness evolution of a $[\#(\pm 45)]_{24}$ laminate under 40% $\sigma_{ult,c}$ ($R = -1$). Longitudinal stiffness remains somewhat constant for the first couple of cycles but then drops significantly until all stiffness is lost and final failure occurs. $G_0 = 2.6$ GPa

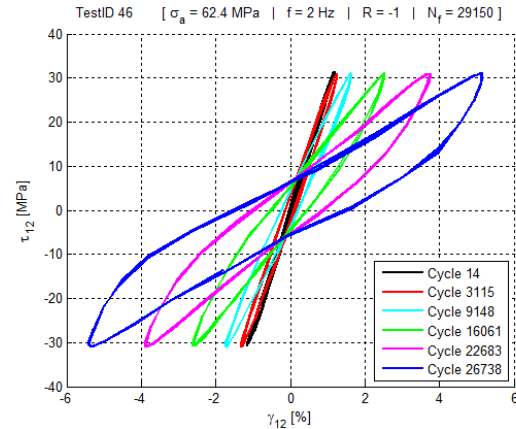


Figure 6.82: Shear stress-strain behavior in a $[\#(\pm 45)]_{24}$ laminate under 40% $\sigma_{ult,c}$ ($R = -1$). Stiffness loss is clearly visualized in the final cycles.

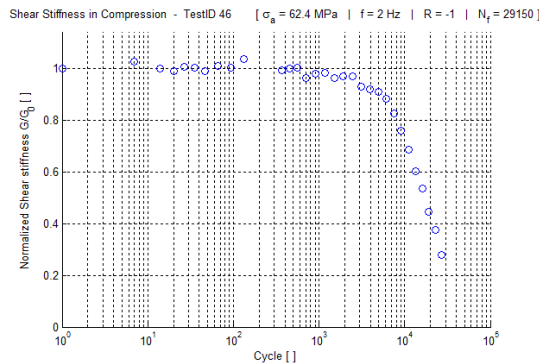


Figure 6.83: Shear stiffness component derived in unloading from a compressive cycle shows some scatter, but overall a similar trend compared to figure 6.81. $G_{C,0} = 2.7$ GPa

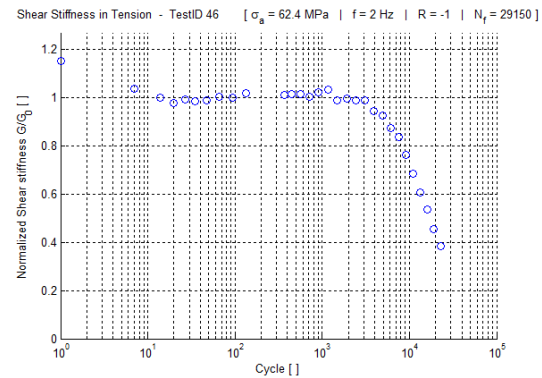


Figure 6.84: Shear stiffness component derived in unloading from a tensile cycle shows some scatter, but overall a similar trend compared to figure 6.81. $G_{T,0} = 2.7$ GPa

6.7. Microscopy

One of the goals in this research is to obtain a greater insight into the investigated fatigue behavior by obtaining as much information as possible. One additional source of information here is **microscopy**. In a typical static or fatigue test, the sample is damaged significantly (in particular because all samples fail in the compressive part of a cycle) and microscopy is less straight-forward. Therefore, several run-out tests have been investigated under a microscope to have a better view on damage mechanisms behind different lay-up/R-ratio combinations. Additionally, one $[\#(0/90)]_{24}$ sample was tested under T-C fatigue and, at different points in its fatigue life, it was taken out of the machine and its side investigated microscopically. These results are presented in this section.

6.7.1. $[\#(0/90)]_{24}$

When observing $[\#(0/90)]_{24}$ laminates under the microscope from their side, warp and weft fibers can be distinguished. Both C-C and T-C run-outs have been investigated. Some results are shown in figure 6.85 (C-C) and figures 6.86 and 6.87 (T-C). In C-C fatigue, the only damage that can be observed under a microscope are **(meta-)delaminations in the outer layers**. (a meta-delamination is a small delamination where a warp (0°) bundle debonds from one weft bundle. [21, 47]) Weft fiber bundles show no damage in all samples investigated.

This is not the case for T-C fatigue. Run-out samples of this load case show numerous **cracks in transverse fiber bundles**, see figure 6.86. To illustrate this, a stitched image of all 24 layers was investigated and cracks were indicated in as red circles. (figure 6.87). While many cracks are present, they are stopped by interfaces with warp fiber bundles.

One sample (testID 25) was tested in fatigue ($R = -1$, 60%) with one edge sanded and polished. The test was discontinued at certain times for microscopic investigation. The first two times this was done (after 51 and 501 cycles), no difference could be observed with a virgin sample. Only after $\pm 4,000$ cycles, in the tensile portion of the cycles, a 'ticking' sound started becoming apparent. The test was stopped after 4,500 cycles after which some **cracks in transverse bundles** could be observed, as well as a meta-delamination in one of the stress concentration regions, see figures 6.88 and 6.89. After 11,750 cycles, the test was stopped again and showed that this delamination had grown significantly, see figure 6.90 and that the number of cracks had grown. Unfortunately, multiple cycles of clamping/releasing the specimen combined with the loading applied caused degradation of the adhesive layer of the tab material and one of the tabs was prematurely debonded before failure.

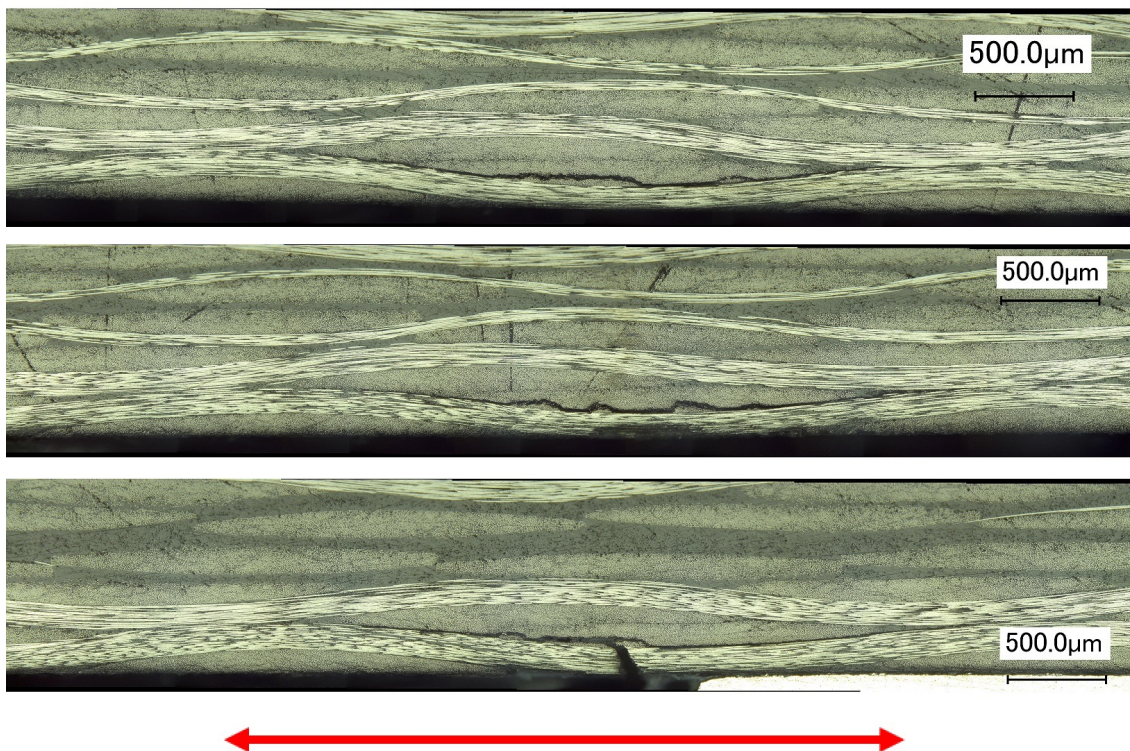


Figure 6.85: $[\#(0/90)]_{24}$ ($R = 10$) run-outs show no damage other than minor meta-delaminations. Loading direction indicated in red.

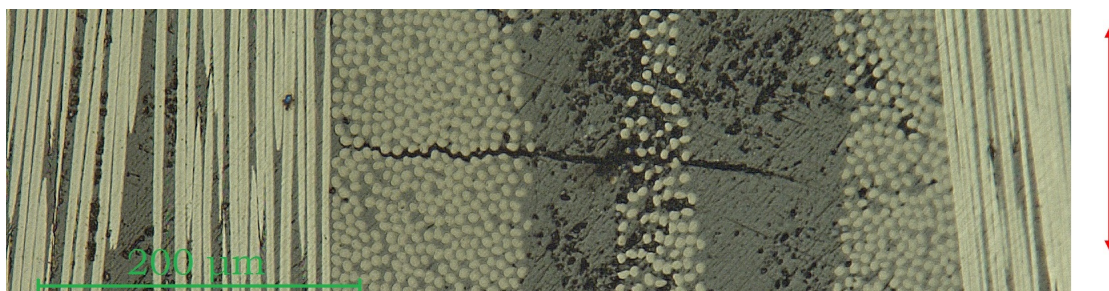


Figure 6.86: $[\#(0/90)]_{24}$ ($R = -1$) example of a crack in transverse fiber bundles. Loading direction indicated in red.

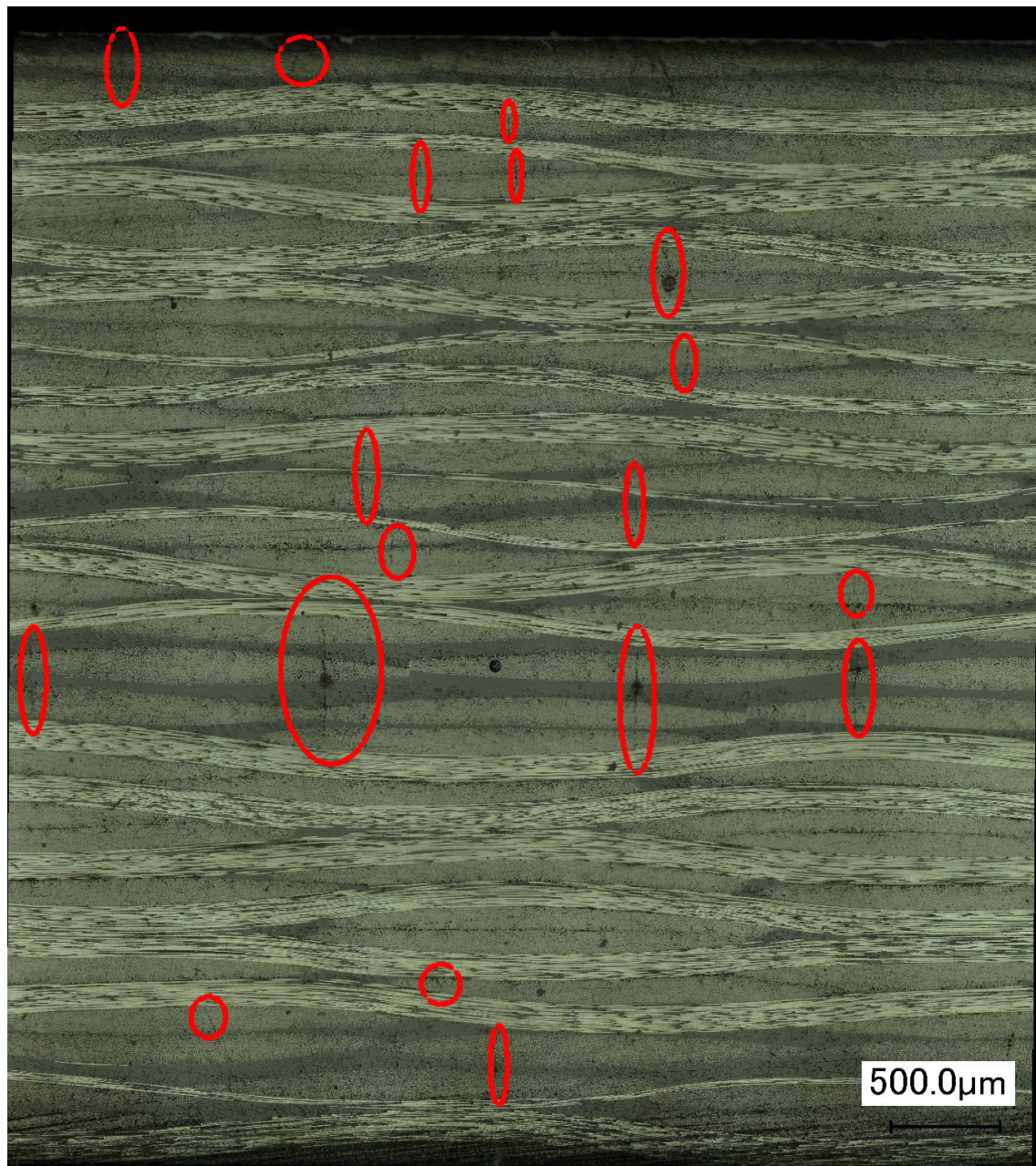


Figure 6.87: $[\#(0/90)]_{24}$ ($R = -1$) show numerous cracks in transverse fiber bundles. Loading direction indicated in red.



Figure 6.88: After 4,500 cycles, the sample showed a meta-delamination in the stress concentration region.

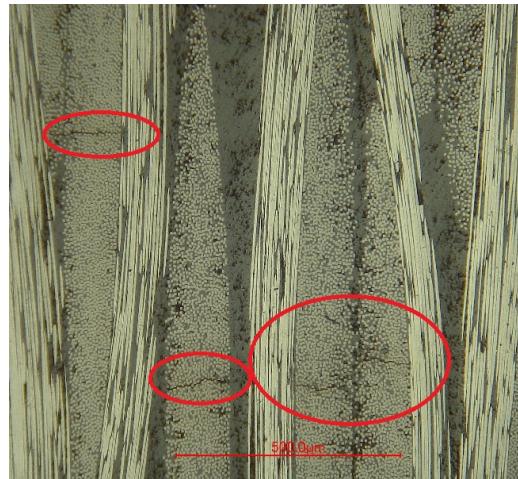


Figure 6.89: After 4,500 cycles, the sample showed the first cracks.



Figure 6.90: After 11,750 cycles, the meta-delamination has grown into a larger delamination. Note that the big spot is probably degraded matrix material which is expelled from the larger defect upon final cleaning of the polished surface.

6.7.2. $[\#(\pm 45)]_{24}$

For the $[\#(\pm 45)]_{24}$ laminates investigated under the microscope from their side, different bundles can still be well distinguished. For both R-ratios, many **transverse cracks** are visible in run-out samples. For the T-C sample investigated, this is however the only damage visible. Although these cracks are visible throughout the entire cross-section, they rarely combine to form larger damage, see figure 6.92. For the C-C run-out tested however, cracks seem to coalesce through bundle debonds at some locations, see an example in figure 6.91.



Figure 6.91: For a $[\#(\pm 45)]_{24}$ laminate under C-C loading, cracks in bundles often combine through bundle debonding.



Figure 6.92: For a $[\#(\pm 45)]_{24}$ laminate under T-C loading, many cracks can be observed

7

Evaluation of Results

This chapter serves as an evaluation of the results presented in chapter 6. Despite the relatively limited amount of tests performed over a wide range of loading conditions, some trends can be derived from these tests.

7.1. Stress-Life

A limited amount of fatigue tests have been performed for multiple load cases, results in terms of stress-life data are discussed more in depth in this section.

7.1.1. Effect of temperature

As already shortly discussed in the previous chapter, careful consideration of temperature variations throughout a fatigue test are important. For $[\#(\pm 45)]_{24}$ specimens, significant temperature increases were encountered at high frequencies and/or loads. However, when considering stress-life behavior of these tests, they did not differ much from tests at the same load level with a lower frequency. For both C-C and T-C loading, the S-N curve fit is not changed by much when these tests are included, see figures 6.12, 6.13, 6.15 and 6.16. Despite the limited amount of tests, this could indicate that the effect of temperature on fatigue performance discussed in section 6.3 is less excessive than expected.

7.1.2. Curve Shape

Literature on carbon-epoxy composites loaded under T-T loading indicates flat S-N curves with a significant amount of scatter. [8, 30, 32, 59] For C-C experiments in this work for both lay-ups, the general curve shapes are also relatively **flat**, see figure 7.1. For T-C loading, the curves are **steeper**, see figure 7.2. Quaresimin noticed similar differences between T-T and T-C loading for S-N curves of woven carbon-epoxy and concludes that the material is more sensitive to reversed loading. Note however, that the stress in this representation is the largest applied compressive stress, and that for $R = -1$, the stress amplitude is more than double of that for $R = 10$ at the same σ_a . This, combined with the fact that the mechanisms involved are completely different in nature, makes drawing conclusions on differences in R-ratio difficult.

7.1.3. Off-axis loading

Kawai et al. compare the normalized S-N behavior for on- and off-axis loading of plain woven carbon-epoxy loaded under T-T with their static strength. They note an **increased sensitivity on fatigue loading for off-axis** specimens. A similar curve for all C-C tests in this project is shown in figure 7.1. Data points are added in this graph to indicate the scatter involved in this. Nevertheless, this graph also shows an indication of a larger sensitivity on fatigue loading for $[\#(\pm 45)]_{24}$ specimens. A similar effect is seen for T-C loading, where the effect is even more pronounced, see figure 7.2

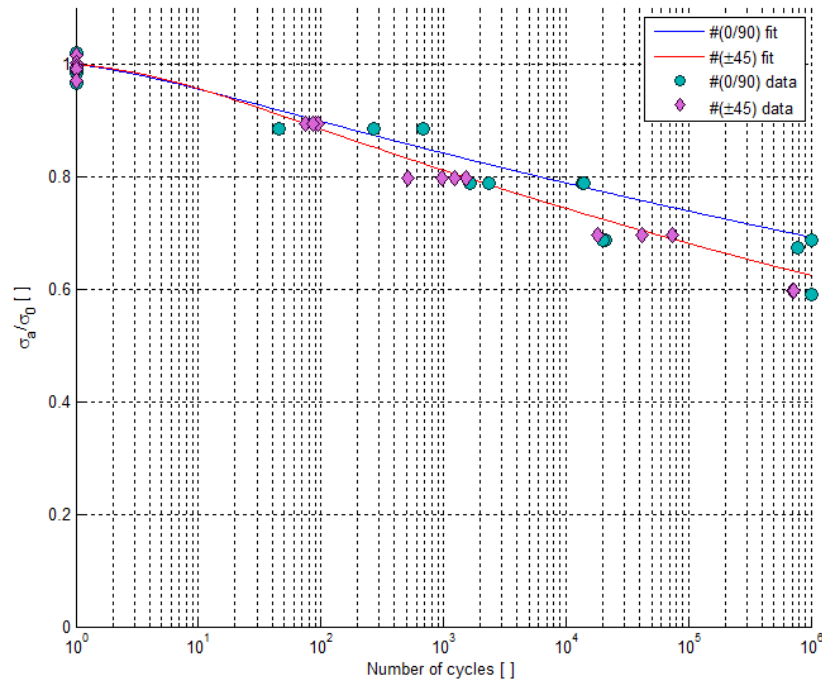


Figure 7.1: S-N curves for C-C experiments. Off-axis loading of specimens is more sensitive to fatigue.

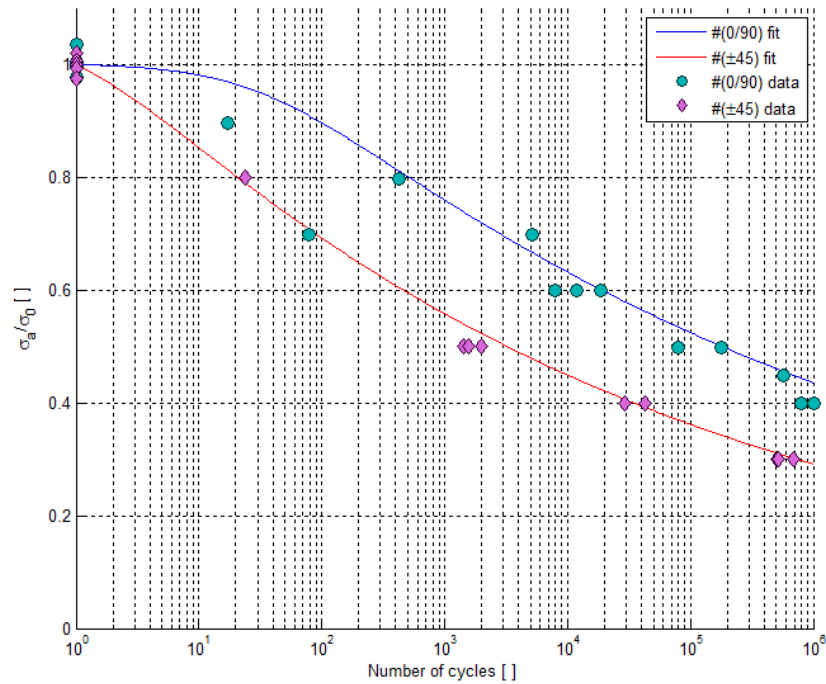


Figure 7.2: S-N curves for T-C experiments. Off-axis loading of specimens is more sensitive to fatigue here as well.

7.1.4. Effect of Frequency

It should be stressed once more that S-N data for $[\#(\pm 45)]_{24}$ originates from tests at **different frequencies**, as indicated in figures 6.11 and 6.14. In section 6.2, it was shown that this laminate's static compressive strength is dependent on loading rate. Fatigue testing at a different frequency means

testing at a different loading rate as well. For low cycle fatigue tests, the frequency was typically lowered. For a constant test frequency, the S-N curves for $[\#(\pm 45)]_{24}$ can therefore be expected to be more steep.

7.1.5. Scatter

In terms of **scatter**, all data sets show an amount of variability which is similar to what can be found in literature. Inherent material imperfections, random stacking of weaves and minor errors introduced in specimen production explain unavoidable variations among specimens. Note that all tests have been performed by a single operator, on a single machine, using a single specimen design,... which can be expected to have reduced scatter.

7.2. Property Evolution and Stress-Strain Behavior

During the fatigue tests, DIC was used to assess the evolution of (shear) stiffness and (shear) stress-strain behavior of the experiments. In this work, experiments have been carried out for two lay-ups, under two different R-ratios and at different load levels. This results in a wide range over which experiments have been carried out. On the other hand, this also means that few repetitions have been performed for each case. One has to be careful in drawing conclusions from a small number of tests. However, some trends are still observed in the data. The results are discussed here. To show reproducibility of the tests, stiffness evolutions for load levels for which more than one fatigue test have been performed are presented in appendix E.

7.2.1. $[\#(0/90)]_{24}$

The overall conclusion for these laminates is that **stiffness remains more or less constant until final failure occurs**. Unless significant damage events take place which compromise the integrity of the structure, the effect on stiffness, regardless of the definition of stiffness (for T-C), is minor. While literature sources do report a significant effect with 3 distinct zones in the stiffness evolution for T-T loading of woven carbon fiber composites. [10, 11, 55] It seems that for loading along the fibers for this material, C-C or T-C fatigue does not exhibit this behaviour significantly. This is similar to conclusions from Pandita et al. [5], who reported little effect on stiffness for T-T loading of plain woven glass-epoxy composites, until at the end of life. For both loading types, **hysteresis** is minimal.

In chapter 2, it was noted that for woven composites under T-T loading along the fibers, damage starts early on in fatigue life with cracking of transverse fiber bundles. [21, 44, 47] A microscopic investigation of the free edge of a C-C run-out specimen shows minor **meta-delaminations**, but no cracks in transverse fiber bundles. For T-C loading, micrographs show that microcracks in transverse fiber bundles only arose after a few thousand cycles in a specimen loaded at 60% $\sigma_{ult,c}$. Run-outs also show cracks in transverse fiber bundles and some meta-delaminations. Final failure for all specimens occurred in the compressive part of a cycle.

Permanent strain deformations are also very minor and cannot be considered significant.

7.2.2. $[\#(\pm 45)]_{24}$

For $[\#(\pm 45)]_{24}$ laminates, the nature of the loading and damage creation is different, which also shows in the test results. Unlike the $[\#(0/90)]_{24}$ laminates, a **significant evolution of stiffness and clear hysteresis behavior** was observed for both R-ratios, at all load levels considered. This is similar to the conclusions for T-T loading in [5]. Microscopic investigations of a run-out for C-C and one for T-C loading reveal microcracks in fiber bundles for both cases.

7.2.2.1. Stiffness Evolution for C-C loading

For C-C loading, $[\#(\pm 45)]_{24}$ laminates show an **initial increase in (shear) stiffness, followed by a steady decrease**. Transverse stiffness (based on transverse strain ϵ_x and applied stress σ_y) shows the same effect. For run-out tests, this decrease seems to flatten out, for others (shear) stiffness

degrades below 60-80% of its initial value before final failure. An explanation for this effect could not be found in literature but one could imagine a sort of scissoring effect of the fibers, where they can move easily for small strains but sort of 'interlock' at higher strains, where movement becomes more difficult. After this, transverse cracks in fiber bundles and potentially other damage types could result in a decreasing stiffness. This could be investigated more in depth to be able to draw conclusions from it, see recommendations in chapter 8.

In chapter 2, the notion of **3 regions in the stiffness evolution** graph for T-T loading was mentioned. The graphs presented for woven carbon fabric (figures 2.11, 2.12 and 2.13) indicate three regions of fatigue life with an initial decrease in stiffness followed by a smaller effect and then followed by a final drop before final failure. Note however that these graphs use linear x-axes. Plotting results from these C-C experiments and normalized to the peak stiffness for $[\#(\pm 45)]_{24}$ shows a similar effect. Figure 7.3 shows that the stiffness drop becomes less severe for all load levels considered. To capture the drop near the end of a fatigue life, this system is not very efficient since time intervals between measurements increase to limit data size and post-processing effort. The interval near the end of a fatigue life is too large to effectively capture this.

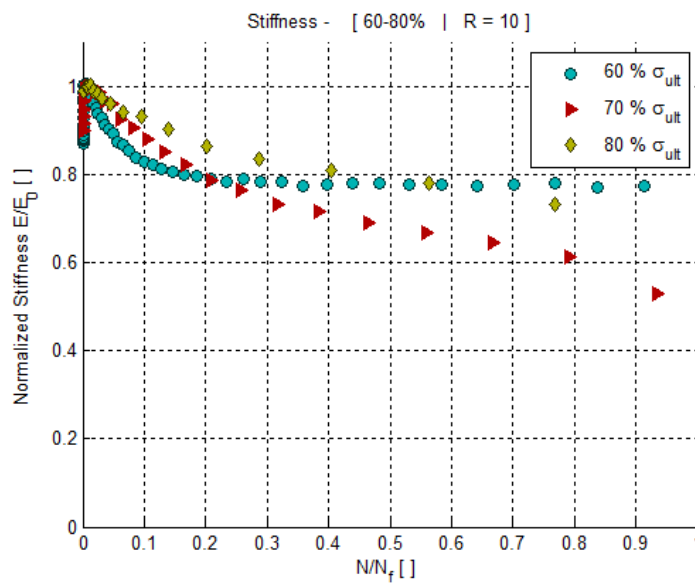


Figure 7.3: Normalizing stiffness evolution over fatigue life for C-C loading shows that evolution tends to be more severe in the initial stages of fatigue life and then drops somewhat less. Note that the 60% result is normalized to 725,000 cycles, after which the test was stopped and it was considered a run-out.

7.2.2.2. Stiffness Evolution for T-C

For T-C loading, $[\#(\pm 45)]_{24}$ laminates tested at 30-50% all show a significant (shear) stiffness degradation until the end of life (or being considered a run-out), which continues to drop until almost zero stiffness is reached. Typically, when the stiffness has degraded until 50% of its original value, the specimen is only halfway through its fatigue life. To compare the stiffness evolution to the literature references for T-T loading, the longitudinal stiffness evolution for all samples which did not run out, normalized to its fatigue life is presented in figure 7.4. Three regions in the fatigue life cannot be clearly distinguished. The **decrease in stiffness is almost linear throughout its fatigue life**, and the specimen fails when the stiffness has degraded to a point around 10% for all specimens. A linear regression with fixed intercept of the data is included in the figure as well. This equation becomes:

$$\frac{E}{E_0} = -0.9066 \frac{N}{N_f} + 1 \quad (7.1)$$

with $R^2 = 0.9709$.

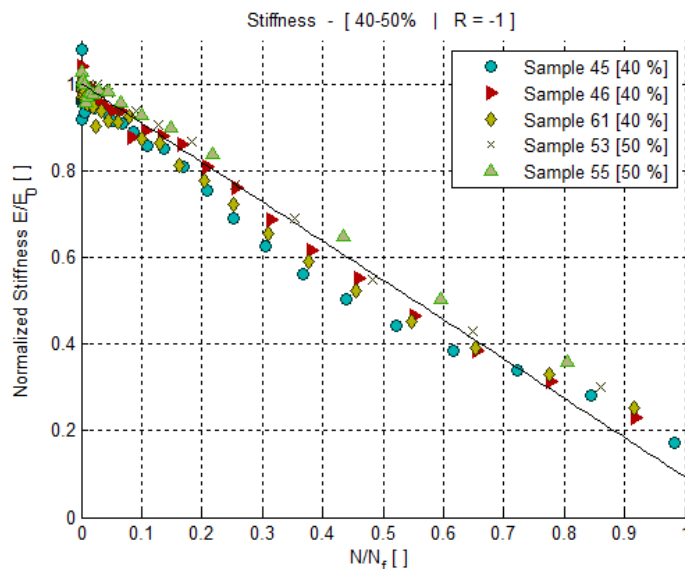


Figure 7.4: Stiffness degradation under T-C fatigue is almost linear throughout a specimens fatigue life until it reaches a value where the integrity of the structure is lost.

For the run-outs at 30%, stiffness had degraded significantly and there was no indication that it was flattening out. Therefore, conclusions about a **fatigue limit** should not be drawn.

7.2.2.3. Stress-Strain

Stress-strain behavior for this laminate shows a number of trends. First of all, for both R-ratios, **Hysteresis** loops are much more clearly observed than for $[\#(0/90)]_{24}$ laminates. Secondly, hysteresis loops are more significant when stiffness is lower, and become very significant near the end of life of T-C laminates, where stiffness is almost reduced down to zero. This same conclusion was drawn by Giancane et al. for GFRP composites under T-T fatigue. When the applied loads are larger, hysteresis is more obvious as well.

For C-C loading, **permanent (shear) strain evolution** is significant. In the first cycles, permanent (shear) strains grow significantly and continues to grow at a decreasing rate. Plasticity in the first cycles is clearly visible, in particular at higher loads. Permanent shear strain at the end of fatigue life is larger for high loads which, on the static stress-strain curve are well in the plastic region. For T-C loading, hysteresis grows and stiffness drops, however, hysteresis loops seem to remain centered around approximately 0 strain in all cases considered, due to the reversed loading.

8

Conclusions and Recommendations

This chapter summarises the most important conclusions from the experimental work performed in this thesis as well as recommendations for further work on this topic. The main goal for this master thesis was to develop a test set-up capable of characterisation of woven carbon-epoxy material loaded under compression-compression (C-C) or tension-compression (T-C) fatigue. Results from these experiments reveal information on the stress-life (S-N) behavior of this material, as well as evolution of properties such as (shear) stiffness and permanent (shear) strain, combined with an assessment of damage events at the free edge. A better understanding of the evolution of these properties can lead to improved predictive modeling which could in turn result in more efficient designs. This chapter combines conclusions from this work, and presents possible recommendations for further work.

8.1. Conclusions

A **literature study** (chapter 2) concludes that fatigue failure of woven composite materials is a complex phenomenon. Modeling is difficult due to the complexity of the damage and multiple scales on which it occurs. Some potentially promising models lack experimental input since performing these experiments is difficult and expensive. Experimental efforts are often limited to T-T loading, and where results are presented, they are mainly based on S-N curve generation. No standards exist for the measurement of the evolution of properties such as (shear) stiffness and permanent (shear) strain, even though these could be valuable in modeling. DIC was identified as a potentially powerful method for measuring these properties..

The development of the **test set-up** is shown in chapter 4. The system uses DIC cameras to capture images during fatigue tests and compare the processed results with analog signals from other measurement devices. To characterize the fatigue behavior efficiently, the system measures signals and take images for a number of cycles at a high acquisition rate, then wait for a time period and repeat this. To optimize data size and post-processing effort, this time period grows throughout a test. A system using 2D DIC on 2 different surfaces was tested and used throughout this program to keep track of free edge delaminations, a recurring damage event which is inevitable in coupon testing but could influence the result. High framerates and test frequencies cause a delay in the measurements which has to be corrected for, this is done in post-processing software.

To perform tests involving compression, **specimen design** requires careful consideration. This is discussed in chapter 5. Buckling prevention is done through the design of specimens, short enough for buckling not to occur. While this does introduce stress concentrations in the proximity of the area of interest, the alternative of anti-buckling guides or more exotic techniques typically show lower compressive strengths and the effect of side loading can be considered questionable, particularly in fatigue experiments. An analysis based on analytical and finite element buckling load determinations was performed to determine free length and widths of a specimen. Hereafter these specimens were produced and the effect of load introduction on two tab materials was investigated. The final design consists of short, 24 layer specimens with aluminum tabs loaded in shear to transfer load.

A test program was performed on the woven carbon-epoxy material for two lay-ups: $[\#(0/90)]_{24}$ and $[\#(\pm 45)]_{24}$ loaded under C-C and T-C fatigue. The results are presented in chapter 6 and discussed in chapter 7

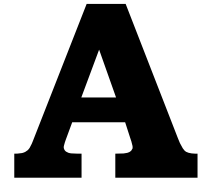
- **Static compression** tests until failure show a stress-strain behavior close to linear for $[\#(0/90)]_{24}$ and a highly non-linear behavior with large deformation for $[\#(\pm 45)]_{24}$. The matrix dominated loading of these laminates also results in a dependence on loading rate.
- **Temperature** was monitored throughout every experiment. For $[\#(\pm 45)]_{24}$ laminates, shearing motion of fibers resulted in heating of the material. To avoid this heating, frequency was adapted for highly loaded tests, in combination with air cooling installed on the set-up. This kept temperature within acceptable limits for most tests, except for high loading at $R = -1$. Since this is an unlikely situation in real life structure for this lay-up, these tests were omitted from the program.
- **Stress-life** behavior in this program is analysed for both laminates and both R-ratios. Despite some scatter and a low number of tests, they show relatively flat S-N curve for C-C experiments. For T-C experiments, both laminates fail from repeated reversed loading at only 50% of their compressive strength or even lower and the curve is more steep. Keep in mind however that for T-C loading, the stress amplitude is more than double of the amplitude under C-C fatigue. Normalizing S-N curves to the ultimate strength shows that when fibers are not aligned with load, the sensitivity to fatigue loading is larger. Adding or discarding tests where heating surpassed acceptable levels for $[\#(\pm 45)]_{24}$ laminates barely influences the S-N curve. This may indicate that the effect of temperature is less excessive than expected.
- **Stiffness evolution** of $[\#(0/90)]_{24}$ laminates is only significant when significant damage events can be observed in the structure. Overall, very little changes in terms of stiffness, permanent strain and hysteresis loops for C-C and T-C loading.
- For $[\#(\pm 45)]_{24}$ loaded under C-C, an initial **(shear) stiffness** increase is observed. This is followed by a decrease in (shear) stiffness which is steady but decreases in steepness. This could be an indication of a similar effect of the three regions of fatigue life presented in chapter 2. However, this test method fails to effectively show the effects near the end of life of a specimen. **Permanent (shear) strain evolution and hysteresis** are more significant when the applied loads are higher and therefore more in the plastic region of the static stress-strain curve.
- For $[\#(\pm 45)]_{24}$ loaded under T-C fatigue, **(shear) stiffness** decreases almost linearly towards the end of life of a specimen, where it is almost 0. Degradation of stiffness is combined with growing **hysteresis** loops. Despite large deformations, these loops remain centered around 0 (permanent) strain.
- **Microscopic investigation** of laminates show little damage in $[\#(0/90)]_{24}$ run-out samples under C-C loading, apart from minor (meta-)delaminations. Under T-C loading, these samples show cracks in transverse fiber bundles, although an interval experiment reveals that these do not initiate from the beginning of fatigue life. For $[\#(\pm 45)]_{24}$ run-out samples, both R-ratios result in numerous cracks in bundles, which are stopped at interfaces for the T-C run-out and tend to coalesce somewhat for the C-C run-out, where the stress is higher.

8.2. Recommendations for further work

This research topic has yielded interesting results already. Unfortunately, time is limited when performing a master thesis. The following recommendations can be of interest for future research:

- For this test series, two laminates have been tested, under two R-ratios, at different stress levels and in some case even at different frequencies. This large number of variables tested in a limited number of fatigue tests makes drawing conclusions confidently difficult in some cases. If time and resources would allow for it, **performing more experiments** could increase this confidence.
- To use the results in further experiments, it is important to realise that coupon testing introduces **free edge delaminations** in the structure, which is not typically found in real life structures. Additional component tests in a design phase are therefore inevitable. Additional material tests could be performed with other specimen shapes such as tubes.

- The DIC system was limited to two **cameras**. However, it can be interesting to use three, four or even more cameras. Using 3D DIC on outer layers could potentially capture the extent of delaminated areas for a more in-depth analysis of these free edge delaminations.
- S-N curves for $[\pm 45]$ laminates were derived using variable frequencies. However, for static compression of these laminates, it was shown that ultimate strength depends on the loading rate. From this, one can expect an **influence of frequency** on the S-N curve as well. A more in-depth investigation of the influence of this frequency on fatigue life can be interesting.
- To further investigate the stiffness evolution of $[\#(\pm 45)]_{24}$ laminates, it can be of interest to microscopically investigate **crack behavior throughout fatigue life** and link this to observed changes in (shear) stiffness.
- To investigate to which extent 3 regions of stiffness evolution mentioned in literature for T-T fatigue can be observed for C-C or T-C fatigue, it could be helpful to run experiments which can **continuously measure until the end of life** of a specimen. Due to very large data sizes for DIC, this set-up did not allow for this. Measurements using an extensometer for example could resolve this.
- The design of compressive specimens results in two artefacts. The effect of a stress concentration on the homogeneity of the stress field and a restriction of Poisson expansion. This can have an effect on the results. To obtain shear properties from $[\pm 45]$ laminates however, it was assumed that the effect of the biaxial stress state was small for both tension and compression. To assess the effects on the shear properties observed for C-C loading, **validation using T-T experiments** on longer specimens where the stress field is more homogeneous and Poisson contraction is less restricted can be interesting.
- Some people claim that there is no fatigue limit for composites. In this sense, it can be interesting to investigate fatigue behavior after **very long fatigue lives**. T-C tests of 30% on $[\#(\pm 45)]_{24}$ laminates can be a particularly interesting case here. Despite being considered run-outs after more than 500,000 cycles, they show a steady decrease in stiffness, which may indicate failure at longer lives. In particular for these tests it might be interesting to perform longer tests.



Digital Image Correlation Analysis

Digital image correlation is a method applied in this thesis for the analysis of images to obtain displacement fields. This appendix shows the procedure for calibration, which parameters/options are chosen for the analysis and evaluates the convergence of strain results.

A.1. Procedure

DIC works by placing one or two cameras so that they face a certain surface, on which a speckle pattern has been applied. Deformations of this surface can then be traced as full-field maps. For this research, all post-processing has been done with vic software by correlated solutions.

To calibrate a 3D system with two cameras, the cameras have to be set up, after which a calibration target is photographed from different angles. The system knows this target and uses this to calculate the camera placements w.r.t. each other, focal lengths, and distances. For a 2D system with a single camera, the calibration procedure is somewhat similar but the system does not recognise targets so distances have to be put in manually. The procedure to correct for lens distortion is to move a rigid speckle pattern in front of the camera over a known distance, in this case the movement is performed by hydraulic test bench. The movement from the analog displacement sensor can then be fed back manually into the software, which then corrects for the distortion through an inverse mapping technique.

DIC processing is hereafter performed by first selecting an area of interest on a reference image with zero force. The system can suggest a subset size (typically around 30-50 pixels) based on the speckle pattern and image resolution, which typically results in a good correlation. Hereafter the correlation algorithm runs. The correlation options used for the analyses are:

- **Gaussian subset weights** of pixels. These will typically provide the best combination of spatial and displacement resolution.
- Optimized **6-tap spline interpolation** for a good combination of accuracy and correlation time.
- **Normalized squared differences** is recommended by correlated solutions for a good combination of flexibility and result.
- Correlation is performed with regards to the reference image. There is another possibility to perform so-called incremental correlation, where images are compared to the previous image instead but unless this is necessary, it is not recommended because of noise building up over time.
- Consistency threshold, confidence margin and matchability threshold are parameters used in the correlation to remove data points with minor correlation. These are left at their default values of 0.02, 0.05 and 0.1, respectively.
- **Strain postprocessing** is done using a Lagrangian finite strain tensor with a filter size of 15, this is also the default.

After correlation, the data is analysed. The inspector extensometer tool is used to obtain a strain value from the displacements of two points selected on the specimen. These points are chosen far enough from the stress concentration zones, but still over a sufficient distance to avoid issues with low resolution or strain differences between warp/weft fibers of the outer layer. To correct for delays in the system (see section 4.2.3), point displacements can be obtained using a point tool on the speckle pattern. These values are then exported to a .csv file, which can be read by the matlab post-processing software, described in section 4.2.4.

A.2. Evaluation

To evaluate this method, for every fatigue test, the strain results were analysed by comparing strains from different extensometers on the specimen, on different locations in terms of height and of different lengths. On an image at largest maximum compressive load, the largest and smallest measured strains from these extensometers were compared. For $[\#(0/90)]_{24}$ laminates, the largest measured difference between two extensometers was never bigger than 3.6 % (R = 10) and 3.3% (R = -1) of the strain value. For $[\#(\pm 45)]_{24}$ laminates, where, as discussed before, the effect of the stress concentration is more pronounced, the differences between two extensometers never exceeded 7.2% (R = 10) or 6.9% (R = -1) of the strain value. In most cases, the differences were much smaller.

B

Abaqus Shell Element Selection

B.1. $[\#(0/90)]_8$

Table B.1: $[\#(0/90)]_8$ element selection

Element type	Computation time (s)	Buckling load 1 [N/mm]	Diff. [%]	Buckling load 2 [N/mm]	Diff. [%]	Buckling load 3 [N/mm]	Diff. [%]
Comparison		2474		2610.3		2935.5	
S4	31	2481.5	-0.30	2616.6	-0.24	2945	-0.32
S4R	28	2481.5	-0.30	2617.5	-0.28	2945	-0.32
S3	40	2481.2	-0.29	2616.7	-0.25	2944.6	-0.31
S8R	66	2474.1	0.00	2610	0.01	2935.1	0.01
S4R5 (thin)	25	2481.5	-0.30	2620.8	-0.40	2945	-0.32

B.2. $[\#(\pm 45)]_8$

Table B.2: $[\#(\pm 45)]_8$ element selection

Element type	Computation time [s]	Buckling load 1 [N/mm]	Diff.e [%]
Comparison		1820	
S4	36	1833	-0.71
S4R	39	1833	-0.71
S3	28	1833	-0.71
S8R	46	1819.2	0.04
S4R5 (thin)	21	1831	-0.60

B.3. $[\#(0/90)]_{24}$ Table B.3: $[\#(0/90)]_{24}$ element selection

Element type	Computation time (s)	Buckling load 1 [N/mm]	Diff. [%]	Buckling load 2 [N/mm]	Diff. [%]	Buckling load 3 [N/mm]	Diff. [%]
Comparison	263	5259.6		6771.1		7971.3	
S4	70	5266.4	-0.13	6782.1	-0.16	7973.9	-0.03
S4R	36	5266.3	-0.13	6782.1	-0.16	7987.8	-0.21
S3	37	5266	-0.12	6781	-0.15	7971	0.00
S8R	58	5259.1	0.01	6770.4	0.01	7971.1	0.00
S4R5 (thin)	31	5266.4	-0.13	6782.1	-0.16	8030	-0.74

B.4. $[\#(\pm 45)]_{24}$ Table B.4: $[\#(\pm 45)]_{24}$ element selection

Element type	Computation time (s)	Buckling load 1 [N/mm]	Diff. [%]	Buckling load 2 [N/mm]	Diff. [%]
Comparison	263	2931.7		4558.3	
S4	40	2951.9	-0.69	4585.3	-0.59
S4R	31	2936.9	-0.18	4572.7	-0.32
S3	31	2963.6	-1.09	4595.1	-0.81
S8R	51	2933.6	-0.06	4558.7	-0.01
S4R5 (thin)	42	2944.6	-0.44	4582.2	-0.52

C

Specimen Preparation

Plate material is provided by Mitsubishi Rayon Co., Ltd. It must be appropriately cut to size and fitted with tab material to be used in the hydraulic machine. In particular when compression is included in the loading pattern, good alignment and attachment of these tabs is crucial in ensuring proper load transfer (see section 5.3). Since there is no go-to method for specimen preparation, the process used is presented in this section. A guideline throughout development of this process was the tabbing guide for composite test specimens by Adams. [17]

- Since tabbing is a tedious process, the composite panels are divided in **subpanels** and fitted with tabbing material, to create a subpanel from which multiple specimens can then be cut using waterjet cutting, which was performed at Odisee Ghent. Subpanel cutting is less critical and was done using a diamond cutter in the workshop. An example of a waterjet cut subpanel for 5 specimens with aluminum tabs is shown below (figure C.1). The cutting leaves a small bridge which can be snapped and sanded down to finalize the specimens. Note that cutting is initiated at the very edge of the subpanel, to avoid delaminations when attempting to penetrate the composite.

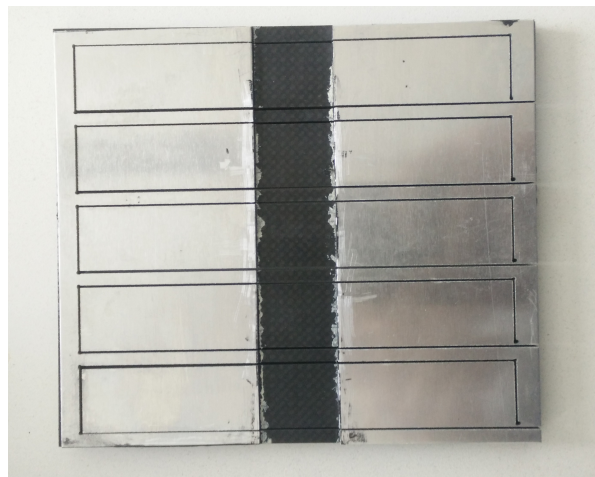


Figure C.1: Subpanel after waterjet cutting

- **Tab material** is cut to size from larger plates, in the workshop or externally, depending on the material. Apart from the actual tab material, a set of **spacers** is also fabricated to ensure correct positioning of all 4 tabs and prevent adhesive flow onto the gauge section during curing. These spacers are the same thickness as the tabbing material and are left on the specimen during curing of the adhesive, to allow for an even pressure distribution.

- After deburring, the spacers are treated with a Chemlease 41-90 EZ **release agent** and air-dried.
- Gauge sections of the subpanel are marked using pencil and then covered using masking tape. Hereafter, the subpanel is sanded (grit 320) in the tab regions to increase surface roughness and remove contaminants. This is followed by rinsing in water and drying of the panels. After removing the masking tape, the entire subpanel is cleaned using acetone and masking tape is re-applied. The masking tape ensures successful removal of the spacers after curing since there is no direct adhesive link between the subpanel and the spacer.
- After deburring, the **tab material** is sanded (grit 320) on one side to increase surface roughness, after which it is cleaned with water, air-dried and cleaned with acetone until all residue is gone.
- The following step is to **attach spacers** to the subpanel, just covering the masking tape. An example is shown in figure C.2.

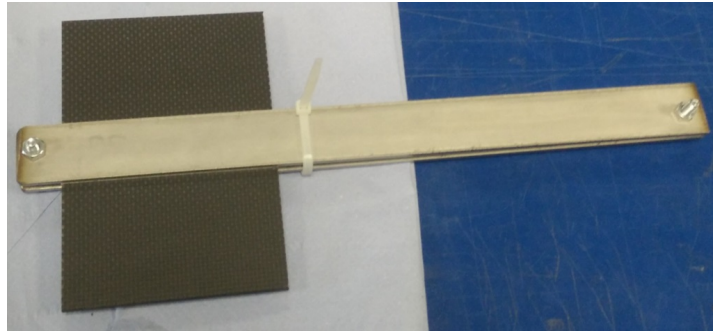


Figure C.2: Subpanel fitted with a thick steel spacer

- After this, rubber toughened **adhesive** (loctite 480) is applied to the gage sections, tab material is applied, fixed in place using tape, and left to dry for at least 24 hours under pressure. Hereafter, specimens are ready for waterjet

D

Overview of Tests performed

This appendix presents a full overview of all tests performed throughout the test program presented in chapters 6 and 7. It shows results from static tests until failure for both lay-ups, including high strain rate tests for $[\#(\pm 45)]_{24}$. Hereafter, all tests performed for the fatigue program are presented in tables, separated by lay-up and R-ratio. Tests are given an ID, a number to keep track of test samples throughout the program. Test IDs with an 'A' originate from the tabbing material tests performed for specimen design (chapter 5). Test A4 has been omitted from the fatigue results due to out-of plane movement of the clamps, as was discussed in this chapter.

D.1. $[\#(0/90)]_{24}$ (Static)

Table D.1: Test overview for $[\#(0/90)]_{24}$ (Static)

Test ID	Width [mm]	Thickness [mm]	Displacement Rate [mm/min]	$\sigma_{ult,c}$ [MPa]	Remarks
1	20	5.4	0.5	530	
2	20	5.4	0.5	511	
3	20	5.3	0.5	511	
A1	20	5.4	0.5	514	
A2	20	5.4	0.5	501	

D.2. $[\#(\pm 45)]_{24}$ (Static)

Table D.2: Test overview for $[\#(\pm 45)]_{24}$ (Static)

Test ID	Width [mm]	Thickness [mm]	Displacement Rate [mm/min]	$\sigma_{ult,c}$ [MPa]	Remarks
29	19.9	5.4	450	179	Paint debond
31	19.9	5.4	0.5	156	Paint debond
32	20	5.4	0.5	159	Paint debond
33	20	5.4	450	178	Paint debond
57	19.9	5.4	0.5	157	Paint debond
58	19.9	5.4	0.5	155	Paint debond
59	19.9	5.4	0.5	156	Paint debond
62	19.9	5.4	0.5	152	
63	19.9	5.4	450	174	
64	19.8	5.4	0.5	155	

D.3. [#(0/90)]₂₄ (R = 10)Table D.3: Test overview for [#(0/90)]₂₄ (R = 10)

Test ID	Width [mm]	Thickness [mm]	σ_a [MPa]	frequency [Hz]	N_f []	Remarks
A3	20	5.4	350	3	780,000+ (∞)	
4	20	5.4	459	3	45	
5	19.9	5.3	459	3	658	
6	19.9	5.3	459	3	268	
7	20	5.4	357	3	21,014	
8	20	5.4	409	3	13,699	
9	19.9	5.4	357	3	1,000,000+ (∞)	$\sigma_{r,c} = 530$ MPa
10	19.9	5.4	357	3	20,057	
11	19.9	5.4	409	3	1,637	
12	20	5.3	409	3	14,140	
13	19.9	5.3	307	3	1,000,000+ (∞)	
14	20	5.4	307	3	1,000,000+ (∞)	
15	20	5.4	409	3	2,347	

D.4. [#(0/90)]₂₄ (R = -1)Table D.4: Test overview for [#(0/90)]₂₄ (R = -1)

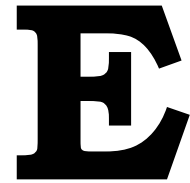
Test ID	Width [mm]	Thickness [mm]	σ_a [MPa]	frequency [Hz]	N_f []	Remarks
16	19.9	5.4	307	3	7,914	
17	19.8	5.3	409	3	429	
18	20	5.3	204	3	800,000+ (∞)	
19	19.9	5.4	307	3	18,741	
20	19.9	5.4	256	3	179,974	
21	19.8	5.4	459	3	17	
22	/	/	/	/	/	Sample was damaged during test set-up
23	19.7	5.3	256	3	78,547	
24	19.9	5.3	230	3	574,400	
25	19.3	5.3	307	3	11,750+	Sample used for interval microscopy. Debonded in one of the tabs after releasing for microscopic inspection.
26	19.9	5.4	204	3	1,000,000+ (∞)	
27	19.9	5.4	358	3	79	
28	19.8	5.3	358	3	5,156	

D.5. [#(± 45)]₂₄ (R = 10)Table D.5: Test overview for [#(± 45)]₂₄ (R = 10)

Test ID	Width [mm]	Thickness [mm]	σ_a [MPa]	frequency [Hz]	N_f []	Remarks
30	19.9	5.4	140	3	91	$\Delta T = 21^\circ\text{C}$
34	19.9	5.4	93.6	3	715,000+ (∞)	$\Delta T = 6.7^\circ\text{C}$
35	19.9	5.5	125	2	514	$\Delta T = 17^\circ\text{C}$
36	19.9	5.4	125	1	1,542	$\Delta T = 10^\circ\text{C}$
37	19.8	5.4	93.6	3	725,732+ (∞)	$\Delta T = 3.5^\circ\text{C}$
38	19.9	5.4	125	3	980	$\Delta T = 20^\circ\text{C}$
39	19.9	5.4	109	2	18,290	$\Delta T = 18.2^\circ\text{C}$
40	19.9	5.4	140	0.25	74	$\Delta T = 6.2^\circ\text{C}$
41	19.9	5.4	125	0.5	1,245	$\Delta T = 6.9^\circ\text{C}$
42	19.8	5.4	93.6	3	725,794+ (∞)	$\Delta T = 5^\circ\text{C}$
43	19.8	5.4	109	1	74,252	$\Delta T = 6.2^\circ\text{C}$
44	19.8	5.4	109	1	41,899	$\Delta T = 7.4^\circ\text{C}$
54	19.8	5.4	140	0.25	87	$\Delta T = 3.2^\circ\text{C}$
60	19.9	5.4	140	2	95	$\Delta T = 20^\circ\text{C}$

D.6. [#(± 45)]₂₄ (R = -1)Table D.6: Test overview for [#(± 45)]₂₄ (R = -1)

Test ID	Width [mm]	Thickness [mm]	σ_a [MPa]	frequency [Hz]	N_f []	Remarks
45	19.8	5.4	62.4	2	43,145	$\Delta T = 7.1^\circ\text{C}$
46	19.8	5.4	62.4	2	29,150	$\Delta T = 9^\circ\text{C}$
47	/	/	/	/	/	Sample used for heating tests
48	19.9	5.4	125	2	24	$\Delta T = 3.4^\circ\text{C}$
49	19.8	5.4	46.8	2	685,302+ (∞)	$\Delta T = 1.5^\circ\text{C}$
50	19.8	5.4	46.8	2	518,098+ (∞)	$\Delta T = 1.8^\circ\text{C}$
51	19.8	5.4	46.8	2	502,399+ (∞)	$\Delta T = -2.2^\circ\text{C}$
52	19.8	5.4	78	2	1,430	$\Delta T = 45^\circ\text{C}$
53	19.8	5.4	78	0.2	1,988	$\Delta T = 4.3^\circ\text{C}$
55	19.9	5.4	78	0.2	1,574	$\Delta T = 2.4^\circ\text{C}$
61	19.9	5.4	62.4	2	29,020	$\Delta T = 9.7^\circ\text{C}$



Reproducibility of Test Results

Including stiffness evolution results for every single test in the report would significantly lengthen it. Therefore, in the text, results are based on representative tests which show the observed trends. This appendix summarizes all available results for the stiffness evolutions measured throughout the test program. When more than one test has been performed at a single load level for a certain case, they are compared to visualise the scatter involved. To be able to actually quantify the scatter numerically however, would require more tests. Nevertheless, this chapter provides some insight in the variations observed.

E.1. $[\#(0/90)]_{24}$ ($R = 10$)

Overall, this combination of lay-up and loading show very little evolution of stiffness over time. For one test under 80% $\sigma_{ult,c}$ (testID 15), a changing stiffness was observed but this was correlated with a significant damage on the free edge before final failure. Apart from this test, tests show a relatively constant stiffness until final failure.

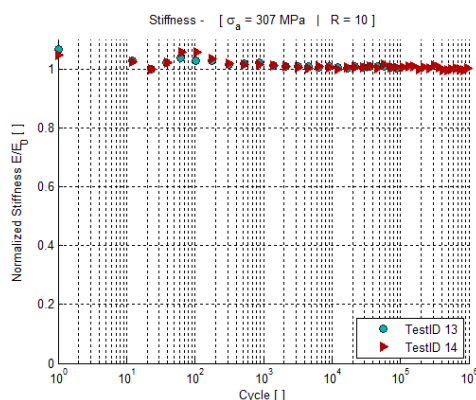


Figure E.1: Stiffness evolution of $\#(0/90)$ laminates under 60% $\sigma_{ult,c}$ ($R = 10$) [$E_{0,13} = 46.6$ GPa | $E_{0,14} = 46.9$ GPa]

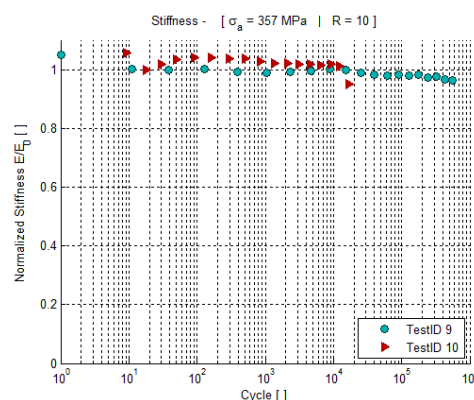


Figure E.2: Stiffness evolution of $\#(0/90)$ laminates under 70% $\sigma_{ult,c}$ ($R = 10$) [$E_{0,9} = 46.5$ GPa | $E_{0,10} = 46.6$ GPa]

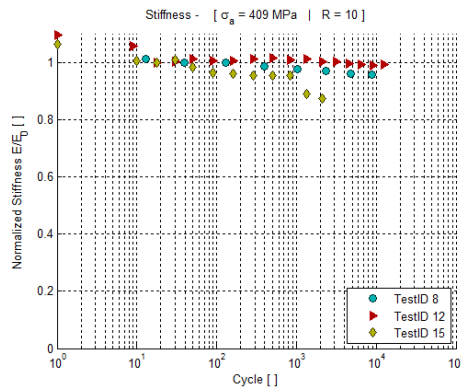


Figure E.3: Stiffness evolution of #(0/90) laminates under 80% $\sigma_{ult,c}$ ($R = 10$) [$E_{0,8} = 48.2$ GPa | $E_{0,12} = 45.2$ GPa | $E_{0,15} = 47.5$ GPa]

E.2. [#(0/90)]₂₄ ($R = -1$)

For this combination of lay-up and loading, the effect on the stiffness is also minimal. Sudden stiffness drops were related to damage events (chapter 6). Both peak-to-peak stiffness E , and stiffness in compression/tension E_C/E_T are shown for every test. Scatter in compression and tension components can clearly be seen. For the case of 50% $\sigma_{ult,c}$, one test (testID 23) shows a constant stiffness until failure, the other (testID 20) shows a more steady decrease over its fatigue life. Conclusions on stiffness evolution at this load level are therefore difficult to draw from these tests. At 60% $\sigma_{ult,c}$, stiffness also shows very little evolution.

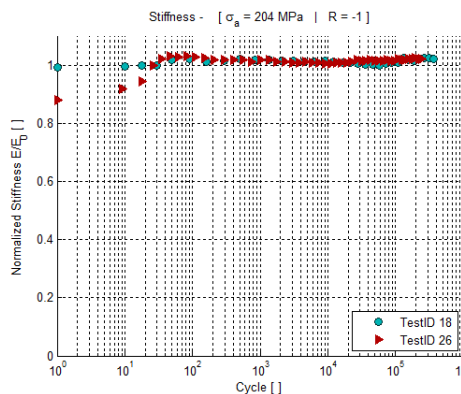


Figure E.4: Stiffness evolution of #(0/90) laminates under 40% $\sigma_{ult,c}$ ($R = -1$) [$E_{0,18} = 50.3$ GPa | $E_{0,18} = 49.8$ GPa]

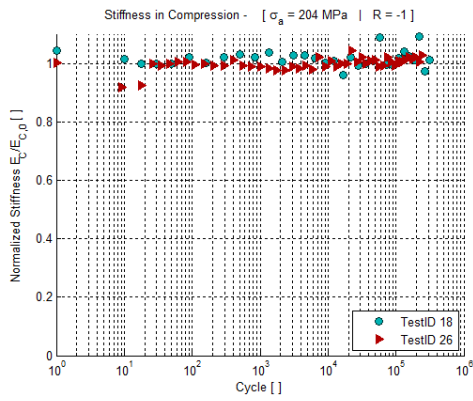


Figure E.5: Evolution of stiffness in compression of $\#(0/90)$ laminates under 40% $\sigma_{ult,c}$ ($R = -1$) [$E_{C0,18} = 47.7$ GPa | $E_{C0,26} = 48.2$ GPa]

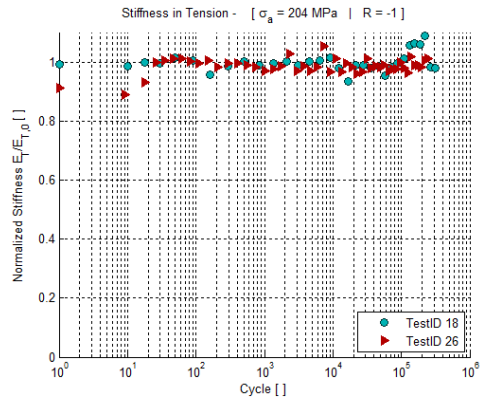


Figure E.6: Evolution of stiffness in tension of $\#(0/90)$ laminates under 40% $\sigma_{ult,c}$ ($R = -1$) [$E_{T0,18} = 53.1$ GPa | $E_{T0,26} = 54.0$ GPa]

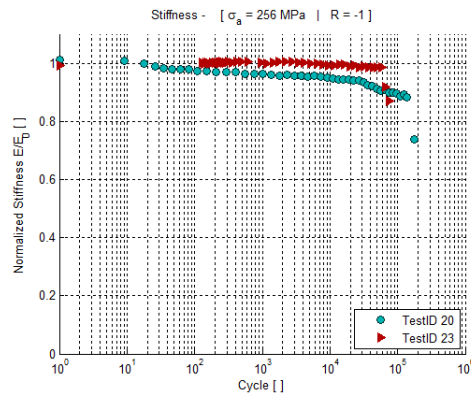


Figure E.7: Stiffness evolution of $\#(0/90)$ laminates under 50% $\sigma_{ult,c}$ ($R = -1$) [$E_{0,20} = 51.9$ GPa | $E_{0,23} = 52.2$ GPa]

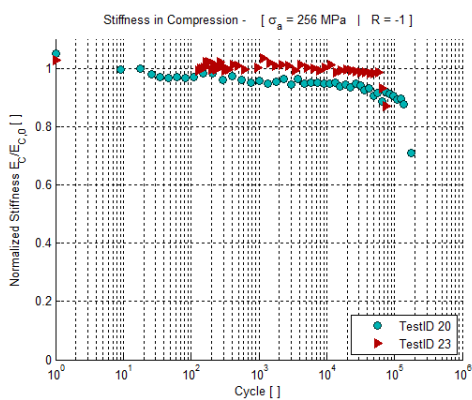


Figure E.8: Evolution of stiffness in compression of $\#(0/90)$ laminates under 50% $\sigma_{ult,c}$ ($R = -1$) [$E_{C0,20} = 48.2$ GPa | $E_{C0,23} = 50.5$ GPa]

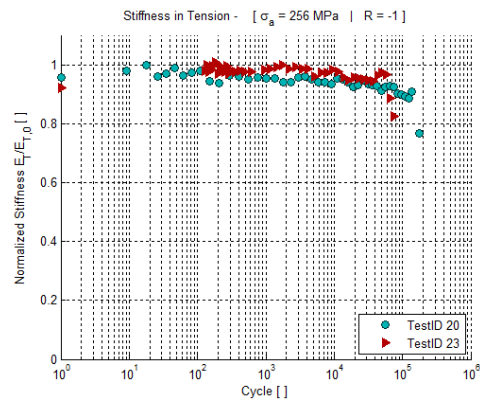


Figure E.9: Evolution of stiffness in tension of $\#(0/90)$ laminates under 50% $\sigma_{ult,c}$ ($R = -1$) [$E_{T0,20} = 57.4$ GPa | $E_{T0,23} = 57.8$ GPa]

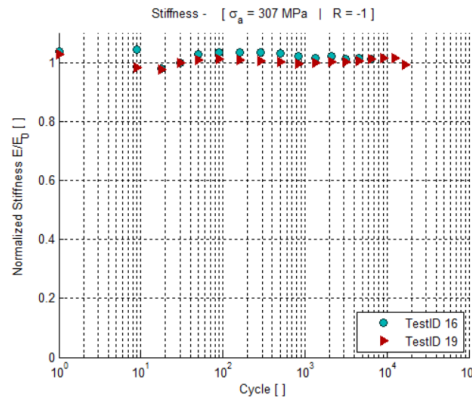


Figure E.10: Stiffness evolution of # (0/90) laminates under 60% $\sigma_{ult,c}$ ($R = -1$) [$E_{0,16} = 50.0$ GPa | $E_{0,19} = 52.8$ GPa]

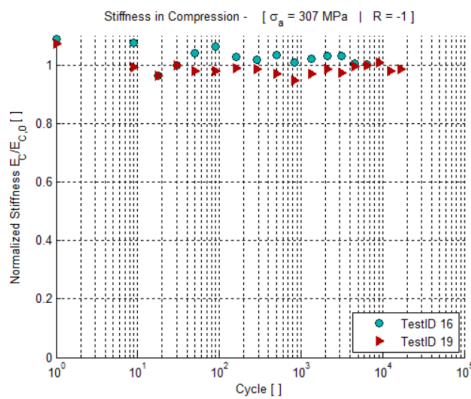


Figure E.11: Evolution of stiffness in compression of # (0/90) laminates under 60% $\sigma_{ult,c}$ ($R = -1$) [$E_{c0,16} = 46.9$ GPa | $E_{c0,19} = 51.0$ GPa]

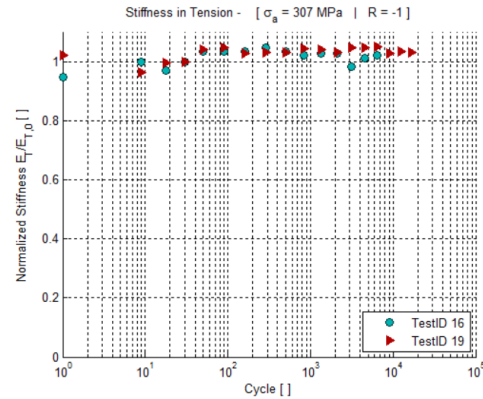


Figure E.12: Evolution of stiffness in tension of # (0/90) laminates under 60% $\sigma_{ult,c}$ ($R = -1$) [$E_{T0,16} = 54.6$ GPa | $E_{T0,19} = 55.8$ GPa]

E.3. [#(± 45)]₂₄ ($R = 10$)

Similarly to what was discussed in chapter 6, for high cycle fatigue, stiffness tends to rise in the initial stage of its fatigue life after which a steady descent is initiated. For 3 run-out tests at 60% $\sigma_{ult,c}$, this descent flattens out. At 70% $\sigma_{ult,c}$, this descent continues until final failure. Note that the effect is visible in both longitudinal and shear stiffness expressions. At higher load levels, most samples show an initial constant stiffness which declines rapidly until final failure afterwards.

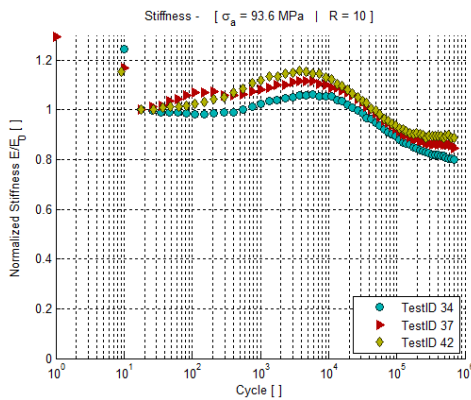


Figure E.13: Stiffness evolution of # (± 45) laminates under 60% $\sigma_{ult,c}$ ($R = 10$) [$E_{0,34} = 8.5$ GPa | $E_{0,37} = 8.7$ GPa | $E_{0,42} = 8.1$ GPa]

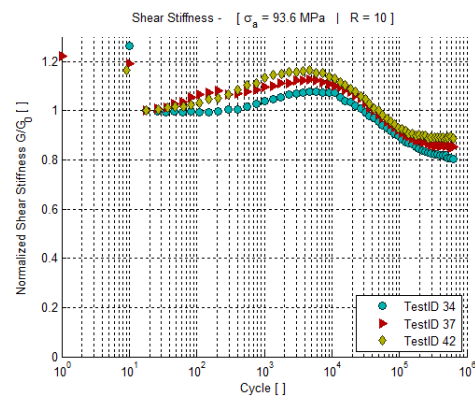


Figure E.14: Shear stiffness evolution of # (± 45) laminates under 60% $\sigma_{ult,c}$ ($R = 10$) [$G_{0,34} = 2.2$ GPa | $G_{0,37} = 2.3$ GPa | $G_{0,42} = 2.3$ GPa]

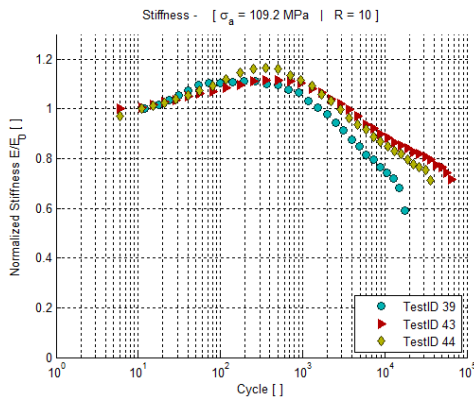


Figure E.15: Stiffness evolution of $\#(\pm 45)$ laminates under 70% $\sigma_{ult,c}$ ($R = 10$) [$E_{0,39} = 6.9$ GPa | $E_{0,43} = 7.2$ GPa | $E_{0,44} = 6.6$ GPa]

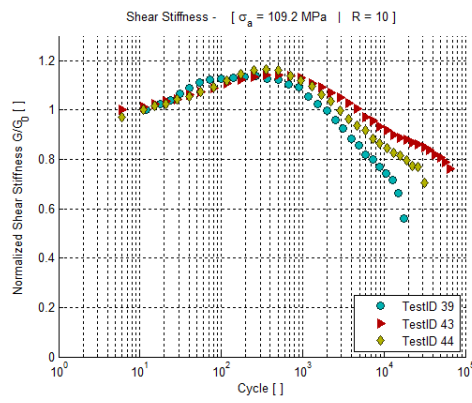


Figure E.16: Shear stiffness evolution of $\#(\pm 45)$ laminates under 70% $\sigma_{ult,c}$ ($R = 10$) [$G_{0,39} = 1.8$ GPa | $G_{0,43} = 1.9$ GPa | $G_{0,44} = 1.8$ GPa]

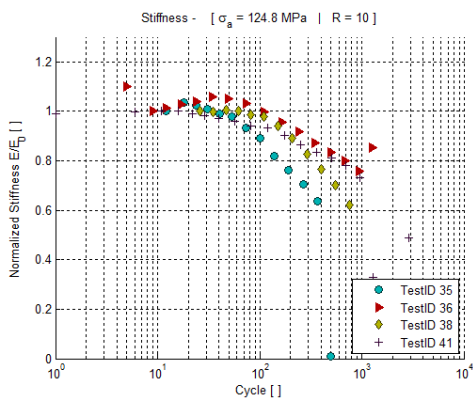


Figure E.17: Stiffness evolution of $\#(\pm 45)$ laminates under 80% $\sigma_{ult,c}$ ($R = 10$) [$E_{0,35} = 6.9$ GPa | $E_{0,36} = 6.1$ GPa | $E_{0,38} = 6.3$ GPa | $E_{0,41} = 6.1$ GPa]

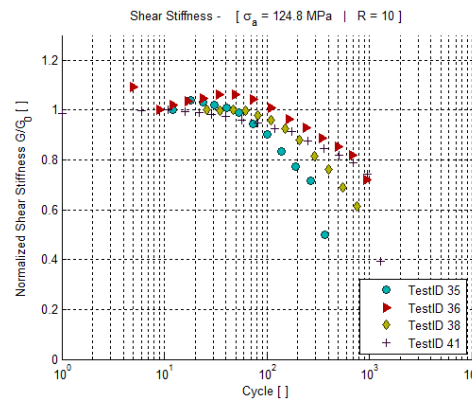


Figure E.18: Shear stiffness evolution of $\#(\pm 45)$ laminates under 80% $\sigma_{ult,c}$ ($R = 10$) [$G_{0,35} = 1.8$ GPa | $G_{0,36} = 1.6$ GPa | $G_{0,38} = 1.7$ GPa | $G_{0,41} = 1.6$ GPa]

E.4. $[\#(\pm 45)]_{24}$ ($R = -1$)

Despite some scatter in the results, the overall behavior of these tests at 30, 40 and 50% $\sigma_{ult,c}$ is a stiffness which is relatively constant until a steep descent begins. Tests at 30% $\sigma_{ult,c}$ were considered a run-out, however, descending stiffness might indicate potential failure at a later point in fatigue life. Overall, the scatter between curves is not very large here, although the components in tension and compression still show some variations. In terms of scatter and variability, the shear representation seems to be somewhat less sensitive.

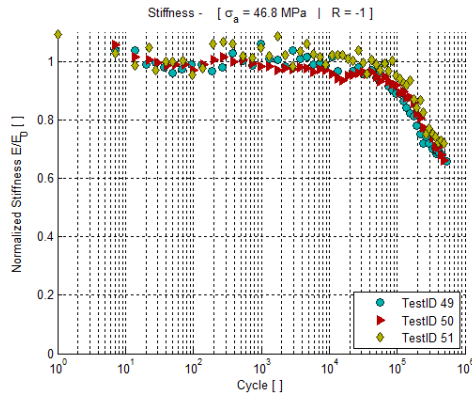


Figure E.19: Stiffness evolution of #(\pm 45) laminates under 30% $\sigma_{ult,c}$ ($R = -1$) [$E_{0,49} = 10.4$ GPa | $E_{0,50} = 10.7$ GPa | $E_{0,51} = 10.3$ GPa]

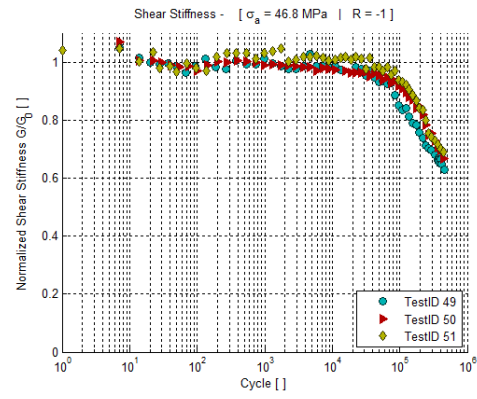


Figure E.20: Shear stiffness evolution of #(\pm 45) laminates under 30% $\sigma_{ult,c}$ ($R = -1$) [$G_{0,49} = 2.9$ GPa | $G_{0,50} = 2.9$ GPa | $G_{0,51} = 2.9$ GPa]

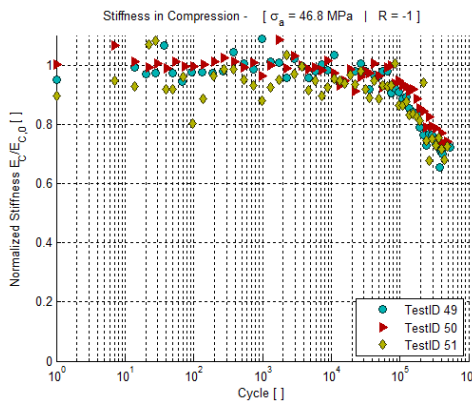


Figure E.21: Evolution of stiffness in compression of #(\pm 45) laminates under 30% $\sigma_{ult,c}$ ($R = -1$) [$E_{C0,49} = 10.7$ GPa | $E_{C0,50} = 10.9$ GPa | $E_{C0,51} = 11.6$ GPa]

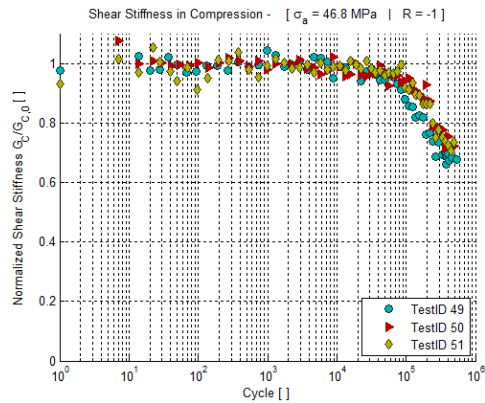


Figure E.22: Evolution of shear stiffness in compression of #(\pm 45) laminates under 30% $\sigma_{ult,c}$ ($R = -1$) [$G_{C0,49} = 3.0$ GPa | $G_{C0,50} = 3.0$ GPa | $G_{C0,51} = 3.0$ GPa]

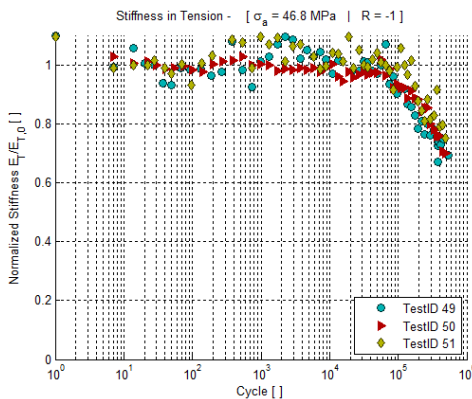


Figure E.23: Evolution of stiffness in tension of #(\pm 45) laminates under 30% $\sigma_{ult,c}$ ($R = -1$) [$E_{T0,49} = 10.6$ GPa | $E_{T0,50} = 11.1$ GPa | $E_{T0,51} = 10.7$ GPa]

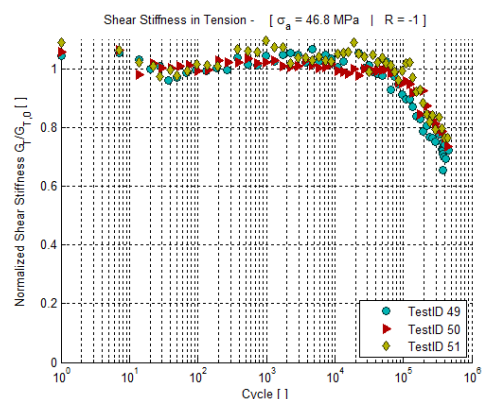


Figure E.24: Evolution of shear stiffness in tension of #(\pm 45) laminates under 30% $\sigma_{ult,c}$ ($R = -1$) [$G_{T0,49} = 2.9$ GPa | $G_{T0,50} = 3.0$ GPa | $G_{T0,51} = 3.0$ GPa]

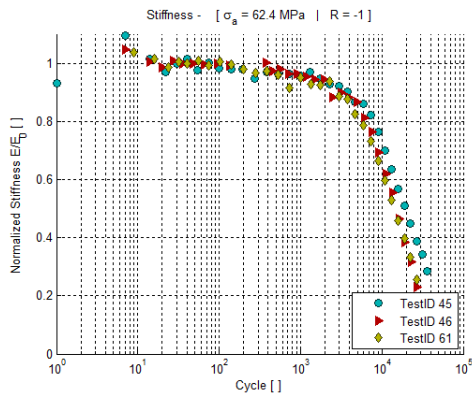


Figure E.25: Stiffness evolution of $\#(\pm 45)$ laminates under 40% $\sigma_{ult,c}$ ($R = -1$) [$E_{0,45} = 9.5$ GPa | $E_{0,46} = 9.8$ GPa | $E_{0,61} = 9.8$ GPa]

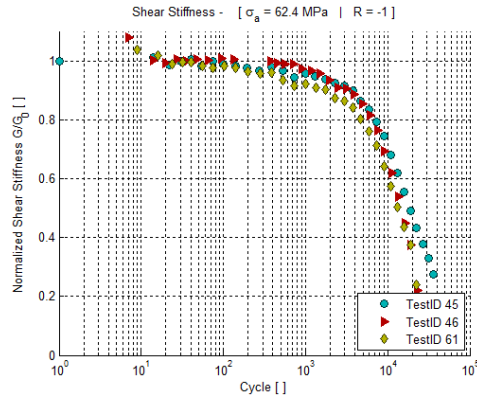


Figure E.26: Shear stiffness evolution of $\#(\pm 45)$ laminates under 40% $\sigma_{ult,c}$ ($R = -1$) [$G_{0,45} = 2.6$ GPa | $G_{0,46} = 2.6$ GPa | $G_{0,61} = 2.7$ GPa]

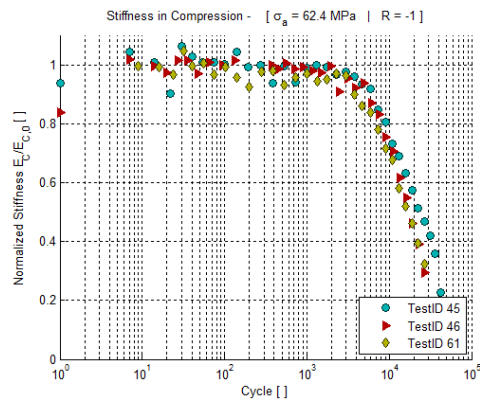


Figure E.27: Evolution of stiffness in compression of $\#(\pm 45)$ laminates under 40% $\sigma_{ult,c}$ ($R = -1$) [$E_{C0,45} = 9.9$ GPa | $E_{C0,46} = 10.0$ GPa | $E_{C0,61} = 10.5$ GPa]

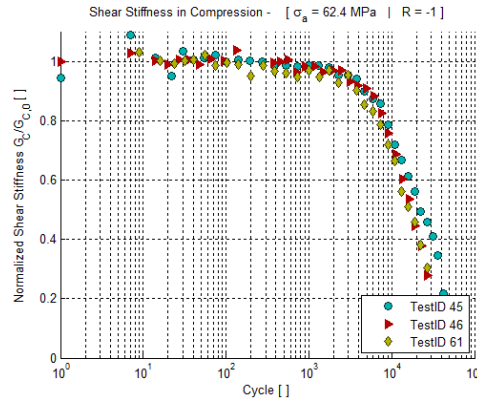


Figure E.28: Evolution of shear stiffness in compression of $\#(\pm 45)$ laminates under 40% $\sigma_{ult,c}$ ($R = -1$) [$G_{C0,45} = 2.7$ GPa | $G_{C0,46} = 2.7$ GPa | $G_{C0,61} = 2.8$ GPa]

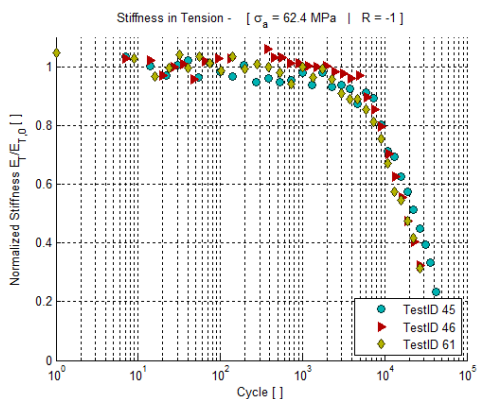


Figure E.29: Evolution of stiffness in tension of $\#(\pm 45)$ laminates under 40% $\sigma_{ult,c}$ ($R = -1$) [$E_{T0,45} = 10.4$ GPa | $E_{T0,46} = 10.2$ GPa | $E_{T0,61} = 10.3$ GPa]

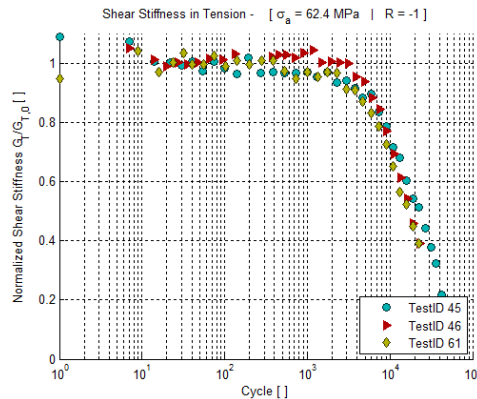


Figure E.30: Evolution of shear stiffness in tension of $\#(\pm 45)$ laminates under 40% $\sigma_{ult,c}$ ($R = -1$) [$G_{T0,45} = 2.8$ GPa | $G_{T0,46} = 2.8$ GPa | $G_{T0,61} = 2.8$ GPa]

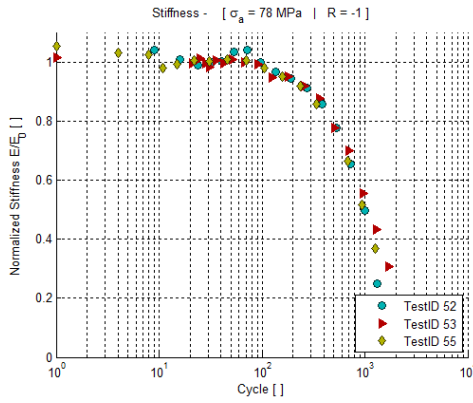


Figure E.31: Stiffness evolution of #(\pm 45) laminates under 50% $\sigma_{ult,c}$ ($R = -1$) [$E_{0,52} = 8.8$ GPa | $E_{0,53} = 8.2$ GPa | $E_{0,55} = 7.5$ GPa]

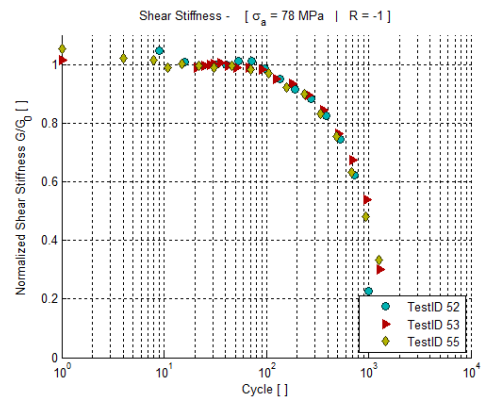


Figure E.32: Shear stiffness evolution of #(\pm 45) laminates under 50% $\sigma_{ult,c}$ ($R = -1$) [$G_{0,52} = 2.5$ GPa | $G_{0,53} = 2.2$ GPa | $G_{0,55} = 2.1$ GPa]

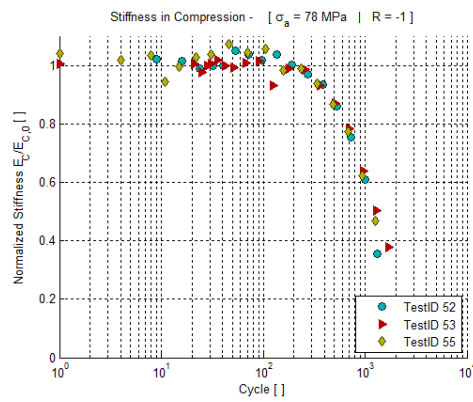


Figure E.33: Evolution of stiffness in compression of #(\pm 45) laminates under 50% $\sigma_{ult,c}$ ($R = -1$) [$E_{C0,52} = 9.4$ GPa | $E_{C0,53} = 9.0$ GPa | $E_{C0,55} = 8.0$ GPa]

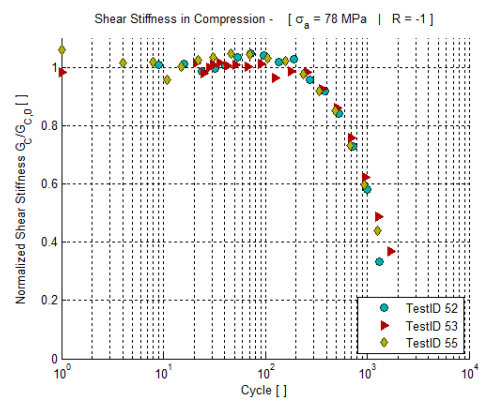


Figure E.34: Evolution of shear stiffness in compression of #(\pm 45) laminates under 50% $\sigma_{ult,c}$ ($R = -1$) [$G_{C0,52} = 2.6$ GPa | $G_{C0,53} = 2.5$ GPa | $G_{C0,55} = 2.3$ GPa]

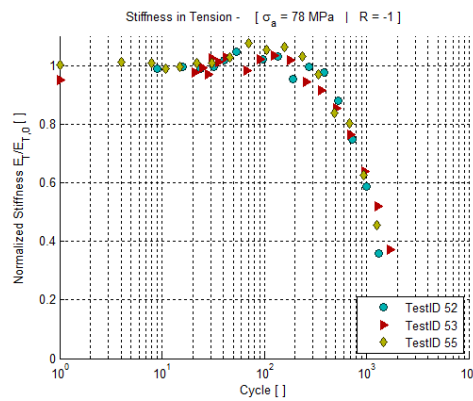


Figure E.35: Evolution of stiffness in tension of #(\pm 45) laminates under 50% $\sigma_{ult,c}$ ($R = -1$) [$E_{T0,52} = 9.7$ GPa | $E_{T0,53} = 9.3$ GPa | $E_{T0,55} = 8.2$ GPa]

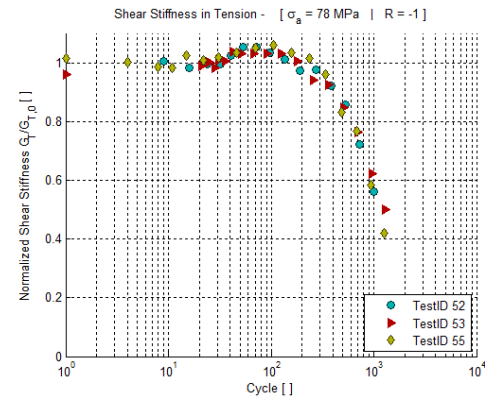


Figure E.36: Evolution of shear stiffness in tension of #(\pm 45) laminates under 50% $\sigma_{ult,c}$ ($R = -1$) [$G_{T0,52} = 2.7$ GPa | $G_{T0,53} = 2.5$ GPa | $G_{T0,55} = 2.3$ GPa]

Bibliography

- [1] D. Kögl and D. Dölle, *Simulation and testing of cfrp parts in the automotive industry: New material meets old processes*, Daimler AG (2011).
- [2] N. A. Fleck, *Compressive failure of fiber composites*, *Advances in Applied Mechanics* **33**, 43 (1997).
- [3] N. K. Naik and R. S. Kumar, *Compressive strength of unidirectional composites: Evaluation and comparison of prediction models*, *Composite Structures* **46**, 299 (1999).
- [4] N. V. D. Carvalho, S. T. Pinho, and P. Robinson, *An experimental study of failure initiation and propagation in 2d woven composites under compression*, *Composites Science and Technology* **71**, 1316 (2011).
- [5] S. D. Pandita, G. Huysmans, M. Wevers, and I. Verpoest, *Tensile fatigue behavior of glass plain-weave fabric composites in on- and off-axis directions*, *Composites Part A Applied Science and Manufacturing* **32** (2001).
- [6] A. P. Vassilopoulos and T. Keller, *Fatigue of Fiber-Reinforced Composites*, edited by S. S. Media (Springer-Verlag, 2011).
- [7] B. Harris, G. D. Sims, M. M. Shokrieh, L. B. Lessard, F. R. Jones, C. Galiotis, C. Koimtzoglou, R. Martin, G. F. Fernando, A. P. Mouritz, G. Gavrino, N. K. Naik, E. K. Gamstedt, M. P. Ansell, P. Beaumont, K. Reifsnider, S. Case, P. Ladeveze, G. Lubineau, X. Diao, L. Ye, Y.-W. Mai, M. Kash-talyan, C. Soutis, T. P. Philippidis, A. P. Vassilopoulos, L. J. Lee, K. E. Fu, J. A. Lee, D. P. Almond, M. D. Gilchrist, J. Schön, R. Starikov, D. Perreux, F. Thiébaud, J. Cadei, A. J. Davies, P. T. Curtis, P. Davies, and D. Choqueuse, *Fatigue in Composites - Science and technology of the fatigue Response of Fibre-Reinforced Plastics*, edited by B. Harris (Woodhead Publishing, 2003).
- [8] M. Quaresimin, *Fatigue of woven composite laminates under tensile and compressive loading*, in *Tenth European Conference on Composite Materials* (2002).
- [9] M. Kawai and T. Taniguchi, *Off-axis fatigue behaviour of plain weave carbon/epoxy fabric laminates at room and high temperatures and its mechanical modeling*, *Composites part A: Applied Science and Manufacturing* **37**, 243 (2006).
- [10] Z. Khan, F. A. Al-Sulaiman, J. K. Farooqi, and M. Younas, *Fatigue life predictions in woven carbon fabric/polyester composites based on modulus degradation*, *Journal of Reinforced Plastics and Composites* **20**, 377 (2001).
- [11] K. Yoshioka and J. C. Seferis, *Modeling of tensile fatigue damage in resin transfer molded woven carbon fabric composites*, *Composites Part A Applied Science and Manufacturing* **33**, 1593 (2002).
- [12] J. Montesano, M. Selezneva, M. Levesque, and Z. Fawaz, *Modeling fatigue damage evolution in polymer matrix composite structures and validation using in-situ digital image correlation*, *Composite Structures* **125** (2015).
- [13] S. Yoneyama and G. Murasawa, *Digital image correlation*, *Experimental Mechanics* (2010).
- [14] S. Giancane, F. Panella, R. Nobile, and V. Dattoma, *Fatigue damage evolution of fiber reinforced composites with digital image correlation analysis*, *Procedia Engineering* **2**, 1307 (2010).

- [15] R. D. B. Sevenois, D. Garoz, F. Gilabert, S. Spronk, S. Fonteyn, M. Heyndrickx, L. Pyl, D. Van Hemelrijck, J. Degrieck, and W. Van Paepegem, *Avoiding interpenetrations and the importance of nesting in analytic geometry construction for representative unit cells of woven composite laminates*, *Composites Science and Technology* **136** (2016).
- [16] M. Xie and D. F. Adams, *Effect of loading method on compression testing of composite materials*, *Journal of Composite Materials* **29**, 1581 (1995).
- [17] D. Adams and D. F. Adams, *Tabbing Guide For Composite Test Specimens*, resreport (Department of Mechanical Engineering, University of Utah and Wyoming Test Fixtures, Inc., 2002).
- [18] K. Gross, *THE CO2 EMISSIONS CHALLENGE: The carmakers' race to 2021 has started*, techreport (PA Consulting, 123 Buckingham Palace Road London SW1W 9SR United Kingdom, 2016).
- [19] Dupont, *Vehicle weight reduction for optimal performance*, Website (2017).
- [20] E. F. for Transport and Environment, *Weight-based standards make CO2 targets harder to reach*, techreport (European Federation for Transport and Environment, 2008).
- [21] R. D. B. Sevenois and W. Van Paepegem, *Fatigue damage modeling techniques for textile composites: Review and comparison with unidirectional composite modeling techniques*, *Applied Mechanics Reviews* **67** (2015).
- [22] W.-S. Kuo, T.-H. Ko, and C.-P. Chen, *Effect of weaving processes on compressive behaviour of 3d woven composites*, *Composites part A: Applied Science and Manufacturing* **38**, 555 (2007).
- [23] SIM-Flanders, *Macro-level predictive modeling, design and optimization of advanced lightweight material systems*, Online presentation (2015).
- [24] A. C. Long, S. Lomov, I. Verpoest, F. Robitaille, P. Harrison, M. Clifford, W.-R. Yu, J. Dominy, C. Rudd, M. D. Wakeman, J.-A. E. Manson, A. Gokce, S. G. Advani, I. A. Jones, A. R. Horrocks, B. K. Kandola, J. Lowe, J. Chilton, J. G. Ellis, and K. Van De Velde, *Design and Manufacture of Textile Composites*, edited by A. C. Long (CRC Press and Woodhead Publishing Limited, 2005).
- [25] D. Hull and Y. Shi, *Damage mechanism characterization in composite damage tolerance investigations*, *Composite Structures* **23**, 99 (1993).
- [26] P. Ladeveze and E. L. Dantec, *Damage modelling of the element ply for laminate composites*, *composites Science and Technology* **43** (1992).
- [27] E. K. Gamstedt and B. A. Sjögren, *Micromechanisms in tension-compression fatigue of composite laminates containing transverse plies*, *composites Science and Technology* **59**, 167 (1999).
- [28] C. R. Schultheisz and A. M. Waas, *Compressive failure of composites part i: Testing and micromechanical theories*, *Prog. Aerospace. Sci.* **32**, 1 (1996).
- [29] W. S. Slaughter and N. A. Fleck, *Compressive fatigue of fibre composites*, *J. Mech. Phys. Solids* **41**, 1265 (1993).
- [30] W. S. Slaughter, J. Fan, and N. A. Fleck, *Dynamic compressive failure of fiber composites*, *J. Mech. Phys. Solids* **44**, 1867 (1996).
- [31] P. M. Jelf and N. A. Fleck, *Compression failure mechanisms in unidirectional composites*, *Journal of Composite Materials* **26**, 2706 (1992).
- [32] C. Kassapoglou, *Modeling the Effect of Damage in Composite Structures - Simplified Approaches*, 1st ed. (John Wiley & Sons Ltd, 2015).
- [33] J. W. Mar, M. J. Graves, and D. P. Maass, *Effect of compression-compression fatigue on balanced graphite/epoxy laminates with holes*, *J. Aircraft* (1980).
- [34] P. Prabhakar and A. M. Waas, *Interaction between kinking and splitting in the compressive failure of unidirectional fiber reinforced laminate composites*, *Composite Structures* **98**, 85 (2013).

- [35] P. Berbinau, C. Soutis, and I. A. Guz, *Compressive failure of 0 degree unidirectional carbon-fibre-reinforced plastic (cfrp) laminates by fibre microbuckling*, *composites Science and Technology* **59**, 1451 (1999).
- [36] M. H. Aliabadi, ed., *Woven Composites* (Imperial College Press, 2015).
- [37] S. H. Lee and A. M. Waas, *Compressive response and failure of fiber reinforced unidirectional composites*, *International Journal of Fracture* **100**, 275 (1999).
- [38] Y. Thollon and C. Hochard, *A general damage model for woven fabric composite laminates up to first failure*, *Mechanics of Materials* **41**, 820 (2009).
- [39] C. Bordreuil and C. Hochard, *Finite element computation of woven ply laminate composite structures up to rupture*, *Applied Composite Materials* **11** (2004).
- [40] C. Kassapoglou, *Predicting the Structural Performance of Composite Structures Under Cyclic Loading*, Ph.D. thesis, Delft University of Technology (2012).
- [41] Y. Mahadik and S. R. Hallet, *Effect of fabric compaction and yarn waviness on 3d woven composite compressive properties*, *Composites part A: Applied Science and Manufacturing* **42**, 1592 (2011).
- [42] M. Mitrovic and G. P. Carman, *Effect of fatigue damage in woven composites on thermo-mechanical properties and residual compressive strength*, *Journal of Composite Materials* **30**, 164 (1996).
- [43] Z.-M. Huang, *Fatigue life prediction of a woven fabric composite subjected to biaxial cyclic loads*, *Composites Part A Applied Science and Manufacturing* **33**, 253 (2002).
- [44] A. P. Vassilopoulos, W. Van Paepegem, M. Kawai, M. Quaresimin, P. Abel, A. N. Anoshkin, P. Brondsted, P. A. Carraro, V. Carvelli, T. Gries, M. Gude, A. Jain, I. Koch, C. Lauter, S. Lomov, A. Mouritz, M. Ricotta, R. Talreja, T. Troester, K. Vallons, J. Xu, J. Zangenberg, and V. Zuiko, *Fatigue of Textile Composites*, edited by V. Carvelli and S. V. Lomov (Woodhead Publishing, 2015).
- [45] C. A. Squires, K. H. Netting, and A. R. Chambers, *Understanding the factors affect the compressive testing of unidirectional carbon fibre composites*, *Composites Part B* **38** (2007).
- [46] H. Hsiao and I. Daniel, *Effect of fiber waviness on stiffness and strength reduction of unidirectional composites under compressive loading*, *Composites Science and Technology* **56**, 581 (1996).
- [47] S. Daggumati, I. De Baere, W. Van Paepegem, J. Degrieck, J. Xu, S. V. Lomov, and I. Verpoest, *Fatigue and post-fatigue stress-strain analysis of a 5-harness satin weave carbon fibre reinforced composite*, *Composites Science and Technology* **74**, 20 (2013).
- [48] R. K. Fruehmann, J. M. Dulieu-Barton, and S. Quinn, *Assesment of fatigue damage evolution in woven composite materials using infra-red techniques*, *composites Science and Technology* **70**, 937 (2010).
- [49] S. Wicaksono and G. B. Chai, *Life prediction of woven cfrp structure subject to static and fatigue loading*, *Composite Structures* **119**, 185 (2015).
- [50] J. S. Tate and A. D. Kelkar, *Stiffness degradation model for biaxial braided composites under fatigue loading*, *Composites: part B* **39**, 548 (2008).
- [51] W. Van Paepegem and J. Degrieck, *Experimental set-up for and numerical modelling of bending fatigue experiments on plain woven glass/epoxy composites*, *Composite Structures* **51**, 1 (2001).
- [52] W. Van Paepegem and J. Degrieck, *Fatigue degradation modelling of plain woven glass/epoxy composites*, *Composites part A: Applied Science and Manufacturing* **32**, 1433 (2001).
- [53] W. Van Paepegem and J. Degrieck, *A new coupled approach of residual stiffness and strength for fatigue of fibre-reinforced composites*, *International Journal of Fatigue* (2002).

- [54] R. Kumar and R. Talreja, *Fatigue damage evolution in woven fabric composites*, in *Structures, Structural Dynamics, and Materials* (2000).
- [55] J. Montesano, Z. Fawaz, and H. Bougherara, *Non-destructive assesment of the fatigue strength and damage progression of satin woven fiber reinforced polymer matrix composites*, *Composites Part B Engineering* **71**, 122 (2015).
- [56] K. Vallons, S. V. Lomov, and I. Verpoest, *Fatigue and post-fatigue behaviour of carbon/epoxy non-crimp fabric composites*, *Composites Part A Applied Science and Manufacturing* **40**, 251 (2009).
- [57] W. Ling, G. Yingnan, and L. Yulong, *An experimental study on the mechanical performance and damage evolution of woven fabric e-glass fiber reinforced epoxy composite*, *Key Engineering Materials* **417-418**, 137 (2010).
- [58] A. P. Vassilopoulos, R. P. L. Nijssen, N. L. Post, J. J. Lesko, S. W. Case, W. Van Paeppegem, E. F. Georgopoulos, M. Kawai, Y. Liu, M. M. Shokrieh, F. Taheri-Behrooz, M. Quaresimin, T. P. Philippidis, E. N. Eliopoulos, T. Keller, T. T. Assimakopoulou, and R. Rafiee, *Fatigue Life Prediction of Composites and Composite Structures*, edited by A. P. Vassilopoulos (Woodhead Publishing in Materials, 2010).
- [59] C. Soutis, N. A. Fleck, and P. A. Smith, *Compremon fatigue behaviour of notched carbon fibre-epoxy laminates*, *International Journal of Fatigue* **13**, 303 (1991).
- [60] R. Nijssen, O. Krause, and T. Philippidis, *Benchmark of lifelife rediction methodologies*, [Optimat blades Technical report](#) (2004).
- [61] L. Toubal, M. Karama, and B. Lorrain, *Damage evolution and infra-red thermography in woven composite laminates under fatigue loading*, *International Journal of Fatigue* **28**, 1867 (2006).
- [62] J. F. Harper, N. A. Miller, and S. C. Yap, *Problems associated with the compression testing of fibre reinforced plastic composites*, *Polymer Testing* **12**, 15 (1993).
- [63] *D 3410/d 3410m - standard test method for compressive properties of polymer matrix composite materials with unsupported gage section by shear loading*, .
- [64] *D 3039/d 3039m - standard test method for tensile properties of polymer matrix composite materials*, .
- [65] *D 3518/d 3518m – 94 - standard test method for in-plane shear response of polymer matrix composite materials by tensile test of a $\pm 45^\circ$ laminate*, .
- [66] N. McCormick and J. Lord, *Digital image correlation*, *Materials Today* **13**, 52 (2010).
- [67] T. Chu, W. Ranson, M. Sutton, and W. Peters, *Applications of digital image correlation techniques to experimental mechanics*, *Experimental Mechanics*, 232 (1985).
- [68] J. Abanto-Bueno and J. Lambros, *Investigation of crack growth in functionally graded materials using digital image correlation*, *Engineering Fracture Mechanics* **69**, 1695 (2002).
- [69] S. R. McNeill, W. H. Peters, and M. Sutton, *Estimation of stress intensity factor by digital image correlation*, *Engineering Fracture Mechanics* **28**, 101 (1987).
- [70] F. Laurin, J.-S. Charrier, D. L  v  que, J.-F. Maire, A. Mavel, and P. Nu  ez, *Determination of the properties of composite materials thanks to digital image correlation measurements*, *Procedia IUTAM* **4** (2012).
- [71] S. Roux, F. Hild, and H. Leclerc, *Full field measurements and identification in solid mechanics - mechanical assistance to dic*, *Procedia IUTAM* **4**, 159 (2012).
- [72] Y. Wang, H. Xu, D. L. Erdman, M. J. Starbuck, and S. Simunovic, *Characterization of high-strain rate mechanical behavior of az31 magnesium alloy using 3d digital image correlation*, *Advanced Engineering Materials* **13**, 943 (2011).

- [73] J. C. Faes, A. Rezaei, W. Van Paepegem, and J. Degrieck, *Meso-Scale Analysis of Ductile Steel Fabric-Epoxy Composites: Numerical Modelling and Experimental Validation*, techreport (Department of Materials Science and Engineering, Faculty of Engineering and Architecture, Ghent University, 2014).
- [74] G. Sendeckyj, *Life prediction for resin-matrix composite materials in Fatigue of Composite Materials*, edited by K. Reifsnider (Elsevier, 1991).
- [75] P. Ladeveze, *Multiscale modelling and cocomputation strategies for composites*, International Journal for Numerical Methods in Engineering **60** (2004).
- [76] J. Degrieck and W. Van Paepegem, *Fatigue damage modeling of fibre-reinforced composite materials: Review*, Appl Mech Rev **54**, 279 (2001).
- [77] M. Kawai, K. Yang, and S. Oh, *Effect of alternate change in stress ratio on fatigue strength of woven fabric cfrp laminate and life prediction using the anisomorphic cfl diagram*, 16th European Conference on Composite Materials (2014).
- [78] C. Kassapoglou, *Fatigue life prediction of composite structures under constant amplitude loading*, Journal of Composite Materials **41**, 2737 (2007).
- [79] C. Kassapoglou, *Fatigue of composite materials under spectrum loading*, Composites Part A Applied Science and Manufacturing **41**, 663 (2010).
- [80] C. Kassapoglou and M. Kaminski, *Modeling damage and load redistribution in composites under tension-tension fatigue loading*, Composites Part A Applied Science and Manufacturing **42**, 1783 (2011).
- [81] A. Vania and V. Carvellie, *Fitting approach of the fatigue tensile response of textile composite materials*, Destech publications, Inc. (2010).
- [82] W. Van Paepegem and J. Degrieck, *Modelling damage and permanent strain in fibre-reinforced composites under in-plane fatigue loading*, composites Science and Technology **63**, 677 (2003).
- [83] W. Van Paepegem and J. Degrieck, *Simulating in-plane fatigue damage in woven glass fibre-reinforced composites subject to fully reversed cyclic loading*, Fatigue and Fracture of Engineering Materials and Structures **27** (2004).
- [84] W. Van Paepegem, *Fatigue of Textile Composites*, edited by V. Carvelli and S. V. Lomov, Woodhead Publishing Series in Composites Science and Engineering (Elsevier, 2005).
- [85] C. Hochard, J. Payan, and C. Bordreuil, *A progressive first ply failure model for woven ply cfrp laminates under static and fatigue loads*, International Journal of Fatigue **28**, 1270 (2006).
- [86] C. Hochard and Y. Thollon, *A general damage model for woven ply laminates under static and fatigue loading conditions*, International Journal of Fatigue **32** (2010).
- [87] C. Hochard, M. St., and Y. Thollon, *Fatigue of laminated composite structures with stress concentrations*, Composites: part B **65**, 11 (2014).
- [88] M. Benamira, C. Hochard, and A. Haiahem, *Behaviour to failure of fibre mat reinforced composite under combined loading conditions*, Composites: part B **42**, 1412 (2011).
- [89] J. Payan and C. Hochard, *Damage modelling of laminated carbon/epoxy composites under static and fatigue loadings*, International Journal of Fatigue **24**, 299 (2002).
- [90] U. Icardi, S. Locatto, and A. Longo, *Assessment of recent theories for predicting failure of composite laminates*, Transactions of the ASME **60**, 76 (2007).
- [91] S. Jacques, I. De Baere, and W. Van Paepegem, *Application of periodic boundary conditions on multiple part finite element meshes for the meso-scale homogenization of textile fabric composites*, composites Science and Technology **92**, 41 (2014).

- [92] P. Potluri, A. Manan, R. J. Young, and S. Y. Lei, *Experimental validation of micro-strains predicted by meso-scale models for textile composites*, in *Structures, Structural Dynamics and Materials Conference* (2007).
- [93] W. Ruijter, J. Crookston, A. Long, and A. Jones, *Cocomputation meso-scale analysis of textile composites using adaptive finite element analysis*, in *Structures, Structural Dynamics and Materials Conference* (2006).
- [94] N. K. Naik, S. I. Tiwari, and R. S. Kumar, *An analytical model for compressive strength of plain weave fabric composites*, *composites Science and Technology* **63**, 609 (2003).
- [95] N. K. Naik, K. S. Reddy, and B. R. N, *Damage evolution in woven fabric composites: Transverse static loading*, *Journal of Composite Materials* **37**, 21 (2003).
- [96] J. Xu, V. Lomov, I. Verpoest, S. Daggumati, W. Van Paepegem, J. Degrieck, and M. Olave, *A progressive damage model of textile composites on meso-scale using finite element method: Static damage analysis*, *Journal of Composite Materials*, 1 (2014).
- [97] R. Mishra, *Meso-scale finite element modeling of triaxial woven fabric for composite in-plane reinforcement properties*, *Textile Research Journal* **83**, 1836 (2013).
- [98] C. Zhang and X. Xu, *Finite element analysis of 3d braided composites based on three unit-cells models*, *Composite Structures* **98**, 130 (2013).
- [99] C. Zhang and W. K. Binienda, *A meso-scale finite element model for simulating free-edge effect in carbon/epoxy textile composite*, *Mechanics of Materials* **76**, 1 (2014).
- [100] *Iso 7500-1 - verification of static uniaxial testing machines, part 2: Tension/compression testing machines - verification and calibration of the force-measuring system*, (2004).
- [101] I. De Baere, W. Van Paepegem, M. Quaresimin, and J. Degrieck, *On the tension-tension fatigue behaviour of a carbon reinforced thermoplastic part i: Limitations of the astm d3039/d3479 standard*, *Polymer Testing* **30**, 625 (2011).
- [102] J. Z. Hansen, P. Brøndsted, and R. Østergaard, *The Effect of Fibre Architecture on Fatigue Life-time of Composite Materials*, phdthesis, Technical University of Denmark (2013).
- [103] B. Abel, A. Schumacher, and M. Bartsch, *Application of gradient based algorithms for robust shape optimization of a tensile test specimen*, *Proceedings in Applied Mathematics and Mechanics* **8**, 10025 (2008).
- [104] K. M. Jespersen, J. Z. Hansen, and L. P. Mikkelsen, *Micromechanical investigation of fatigue damage in unidirectional fibre composites*, in *6th International Conference on Fatigue of Composites* (2015).
- [105] C. Kassapoglou, *Design and Analysis of Composite Structures - With Applications to Aerospace Structures*, 2nd ed. (John, 2013).
- [106] D. O. Adams, *Comparative Testing to Assess the Equivalence of CEN and ASTM test methods for Composite Materials*, techreport (Department of Mechanical Engineering - University of Utah, 2005).
- [107] J. C. Malzahn and J. M. Schultz, *Tension-tension and compression-compression fatigue behavior of and injection-molded short-glass-fiber/poly(ethylene terephthalate) composite*, *composites Science and Technology* (1986).
- [108] T. R. Porter, *Compression And Compression Fatigue Testing Of Composite Laminates*, Tech. Rep. (National Aeronautics and Space Administration, 1982).
- [109] J. A. Rice, *Mathematical Statistics and Data Analysis* (Thomson Brooks/Cole, 2007).

-
- [110] G. Sendeckyj, *Test methods and design allowables for fibrous composites, astm stp 734*, (American Society for Testing and Materials, 1981) Chap. Fitting Models to Composite Materials Fatigue Data, pp. 245–260.
- [111] J. Tomblin and W. Seneviratne, *Determining the fatigue life of composite aircraft structures using life and load-enhancement factors*, DOT/FAA/AR-10/6 (2011).
- [112] United States of America Department of Defense, *Composite Materials Handbook Volume 1. Polymer Matrix Composites Guidelines for Characterization of Structural Materials*, edited by United States of America Department of Defense, Vol. 1 (CRC Press, 2002).